RENSIT:
RadioElectronics. NanoSystems. Information Technologies

Journal "Radioelectronics. Nanosystems. Information Technologies" (abbr. RENSIT)
publishes original articles, reviews and brief reports, not previously published, on topical problems in **radioelectronics (including biomedical) and fundamentals of information, nano- and biotechnologies and adjacent areas of physics and mathematics.**

Designed for **researchers, graduate students, physics students of senior courses and teachers**.
It turns out **4 times a year** (that includes 4 issues)

Authors of journal are academicians, corresponding members and foreign members of Russian Academy of Natural Sciences (RANS) and their colleagues,
as well as other russian and foreign authors on presentation of their manuscripts by the members of RANS, which can be obtained by authors before sending articles to editors.
And also after its receiving - on recommendation of a member of editorial board of journal, or another member of Academy of Natural Sciences, that gave her opinion on article at request of editor.
The editors will accept articles in both **Russian and English** languages.

Articles are internally peer reviewed (**double-blind peer review**) by members of the Editorial Board.
Some articles undergo external review, if necessary.

Journal RENSIT is included in the **DB SCOPUS (21.10.2017, Elsevier, Amsterdam, Netherlands), EBSCO Publishing,** in the international abstracts database - **Ulrich's International Periodicals Directory** (USA, New York, http://www.ulrichsweb.com), in the **AJ and DB VINITI RAS** (http://www.viniti.ru), and DB **Russian Science Citation Index (RSCI** http://elibrary.ru/project_risc.asp). Included in the **List of Higher Attestation Commission of the Ministry of Education and Science of the Russian Federation (15.01.2018, No. 757).**
Full-text content is posted in the DB of the **Russian Scientific Electronic Library**
- information resource on the Internet http://elibrary.ru and is available for registered users.
And also - in Open Access **CyberLeninka NEB** of Russian Federation http://cyberleninka.ru.
On journal's website http://www.rensit.ru posted metadata publications
and **RENSIT: Radioelectronics. Nanosystems. Infomation Technologies - english version** (cover-to-cover translation) of journal, which is a party to **CrossRef.**

The founder - the **Russian Academy of Natural Sciences**
Publisher - Publishing Center of the Russian Academy of Natural Sciences
Publisher Address: 119002 Moscow, per. Sivtsev Vrazhek 29/16

CONTENTS

RUSSIAN ACADEMY OF NATURAL SCIENCES

DEPARTMENT OF RADIOELECTRONICS, NANOPHYSICS AND INFORMATION TECHNOLOGIES PROBLEMS

RENSIT:

RADIOELECTRONICS. NANOSYSTEMS. INFORMATION TECHNOLOGIES.

2022, Vol. 14, no. 4

FOUNDED IN 2009
4 ISSUES PER YEAR
MOSCOW

ISSN 2414-1267

The journal on-line is registered by the Ministry of Telecom and Mass Cjmmunications of the Russian Federation. Certificate El. no. FS77-60275 on 19.12.2014

EDITORIAL BOARD ADDRESS
218-219 of., 7 b., 11, Mokhovaya str., 125009 MOSCOW, RUSSIAN FEDERATION,
TEL. **+7 495 629 3368**
FAX **+7 495 629 3678** FOR GRACHEV

DOI: 10.17725/rensit.2022.14.351

Excitation of Circularly Polarized Electromagnetic Waves Based on Striped Transmission Lines

Dmitry V. Polozov

Moscow Power Engineering Institute, https://mpei.ru/
Moscow 111250, Russian Federation
E-mail: dmitry_polozov@mail.ru,

David A. Gabrielyan, Ansar R. Safin, Dmitry V. Kalyabin

Kotelnikov Institute of Radioengineering and Electronics of RAS, http://www.cplire.ru/
Moscow 125009, Russian Federation
E-mail: davidgabrielyan1997@gmail.com, arsafin@gmail.com, dmitry.kalyabin@phystech.edu

Received 18 November 2022, peer-reviewed 25 November 2022, accepted 02 December 2022

Abstract: **The article investigates the scheme of excitation of an electromagnetic field with circular polarization due to crossed strip transmission lines. Two variants are compared: coplanar and microstrip transmission lines that excite circular polarization of the magnetic field in the space above the intersection of strip structures. The degree of ellipticity of the field at the intersection of strip structures can be changed by changing the phase mismatch between exciting oscillation sources. Modeling of these devices in the computer-aided design system made it possible to quantify the amplitudes of the components of the electromagnetic field, from which the ellipticity coefficient was calculated at different values of frequency and phase. The obtained results allow us to determine the conditions necessary for the realization of circular polarization of the magnetic field. The studied structures are planned to be used in an integral design to excite circular polarization oscillations in magnetic micro- and nanostructures.**

Keywords: **circular polarization, strip transmission line, ellipticity coefficient, magnetism, ferromagnetic resonance**

Acknowledgements: The work was carried out within the framework of the state task of the Ministry of Science and Higher Education of the Russian Federation (topic No. FFWZ-2022-0015).

For citation: Dmitry V. Polozov, David A. Gabrielyan, Ansar R. Safin, Dmitry V. Kalyabin. Excitation of Circularly Polarized Electromagnetic Waves Based on Striped Transmission Lines. *RENSIT: Radioelectronics. Nanosystems. Informanion technologies*, 2022, 14(4):351-358e. DOI: 10.17725/rensit.2022.14.351.

Contents

1. INTRODUCTION

Excitation of electromagnetic (EM) waves with controlled magnetic field polarization is a crucial task in the area of magnetism. Changing the polarization of EM waves gives a wider possibility to excite own

frequencies of different resonators. Excitation of linearly polarized radiation is a standard problem of practical electrodynamics. On the other hand, the excitation of EM waves with circular or, more widely, elliptical polarization presents significant difficulties. The elementary way to excite circularly polarized EM waves is to use cavity waveguides and resonators [1-8]. At the same time there is a necessary to implement circular or elliptical polarized EM waves in integral design using strip transmission lines in the microwave frequency range.

In this work we consider the scheme of EM waves excitation with circular polarization due to the crossed stripline transmission lines [9]. We are interested in the realization of circular polarization of the magnetic component of EM waves, which is explained by the need to excite different modes of oscillations of magnetic materials: ferro-, ferri- and antiferromagnets in the microwave range, up to the subterahertz frequency range (at frequencies up to 100 GHz). Comparison of two variants was carried out: coplanar and microstrip transmission lines, which excite circular polarization of the magnetic field in the space above the intersection of the strip structures. Ellipticity degree of the field at the intersection of strip structures can be changed by changing the phase mismatch between the excitation sources of oscillations. Modeling of these devices in the system of computer-aided design allowed to quantify the amplitudes of electromagnetic field components, according to which the ellipticity coefficient at different values of frequency and phase was calculated. These results make it possible to determine the conditions necessary for realization of circular polarization of the magnetic field. The investigated structures are planned to be used in integral design for excitation of circular polarization oscillations in magnetic micro- and nanostructures.

2. MODELING AND CALCULATION OF A CROSSED COPLANAR TRANSMISSION LINE

To excite EM waves with circularly polarized magnetic field, it is possible to use two grounded coplanar transmission lines and place them perpendicular to each other so that at the crossroads the addition of electromagnetic oscillations takes place (see **Fig. 1**). The result of adding the two waves will be a wave with polarization depending on the spatial and temporal configurations of the folding waves. In order to achieve circular polarization of the magnetic field it is necessary to adhere to the condition of spatial and temporal quadrature in the excitation of EM waves with two crossed transmission line [7,8]. The result of modeling of this transmis-sion line is the dependence of changes in parameters, characterizing EM waves polarization at the intersection of transmission lines on changes of frequency and phase. Fig. 1 shows transmission line, which has four

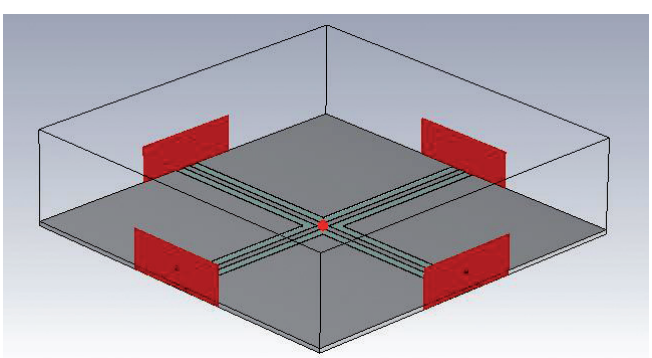

Fig. 1. *Model of the crossed coplanar transmission line.*

ports. At that, two adjacent inputs excite oscillations in the transmission line. Signals excited from these ports will be different by the value of the initial phase specified in the simulation.

The ferrite material can be placed at the point of maximum of circular polarization of the magnetic field. For this purpose, it is necessary to investigate the electric and magnetic components of the fields at the intersection of the two coplanar transmission lines, because it is at the intersection that the vectors will be added and the circular polarization will appear. Investigated magnetic material has a height of 3 mm, therefore field measurement is carried out in three points, on the surface of the transmission line H = 0 mm and on the heights H = 1.5 mm and H = 3 mm.

For a quantitative assessment of the magnetic field polarization parameter ellipticity coefficient will be used, which is calculated by the following expression [6]:

$$k = \frac{|H_r| - |H_l|}{|H_r| + |H_l|}, \quad (1)$$

where the quadrature components of the fields

$$H_r = \frac{1}{\sqrt{2}}(H_x + jH_y),$$

$$H_l = \frac{1}{\sqrt{2}}(H_x - jH_y),$$

where $H_{x,y}$ – are the magnetic field components.

The ellipticity coefficient can take values from –1 to 1, where k = 0 – linear polarization, and k = 1 (k = –1) – right (left) circular polarization. Below are numerically obtained data of magnetic field vector components, and calculated values of ellipticity coefficients.

Table1

Numerical data of magnetic field components at 20 GHz with phase difference of 90 degrees.

H, A/m / H, mm	ReH_x	ImH_x	ReH_y	ImH_y	k
0	17.5	27	-25.5	18	-0.95
1.5	1.1	1.9	-1.9	1.2	-0.96
3	0.14	0.45	-0.42	0.17	-0.91

The results obtained from **Table 1** show that in each of the three calculated points elliptic polarization is realized with ellipticity coefficient k = –0.94 (average value), which is close to circular polarization value. The total magnetic field vector will be maximum at the surface of the coplanar transmission line and will decrease with distance, so the minimum field value will be at the height of 3 mm.

For the analysis of the magnetic field amplitude, determine its dependence on the height above the coplanar transmission line structure.

We show in **Fig. 2** that the maximum value of the field is limited by the value of H = 40 A/m. The field of EM waves spreading perpendicular to the transmission line decreases. EM wave field tends to zero when spreading along the transmission line. At a height

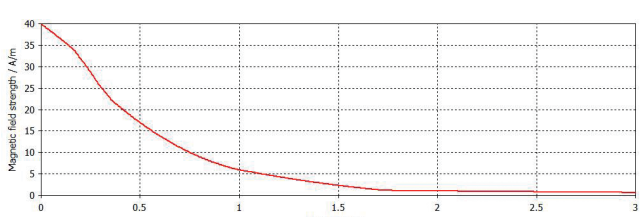

Fig. 2. *The H-field amplitude dependence on the distance at 20 GHz, for the model of crossed coplanar transmission line.*

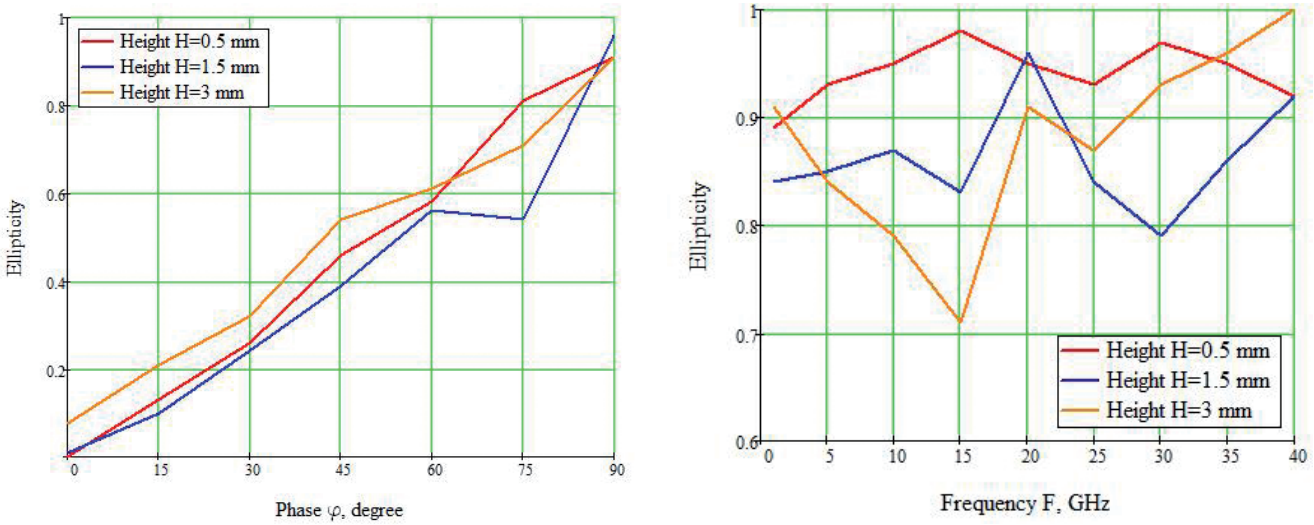

a *b*

Fig. 3. *Ellipticity coefficient (K) dependence on the phase difference (a) of the excited electromagnetic waves and on the frequency (b) at different heights in the structure of crossed transmission lines*

of 3 mm, the field has a value of H = 1A/m. **Fig. 3***a* plots the dependence of the ellipticity coefficient on the phase difference of the excited EM waves. It can be seen that with approaching the phase difference of excited oscillations in 90 degrees, the ellipticity coefficient approaches 1 at different heights above the structure. In Fig. 3*b* plots the dependence of the ellipticity coefficient on frequency (from 0 to 40 GHz). It can be seen that for different values of the height above the structure, there is an optimal value, which corresponds to the maximum ellipticity coefficient. At the same time, the ellipticity coefficient decreases with increasing distance above the structure.

3. MODELING AND CALCULATION OF A CROSSED COPLANAR TRANSMISSION LINE WITH GROUNDING

As a second example of crossed stripline transmission lines to excite EM waves with circular polarization, consider a broadband transmission line consisting of two coplanar transmission lines crossed at right angles, with a short-circuit at the end. Similar in purpose design can be implemented without resorting to two different sources of EM waves with a phase difference of 90 degrees, but then it is necessary to observe the difference in distances to the crossing, so that the electromagnetic wave, reaching the center, had a phase delay relative to the second in 90 degrees. To idealize and model the short-circuit transmission line, a model was used in which the phase difference is set in the power sources.

In [7] the dimensions of a similar device are presented, but this design is difficult to imple-ment in practice, since high-tech production is required. Specifically, the width of the metal conductor of 10 (μm) and a gap of about 5 (μm) is difficult to implement, in view of the lower accuracy of the laser, as a consequence already at the stage of production model, will not meet the stated characteristics. Therefore, a transmission line model with excellent geometry was taken as a basis. Also, this type of transmission line is easy to implement in practice, as it has the

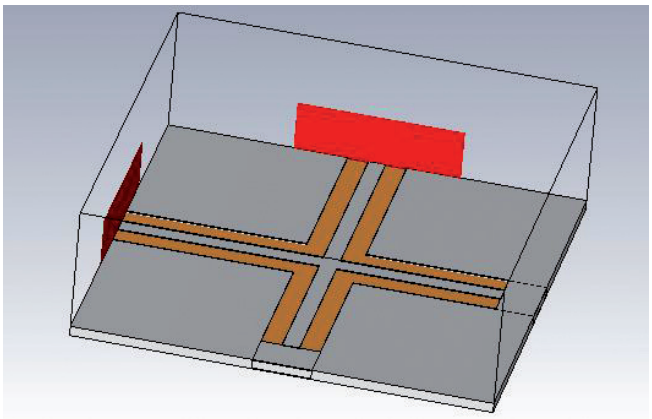

Fig. 4. *Model of the crossed coplanar short-circuit transmission lines.*

dimen-sions often used in the microwave range. In this regard, the real device will have close characteristics compared to the device calculated in the CAD systems. In **Fig. 4** the construction of the coupled transmission lines from the CAD tool is shown in Fig. 4.

Fig. 5 shows the dependence of the magnetic field amplitude on the height above the coplanar transmission line structure, and **Table 2** shows the calculated values of the magnetic field component amplitudes at three points.

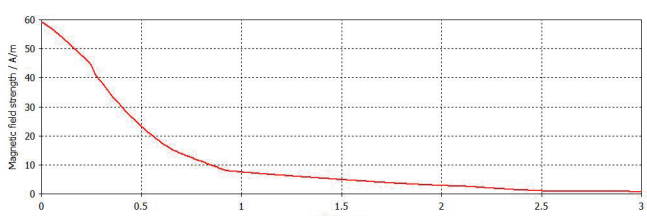

Fig. 5. *H-field amplitude dependence on distance at 20 GHz for the model crossed coplanar short-circuit transmission lines.*

Table 2
Numerical data of magnetic field components at 20 GHz

H, A/m / H, mm	ReH_x	ImH_x	ReH_y	ImH_y	k
0	-13.7	-55.2	40	11.2	-0.53
1.5	-1.31	-4.03	3.05	0.96	-0.48
3	0.15	-0.6	0.38	0.3	-0.61

Comparing the plots of magnetic field spread in the two coplanar transmission lines, namely Fig. 2 and Fig. 5, it follows that the crossed coplanar transmission line with short-circuit has a higher value of excitation of circular polarization of the magnetic field. The field values at the surface of the transmission line are 1.5 times greater than those of the model without short-circuiting in Fig. 2. The amplitude of the field decreases according to the same law, hence, at a distance of 3 mm the amplitude value is higher, and as a consequence, greater excitation of the magnetic material.

According to the calculated amplitudes of the magnetic field components, the ellipticity coefficient equal to one was not obtained, on average it is –0.54. This indicates that the transmission line values are not optimized. Despite this, according to the dependences of the field amplitude on the length of Fig. 2, 5 it can be seen that for a short-circuited transmission line we can obtain ellipticity characteristics better than in a transmission line with 4 ports, and therefore there is more effective excitation.

4. MODELING AND CALCULATION OF MEANDER TYPE TRANSMISSION LINE

Below are the results of simulation of another type of transmission line, which excites circular polarization of the magnetic field. The structure is a microstrip transmission line, in which the strips are arranged in the form of a meander, where the addition of two waves also occurs, result-ing in the realization of circular polarization [11]. In contrast to the previous types, this transmis-sion line has

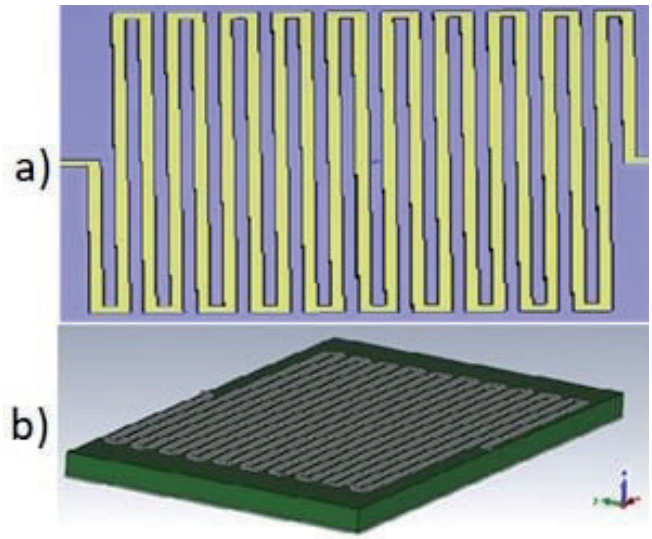

Fig. 6. *Model of microstrip transmission line of meander type: a) top view, b) side view.*

a significant disadvantage, which is that it operates only at a certain frequency, that is, it is narrowband, whereas the transmission lines discussed above are broadband [4]. The advantage of this transmission line in comparison with those considered above is the ability to im-plement circular polarization of the EM wave in the plane perpendicular to the plane of the structure, whereas the transmission lines considered in the previous section, implement circular polar-ization of the field in the plane of the sample. The geometry of the structure is presented in **Fig.** 6. The determination of the amplitude of the magnetic field vectors in three points and the calcu-lation of the ellipticity coefficient is performed according to formula (1) and is presented in **Table 3**.

Table 3
Numerical data of magnetic field components at 20 GHz.

H, A/m / H, mm	ReH_x	ImH_x	ReH_y	ImH_y	k
0	18	6	-8	-15	0.4
1.5	-2.5	-1.4	1.1	3.4	0.38
3	-0.07	-0.12	-0.19	-0.06	0.35

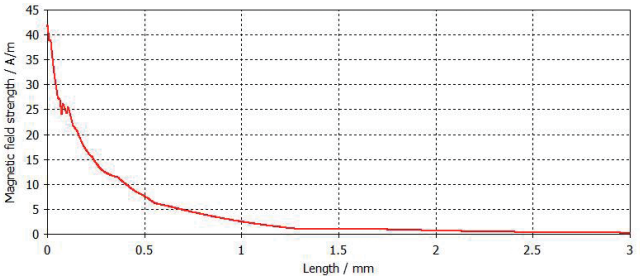

Fig. 7. *H-field amplitude dependence on length at 20 GHz, for a meander-type microstrip transmission line model.*

According to the calculation results, it can be seen that the transmission line has an elliptical polarization of the magnetic field. **Fig. 7** shows the dependence of the amplitude of the H-field vector on the height above the transmission line structure by analogy with Figs. 2, 5.

This transmission line has a high amplitude on the surface of the strip, but since circular polarization is formed only between the lines, this polarization only in some points will be circular, which significantly limits the use of this structure to excite EM waves in magnetic materials. There also remains the problem of the complexity of implementation in practice, since to obtain high characteristics of the amplitude of the magnetic field it is required to reduce the size of both the board and the width of the strip, at a size of 0.01 mm will be a large error in manufacturing, and as a consequence, the deterioration of the characteristics of obtaining circular polarization.

5. DISCUSSION OF RESULTS

Analyzing **Table 4**, it can be concluded that the crossed coplanar transmission line is the best option for the excitation of magnetic materials in a wide range of frequencies. Although this device does not have the maximum amplitude of the

Table 4

Comparison of transmission line characteristics.

Parameter	Ellipticity coefficient (k)	Frequency Range (GGz)	Amplitude of the magnetic field H on the surface of the line (A/m)	Feasi-bility
Crossed coplanar transmission line	-1	1-40	40	good
Crossed coplanar short-circuit transmission line	-0.54	1-40	59	good
Meander type transmission line	-0.38	20	42	bad

magnetic field on the surface of the strip, but provided that the EM wave with circular polarization more effectively excites the magnetic material, we can neglect the amplitude in favor of the ellipticity factor, since this type of transmission line excites the polarized magnetic field with the ellipticity factor $|k| \approx 1$.

6. CONCLUSION

The CAD modeling performed in this work made it possible to evaluate numerically the possibility of designing strip structures that excite EM waves with circular polarization. It was realized that effective excitation of magnetic materials requires circular polarization of the magnetic field in the location space of this material. For this reason, transmission lines with different structures were investigated. Based on the results of numerical simulations, it can be concluded that the best option for excitation of ferrite materials, in the location space of a given material, in an integral configuration would be a crossed coplanar transmission line with loaded outputs. In this configuration, circular polarization of the EM waves magnetic component is realized, with the ellipticity coefficient practically equal to 1. It can be noted that this type of transmission line is easy to implement in practice, which is its great advantage. Currently, the construction of integrated microwave circuits is trying to minimize the size of the main components. Analyzing the frequency and phase dependence for different transmission lines, it can be concluded that there is a possibility to control the ellipticity coefficient, changing the phase difference of oscillation sources. Note that the values of ellipticity coefficients at different ratios between the phases of excited oscillations will be constant and do not change from the frequency in a given transmission line structure.

REFERENCES

1. Kolomeitsev VA, Kovryakov PV, Semenov AE, Drogaitseva OV. Excitation of electro-magnetic field in a rectangular resonator partially filled with dielectric material. *Vestnik SGTU,* 2014, 1(77):47-54 (in Russ.).
2. Nelson CE. Circularly Polarized Microwave Cavity Filters. *IRE Transactions on Micro-wave Theory and Techniques*, 1957, 5(2):136-147.
3. Dionne GF, Oates DE, Temme DH, Weiss JA. Superconductivity for Improved Micro-wave Ferrite Devices. *The Lincoln Laboratory Journal*, 1996, 9(1):19-32.
4. Mohebbi HR, Majedi AH. CAD model for circuit parameters of superconducting-based hybrid planar transmission lines. *Supeconductor Science and Technology*, 2009, 22(1):12.
5. Sazonov DM. *Antenny i ustroystva SVCH* [Antennas and microwave devices].

Moscow, Vysshaya shkola Publ., 1988, 432 p. (in Russ.).

6. Kogan BL. *Polyarizatsionnye kharakteristiki antenn* [Polarization characteristics of antennas]. Moscow, MEI Publ., 2013, 42 p. (in Russ.).
7. Kan I, Soeno Y, Roppongi T, Nozaki Y. Circularly polarized magnetic field generated by two microfabricated crossed coplanar waveguides. *Applied Physics Letters*, 2017, 110(20).
8. Broeder FJ, Janssen E, Hoving W, Zeper WB. Perpendicular magnetic anisotropy and co-ercivity of Co/Ni multilayers. *IEEE Transactions on Magnetics,* 1992, 28(5):2760-2765.
9. Dionne GF, Oates DE, Temme DH. YBCO/ferrite low-loss microwave phase shifter. *IEEE Transactions on Applied Superconductivity*, 1995, 5(2):2083-2086.
10. Lax B, Button KJ. Microwave ferrites and ferrimagnetics. *Solid State Electronics,* 1963, 6(4):392-393.
11. Lax B. Frequency and Loss Characteristics of Microwave Ferrite Devices. *Proceedings of the IRE*, 1956, 44(10):1368-1386.

DOI: 10.17725/rensit.2022.14.359

The Own Radiothermal Radiation of the Earth's Surface Receiving Process Modeling

Igor A. Sidorov, Alexander G. Gudkov, Sergey V. Chizhikov
Bauman Moscow State Technical University, https://bmstu.ru/
Moscow 105005, Russian Federation
E-mail: igorasidorov@yandex.ru, profgudkov@gmail.com, chigikov95@mail.ru

Evgeny P. Novichikhin
Kotelnikov Institute of Radioengineering and Electronics of RAS, Fryazino Branch, http://fire.relarn.ru/
Fryazino 141190, Moscow Region, Russian Federation
E-mail: *epnov@mail.ru*

Andrey G. Bolotov, Nikolay F. Khokhlov
Russian State Agrarian University-Moscow Timiryazev Agricultural Academy, https://www.timacad.ru/
Moscow 127434, Russian Federation
E-mail: agbolotov@gmail.com, dok-hohlov.ru@mail.ru

Igor O. Porokhov
Berg Central Scientific-Research Radioengineering Institute, http://cnirti.ru/
Moscow 107078, Russian Federation
E-mail: ds4@cnirti.ru

Received July 27, 2022, peer-reviewed August 03, 2022, accepted August 10, 2022

Abstract: **The receiving model of the own soil radiothermal radiation by a bipolarized microwave radiometer when remote sensing the soil moisture from an unmanned aerial vehicle on low altitude is considered. The simulation is carried out taking into account the receiving antenna pattern with side lobes. The height, speed of the carrier and the main lobe axis angle are taken into account. The main parameters of the microwave radiometer for remote determination of portraits of moistened soils are given. The Earth's surface is modeled by a two-dimensional distribution function of the soil permittivity on the thickness of the near-surface layer and a deeper layer with a different permittivity value. The two-dimensional permittivity distribution function represents as "checkerboard" with a periodic change in the permittivity of the soil by "cells". Both the proper radiothermal radiation of the soil and the relict sky radiation of the celestial sphere, re-reflected by the earth's surface, are taken into account. The perspective of using the simulation results to optimize the parameters of the radiometer and remote sensing system according to the criterion of maximum sensitivity of the system to variations in soil moisture content is analyzed.**

Keywords: **microwave radiometer, remote sensing, soil moisture, radiation pattern, two-polarization antenna, radio brightness temperature, relict sky radiation**

UDC 612.087

Acknowledgments: The study was carried out with a grant from the Russian Science Foundation No. 22-19-00063 https://rscf.ru/project/22-19-00063.

For citation: Igor A. Sidorov, Evgeny P. Novichikhin, Alexander G. Gudkov, Sergey V. Chizhikov, Andrey G. Bolotov, Nikolay F. Khokhlov, Igor O. Porokhov. The Own Radiothermal Radiation of the Earth's Surface Receiving Process Modeling. *RENSIT: Radioelectronics. Nanosystems. Information technologies,* 2022, 14(4):359-372e. DOI: 10.17725/rensit.2022.14.359.

Contents

1. INTRODUCTION

Precision farming has been developing intensively over the past decade in response to the growing demand for food for a growing population. Precision farming technologies ensure efficient use and management of available resources to increase crop production, reduce freshwater consumption, preserve land fertility and protect the environment. Unlike traditional agricultural technologies, precision farming uses an approach with a variable rate of application of fertilizers, water and protective equipment in the practice of growing plants [1].

Large-scale effective implementation of precision farming depends on the availability and cost of advanced tools and technologies suitable for the agricultural industry, such as intelligent machinery and robotics, global positioning system (GPS), sensor networks and monitoring, information collection and processing systems, etc. One of the key components of precision agriculture is remote sensing equipment responsible for measuring and processing data on the state (soil and agrophytocenoses). Remote monitoring in combination with satellite navigation data is used to build geographic digital maps of field humidity and temperature to control and optimize crop cultivation modes [2-4].

In the field of remote sensing, monitoring of soil moisture is of particular interest due to global climate change in the main agricultural regions and the extremely large volume of fresh water used for irrigation. Campbell et al. [5] reported that more than 70% of the world's fresh water is used for agricultural purposes. The level of moisture content in the soil mainly determines the biophysical processes that affect crop yields and the state of soil fertility. Thus, extended and detailed information about soil moisture is a key input parameter for a precision farming system and water flow control. Further processing of geoinformation data on humidity with the help of advanced digitized agricultural management leads to a significant improvement in freshwater conservation and an increase in crop production [4].

Over the past decades, several technologies for determining soil moisture have been developed, based on various physical principles and applicable for precision farming. These technologies differ in their intended purpose, practical application, accuracy, cost, weight, etc. However, the most suitable solution for determining soil moisture for precision farming is a mobile, lightweight, high-precision measuring system that provides remote measurement of soil temperature and humidity. The demand for such a system is associated with a growing number of monitoring applications based on unmanned aerial vehicles integrated into the infrastructure of precision agriculture. Mobile sensor equipment is also suitable for integration into agricultural intelligent machinery and robotics [2], [3], [6].

Traditional methods for determining soil moisture are usually based on stationary sensors or sampling soil with analysis in the laboratory. These methods use various physical principles, such as laboratory analysis of a soil layer sample

by gamma radiation; the method of borehole neutron scattering (neutron probe); various electromagnetic sensing technologies, etc. [7]-[9] Traditional methods are actually point-based measurement methods that make the development of a soil moisture map extremely difficult if the number of measurement points is insufficient. Obviously, these methods cannot be widely used in applications where the mobility of a sensitive device is important.

For the purposes of aerial and satellite monitoring, various advanced methods have been developed to provide remote measurement of soil moisture. Technologies of remote sensing of soil moisture are widely represented by two methods: active sensing, in which the device reads reflected electromagnetic energy (radar), and passive sensing, in which the energy emitted by the earth is recorded (radiometry). Remote sensing systems deployed in the Earth observation satellite system are designed to work on a large scale or global mapping. Two projects were launched to collect data on soil moisture using satellite monitoring systems: (1) NASA Mission "Active Passive Soil Moisture" (SMAP) [10], [11] and "Soil Moisture and Ocean Salinity" (SMOS) of the European Space Agency (ESA) [12], [13]. However, the measurement accuracy provided by satellite monitoring systems is not suitable for precision farming. The best resolution of SMAP is 3 km in radar mode [11], while the spatial resolution of the SMOS system is approximately 40 km [13]. Such spatial resolution is sufficient to solve global problems of meteorology, but it is completely insufficient for the use of data in a precision farming system. Promising methods developed in recent years include various ground-based radiometric and radar systems, as well as sensing methods using electromagnetic induction. Such systems for measuring soil moisture are considered the best sensors for unmanned mobile applications of precision farming. The most promising method is the technology of microwave radiometry. This is a passive method of microwave sensing using a highly sensitive radiometric receiver – a microwave radiometer that determines the parameters of natural thermal radiation emitted by the earth's surface. The received data of the microwave radiometer represent the radio brightness temperature of the earth's surface [14]. Further processing of the data converts them into a soil moisture value linked to a specific geographical location. The microwave radiometer technology makes it possible to develop a device for monitoring soil moisture with minimal size, weight and cost. Simultaneous use of several frequency reception bands permits to obtain data for calculating soil moisture at different depths, that is, to determine the portrait of the soil moisture profile.

The development of a new portable multi-frequency dual–polarization microwave radiometer for precision farming systems capable of operating on board an unmanned aerial vehicle is an urgent task. Microwave radiometric moisture meters are used not only for precision farming tasks, but also for solving a number of practical tasks [15], such as monitoring the hydrological situation along highways [16] and pipelines [17], as well as for searching for places of underground leaks of earthen dams and places of erosion of dams [18], detecting foci of forest fires [19] and the detection of oil films on the water surface [20]. When developing a microwave radiometer, an important aspect is to optimize the selection of parameters of the microwave radiometer and the remote sensing system as a whole, ensuring maximum sensitivity of the sensing system to variations in soil humidity and temperature. The fastest and cheapest way to optimize the selection of parameters of a microwave radiometric system is modeling.

The purpose of this article is to demonstrate the results of modeling the process of radiometric reception of own radiothermal radiation of the Earth's surface, taking into account the antenna pattern, the model of the underlying surface and the model of the sounding system, taking into account the altitude and flight speed of the carrier, as well as the angle of inclination of the axis of the main lobe of the antenna pattern.

A model is known for receiving the human body's own radiothermal radiation [21], [22] by a multi-channel, multi-frequency microwave radiothermograph used for non-invasive detection of thermal anomalies inside the human or animal body [23]-[27]. The known model cannot be used to calculate the radio brightness temperatures of the underlying surface, since it does not take into account the radiation pattern of the antenna applicator, but can be taken as a basis for modeling the earth's surface.

2. OPERATION PRINCIPLE

The principle of remote measurement of soil moisture is known [15] and is used in practice together with an unmanned aerial vehicle to build maps of soil moisture and temperature in the interests of precision farming systems. The placement of the microwave radiometer on an unmanned aerial vehicle (quadcopter) is shown in **Fig. 1** of the L-band microwave radiometer represents the assembly of a bipolarized antenna with a receiver. The size of the microwave radiometer is determined by the size of the antenna, which is determined by the operating wavelength and the required width of the main lobe of the antenna pattern. The printed type antenna is assembled from two printed circuit boards with a size of 360x360 mm. There are four vibrators on the outer board, microstrip adders and output connectors for signals of "horizontal" and "vertical" polarization are located on the inner board. The picture of the antenna with an infrared temperature sensor is shown in **Fig. 2**. The main technical parameters of the microwave radiometer are presented in **Table 1**.

The microwave radiometer is assembled according to the well-known [15] scheme of a two-references modulation radiometer, has two internal temperature reference source with different temperatures and a microwave switch for periodic connection to the receiver input the signals from the antenna outputs and reference sources. The output signal of the receiver is converted into digital form

Fig. 1. *The microwave radiometer on a quadrocopter installation.*

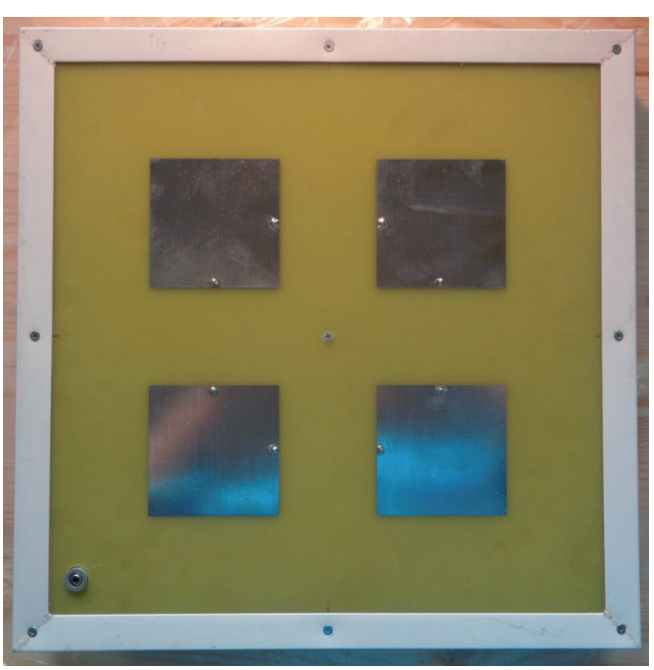

Fig. 2. *The antenna with an IR sensor picture.*

Table 1

The main technical parameters of the microwave radiometer

Parameter	Value
Central frequency, MHz	1420
Receiver band, MHz	50
The receiving channels Number Vertical and horizontal polarizations	2
Observation method	Along fligh
Observation width, resolving element, H-flight altitude	1.0xH
Sensitivity, K	1.0
Memory type	SD-Card
Recording time, not less, Hours	3
Antenna pattern main lob width, deg.	±30
Antenna scattering walue, %	73
Supply voltage, V	12
Power consumption, Wt	5.8
Mass, kg	2.8
Size, mm	360x360x40

and transmitted to the microcontroller, which stores data on a flash card together with information from the infrared sensor located in the antenna box and navigation sensors – the receiver of the satellite navigation system, as well as from the three-axis accelerometer. The block diagram of a microwave radiometer with sensors is shown in **Fig. 3**. The microwave radiometer is placed on an unmanned aerial vehicle so that the axis of the main lobe of the antenna pattern would be directed forward along the course of the aircraft at an angle

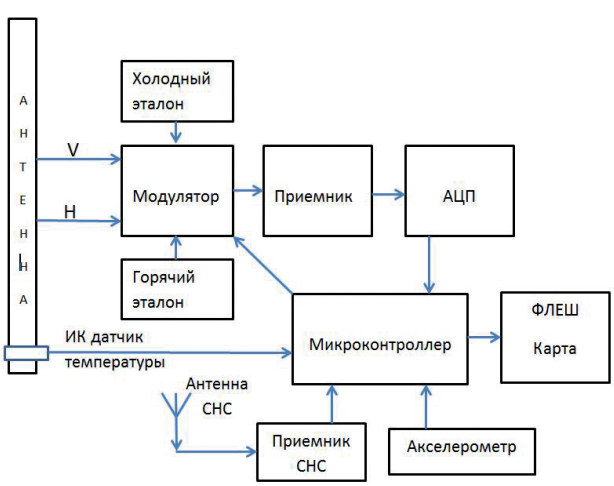

Fig. 3. *The microwave radiometer with sensors block diagram.*

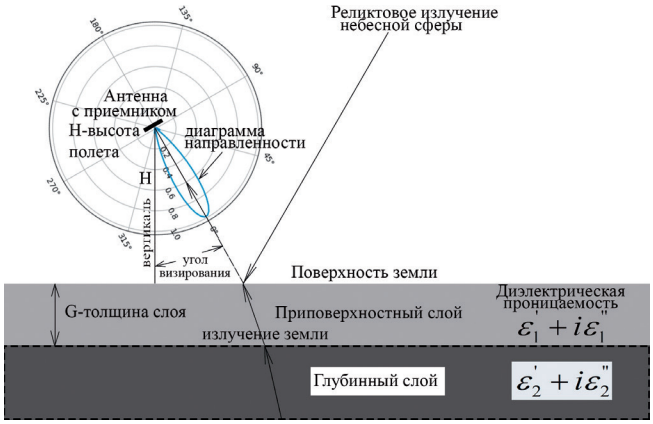

Fig. 4. *The Earth's surface sensing from a quadrocopter scheme.*

of 30 degrees to the vertical. The scheme of sensing the Earth's surface from a quadcopter is shown in **Fig. 4**. The quadcopter, according to a given control program, automatically flies at a given altitude along parallel lines above the test field, with data recorded on a memory card. After landing, the data card is transferred the personal computer and the data are processed. As a result of data processing, two geo–referenced maps are created - a map of soil moisture content and a map of soil surface temperatures.

The data from an infrared temperature sensor and navigation data are used to make a temperature map. The humidity map is calculated in two stages, first the radio brightness temperatures are calculated by horizontal and vertical polarizations, then on their basis and taking into account the temperature of the soil surface, the complex dielectric permittivity of the soil is calculated, which can be converted into soil moisture and the degree of soil mineralization. It should be noted that the accuracy of the brightness-humidity recalculation of the known algorithms depends on many factors, in particular, on the type of vegetation cover, the amount of biomass, plant height, etc. The recalculation algorithms are known [15] and are not the subject of this article. In this article,

the simplest two-layer soil model will be considered without taking into account the shielding effect of vegetation cover.

3. ANTENNA PATTERN MODEL

The antenna is the most important element of the radiometric system that determines overall dimensions, spatial resolution, noise protection and other parameters. The antenna pattern is the most important characteristic of the antenna. The radiation pattern of the real antenna (Fig. 2) of the radiometric system was measured on a special collimator and is known. However, for modeling, it is convenient to use a simulated radiation pattern so that it would be possible to track the influence of antenna radiation pattern parameters on the parameters of the radiometric system as a whole. The simplest idealized antenna with a square aperture of size D cm and with an average wavelength λ cm. was chosen as the model. The amplitude-phase distribution of the field in the antenna opening is considered uniform. The radiation pattern of the power of such an antenna is described by the function:

$$D_n(\alpha,\beta)=\left(\frac{\sin(\pi\frac{D}{\lambda}\alpha)}{\pi\frac{D}{\lambda}\alpha}\right)^2\times\left(\frac{\sin(\pi\frac{D}{\lambda}\beta)}{\pi\frac{D}{\lambda}\beta}\right)^2, \quad (1)$$

where α and β are angular coordinates in radians, calculated from the normal to the antenna plane or the axis of the main lobe of the radiation pattern. The graph of the function of the radiation pattern in the Cartesian coordinate system for the wavelength λ = 21 cm and D = 2λ at one of the angles is shown in **Fig. 5**. When modeling the antenna, only radiation from the front hemisphere was taken into account. The radiation from the rear hemisphere was considered to be zero. With these antenna parameters, the width of the main lobe of

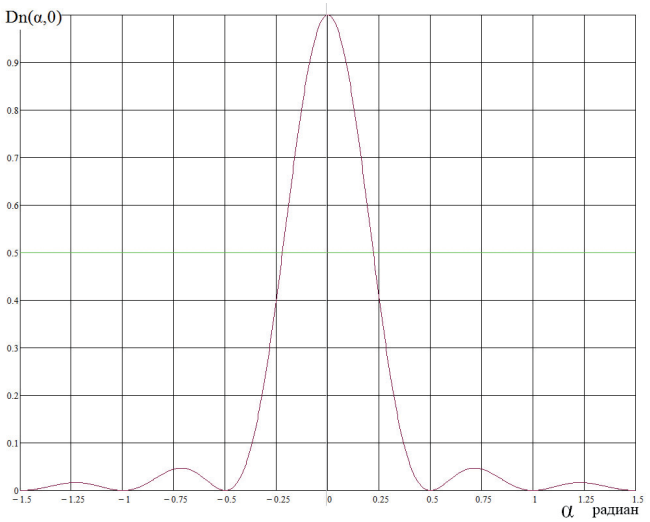

Fig. 5. *Antenna radiation pattern on one of the coordinates.*

the radiation pattern at the level of –3 db. is ±s, where s = 0.22 radians. An important parameter of the antenna is the scattering coefficient γ, which is defined as:

$$\gamma=1-\frac{\int_{-s}^{+s}Dn(\alpha,0)d\alpha}{\int_{-\pi}^{+\pi}Dn(\alpha,0)d\alpha}. \quad (2)$$

The physical meaning of it is that it shows what proportion of the signal energy is received along the side lobes, in relation to the total energy along the entire directional pattern. For the considered case, the antenna

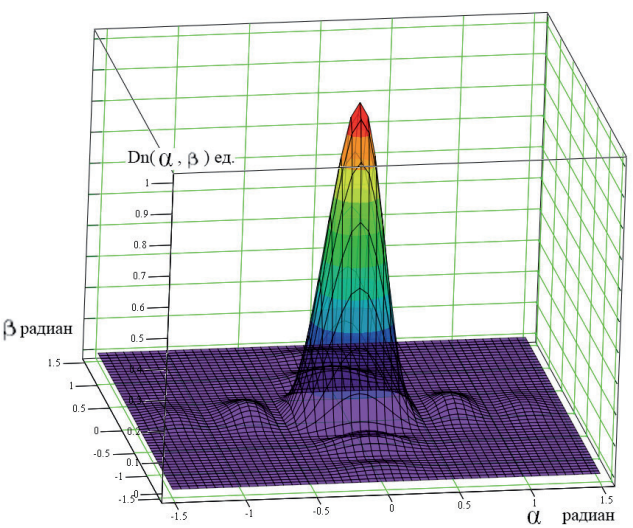

Fig. 6. *Antenna radiation pattern on 3D graph.*

scattering coefficient is approximately 27%. From the graph in Fig. 5, it can be seen that in the anterior hemisphere along the α coordinate, in addition to the main lobe, there are two side lobes to the right and left of the main one. The level of the first side lobe is about –13 db. The level of the second side lobe is about –18 db. The appearance of the radiation pattern in the form of a 3*D* graph is shown in **Fig. 6**.

4. THE EARTH'S LITHOSPHERE SURFACE LAYER MODEL

In physical and geological terms, the soil as an object of modeling is a complex material formed from solid-phase individual particles, as well as voids filled with aqueous solutions of salts or gaseous bubbles. Due to this, they occupy a place between the solid and the fluids. Modeling the soil's own electromagnetic radiation is an extremely difficult task, due to the wide variety of soil types, biochemical composition, vegetation cover, relief, surface roughness and hydrology. In general, the problem has not been solved so far. Therefore, simplified models are used in practice [28], taking into account only a part of the listed soil parameters.

In the proposed model, the soil is considered as a homogeneous two-layer medium with flat surfaces of sections without vegetation cover and roughness. The thickness of the near-surface layer *G,* the complex dielectric permittivity of the near-surface layer $\varepsilon_1' + i\varepsilon_1''$,, where are used as soil parameters. ε_1' is the real part, and ε_1'' is the imaginary part. Similarly, the permittivity of the deep layer $\varepsilon_2' + i\varepsilon_2''$, is given, where ε_2' is the real part, and ε_2'' is the imaginary part (see Fig. 4).

The spatial distribution of the dielectric permittivity of the soil over the surface is impractical to consider uniform, since in this case, as a result of modeling, it would not be possible to determine the distortions of the initial field due to the influence of the side lobes of the antenna pattern, and they, more precisely, the possibility of their correction, is of particular interest. As shown in [29], such a correction is possible if the antenna scattering coefficient does not exceed 50%.

As a model of the surface field, a periodic sequence of squares with a side of P meters of two types, arranged like the fields of a chessboard, is chosen. Such a structure is not a model of real soil, but is a convenient tool for studying the characteristic properties of the model.

The squares of the conventionally "white" type have dielectric permittivity of the soil model by layers, as described above $\varepsilon_{1w} = \varepsilon_1' + i\varepsilon_1''$ and $\varepsilon_{2w} = \varepsilon_2' + i\varepsilon_2''$. And conditionally, the "black" squares have additives to the dielectric permittivity of the layers so that the complex dielectric permittivity of the near-surface layer $\varepsilon_{1B} = \varepsilon_1' + \Delta_1' + i(\varepsilon_1'' + \Delta_1'')$, respectively, the complex dielectric permittivity of the deep layer $\varepsilon_{2B} = \varepsilon_2' + \Delta_2' + i(\varepsilon_2'' + \Delta_2'')$.

It is convenient to set a mathematically described two-dimensional function describing the terrain of the "chessboard" type using a

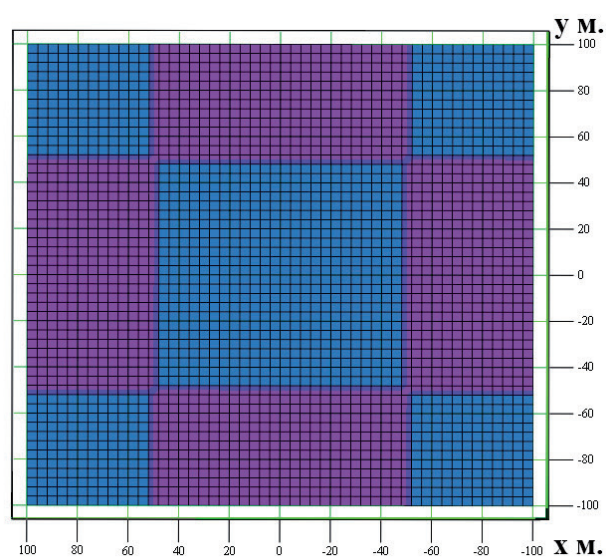

Fig. 7. *The "Chessboard" function sample.*

function in a rectangular Cartesian coordinate system:

$$W(x,y)=\left|\Theta\left(\cos\left(P\pi x\right)\right)+\Theta\left(\cos\left(P\pi y\right)\right)-1\right|, \quad (3)$$

where P is a parameter specifying the size of the "chessboard" cell, and Θ is a Heaviside function equal to zero for negative argument values and one for all others. The appearance of the function $W(x,y)$ for $P = 2$ is shown in **Fig. 7**.

Using the function $W(x,y)$, it is easy to describe the distribution of the dielectric constant of the field in x,y coordinates over the layers:

$$W_{\varepsilon 1}(x,y)=\varepsilon_1^{'}+i\varepsilon_1^{''}+\left(\Delta_1^{'}+i\Delta_1^{''}\right)\cdot W(x,y), \quad (4)$$

$$W_{\varepsilon 2}(x,y)=\varepsilon_2^{'}+i\varepsilon_2^{''}+\left(\Delta_2^{'}+i\Delta_2^{''}\right)\cdot W(x,y). \quad (5)$$

The functions $W_{\varepsilon 1}(x,y)$ and $W_{\varepsilon 2}(x,y)$ are used to simulate the soil's own radiation and simulate the relic radiation of the celestial sphere reflected from the earth.

5. THE SURFACE RADIO THERMAL EMISSION RECEPTION MODEL

When making field experiments, a microwave radiometer is installed on an unmanned aerial vehicle (Fig. 1), which, according to the program, flies over a given trajectory at a given height H and at a given speed V. The sensing scheme is shown in Fig. 4. The viewing angle Q_0 is calculated from the vertical and is usually selected about 30 degrees. As a result of probing the surface, the microwave radiometer measures two antenna temperatures in horizontal and vertical polarizations at each spatial position.

As a result of the simulation, two antenna temperatures should also be calculated by horizontal and vertical polarizations as a function of the parameters of the antenna pattern models, the parameters of the Earth surface model and the parameters of the surface survey system model.

$$T_{AV}=f_V(x_0,y_0,D,\lambda,G,\varepsilon_1,\varepsilon_2,\Delta_1,\Delta_2,Q_0,H,T_0,T_S), \quad (6)$$

$$T_{AH}=f_H(x_0,y_0,D,\lambda,G,\varepsilon_1,\varepsilon_2,\Delta_1,\Delta_2,Q_0,H,T_0,T_S), \quad (7)$$

where x_0, y_0 and H are the Cartesian coordinates of a quadrocopter with a microwave radiometer, T_0 is the thermodynamic temperature of the soil surface, T_s is the temperature of the relic radiation of 2.33 degrees on the Kelvin scale. It is assumed that the flight speed and the axis of sight are directed along the X axis. Modeling consists in finding analytical expressions or algorithms for calculating the functions f_V and f_H and calculating antenna temperatures from vertical and horizontal polarizations. The antenna temperature for any polarization is calculated using the antenna smoothing equation [29]:

$$T_A(\alpha_0,\beta_0)= \\ =\iint T_b(\alpha,\beta)D_n(\alpha-\alpha_0,\beta-\beta_0)\,d\beta d\alpha, \quad (8)$$

were α_0, β_0 – coordinates of the point of sight in the polar coordinate system associated with the antenna. In formula (8), both the radiation pattern and the distribution of the brightness temperature field over the earth's surface are set in the polar coordinate system associated with the antenna. The brightness temperature map is constructed in a system of Cartesian coordinates (or geographical latitude-longitude) associated with the terrain (or north-east directions). To create a single model that takes into account both the antenna pattern model and the model of the Earth's surface and the sounding model, it is necessary to reduce all models to one common coordinate system, for example, to a Cartesian coordinate system associated with the earth.

The conversion of polar coordinates to Cartesian coordinates can be done using the formulas:

$$\alpha(x)=Q_0-arctg\left(x/H\right), \quad (9)$$

$$\beta(x,y) = arctg\left(\frac{y\cdot\cos(Q_0)}{H}\right). \quad (10)$$

Substituting (9) and (10) into (1) we obtain the expression of the radiation pattern in Cartesian coordinates

$$D_nXY(x,y) = D_n(\alpha(x),\beta(x,y)). \quad (11)$$

The function *DnXY(x,y)* represents the weighting factor for the plot with the coordinates *x,y* of the terrain area of the size dxdy. The view of the function *DnXY(x,y)* for viewing from a height of 10 meters from a point with coordinates (0, 0, 10 m) at an angle of 30 degrees to the vertical is shown in **Fig. 8**.

From the formula (6) and (7) can be obtained from (8) taking into account (11)

$$T_{av}(x_0,y_0) = \iint T_{bv}(x,y)\cdot D_nXY(x-x_0,y-y_0)\,dydx, \quad (12)$$

$$T_{ah}(x_0,y_0) = \iint T_{bh}(x,y)\cdot D_nXY(x-x_0,y-y_0)\,dydx. \quad (13)$$

To complete the construction of the model, it remains to express the distribution functions of brightness temperatures over the vertical and horizontal polarizations $T_{BV}(x,y)$ and $T_{BH}(x,y)$ through the distribution functions of the dielectric permittivity of the field in *x,y* coordinates over the layers from formulas (4) and (5). The soil model

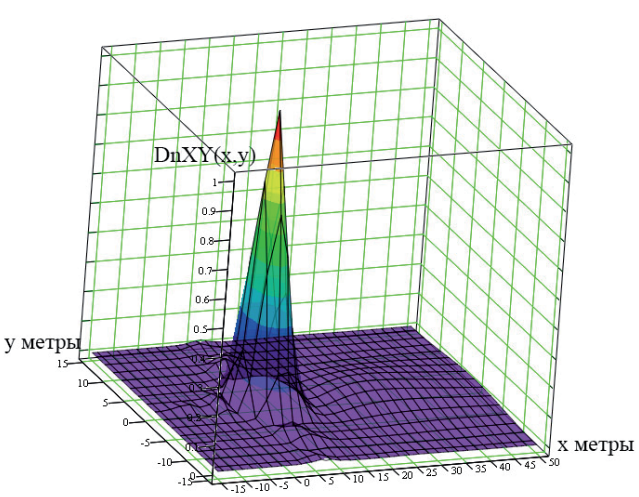

Fig. 8. *Weight function DnXY(x,y) Sample.*

described above is considered in detail in [30], where it is called a single-layer homogeneous model. The model takes into account the reflection from the surface layer of the earth:

$$T_{bv}(x,y) = T_S\cdot R_v(W_{\varepsilon 1}(x,y),H) + \\ +T_0\cdot\left(1-R_v\left(W_{\varepsilon 1}(x,y),H\right)\right), \quad (14)$$

$$T_{bh}(x,y) = T_S\cdot R_h(W_{\varepsilon 1}(x,y),H) + \\ +T_0\cdot\left(1-R_h\left(W_{\varepsilon 1}(x,y),H\right)\right), \quad (15)$$

were R_V and R_H – Fresnel reflection coefficients for vertical and horizontal polarizations, Q is the angle relative to the vertical under which the surface point with coordinates (*x, y,* 0) is visible from the antenna location point (point with coordinates (0, 0, *H*)):

$$R_v(x,y) = \\ = \left|\frac{W_{\varepsilon 1}(x,y)\cdot\cos(Q)-\sqrt{W_{\varepsilon 1}(x,y)-\sin^2(Q)}}{W_{\varepsilon 1}(x,y)\cdot\cos(Q)+\sqrt{W_{\varepsilon 1}(x,y)-\sin^2(Q)}}\right|^2, \quad (16)$$

$$R_h(x,y) = \left|\frac{\cos(Q)-\sqrt{W_{\varepsilon 1}(x,y)-\sin^2(Q)}}{\cos(Q)+\sqrt{W_{\varepsilon 1}(x,y)-\sin^2(Q)}}\right|^2. \quad (17)$$

The angle of sight Q of a point with coordinates (*x, y,* 0) depends on the coordinates x,y and the height of the antenna location *H* can be calculated by the formula (18)

$$Q = arctg\left(\frac{\sqrt{x^2+y^2}}{H}\right). \quad (18)$$

The cosine and the square of the sine of the angle Q can also be represented in terms of the coordinates *x,y* and height *H*:

$$\cos(Q) = \frac{H}{\sqrt{H^2+x^2+y^2}}, \quad (19)$$

$$\sin^2(Q) = \frac{x^2+y^2}{\left(H^2+x^2+y^2\right)}. \quad (20)$$

The partially incident electromagnetic wave of the relic radiation is refracted, passes through the near-surface layer, is partially absorbed, is reflected from the interface of the near-surface and deep layer, is partially absorbed again, is partially reflected from the soil surface and is partially radiated into the open space again. The attenuation coefficient of the electromagnetic wave in the near-surface layer, according to [30]:

$$\delta(G,\lambda)=\exp\left(-4\pi\varepsilon_1''\frac{G}{\lambda\cos(Q_r)}\right), \quad (21)$$

were Q – incidence angle, G – layer thickness.

The reflection coefficients from the section of the near-surface and deep layer are given in [31] and in the accepted designations can be represented as:

$$R_{V2}(x,y,Q_r)=$$
$$=\left|\frac{W_{\varepsilon 2}(x,y)\cdot\cos(Q_r)-\sqrt{W_{\varepsilon 1}(x,y)}F(x,y,Q_r)}{W_{\varepsilon 2}(x,y)\cdot\cos(Q_r)+\sqrt{W_{\varepsilon 1}(x,y)}F(x,y,Q_r)}\right|^2, \quad (22)$$

$$R_{H2}(x,y,Q_r)=\left|\frac{W_{\varepsilon 1}(x,y)\cdot\cos(Q_r)-F(x,y,Q_r)}{W_{\varepsilon 1}(x,y)\cdot\cos(Q_r)+F(x,y,Q_r)}\right|^2, \quad (23)$$

where

$$F(x,y,Q_r)=\sqrt{W_{\varepsilon 2}(x,y)-W_{\varepsilon 1}(x,y)\cdot\sin^2(Q_r)}.$$

The refraction angle Q_r is related to the angle of incidence Q by the Snellius law expressed by the well-known formula (24):

$$\frac{\sin(Q_r)}{\sin(Q)}=\frac{\sqrt{W_{\varepsilon 1}(x,y)}}{\sqrt{W_{\varepsilon 2}(x,y)}}. \quad (24)$$

The formulas given completely define the functions (6) and (7) and are sufficient to construct a model for receiving radiothermal radiation from the soil surface.

The calculations results of using the above model are representing below.

6. SIMULATION RESULTS

The presented model can be used to calculate antenna temperatures at the output of the radiometer by vertical and horizontal polarizations depending on the parameters of the antenna, sensing and soil. As a result of calculations of integral expressions in formulas (12) and (13), two-dimensional graphs of weight functions were obtained, shown in **Fig. 9**. The functions are calculated for a uniform temperature field of 300° K, when viewed from a height of H = 10 m. from the origin at an angle of 30° in the direction of the X axis.

The cross sections of the surfaces represented by the plane Y = 0, in the range from 0 to 10 meters, are shown in **Fig. 10**. Analysis of the graphs presented in Fig. 10 shows that the coordinates of the maxima of the weight functions in vertical and horizontal polarizations do not coincide, but differ by about half a meter and do not coincide with the coordinate of the point of sight. The analysis showed that the differences arose due to differences in the properties of the Fresnel coefficients for vertical and horizontal polarizations.

The presented model allows simulating the flight of a carrier with a radiometer and calculating antenna temperatures by vertical and horizontal polarizations. An example of

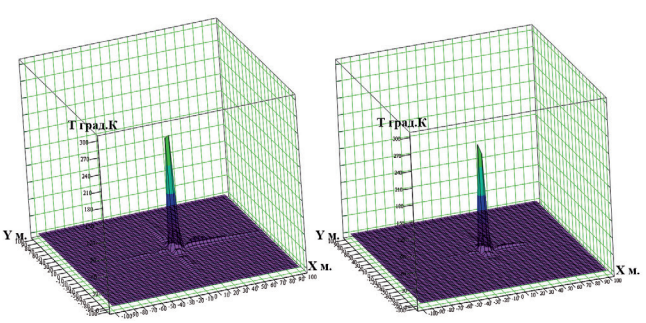

Fig. 9. *Weight functions Tv(x,y)·DnXY(x,y) and Th(x,y)·DnXY(x,y).*

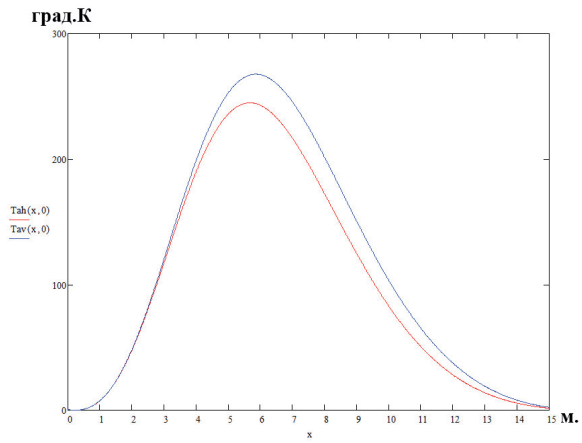

Fig. 10. *The cross section of the functions Tv(x,y)·DnXY(x,y) and Th(x,y)·DnXY(x,y) by plane Y = 0.*

calculating antenna temperatures when the carrier moves along the *X* axis is shown in **Fig. 11**. The dotted line on the graph shows the boundaries of the "chessboard" cell.

The characteristic advance of the temperature graphs in comparison with the cell boundary is associated with the inclination of the axis of the radiation pattern in the direction of the flight line.

A small oscillatory process on the antenna temperature charts is due to the presence of side lobes of the antenna.

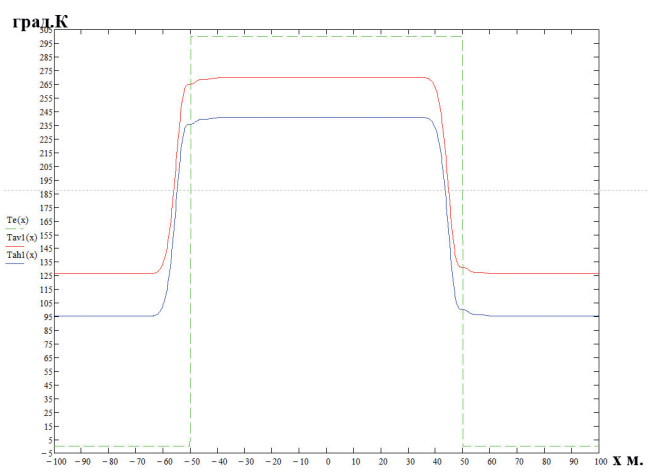

Fig. 11. *Graph of calculated temperatures when the carrier moves along the X axis.*

7. DISCUSSION

The presented model was calculated using a specialized mathematical program and a program written in the Delphy language. The coincidence of the calculation results confirms the adequacy of the constructed model. To calculate the graph (Fig. 11) with a mathematical program on a laptop with a quad-core processor, it took more than one hour. The same result was obtained in the Delphi program in less than one second.

The resulting model is planned to be developed, improved and used to develop a modern algorithm for correcting amplitude distortions caused by the presence of side lobes of the antenna instead of the known one [29], as well as to optimize the parameters of the radiometer and the survey system according to the criterion of maximum sensitivity to variations in soil moisture by layers.

8. CONCLUSION

As a result of the research and modeling within the framework of the represented model, the following new results were obtained:

- a model of the brightness temperature formation of the underlying surface is obtained, regarding the parameters of the antenna, radiometer, Earth's surface and the sensing system;
- the antenna temperatures on vertical and horizontal polarizations were calculated using the model, when simulating the flight of the carrier;
- the mismatch of the coordinates of the maxima of weight functions for vertical and horizontal polarizations as a result of the analysis of graphs, was found;
- the graphs for calculating antenna temperatures at the front and the decline of

the spatial pulse show a transition process due to the presence of side lobes of the antenna pattern;

REFERENCES

1. Shafi U, Mumtaz R, Garcia-Nieto J, Hassan SA, Zaidi SAR, Iqbal N. Precision agriculture techniques and practices: From considerations to applications. *Sensors*, 2019, 19(17):3796, doi: 10.3390/s19173796.
2. Tsouros DC, Bibi S, Sarigiannidis PG. A review on UAV-based applications for precision agriculture. *Information*, 2019, 10(11):349, doi: 10.3390/info10110349.
3. Maes WH, Steppe K. Perspectives for remote sensing with unmanned aerial vehicles in precision agriculture. *Trends in Plant Science*, 2019, 24(2):152-164, doi: 10.1016/j.tplants.2018.11.007.
4. Kashyap B, Kumar R. Sensing methodologies in agriculture for soil moisture and nutrient monitoring. *IEEE Access*, 2021, 9:14095-14121, doi: 10.1109/ACCESS.2021.3052478.
5. Bruce M. Campbell, Douglas J. Beare, Elena M. Bennett, Jason Hall-Spencer, John S. I. Ingram, Fernando Jaramillo, Rodomiro Ortiz, Navin Ramankutty, Jeffrey A. Sayer, Drew Shindell. Agriculture production as a major driver of the earth system exceeding planetary boundaries. *Ecology and Society,* 2017, 22(4):1-11, doi: 10.5751/ES-09595-220408.
6. Inoue Y. Satellite- and drone-based remote sensing of crops and soils for smart farming – a review. *Soil Science and Plant Nutrition*, 2020, 66(6):798-810, doi: 10.1080/00380768.2020.1738899.
7. Kodikara J, Rajeev P, Chan D, Gallage C. Soil moisture monitoring at the field scale using neutron probe. *Canadian Geotechnical Journal*, 2014, 51(3):332-345, doi: 10.1139/cgj-2012-0113.
8. Balaghi S, Ghal-Eh N, Mohammadi A, Vega-Carrillo HR. A neutron scattering soil moisture measurement system with a linear response. *Applied Radiation and Isotopes,* 2018, 142:167-172, doi: 10.1016/j.apradiso.2018.10.002.
9. Babaeian E, Sadeghi M, Jones SB, Montzka C, Vereecken H, Tuller M. Ground, proximal, and satellite remote sensing of soil moisture. *Reviews of Geophysics*, 2019, 57:530-616, doi: 10.1029/2018RG000618.
10. Entekhabi D, Njoku EG, O'Neill PE, Kellogg KH, Crow WT, Edelstein WN, Entin JK, Goodman SD, Jackson TJ, Johnson J, Kimball J, Piepmeier JR, Koster RD, Martin N, McDonald KC, Moghaddam M, Moran S, Reichle R, Shi JC, Spencer MW, Thurman SW, Tsang L, Van Zyl J. The Soil Moisture Active Passive (SMAP) mission. *Proc. of the IEEE*, 2010, 98(5):704-716, doi: 10.1109/JPROC.2010.2043918.
11. Steven K. Chan, Rajat Bindlish, Peggy E. O'Neill, Eni Njoku, Tom Jackson, Andreas Colliander, Fan Chen, Mariko Burgin, Scott Dunbar, Jeffrey Piepmeier, Simon Yueh, Dara Entekhabi, Michael H. Cosh, Todd Caldwell, Jeffrey Walker, Xiaoling Wu, Aaron Berg, Tracy Rowlandson, Anna Pacheco, Heather McNairn, Marc Thibeault, José Martínez-Fernández, Ángel González-Zamora, Mark Seyfried, David Bosch, Patrick Starks, David Goodrich, John Prueger, Michael Palecki, Eric E. Small, Marek Zreda, Jean-Christophe Calvet, Wade T. Crow, and Yann Kerr. Assessment of the SMAP passive soil moisture product. *IEEE Trans. on Geoscience and Remote Sensing*, 2016, 54(8):4994-5007, doi: 10.1109/TGRS.2016.2561938.

12. Kerr YH, Waldteufel P, Wigneron J-P, Martinuzzi J-M, Font J, Berger M. Soil moisture retrieval from space: The soil moisture and ocean salinity (SMOS) mission. *IEEE Trans. on Geoscience and Remote Sensing*, 2001, 39(8):1729-1735, doi: 10.1109/36.942551.
13. Mecklenburg Susanne, Matthias Drusch, Yann H. Kerr, Jordi Font, Manuel Martin-Neira, Steven Delwart, Guillermo Buenadicha, Nicolas Reul, Elena Daganzo-Eusebio, Roger Oliva, Raffaele Crapolicchio. ESA's soil moisture and ocean salinity mission: mission performance and operations. *IEEE Trans. on Geoscience and Remote Sensing,* 2012, 50(5):1354-1366, doi: 10.1109/TGRS.2012.2187666.
14. Ulaby FT, Long DG. *Microwave Radar and Radiometric Remote Sensing*. Ann Arbor, The University of Michigan Press, 2014.
15. Verba VS, GulyaevYuV, Shutko AM, Krapivin VF (eds.). *Microware Radiometry of Land and Water Surfaces: From Theory to Practice*. Sofia, Marin Drinov Academic Publishing, 2014.
16. Sidorov IA, Soldatenko AP, Gudkov AG, Leushin VY, Novochikhin EP. Results of field experiments on monitoring the hydrological situation along highways with a multifrequency polarimetric system of microwave radiometers. *Mashinostroitel*, 2015, 12:46-55.
17. Sidorov IA, Gudkov AG, Sister VG, Ivannikova EM, Leushin VY. Monitoring of the hydrological situation along pipeline routes by means of microwave radiometry methods. *Chemical and Petroleum Engineering,* 2021, 56:929-234, doi: 10.1007/s10556-021-00864-6.
18. de Jeu R, Parinussa R, Biemond L, Haarbrink R, Shutko A, Demontoux F, Provoost Y. Safety inspection of levees with L-band radiometry. *Proc. 11th Specialist Meeting on Microwave Radiometry and Remote Sensing of the Environment*, USA, Washington, DC, 1-4 March 2010, pp. 96-98, doi: 10.1109/MICRORAD.2010.5559583.
19. Sister VG, Ivannikova EM, Gudkov AG, LeushinVYu, Sidorov IA, PlyushchevVA, Soldatenko AP. Detection of forest and peat-bog fire centers by means of microwave radiometer sounding. *Chemical and Petroleum Engineering*, 2016, 52:123-125, doi: 10.1007/s10556-016-0160-2.
20. Gudkov AG, Sister VG, Ivannikova EM, Leushin VYu, Plyushchev VA, Sidorov IA, Chetyrkin DYu. On the possibility of detecting oil films on water surface by microwave radiometry methods. *Chemical and Petroleum Engineering,* 2019, 55:57-62, doi: 10.1007/s10556-019-00580-2.
21. Evgeny P. Novichikhin, Igor A. Sidorov, Vitaly Y. Leushin, Svetlana V. Agasieva and Sergey Chizhikov. The local heat source detection inside of the human body by means of microwave radiothermography, *RENSIT: Radioelectronics. Nanosystems. Information technologies,* 2020, 12(2):305-312, doi: 10.17725/rensit.2020.12.305.
22. Evgeny P. Novichikhin, Igor A. Sidorov, Vitaly Yu. Leushin, Svetlana V. Agasieva, Sergey V. Chizhikov. Local heat source detection inside of the human body by means of microwave radiothermography. *RENSIT: Radioelectronics. Nanosystems. Information technologies*, 2022, 14(1):103-110, doi: 10.17725/rensit.2022.14.103.
23. Sidorov IA, Gudkov AG, Leushin VY, Gorlacheva EN, Novichikhin EP, Agasieva SV. Measurement and 3D Visualization of the Human Internal Heat Field by Means of Microwave

Radiometry. *Sensors*, 2021, 21:4005, doi: 10.3390/s21124005.

24. Vesnin S, Turnbull AK, Dixon JM, Goryanin I. Modern Microwave Thermometry for Breast Cancer. *J. Mol. Imaging Dyn.*, 2017, 7(10):1109.
25. Gudkov AG, Leushin VY, Sidorov IA, Vesnin SG, Porokhov IO, Sedankin MK, Agasieva SV, Chizhikov SV, Gorlacheva EN, Lazarenko M. et al. Use of Multichannel Microwave Radiometry for Functional Diagnostics of the Brain. *Biomed. Eng.*, 2019, 53:108-111.
26. Leushin VYu, Gudkov AG, Porokhov IO, Vesnin SG, Sedankin MK, Solov'ev YuV, Agasieva SV, Chizhikov SV. Possibilities of increasing the interference immunity of radiothermograph applicator antennas for brain diagnostics. *Sensors and Actuators A: Physical*, 2022, 337:113439, doi: 10.1016/j.sna.2022.113439.
27. Vesnin SG, Sedankin MK, Ovchinnikov LM, Gudkov AG, Leushin VY, Sidorov IA, Goryanin II. Portable microwave radiometer for wearable devices. *Sensors and Actuators A: Physical*, 2021, 318:112506, doi: 10.1016/j.sna.2020.112506.
28. Maheshwari Neelam, Andreas Colliander, Binayak P. Mohanty, Michael H. Cosh, Sidharth Misra, Thomas J. Jackson. Multiscale Surface Roughness for Improved Soil Moisture Estimation. *IEEE Transactions on Geoscience and Remote Sensing*, 2020, 58(8):5264-5276, doi: 10.1109/TGRS.2019.2961008.
29. Egorov ST, Pluschev VA, Vlasov AA. Method of correction of radio brightness distribution distortions caused by the side lobes of the antenna radiation pattern, *Radioengineering and electronics*, 1981, 8:1-7.
30. Finkelstein MI, Mendelson VL, Kutev VA. *Radar of layered earth covers*. Moscow, Sovetskoe radio Publ., 1977, 176 pp.
31. Grudinskaya GP. *Propagation of radio waves*. Moscow, Vysshaya shkola Publ., 1975, 155 pp.

DOI: 10.17725/rensit.2022.14.373

Statistical Properties of the Earth's Magnetic Field Before an Earthquake Accompanied by a Tsunami

Alexander E. Volvach
Crimean Astrophysical Observatory, https://crao.ru/
Nauchny 298688, Crimea, Russian Federation
E-mail: volvach@bk.ru

Lev P. Kogan
Nizhny Novgorod State University of Architecture and Civil Engineering, https://nngasu.ru/
Nizhny Novgorod 603950, Russian Federation
E-mail: l_kog@list.ru

Tatiana M. Zaboronkova
R.E.Alexeev Nizhny Novgorod State Technical University, https://www.nntu.ru/
Nizhny Novgorod 603950, Russian Federation
Institute of Applied Physics of the Russian Academy of Sciences, https://ipfran.ru/
Nizhny Novgorod 603950, Russian Federation
E-mail: t.zaboronkova@rambler.ru

Received 30 October 2022, peer-reviewed 07 November 2022, accepted 14 November 2022

Abstract: **A method for predicting earthquakes accompanied by tsunamis based on changes in the statistical properties of the Earth's magnetic field is proposed. Geomagnetic field is analyzed using the measurements taken a few days before the earthquake in the Pacific Ocean. With the help of a statistical functional, which allows one to study the variations in the level of chaos in the random process, the arising a set of structures with a high degree of determinism is revealed. The properties of these structuews can be interpreted as precursors of an earthquake accompanied by a tsunami.**

Keywords: **earthquake, tsunamis, statistical functionality, precursor of earthquake**

UDC 550.343

Acknowledgments: Work was supported by the Russian Science Foundation (project no. 21-12-00-385). The authors are grateful to IZMIRAN researcher Kanonidi K.Kh. for the provided data of measurements of the Earth's magnetic field.

For citation: Alexander E. Volvach, Lev P. Kogan, Tatiana M. Zaboronkova. Statistical Properties of the Earth's Magnetic Field Before an Earthquake Accompanied by a Tsunami. *RENSIT: Radioelectronics. Nanosystems. Information Technologies*, 2022, 14(4):373-380e. DOI: 10.17725/rensit.2022.14.373.

Contents

1. INTRODUCTION

In [1–3], based on the study of the properties of small-scale fluctuations in the probability density of the magnetic field,

the critical frequency of the ionosphere, and the noise of complex biological systems in seismically active regions, a method was proposed and tested for detecting precursors of approaching earthquakes. The proposed approach makes it possible, in particular, to determine the precursors of seismic events at much shorter time intervals (several days instead of several months) than prediction based on the Gutenberg-Richter theorem [4–8], as well as other statistical approaches [9–12]. In this article, based on the methodology [1-3], the properties of a statistical functional describing the characteristics of small-scale fluctuations in the probability density of the Earth's magnetic field are analyzed. Geomagnetic field measurements were carried out from March 12 to March 16, 2022 at the KNY magnetic variation station (Kanoya), located in southern Japan. The change in the amplitude of fluctuations in the probability density of the geomagnetic field in seismically active regions a few days before of an earthquake is associated with the appearance of a random component in the measurement process, caused, for example, by a fracture of lithospheric plates in the most weakened parts of the earth's crust. Note that this random process is weakly dependent on the background noise due to a set of phenomena that usually take place in the corresponding region of the world.

2. PROBLEM STATEMENT AND SOLUTION METHOD

The purpose of this study is to determine the statistical properties of the Earth's magnetic field, which are precursors of an approaching earthquake accompanied by a tsunami. To identify such precursors, the statistical functional previously introduced and tested in [1] is used:

$$L(n) = \frac{A}{M} \sum_{n=l-(M-1)}^{n} |\Theta_l|, \qquad \Theta_l = \sum_{m=0}^{N-1} P_{m,l}(-1)^m. \tag{1}$$

In formula (1), we take A = 1000 and M = 100 min. The chosen value of the coefficient A makes it possible to pass to the range of values of the functional $L(n)$ convenient for analysis with the specified width M of the averaging time interval. The coefficients $P_{m,l}$ are the probabilities that the values of the auxiliary function $F[x]$ used in the problem fall within the interval

$$F[x(t)]_{\min} + mh \le F[x(t)] \le \le F[x(t)]_{\min} + (m+1)h, \quad 0 \le m \le N-1. \tag{2}$$

Unlike the distribution function of the measured random variable $x = x(t)$, the function $F[x]$ must have a probability density with integrable singularities. Taking into account this requirement, the function $F[x] = \sin[x(t)]$ was chosen for calculations. For the specified type of function $F[x]$ with the discretization interval width h = 0.1, the value of N in (1) is $N = 2h^{-1} = 20$. Statistics (2) based on the results of measurements of the X-, Y- and Z-components of the geomagnetic field (in nT). The duration of any segment of the implementation is 60 seconds, during which 60 measurements of the corresponding component of the magnetic field are carried out. Thus, the value of n in (1) is equal to the number of minutes from the start of measurements at 00:00 03/12/2022 UTC (Coordinated Universal Time) to the current time.

The article shows that the entropy of the geomagnetic field increases with the

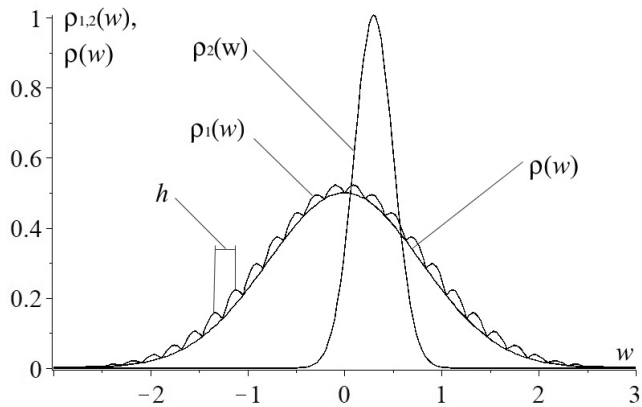

Fig. 1. *Schematic probability distributions* $\rho_1(w)$, $\rho_2(w)$ *and* $\rho(w)$.

approach of an earthquake. Let us explain the above theoretically.

Fig. 1 schematically shows the dependences of the probability density $\rho_1(w)$ and $\rho_2(w)$ for the background noise $x_1(t)$ and, accordingly, the additional (independent of the background noise) random process $x_2(t)$, as well as the probability density $\rho(w)$ of the total random process $x(t) = x_1(t) + x_2(t)$ corresponding to the convolution of the form

$$\rho(w)=\int_{-\infty}^{\infty}\rho_1(w-w')\rho_2(w')dw'.$$

It was theoretically shown in [3] that smoothing of small-scale fluctuations of the curve $\rho_1(w)$ takes place under the condition that the standard of fluctuations of the random variable x_2, which determines the width of the distribution $\rho_2(w)$, is at least several times larger than the sampling interval h, which determines the effective period indicated fluctuations (see Fig. 1).

3. METHOD OF ANALYZING THE RESULTS OF MEASUREMENTS

When analyzing the statistical properties of the magnetic field, the concepts previously introduced in [1] are used: local trends, channels, testing, sliding boundaries. These terms are illustrated by the example in **Fig. 2**, which shows the dependence of the functional $L(n)$ corresponding to measurements of the X-component of the geomagnetic field.

1. Let us call *local trends* the sections of the dependence $L(n)$ located between the points of extrema of this curve and corresponding to variations in δL (the difference between the values of the

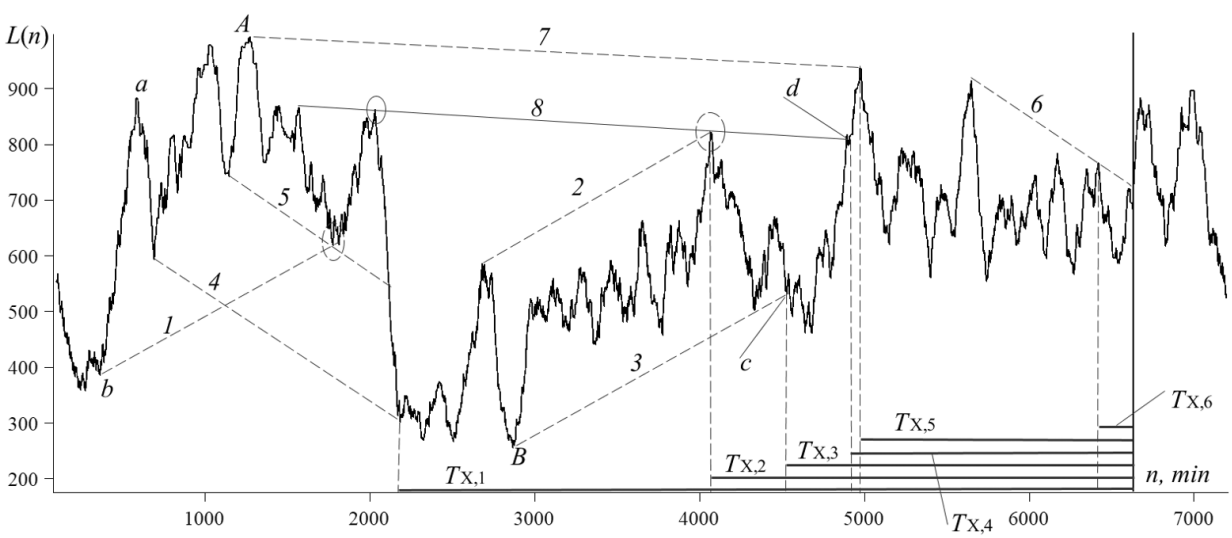

Fig. 2. *Dependence L(n) corresponding to the X-component of the geomagnetic field.*

functional $L(n)$ at the points of maximum and minimum), satisfying the condition $\delta L \geq 0.2\Delta L_{\max}$.

Here $\Delta L_{\max}$ is the maximum variation of the $L(n)$ values throughout a region from the origin to the moment of the earthquake, that is, the difference between the values of the largest minimum and the smallest maximum (respectively, points *A* and *B* in Fig. 2) of the statistical functional $L(n)$ on specified period of time. In this case, the condition is introduced that the geometric deviation ΔS of the curve $L(n)$ from the straight line segment connecting the boundary points of the given local trend satisfies the condition

$$\Delta S \leq 0.2\Delta l, \quad (3)$$

where Δl is the length of this segment. Condition (3) is necessary to ensure the quasi-straightness of the local trend. In Fig. 2 the local trend is, for example, section *ab* of the curve $L(n)$. The points of the boundaries of local trends will be called guiding points. We assume that each such point is horizontally removed from the nearest point of the curve $L(n)$ by no less than the interval $\Delta n = 100$ min.

2. A *channel* is a collection of two lines, each of which passes exactly through two guiding points, and the angle $\Delta\alpha$ between the directions of these lines satisfies the inequality

$$\Delta\alpha \leq 1.4°. \quad (4)$$

In (4), the angle $\Delta\alpha$ is determined using the scalar product of two vectors parallel to the channel boundaries (assuming that the geometric dimensions of the units of the Cartesian axes are equal). The time interval between the guide points through which the channel boundary is drawn must be at least 150 minutes. On Fig. 2 channels are marked: *1–2, 2–3, 4–5, 4–6*, which are formed by two inclined straight segments indicated in the figure by a dotted line. Note that segments *7–8* also form a channel (the properties of its lower boundary *8* will be discussed below).

3. The term *testing* means either the intersection at some point of the curve $L(n)$ and the corresponding channel boundary, or the passing the boundary at a distance ΔL_t vertically from the control point with coordinates $\{n_t, L(n_t)\}$ that satisfies the condition $\Delta L_t \leq 0.012\, L(n_t)$.

As the moment of registration of a precursor of an approaching earthquake, we will consider the time of the last (before the earthquake) testing of the channel boundaries by the dependence $L(n)$ (for example, point *c* for channel *2–3* in Fig. 2).

4. *Sliding boundary* is a straight line drawn through two control points and tested by the $L(n)$ curve at least one more guiding point that satisfies condition (5) (we will call such points additional and highlight them in the figures as a solid ellipse). As in section 3, we assume that the time of registration of the precursor of an approaching earthquake corresponds to the moment of the last testing of this curved line of the sliding boundary (see, for example, point *d* for the sliding boundary *8* in Fig. 2). Sliding boundaries are marked in the figures by solid oblique straight lines.

4. RESULTS OF PROCESSING THE MEASUREMENTS OF THE GEOMAGNETIC FIELD

Figs. 2-4 show the dependences of the functional $L(n)$, which correspond to the measurements of the geomagnetic field

components on the KNY magnetometer located in southern Japan during the period from 00:00 on March 12, 2022 to 23:59 on March 16, 2022. The horizontal axis shows discrete values of time n in minutes $n \geq M = 100$ min counted from the start of measurements. The solid vertical line marks the start of the earthquake with a magnitude of 7.3, which occurred on March 16, 2022 at 14:37 UTC (the epicenter coordinates are 37.702°*N*, 141.587°*E*) and was accompanied by a tsunami.

Fig. 2 corresponds to the dependence $L(n)$ for measurements of the *X*-component of the geomagnetic field. The intervals $T_{X,1} = 4451$ min, $T_{X,2} = 2565$ min, $T_{X,3} = 2104$ min, $T_{X,5} = 1659$ min, and $T_{X,6} = 213$ min correspond to the time intervals between the beginning of the earthquake and the moment of the fifth test for the boundaries of channels *4–5, 1–2, 2–3, 7–8, 4–6*, and the time interval $T_{X,4} = 1743$ min corresponds to the last test point for the sliding boundary *10*. The area near the additional point of the sliding boundary *10* is indicated by a solid ellipse.

Fig. 3 illustrates the dependence $L(n)$ for the *Y*-component of the geomagnetic field. In this case, the intervals $T_{Y,1} = 1896$ min, $T_{Y,2} = 682$ min, $T_{Y,3} = 662$ min, $T_{Y,4} = 662$ min, $T_{Y,5} = 548$ min and $T_{Y,6} = 24$ min. Here $T_{Y,1\text{-}5}$ are the time intervals between the beginning of the earthquake and the moment of the last testing for the boundaries of channels *1–2, 4–5, 6–7*, and *2–3*, and the interval $T_{Y,6}$ corresponds to the last testing of the $L(n)$ curve of the sliding boundary *9*.

In **Fig. 4**, the dependence $L(n)$ corresponds to measurements of the *Z*-component of the geomagnetic field. In this case, there are no sliding boundaries, and the intervals $T_{Z,1} = T_{Z,2} = T_{Z,3} = 1820$ min correspond to the time intervals between the beginning of the earthquake and the moment of the last testing for

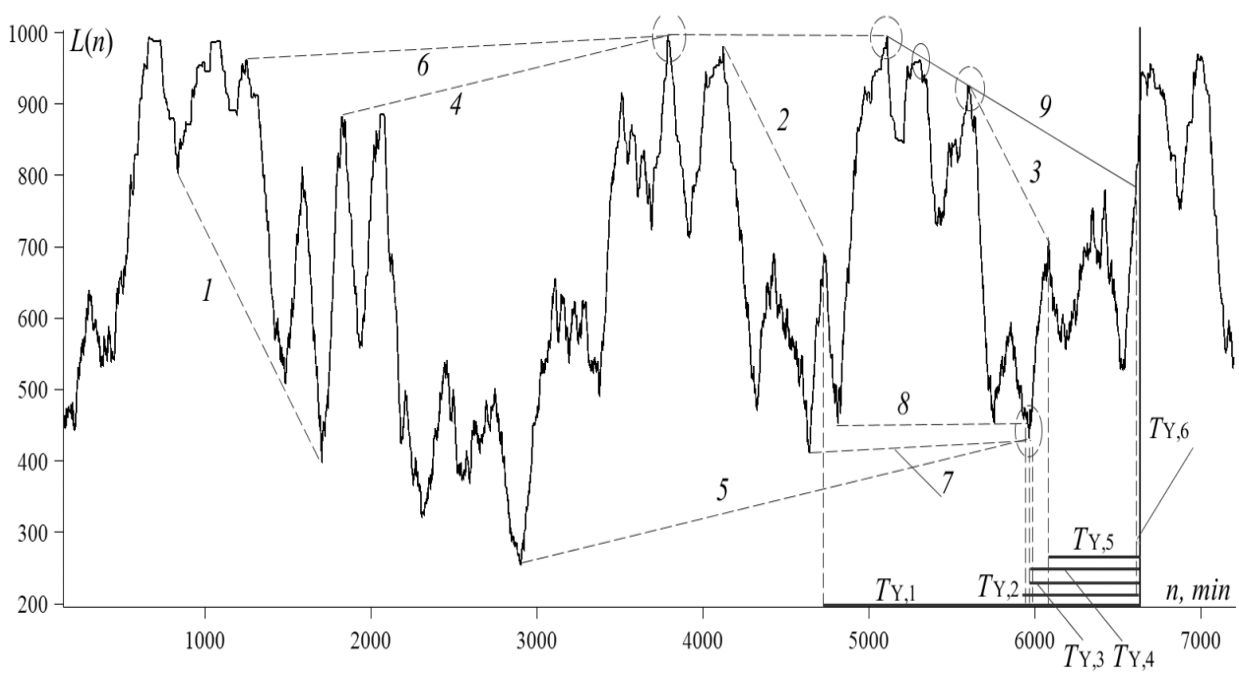

Fig. 3. *Dependence L(n) corresponding to the Y-component of the geomagnetic field.*

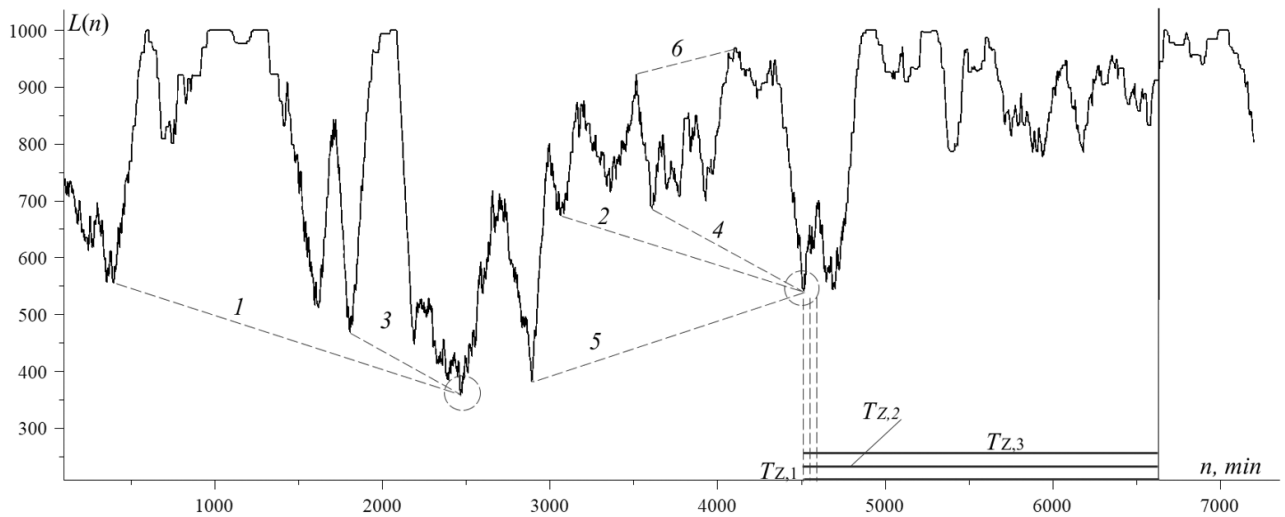

Fig. 4. *Dependence L(n) corresponding to the Z-component of the geomagnetic field.*

the boundaries of channels *1–2, 3–4, 5–6,* respectively.

Note that, as follows from the analysis of Fig. 2–4, before the earthquake, for the *L*(*n*) dependences corresponding to the *X-, Y-,* and *Z*-components of the geomagnetic field, numerous linear structures appeared, similar to those that preceded the seismic events considered in [1-3].

The values indicated in Figures 2-4 of the time intervals from the moment of registration of the precursor to the beginning of the earthquake are given in the **Table**.

As can be seen from the data given in the Table, almost all registered precursors refer to the interval from ten hours to two and a half days before a seismic event. The analysis of behavior of dependences *L*(*n*) showed that the number of precursors in the considered time interval of the order of several days before an earthquake increases in proportion to the duration of the time interval preceding the seismic event.

Table

Time interval values $T_{X,i}$, $T_{Y,i}$ *и* $T_{Z,i}$.

i	$T_{X,}$, min	$T_{Y,i}$, min	$T_{Z,i}$, min
1	4451	1896	1820
2	2565	682	1820
3	2104	682	1820
4	1743	682	
5	1569	548	
6	213	24	

5. DISCUSSION AND CONCLUSIONS

As a result of the analysis of processing measurements of the geomagnetic field, we come to the following conclusions:

1. For each channel, at least one of its boundaries passes through a critical point belonging to the boundary of another channel. This property indicates the mutual influence of seismic processes at the stage of "final preparation" of an approaching earthquake.
2. A seismic event is preceded by critical points associated with the synchronous or very close in time occurrence of three precursors, defined as the points of the last testing of the corresponding

channels. This can be interpreted as the simultaneous occurrence of three or more processes associated with the "final preparation" of the approaching earthquake.

3. In all presented cases, linear structures of the functional $L(n)$ pass through the point of its deepest minimum. This effect is quite consistent with the theoretical assumption that the specified minimum corresponds to the moment of the greatest compression of the lithospheric plates. Such compression with a high probability can lead to the occurrence of processes of destruction of the most weakened blocks of the earth's crust, which are accompanied by the formation of sliding boundaries and channels of the statistical functional.
4. As follows from the table, seven out of 15 recorded precursors are located in a relatively narrow interval from 30 to 35 hours before the earthquake, and the same number of precursors are located in a time interval of about 11 hours before this event, which confirms the relationship between the ongoing processes and the reliability of the methodology used.

Thus, we come to the conclusion that the set of the analyzed properties of the statistical functional $L(n)$ can be an indicator of the approaching moment of an earthquake, accompanied by a tsunami. It should be noted that the use of the statistical technique allows not only to fix the set of precursors of the approach of the seismic event, but also to identify time points at which extremely high levels of seismic compression of lithospheric plates in the earthquake preparation zone are achieved with a high probability.

REFERENCES

1. Volvach AE, Kogan LP, Kanonidi KH, Nadezhka LI, Bubukin IT, Shtenberg VB, Gordetsov AS, Krasnikova OV, Kislitsyn DI. Changes in the properties of the statistics of physical and biophysical fields as earthquake precursor. *Communications in Nonlinear Science and Numerical Simulation,* 2022, 108(1):106200-1–106200-18.
2. Volvach AE, Kogan LP, Kanonidi KH, Bubukin IT, Shtenberg VB, Volvach LN, Biazitov DT. Statistical precursors of a strong earthquake on April 6, 2009 on the Apennine Peninsula. *Heliyon*, 2022, 8(8):e10200-1–e10200-22.
3. Kogan LP. Change in statistical functionals of critical frequency prior to strong earthquakes. *Geomagn. Aeron.*, 2015, 55:507-520.
4. Gutenberg B, Richter CF. Frequency of Earthquakes in California. *Bulletin of the Seismological Society of America*, 1944, 34(4):185-188.
5. Gutenberg B and Richter CF. *Seismicity of the Earth and Associated Phenomena*. 2nd ed. Princeton, N.J., Princeton University Press, 1954, 255 p.
6. Amitrano D. Variability in the power-law distributions of rupture events, How and why does b-value change. *Eur. Phys. J.,* 2012, 205:199-215.
7. Popandopoulos GA, Lukk AA. The depth variations in the b-value of frequency-magnitude distribution of the earthquakes in the Garm region of Tajikistan. *Izvestiya. Physics of the Solid Earth*, 2014, 50(2):273-288.

8. Popandopoulos GA. Spatiotemporal variations in Gutenberg–Richter b-value depending on the depth and lateral position in the earth's crust of the Garm region, Tajikistan. *Izvestiya. Physics of the Solid Earth,* 2020, 56(3):337-356.
9. Han Q, Wang L, Xu J, Carpinteri A, Lacidogna G. A robust method to estimate the b-value of the magnitude–frequency distribution of earthquakes. *Chaos, Solitons and Fractals,* 2015, 81(A):103-110.
10. Novopashina AV, Sankov VA. Migracii realizovannoi seismicheskoi energii v razlichnih geodinamicheskih usloviyah. [Migrations of released seismic energy in various geodynamic conditions]. *Geodinamika i Tektonofizika*, 2018, 9(1):139–163 (in Russ.).
11. Gkarlaouni C, Lasocki S, Papadimitriou E, Tsaklidis G. Hurst analysis of seismicity in Corinth rift and Mygdonia graben (Greece). *Chaos, Solitons & Fractals*, 2017, 96(C):30-42.
12. Trofimenko SV, Bykov VG, Merkulova TV. Space-time model for migration of weak earthquakes along the northern bound Seismol. *Journal of Seismology*, 2017, 21:277–286.

DOI: 10.17725/rensit.2022.14.381

On the Stability of Catalyst Drops at the Vapor-Liquid-Solid Contact during the Nanowires Growth

Valery A. Nebol'sin, Vladimir A. Yuriev, Nada Swaikat, Valeria V. Korneeva
Voronezh State Technical University, http: /www.cchgeu.ru/
Voronezh 394006, Russian Federation
E-mail: vcmsao13@mail.ru, yuryevva@gmail.com, nada.s84@mail.ru, vkorneeva@vgasu.vrn.ru

Evgeniy N. Vasnin
Experimental Design Bureau of Motor Engineering, http: /www.okbm.ru/
Voronezh 394055, Russian Federation
E-mail: vasnin11@gmail.com

Received September 22, 2022, peer-reviewed September 29, 2022, accepted October 6, 2022.

Abstract: **This paper gives a physical justification for the wettability conditions for the limited area crystal surface by a small-volume catalyst droplet at the end of the growing nanowires (NW) characterized by a contact angle β, shown that under the stationary conditions NW's growth with a singular facet, there are the only values of the angles β and γ (the inclination angle of the crystal side surface to this facet), which correspond to the minimum increment of the free energy three-phase system $\alpha_{LV}\cos\beta + \alpha_{SL} = \alpha_{SV}\cos\gamma$ and defines the catalyst droplet's steadiness at the NW's top. With the cylindrical NWs growth, the conditions of indifferent equilibrium are realized at the drop wetting perimeter. A drop, due to the dissolution of a crystallizing substance or its separation from a liquid solution, can take an equilibrium shape with a contact angle β that does not satisfy the equilibrium contact angle condition θ in the Young equation. A concentric fracture (rib) at the NW top should increase the observed wetting angle θ and lead to contact angle hysteresis. The defined restrictions imposed on the contact angle value of a stable catalyst drop at the NW's top. The catalyst drop will take an equilibrium shape if the hysteresis angle β is in the range $\theta < \beta \le \theta' + \gamma$ (θ' is the wetting angle of the NW side walls). For the growth of semiconductor NWs in the form of a straight cylinder, γ = 900 and therefore always β > 90°. Shown that the direction of the three-phase line displacement relative to the droplet surface is determined by the growth angle φ_0: for the nonwetting growth mode of NWs (with a cross facet) $\varphi_0 = \beta - \gamma$; for the wetting growth mode (with an end curved surface near the three-phase line) $\varphi_0 = \arccos((\alpha_{SV}^2 + \alpha_{LV}^2 - \alpha_{SL}^2)/2\alpha_{SV}\alpha_{LV})$.**

Keywords: **nanowires, growth, catalyst, droplet, wetting, contact angle, semiconductor, three-phase line**

UDC 548.52:539.216

Acknowledgments: The study was supported by the Russian Science Foundation grant no. 22-22-00449, https://rscf.ru/project/22-22-00449/.

For citation: Valery A. Nebol'sin, Vladimir A. Yuriev, Nada Swaikat, Valeria V. Korneeva, Evgeniy N. Vasnin. On the Stability of Catalyst Drops at the Vapor-Liquid-Solid Contact during the Nanowires Growth. *RENSIT: Radioelectronics. Nanosystems. Information technologies*, 2022, 14(4):381-392e. DOI: 10.17725/rensit.2022.14.381.

Contents

1. INTRODUCTION

Semiconductor nanowires (NWs) of materials such as Si, Ge, GaAs, InSb, GaP, InAs, etc., are a perspective crystal basis for an element base creation of new generation radio-electronic devices: broadband nanoantennas of the optical range, highly sensitive nanosensors, efficient thermoelectric nanogenerators, microminiature frequency mixers and phase detectors, operating in the range up to 100 MHz at 300 K, and others [1,2]. The most widespread method NWs growing vapor-liquid-solid (VLS), in which is used a nano-sized droplets of metals in liquid-phase as a catalyst for effective collection and decomposition of precursors [3-5].

In the process of VLS growth, the NWs have a lateral crystal surface which is formed without contact with the walls of a crucible or container, such as in many other crystallization methods, which allows providing a high structural perfection of the grown crystals, rule out the appearance dislocations and the emergence of mechanical stresses. At the same time, the NW's morphology and transverse sizes are determined by the shape and volume drops of catalyst on the top of a growing crystal, also the formation conditions of the curved surface of a catalyst drop near the triple phase boundary vapor, liquid, crystal, and strongly depend on the parameters' growth process. Along with the surface energy, a key parameter, characterizing the meniscus of the liquid phase on the NW's top is the contact angle β, defined between the tangent to the surface liquid at a point on the three phases conjugation line and the end facet of NWs. The form of crystalline phase (zinc blende (ZB) or wurtzite (WZ) for nanowires AIIIBV) depends on the value of the contact angle, spatial direction of growth, crystallographic orientation (usually <111> for Si and Ge NWs), edge polarity (111)A or $(\bar{1}\bar{1}\bar{1})$B GaAs NWs, etc. [6-8].

The contact angle is a controlled technological parameter, which makes the possibility to ensure stable repetition of crystals growth with a needed structure and specified electrical characteristics. However, regarding the contact angle of the catalyst drop, there is a misunderstanding and confusion in the literature of the NWs growth [9-13]. So, despite the fact that the equation $\alpha_{SL} = -\alpha_{LV}\cos\beta$, where α_{LV} and α_{SL} are specific free surface energy of interfaces liquid/vapor and crystal/liquid respectively [9], is determining the droplet equilibrium condition on the cylindrical NW's top, which wide applied and used, Recently was written a number of international works which is considering the doubts about indicated expressions and estimates of the angle β, determined by this equation [10,11,13-15]. In most of these works, the droplet contact angle at the NW's top is analyzed based on Young's equation for wetting liquid of an extended solid surface [10-12]. However, the problem is that the contact angle of the catalyst drops on top cylindrical NW is always greater than 90° and does not satisfy the contact angle condition θ in Young's equation [16]. Important works were published important work regarding a role of crystal edges [11,12,14,15,17,18] and the influence of droplet volume to the contact angle [19,20]. In works [11,12] is stated that, to describe the equilibrium wetting condition a catalyst drop of the end surface of a cylindrical crystal which limited by a three-phase line (TL), Young's equation cannot be satisfied, since it includes the specific free surface energy of crystalline phase α_{SV}, characterizing the extended surface of the solid body. Thus, the authors of [14] believe that in some cases, the equilibrium angle predicted by Young's equation can performed only at certain points

on TL. However, according to these authors, such considerations do not mean that a drop is in balance. As a result, hastily is that no conclusions about the quantities specific free surface energy interfaces based on contact angle drops of catalyst on top of the NW cannot be obtained [11,15].

Considering the fundamental angle value of the catalyst drop contact for controlled growth and physical properties of NWs, the goal of this work is the physical substantiation of wettability conditions crystalline surface limited area with a small volume liquid on the NWs top and resolution of the misunderstanding problem of equilibrium conditions for a catalyst drop with an angle contact on the end face of the crystal.

2. MATERIALS AND METHODS

Si and Si_xGe_{1-x} NWs were grown in an oven term concept (GNA, USA) by the crystallization method from the gas phase in the hydrogen chloride process using Ni and Au particles as catalysts from 200 nm. Temperature range of NW growth was 1273-1373 K. Used for growing NW H_2 was purified by modern methods and had a dew point of 215 K mixture H_2 and $SiCl_4$ ($SiCl_4$+ $GeCl_4$) was prepared in standard liquid sources bubbling type mole ratio components M_{SiCl4}/M_{H2} (M_{SiCl4} + $GeCl_4/M_{H2}$) was maintained in the range from 0.005 to 0.01. Growth substrates were polished monocrystalline silicon wafers brand KEF-20(111).ETO.0.035.TU.400±20 μm with orientation {111}. NWs Growth Rate was determined by the "time marks" method [2]. For reproducible results and exclusion of the influence of NWs on each other it is important that the crystals are isolated, those located on the substrate at a sufficient distance (~1 μm). Dependence on NW length Si and Ge on the process temperature in the range from 773 K to 1273 K crystals on the VAK-501 installation (Evatec, Switzerland) by molecular beam epitaxy (MBE). Grown NWs were studied by transmission methods (TEM) 100-BR (Ukraine)) and raster electronic microscopy JSM-6380LV (JEOL, Japan), whose resolution is less than 1-2 nm, which is sufficient to determine the NW growth rate with the required accuracy.

Information about the growth parameters of Si NWs, Ge, GaAs, etc. were also analyzed according to literary sources.

3. RESULTS AND DISCUSSION

Observations of the growth of Si, Ge and Si_xGe_{1-x} NWs, having a circular cross section show that drops of M(metal)-Si, M-Ge and M-Si_xGe_{1-x} do not descend on the side surface of the NWs,and wets the vertex flat face {111}. Drop M-catalyst on the NWs top is a truncated spherical segment of an almost perfect spherical shapes (**Fig. 1***a,b*). In this case, the contact angle value on the face {111} Si, Ge, and Si_xGe_{1-x} NWs always exceeds 90°. The NW crystallization front, as a rule, represented by a crystallographic face family {111}. With good wettability crystal surface catalyst (in systems AuAl-Si, AuGa-Si, Au-Ge, Au-Si, etc.) front crystallization is curved. On **Fig. 2** shown TEM images vertices of Si NWs obtained in [22]. Under conditions of stationary growth of NWs semiconductors, a certain interface area ratio drops of SSL and SLV catalyst, consequently, constant ratio of the crystal radius and droplet radius *r*/*R* (Fig. 1*a,b*). Specified the ratios are obviously geometrically related to the contact angle

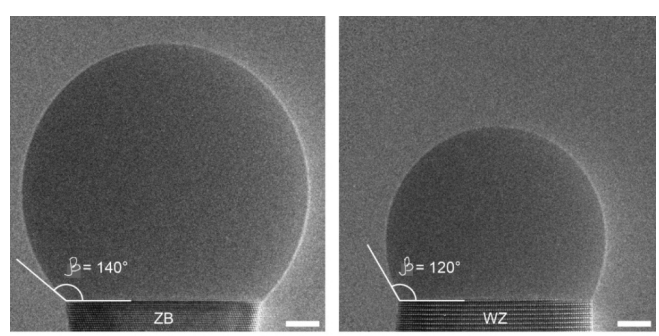

a *b*

Fig. 1. *TEM images of GaAs NW vertices with structure ZB (a) and WZ (b) and a singular end face* [21]. *Scale bars 5 nm.*

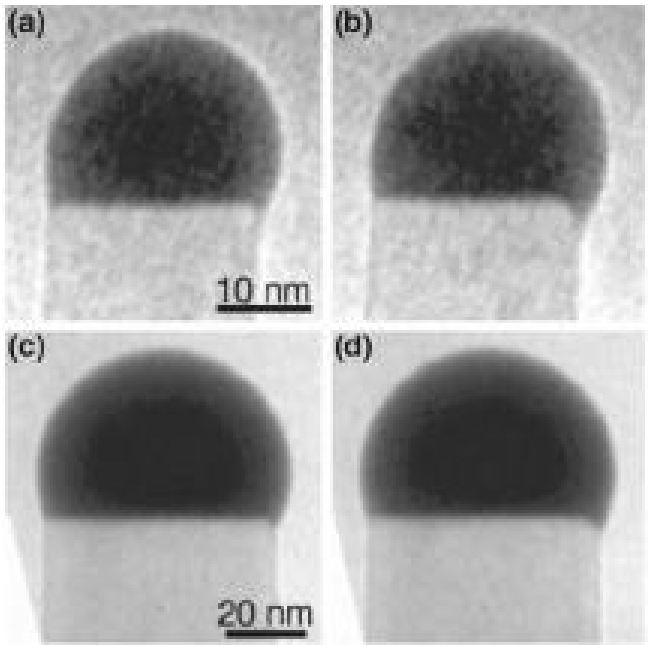

Fig. 2. *TEM images of Si NW vertices with particles AuAl-Si (a, b), AuGa-Si (c, d) and curved near TL by the crystallization front* [22].

of the catalyst drop β on the NW's top. In a real system, it is difficult to eliminate random variations of crystallization conditions. Therefore, random breaks and fragmentation of catalyst drops, leading to NW branching (**Fig. 3***a*), bends crystals (Fig. 3*b*), movement of catalyst droplets on the side walls of the crystal (Fig. 3*c*).

3.1. Solid body wetting with a liquid droplet

It is known [23] that for all possible variations catalyst drop shape during growth NWs under conditions of constant temperature, mass and volume of phases free energy of the system liquid-vapor-solid F must remain constant value (minimum for stable equilibrium), i.e. $\delta F = 0$. B hydrostatic approximation equilibrium the shape of the surface of the liquid drop at the top NW is described by the capillary equation Laplace [24]

$$\alpha_L\left(\frac{1}{R_1(A)}+\frac{1}{R_2(A)}\right)+\rho g w = const, \qquad (1)$$

where $R_1(A)$ and $R_2(A)$ – principal radii of curvature liquid/vapor interface element ds in point A on it, ρ is the density of the liquid phase, g is the free fall acceleration, w is the height of the surface element above selected level. Radius $R_1(A) > 0$ and $R_2(A) > 0$ if positive direction normal n to the curve on the drop surface goes inside the liquid, and $R_1(A) < 0$ and $R_2(A) < 0$ if – from liquid. The w axis is directed vertically up. The value of const depends on the choice of start reference coordinate w and is equal to the pressure, under which contains a drop of catalyst in plane $w = 0$. When the origin coordinates w coincides with a flat surface liquids on a flat crystallization front, then const = 0.

The distribution of the liquid is a peculiar mechanism of its creeping onto hard surface. Considering it, it's easy to understand that if the drop is on the surface solid body, then a complete change in the free energy of the system is expressed as [25]

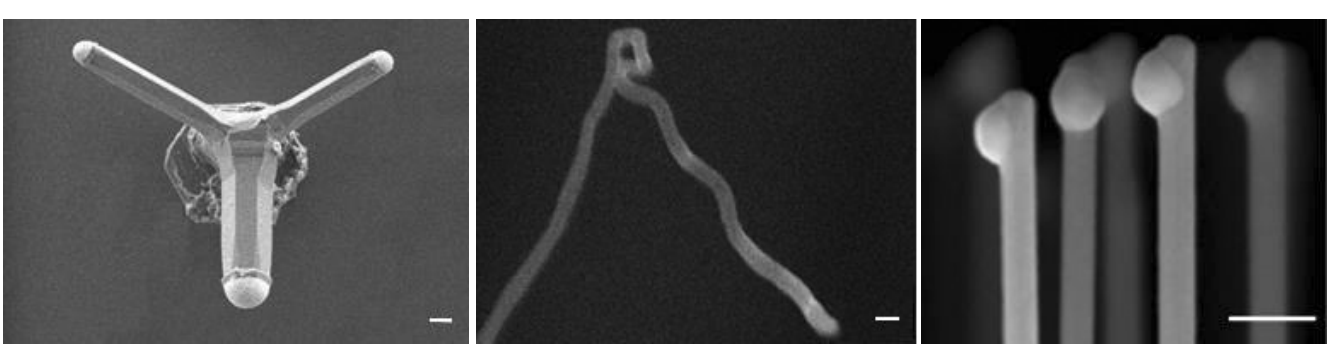

a *b* *c*

Fig. 3. *Uncontrolled PEA growth: (a) NWC Si_xGe_{1-x} with droplet rupture and crystal branching, (b) Si NWs with bends, (c) InAs NWs with droplet migration to the side walls* [11]. *Scale bars 100 nm.*

$$\delta F = \int_s \left[\alpha_{LV} \left(\frac{1}{R_1(A)} + \frac{1}{R_2(A)} \right) + \rho g w \right] ds \cdot \delta n + \\ + \int_l \sum \alpha_{IJ} \delta t \cdot dl = 0, \quad (2)$$

Δn, is the normal component of displacement liquid/vapor interface element *ds, dl* is the length element of the wetting perimeter, δt is shift of this element along the surface of a solid body (along the normal to the perimeter element), α_{IJ} – specific free surface energy individual parts of the liquid surface *I*, in contact with phases *J* (solid/vapor (*SV*), liquid/vapor (*LV*) and solid/liquid (*SL*)). As applied to a drop of catalyst on top of the NW, the first term in (2) reflect the changes in the free energy of a three-phase systems with variations in the droplet shape, and the second the term represents the change free energy of the system for possible the movement of a drop along an extended horizontal surface of the crystal.

Given the independence of *ds* and *dl* changes, for δF to be equal to zero, the equality zero of both integrands in (2)

$$\alpha_{LV} \left(\frac{1}{R_1} + \frac{1}{R_2} \right) + \rho g w = 0, \quad (3)$$

$$\alpha_{SV} - \alpha_{SL} - \alpha_{LV} \cos\theta = 0. \quad (4)$$

Equation (3) describes the effect of curvature surface and gravity to the equilibrium liquid form. Here the condition for complete equilibrium (2) is not satisfied. For nanoscale liquid-phase drops of the M-catalyst by the influence gravity can be neglected $(\rho g w = 0)$.

Then (3) the first term will only reflect the effect of surface curvature (dispersion) of a small-volume liquid on the internal pressure. The first term in (3) should be true when, for example, the equilibrium drop of the catalyst is at top of a cylindrical or prismatic NWs with vertical walls. In the absence of gravity and at a constant droplet volume liquid (V = const), equation (3) can be write as min $\sum_{IJ} \alpha_{IJ} S_{IJ} = \min$ (Gibbs-Curie principle), S_{IJ} is the area of individual parts of liquid surfaces in contact with other phases, and the summation is carried out over the entire surface of the drop.

Expression (4) characterizes the equilibrium drops on the wetting perimeter, described Young's equation. This expression is true when a drop is located on an extended flat surface of a solid body (substrate). The complete equilibrium condition (2) is also is not satisfied, since *ds* depends on δt, and, therefore, the first term depends on specific free surface energy solid/vapor interface α_{SV}, which increases wetting perimeter. In this case, free Gibbs surface energy $\sum_{IJ} \alpha_{IJ} S_{IJ} \neq \min$.

3.2. The equilibrium droplet at the NWs top with a singular cross facet

Let us now consider point *A* on the dividing line of three phases adjacent to the transverse singular {111} faces of the NW crystallization front (**Fig. 4***a,b*). In this case, the catalyst drop dosen't wet the side surface of the crystal. Crystallization on the {111} face occurs

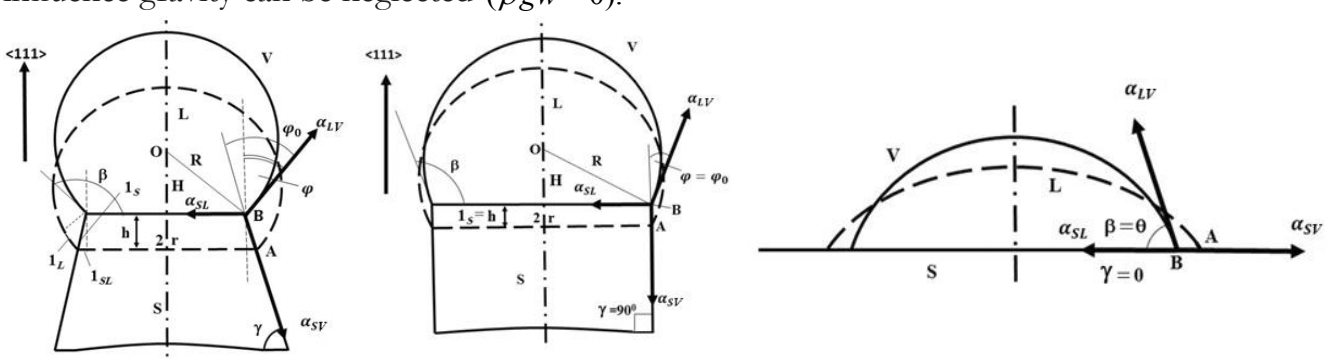

a *b* *c*

Fig. 4. *Conjugation scheme of three phases at the top of conical (0 < γ < 90°) (a), cylindrical (γ = 90°) (b) NW and on the substrate (γ = 0) (c).*

via nucleation and growth in the tangential direction of steps of monoatomic height *h*. Let the steps be generated or absorbed TL in such a way that the emergent of the side surface of the NW at point A is inclined to the horizontal, i.e. to the singular face {111}, at an angle γ (Fig. 4a). Then, when varying the drop height single crystal layer *h* crystal lengthens by $l_S = h/\sin\gamma$, {111} face of the front crystallization is grow down by $l_{SL} = l_S\cos\gamma$, and the surface of the drop is reduced by $l_L = l_S\cos(\beta-\gamma)$.

Change in free energy F_S, associated with a change in the areas of three adjacent surfaces when the TL is displaced from point *A* to point *B* will be [26]

$$F_S = 2\pi r\left(\alpha_S l_S - \alpha_{SL} l_{SL} - \alpha_L l_L\right), \quad (5)$$

or per unit length TL

$$F_S = \frac{h}{\sin\gamma}\left[\alpha_S - \alpha_{SL}\cos\gamma - \alpha_L\cos(\beta-\gamma)\right]. \quad (6)$$

In expression (5), through *2πrl* (*l* with indices *S, L, SL*) marked by the area increment phase boundaries crystal/vapor *S*, liquid/vapor *L* and solid/liquid *SL*, respectively. Sign "–" before the second and third terms in (6) means when TL is displaced from the point *A* to point *B* corresponding surface decreases.

Further, to simplify in expression (6) denote $\alpha = F_S/h$. Then the change in specific free surface energy Δα three-phase system when absorbing a step (calculated per unit of length TL and per one the absorbed step with height *h*) can be written as

$$\Delta\alpha = \alpha - \alpha_{SL}. \quad (7)$$

It consists of a term $-\alpha_{SL}$ (disappearance steps) and the term α associated with the change areas of all three adjacent surfaces [26]. If $\Delta\alpha < 0$, then single-crystal steps can be absorbed (generated) by the line separation of three phases, forming a side surface NWs at an angle γ. This is possible if $\varphi_0 < \theta$, where φ_0 – corner inclination of the segmental surface of the drop to the displacement direction of the line of three phases. Then the drop will move at an angle, sliding down along the step of the formed crystalline layer, reducing the area of its wetting. Drop wetting perimeter will decrease. With such a displacement of the drop changes the location of all three adjacent surfaces near TL, as a result of which is the increase in the angle of inclination of the segmental surface of the catalyst drop at point *A* on the wetting perimeter to the NW growth axis φ, and, respectively, φ_0 to equilibrium θ values.

To fix the condition $\Delta\alpha < 0$, the angle contraction (expansion) NW γ must correspond to minimum free energy of three-phase system after the absorption of the monolayer by the height *h*, i.e. meet the minimum value α. The minimum value $\alpha = \alpha_{min}$ is reached, when for all possible variations of the form liquid surface (while maintaining its volume) free energy F_S remains constant value (minimum for stable equilibrium), i.e. at $dF_S/d\gamma = 0$.

Differentiating (6) to the angle γ and equating zero derivative, we obtain the condition where the minimum $F_S(\gamma)$ is reached

$$\alpha_{LV}\cos\beta + \alpha_{SL} = \alpha_{SV}\cos\gamma. \quad (8)$$

Expression (8) is mechanical balance of forces corresponding to free surface energies of three phases in point *A* on the wetting perimeter. Equation (8) obtained under the assumption that it is not taken into account free surface anisotropy energies of lateral *i*-faces of NWs $\left(\sum_i \frac{\partial\alpha_S^i}{\partial\gamma} = 0\right)$, the contribution of the linear tension is neglected, and the volume of the catalyst droplet V_L in the process NW growth remains constant ($dV_L = 0$), that it must be done the requirement for absolute rigidity of a solid body and its insolubility in liquid. Condition constant volume of liquid catalyst drop and insolubility in it crystallized material can be admitted if we consider stationary process of NW growth at T = const in the absence of chemical carryover and physical evaporation

of the material of the liquid phase, as well as not take into account the loss of metal due to dissolution in solid state and surface diffusion.

From expression (8) it follows that in each time point of NW growth with a transverse singular face, there are only the values of the angles γ and β, i.e. actually implemented such an angle of contraction (expansion) of the crystal γ and such a drop contact angle β that correspond to the minimum increment free energy of a three-phase system after absorption monolayer height *h*

$$\gamma = \arccos\left(\frac{\alpha_{LV}\cos\beta + \alpha_{SL}}{\alpha_{SV}}\right). \quad (9)$$

Thus, for constant values specific free energy of boundaries phase separation α_{SV}, α_{LV} and α_{SL} and when performing above requirements contact angle γ is nonlinearly related to the angle β (**Table 1**). Offset direction TL relative to the surface of the drop at point *A* on the dividing line of three phases adjacent to transverse singular face {111} of the front crystallization, will be determined by the angle $\varphi_0 = \beta - \gamma$, which we will call the growth angle (crystallization) NW, which, in turn, can be found from the expression

$$\varphi_0 = \beta - \arccos\left(\frac{\alpha_{LV}\cos\beta + \alpha_{SL}}{\alpha_{SV}}\right). \quad (10)$$

It must be said that the growth angle φ_0 (10) should not be confused with contact angle *θ*. Corner wetting characterizes partial equilibrium relative to the movement of a liquid through a solid body and, in contrast to φ_0, not directly associated with the process of crystal growth. As the angle β increases in the interval $0 \le \beta \le 1800$, the angle γ also increases.

Table 1

Calculated values of the angle γ depending on the angle β for the Au–Si system for $\alpha_{SV}\{111\}$ = 1.23 J/m² and α_{LV} = 0.91 J/m²

β, degree	90	100	110	120	130	140	150	160	170	180
θ, degree	-	-	0	32	45	54	61	66	68	69

For γ = 0 in according to (8) and (9), we obtain the condition equilibrium of a drop lying on a horizontal extended surface (Fig. 4*c*)

$$\alpha_{LV}\cos\beta + \alpha_{SL} = \alpha_{SV}, \quad (11)$$

those, known Young equation for mechanical equilibrium of a drop on a flat surface (at β = *θ*). Displacement of TL from the equilibrium position here can only be carried out at an angle *θ* horizontally along an extended solid surfaces.

At γ = 90°, from (8) follows the growth condition cylindrical NWs of constant diameter (see expression (2) for *g* = 0 and V_L = const) [6]

$$\alpha_{SL} = -\alpha_{LV}\cos\beta = \alpha_{LV}\sin\varphi. \quad (12)$$

Expression (12) reflects the equilibrium form drops of catalyst on top of a growing NWs in a state of indifferent equilibrium on the wetting perimeter. Through the dissolution crystallizable substance or its excretion from a liquid solution of a drop of *M*-catalyst on at the top of the NWs, the wetting perimeter of the drop is not fixed, and the latter can take balanced form.

From (12) it follows that under conditions of indifferent equilibrium on the wetting perimeter on a round contour at the point of contact with the NW end face *A* the drop must form a fixed equilibrium angle β = const (or φ = const) with the surface of the crystal. Therefore, than the larger the droplet radius *R*, the larger should be the radius *r* of the NW:

$$\frac{r}{R} = \sqrt{1-\left(\frac{\alpha_{SL}}{\alpha_L}\right)^2} = \sqrt{1-\sin^2\varphi} = \sqrt{1-\cos^2\beta}. \quad (13)$$

Thus, the equilibrium form drops on top of the NWs is the result of aspirations of her free superficial energy to a minimum and directly related with its liquid-phase state of aggregation. Here the shape of the drop reaches a stable equilibrium, which ensures self-stabilization of dimensions and cross-sectional shapes of NWs in the process growth.

According to equation (13), the condition minimum free surface energy of an equilibrium drop at the top NWs is proportionality specific free surface energy segments of liquid/vapor interfaces and liquid/solid their distances up to drop center. The more free energy section of the interphase boundary, the farther it located from the center of the drop and the smallerit has a surface.

If a three-phase system due to kinetic limits cannot be reached or maintained the only values of the equilibrium angles γ and β defined by expression (9), then for ensure the indifferent balance of the drop at the top of the NW, the contact angle β must meet the following conditions

$$\begin{cases} \alpha_{LV}\cos\beta \le \alpha_{LV}\cos\theta \\ \alpha_{LV}\cos(\beta-\delta) \ge \alpha_{LV}\cos\theta' \end{cases}. \quad (14)$$

Passing from cosines, directly, to corners, we have

$$\theta \le \beta \le \theta' + \gamma \quad \text{при } \gamma > 0 \quad (15)$$

or

$$\theta - \gamma \le \beta - \gamma \le \theta' \quad \text{при } \gamma < 90°. \quad (16)$$

Similarly, for γ = 90° and β – 90° = φ we have

$$\theta - 90^0 \le \varphi \le \theta' \quad (17)$$

or

$$\theta \le \varphi + 90^0. \quad (18)$$

The first non-strict inequality in (14) determines the boundary condition under which the drop cannot slide along the transverse singular face, increasing the perimeter wetting and decreasing the contact angle. The second inequality (14) specifies the condition at which the drop cannot fall on lateral surface of the NW. In this way, for the equilibrium position of the drop at θ < 90° and γ > 0 contact angle β must be in the interval from θ to θ' + γ. Therefore, on singular extended substrate, when γ = 0, the equilibrium angle β is fixed: β = θ or β = θ', depending on the orientation. Within the limits specified in inequalities (14) - (18) the range of angle change β drop can maintain an indifferent balance wetting perimeter. This combination phases in practice gives a continuous range contact angle values. Theoretically, in according to contact angle hysteresis maximum contact angle β = β_A (β_A = θ' +γ) is called the leakage angle, and the minimum wetting angle β = β_R – receding angle. For example, for the data in Table 1 θ = 35° and β_A = 125°. Next, we explain the occurrence droplet wetting hysteresis at the top NWs.

Let a drop of liquid catalyst spreads spontaneously crystal surface, which is the vertex face of the NW {111}, in the *x* direction (**Fig. 5**). Free surface energy of a three-phase system F_S in this process should decrease: $dF_S/dx < 0$. In this case, will continuously decrease and droplet contact angle β = $f(x)\cdot(d\beta/dx <$ 0). For smooth face {111} this condition is satisfied all the way. Let now on a smooth surface face has a concentric fracture (edge) in the form of a circle. Tilt angle the outer edge of the fracture to the horizon can be arbitrary, but in the case of growth of NWs of constant diameter it is 90°. At the presence

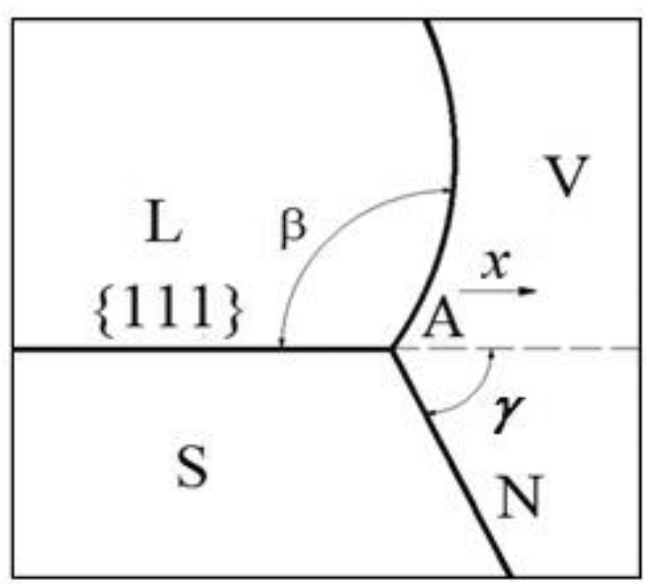

Fig. 5. *Stopping the contour of a spreading drop atconcentric break AN (edge) on the end face {111} NWs.*

of a fracture on the periphery of the end faces {111} for droplet spreading situation is complicated, since when fluid flows behind fracture increases its surface area stronger than when moving the TL along a smooth surface along the x direction (dotted line in Fig. 5). The power of the surface tension acts in relation to new direction of spreading AN under angle ($\beta - \gamma$). Fracture resistance can be overcome by a drop only on condition that the angle formed by the surface liquid and the outer surface of the fracture (NW side surface) ($\beta - \gamma$), more contact angle θ between the drop surface liquid and smooth solid surface. Using equation (12), one can find overflow condition: $\beta > (\theta' + \gamma)$. For $\beta < (\theta' + \gamma)$ the break at the top of the NW is an insurmountable barrier to cross TL can only under external influences (e.g. vibrations) or rather strong energy fluctuations near TL. From here, the contact angle of leakage on side surface of NWs: $\beta_A = \theta' + \gamma$.

Under conditions where $\beta > (\theta' + \gamma)$, the drop falls on the side walls of the NW. Sank at this wetting perimeter provides the possibility of growth expanding to top of the crystal. As a result of growth expanding crystal contact angle side surface will decrease and, in the limit, reaches the receding angle on the side face $\beta_R = \theta - \gamma$. As a result, TL is inevitable should rise to the edge (break) of the crystal. For $\gamma = 90°$, this edge is line of intersection of the transverse singular NW faces with a set of faces crystallographic belt having axes, parallel to the NW axis.

However, if the contact angle θ' of the drop catalyst saturated with crystallizable substance exceeds 90°, then at $\gamma = 90°$ the drop is unable to land on side surface of NWs, because in this case $\beta = \beta_A > 180°$. This means the absence contact of the catalyst drop with the crystal.

Thus, a concentric fracture on top of the NW should increase the observed contact angle (during leakage), which is noted in experience. Available at the top of the NWs hysteresis of the contact angle appears or wettability hysteresis.

It must be said that the occurrence during the growth of NWs significant temperature gradients, significant fluctuations in the flows of crystallized substances, concentration disturbances can remove the drop at the top of the NW from the state indifferent equilibrium (14) and lead to irreversible consequences (fragmentation drops and branching NNK, creeping drops on the lateral surface of the crystal, bends and changes in spatial direction of growth, sharp jumps in diameter and others (Fig. 3)).

3.3. The equilibrium droplet at the NWs top with an end curved surface

Equilibrium on the wetting perimeter drops of catalyst can be obtained by growing NWs with a curved near TL end surface (Fig. 2). If for NW with a curved end surface write down the components of the projections of force vectors, corresponding free surface energies of the interfaces α_{SV}, α_{LV} and α_{SL} in point A on the TL to the continuation direction the existing side surface of the NWC, and also in a direction perpendicular to it, in form of a system of equations and express the angle φ_0 in explicitly, we get the expression

$$\varphi_0 = \arccos\left(\frac{\alpha_{SV}^2 + \alpha_{LV}^2 - \alpha_{SL}^2}{2\alpha_{SV}\alpha_{LV}}\right). \qquad (19)$$

Expression (19) characterizes the growth angle (crystallization) NW φ_0 in full balance of forces on the wetting perimeter (**Fig. 6**). This state of steady equilibrium can only be realized when good wettability of the crystalline surface with a drop of catalyst ($\theta < 90°$). For the values of the Au–Si system $\alpha_{SV}\{110\} = 1.50$ J/m^2, $\alpha_{LV} = 0.91$ J/m^2 and $\alpha_{SL} = 0.75$ J/m^2 [4,9] from expression (19) we obtain the value growth (crystallization) angle of NWs $\varphi_0 = 23.5°$.

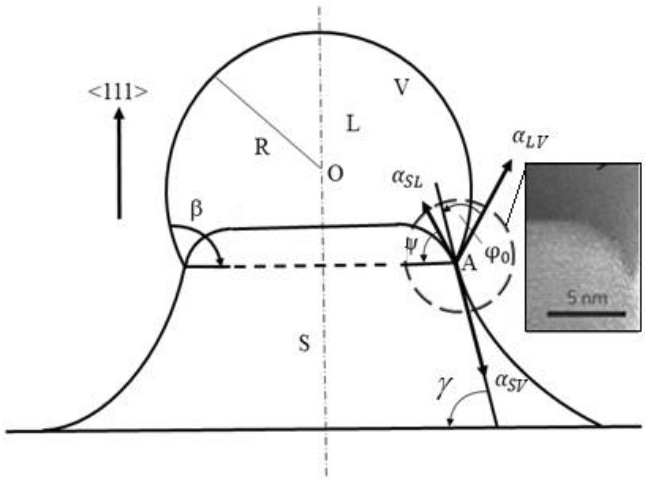

Fig. 6. *Scheme of NWs growth with a curved end surface. The inset shows a TEM image of a section of Si NWs curved near the TL.*

4. CONCLUSION

The physical substantiation of the conditions is given wettability of the crystal surface limited catalytic area liquid of small volume at the end of the growing NWs characterized by contact angle β, which contributes to fundamental understanding of nature contact angle of catalyst droplets on top NWs.

It is shown that under stationary conditions growth of NWs with a transverse singular face there are unique values of the angles β and γ, which correspond to the minimum increment free energy of a three-phase system $\alpha_{LV}\cos\beta + \alpha_{SL} = \alpha_{SV}\cos\gamma$ and determine the drop stability catalyst at the top of the NW.

It has been shown that due to the dissolution crystallizable substance or its excretion from a liquid solution, a drop of catalyst can take shape at the top NWs with an angle β that does not satisfy contact angle condition θ in Young's equation.

The restrictions imposed on the angle β of a stable catalyst drop with the growth of NWs. It has been shown that the concentric a break (rib) at the top of the NW should increase the observed contact angle θ. Therefore, in conditions of indifferent equilibrium on wetting perimeter, a drop of catalyst will be take shape at the top NWs, if the hysteresis angle β is in range $\theta < \beta \le \theta' + \gamma$ or $\theta - \gamma < \varphi \le \theta'$ at $\gamma > 0$. Outside this range, the equilibrium is violated, and the drop is displaced along the end face or side surface of the crystal up to positions where Young's equation is valid. For the growth of NWs of semiconductors in the form straight cylinder $\gamma = 90°$ and therefore always $\beta > 90°$ and $\varphi > 0°$.

It is shown that the total thermodynamic equilibrium on the wetting perimeter drops of catalyst can be achieved at growing NWs with a curved near TL end surface. Direction displacement of the three-phase line relative to droplet surface is determined by the growth angle φ_0: for the growth of NWs with a transverse face $\varphi_0 = \beta - \gamma$; for the growth of NWs with a curved near three-phase line end face $\varphi_0 = \arccos((\alpha_{SV}^2 + \alpha_{LV}^2 - \alpha_{SL}^2)/2\alpha_{SV}\alpha_{LV})$.

The results obtained contribute fundamental understanding of nature contact angle of catalyst droplets on top NWs and expanding our vision on the wetting of solids by liquids. They are can be used both for processes synthesis of NWs, opening up ways to control stable equilibrium of a catalyst drop, and for a wide class of other physical phenomena in which contact is made liquid metal or alloy with a surface more refractory material: welding and soldering contact pins of microcircuits, processes sintering in powder metallurgy, impregnation porous framework of liquid metal binding in the creation of ceramic materials, crystal growth by Verneuil and zone recrystallization and others.

REFERENCES

1. Pissard S, Weperen I, Car D, Verheijen M, Immink G, Kammhuber J, Cornelissen LJ, Szombati DB, Geresdi A, Frolov SM, Kouwenhoven LP, Bakkers E. Formation

and electronic properties of InSb nanocrosses. *Nat. Nanotechnology*, 2013, 8(11):859-864.

2. Kammhuber J, Cassidy MC, Pei F, Nowak MP, Vuik A, Gül Ö, Car D, Plissard SR, Bakkers EP, Wimmer M, Kouwenhove LP. Conductance trough a helical state in an Indium antimonide nanowire. *Nat. Nanotechnology*, 2017, 8(1):478-484.
3. Wagner RS, Ellis WC. Vapor-liquid-solid mechanism of single crystal growth. *Appl. Phys. Lett.,* 1964, 4(5):89-95.
4. Givargizov EI. Fundamental aspects of VLS growth. *J. Cryst. Growth,* 1975, 31:20-30.
5. Güniat L, Caroff P, Fontcuberta i Morral A. Vapor Phase Growth of Semiconductor Nanowires: Key Developments and Open Questions. *Chem. Rev.*, 2019, 119(15):8958-8971.
6. Yuan X, Caroff P, Wong-Leung J, Fu L, Tan H H, Jagadish C. Tunable Polarity in a III-V Nanowire by Droplet Wetting and Surfage Energy Engineering. *Adv. Mater.*, 2015, 27(40):6096-6199.
7. Tornberg M, Dick KA, Lehmann S. Thermodynamic Stability of Gold Assisted InAs Nanowire growth. *J. Phys. Chem. C,* 2017, 121:21678-21684.
8. Jacobsson D, Panciera F, Tersoff J, Reuter MC, Lehmann S, Hofmann S, Dick KA, Ross FM. Interface dynamics and crystal phase switching in GaAs nanowires. *Nature,* 2016, 531:317-339.
9. Nebol'sin VA, Shchetinin AA. Role of Surface Energy in the Vapor–Liquid–Solid Growth of Silicon. *Inorg. Mater.*, 2003, 39(9):1050-1055.
10. Dubrovskii VG. Development of Growth Theory for VLS NWs: Contact Angle, Facets, Crystal Phase. *Cryst. Growth Des.,* 2017, 17(5):2544-2548.
11. Ghisalberti L, Potts H, Friedl M, Zamani M, Güniat L, Tütüncüoglu G, Carter WC, Fontcuberta i Morral A. Questioning liquid droplet stability on nanowire tips: from theory to experiment. *Nanotechnology,* 2019, 30:285604-285613.
12. Nebol'sin V, Levchenko EV, Swaikat N, Yuryev V. About a fundamental uncertainty of the contact angle of the catalyst drop on the top of the nanowire. *J. Appl. Phys.,* 2021, 129:164302-164314.
13. McIntyre PC., Fontcuberta i Morral A. Semiconductor nanowires: to grow or not to grow? *Mater. Today Nano*, 2020, 9:100058-100065.
14. Krogstrup P, Curiotto S, Johnson E, Aagesen M, Nygård J, Chatain D. Impact of the Liquid Phase Shape on the Structure of III-V Nanowires. *Phys. Rev. Lett.*, 2011, 106:125505.
15. Fang G, Amirfazli A. Undestanding the Edge Effect in Wetting: A Thermodynamic Approach. *Langmuir*, 2012, 28:9421-9430.
16. Young T. An Essay on the Cohesion of Fluids. *Philos. Trans. Roy. Soc. London,* 1805, 95:65-87.
17. O'Dowd BJ, O'Dowd1 BJ, Wojtowicz T, Rouvimov S, Liu X, Pimpinella R, Kolkovsky V, Wojciechowski T, Zgirski M, Dobrowolska M, Shvets IV, Furdyna J. Effect of catalyst diameter on vapour-liquid-solid growth of GaAs nanowires. *J. Appl. Phys.*, 2014, 116 063509.
18. Schmidt V, Wittemann JV, Senz S, Gösele U. Silicon Nanowires: A Review on Aspects of their Growth and their Electrical Properties. *Adv. Mater.*, 2009, 21(25-26):2681-2702.
19. Jacobsson D, Panciera F, Tersoff J, Reuter MC, Lehmann S, Hofmann S, Dick KA, Ross FM. Interface dynamics and crystal phase switching in GaAs nanowires. *Nature*, 2016, 531:317-339.

20. Kolíbal M, Vystavěl T, Varga P, Šikola T. Real-Time Observation of Collector Droplet Oscillations during Growth of Straight Nanowires. *Nano Lett.*, 2014, 14:1756.
21. Panciera F, Baraissov Z, Patriarche G, Dubrovskii VG, Glas F, Travers L, Mirsaidov U, Harmand J-C. Phase selection in self-catalysed GaAs nanowires. *Nano Lett,* 2020, 20(3):1669-1675.
22. Wen C-Y, Tersoff J, Hillerich K, Reuter MC, Park JH. Periodically Changing Morphology of the Growth Interface in Si, Ge, and GaP Nanowires. *Phys. Rev. Lett.,* 2011, 107:025503-025507.
23. Nebol'sin VA, Suyatin DB, Dunaev AI, Shmakova SS, Zavalishin MA, Ivannikova EV. Contribution of the Free Energy of the Three Phase Line of Contact to the Thermodynamic Equilibrium Conditions of a Metal Solvent Droplet in Si and Ge Whisker Growth. *Inorg. Mater.*, 2015, 51(3):191-196.
24. Landau LD, Lifshitz EM. Mekhanika sploshnykh sred [Continuum mechanics]. Moscow, Gostekhteorizdat Publ., 1953, 737 p.
25. Gibbs DV. *Thermodynamic works.* Moscow-Leningrad, GITL Publ., 1950, 492 p.
26. Nebol'sin VA, Dunaev AI, Tatarenkov AF, Shmakova SS. Scenarios of Stable VLS Nanowire Growth. *J. Cryst. Growth*, 2016, 450:207-214.

DOI: 10.17725/rensit.2022.14.393

Methods for Studying Parameters Biogenic Metal Nanoparticles, Formed in situ

Dmitry A. Skladnev, Vladimir V. Sorokin
Vinogradsky Institute of Microbiology of RAS, http://www.inmi.ru/
Moscow 117312, Russian Federation
E-mail: skladda@gmail.com, vlvlsorokin@gmail.com

Sergey P. Karlov
Moscow Polytechnic University, http://mospolytech.ru/
Moscow 107023, Russian Federation
E-mail: karlovsp@yandex.ru

Vladimir I. Anisimkin
Kotelnikov Institute of Radioengineering and Electronics RAS, http://www.cplire.ru/
Moscow 125009, Russian Federation
E-mail: anis@cplire.ru

Received 15 November 2022, peer-reviewed 22 November 2022, accepted 29 November 2022

Abstract: **We propose an innovative method for assessing the integral level of metabolic activity of biological objects, based on the natural ability of living cells for generation metal nanoparticles from cations sources (artificially introduced into the samples), while in sterile samples or in the presence of inactive cells, the formation of nanoparticles does not occur. The method is called DBNG (detection of biogenic nanoparticles generation/growth). This article presents several examples of the use of the main analytical approaches applicable to obtain information about the parameters of biogenic nanocrystalline structures that formed in situ(directly in the tested samples), as well as options for the practical use of the proposed nanobiotechnological innovative approach DBNG to assess (estimate) the basic integral properties of living cells.**

Keywords: **metabolic activity of cells, generation de novo nanoparticles, detection of biogenic metal nanoparticles, fluorescence spectrometry, acoustoelectronic technologies**

UDC 57.016.6 +57.033

Acknowledgments: The work was done within the framework of the government task of the Ministry of Science and Higher Education of the Russian Federation, FRC "Fundamental Foundations of Biotechnology" of the RAS (№122040800164-6) and Kotel'nikov IRE RAS (№FFWZ-2022-0002). The work was partially funded by the Russian Foundation for Basic Research (grant # 20-57-7804).

For citation: Dmitry A. Skladnev, Sergey P. Karlov, Vladimir I. Anisimkin, Vladimir V. Sorokin. Methods for Studying Parameters Biogenic Metal Nanoparticles, Formed in situ. *RENSIT: Radioelectronics. Nanosystems. Information Technologies*, 2022, 14(4):393-414e. DOI: 10.17725/rensit.2022.14.393.

Contents

1. INTRODUCTION

Many areas of microbiology, ecology and medicine require measurements to assess the level of metabolism of living cells or the dynamics of its changes present in the investigated samples. There are various research tasks that require an answer to the question, are microorganisms present in the samples or are these samples sterile? Examples of such tasks include the study of samples taken in extreme natural zones of the Earth (Antarctic Lake Vostok), or when it is necessary to accurately determine whether the causative agent of the disease has been eliminated, or the task of detecting and identifying pathogenic bacteria and viruses, including in samples from other planets (Mars soil research project), and others similar to those. An exact and exhaustive answer to the question of whether the tested sample is sterile or not is very difficult, since in some cases the concentration of biological objects can be low. More often, a fairly accurate assessment of the types and abundance of biological objects, an assessment of the level of their metabolic activity is required.

At present, various methods for obtaining such information are widely used, from classical microbiological and biochemical methods to molecular genetics and metagenomics methods. However, some of them require considerable time to obtain a

reliable result, others are characterized by the high cost of the necessary reagents. Previously, an innovative method DBNG (detection of biogenic nanoparticles generation/growth) was proposed to quickly detect the presence of living cells in samples, as well as to assess the integral level of metabolic activity of biological objects. This approach is based on the natural ability of living cells to form metal nanoparticles from sources of cations artificially introduced into the samples, while in the presence of inactive cells or in sterile samples, the generation of nanoparticles does not occur [1].

Nowadays, commercial productions of nanoparticles for practical applications in medicine and biological research are produced *de novo* (from the very beginning) by chemical reduction of cations in reaction with molecules or molecular groups that have reducing properties (electron donors). To date, methods have been developed quite well that allow one to effectively and with a high yield obtain monodisperse preparations of metal nanoparticles with specified sizes, properties, and certain stabilizing coatings, which are necessary for use. Such progress would not have been possible without the development of the measurement and analytical capabilities of scientific instrumentation, without expanding the possibilities of statistical processing of the results obtained.

1.1. Modern concepts on the de novo generation of biogenic metal nanoparticles

Biological objects in natural habitats are constantly encountered with certain cations. Some of them are necessary for the normal functioning of the enzyme systems of cell metabolism. At the same time, excess concentrations of most cations are toxic. Metabolically active cells have a natural ability to reduction of cations, which allows being transferred to a solid non-toxic state by generation metal nanoparticles [2]. Thus, cation detoxification is one of the main protective reactions for the survival of microbial cells from the very first years of their habitat in the environment on Earth.

It is important to emphasize that the *de novo* generated nanoparticles create a new solid nanocrystalline phase in the reaction mixture. The appearance in cell suspensions (i.e. among amorphous structures in the liquid phase) of a new crystalline phase can be detected with high accuracy by many physical methods. It is this phase transition that we propose to use for the detection of biological objects. Using many biological model objects, we have shown that metabolically active cells are able to very quickly generate *de novo* metal nanoparticles from salt solutions as sources of cations artificially introduced into samples, while in the presence of inactive cells or in sterile samples, the formation of nanoparticles does not occur.

The fundamental natural ability of living cells to protect their metabolic activity from the toxic effects of cations (Me^{n+}) is realized by reducing cations to the zero-valent state (Me^0). The absence of a charge on the reduced atoms triggers the process of their agglutination, which leads to the formation of insoluble, much less toxic nanoclusters (Me^0NCs). Primary clusters with a small number of atoms can partially retain their charge, since they can include atoms of both types (Me^{n+} and Me^0) [3,4]. In this case, if electron donors are constantly present in the reaction mixture, the proportion of cations in nanoclusters proportionally decreases.

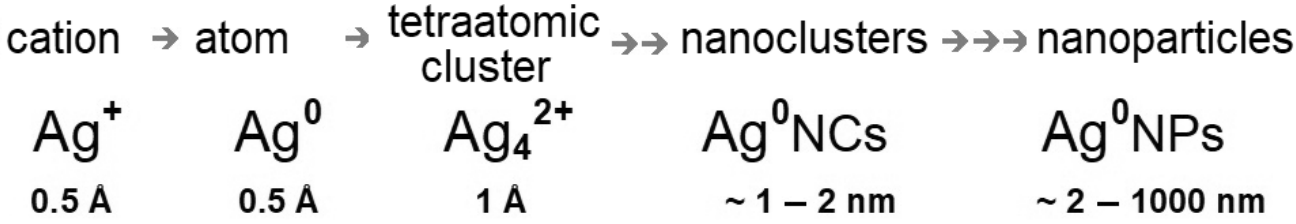

Fig. 1. *Successive stages of cation reduction and de novo formation of nanocrystalline structures.*

Continued agglutination of less and less charged nanoclusters leads to the generation of larger and larger crystalline structures called metal nanoparticles (Me^0NPs) (**Fig. 1**).

When developing the proposed approach, we took into account the observed significant differences in the parameters and properties of nanoparticles generated in cultures of different microorganisms, in cultures of different ages or the physiological state of their cells, differing in the chemical composition of surface cell biopolymers, as well as in cases of different compositions of growth media and reaction conditions [5,6,7]. It should be noted that during the generation of nanoparticles, active cells can secrete various organic compounds – stabilizers that interfere with the process of self-assembly of larger nanocrystalline structures [1,8,9] (see also Fig. 13).

In the last twenty years, metal nanoparticles have attracted increased attention due to their unique optical properties due to the phenomenon of surface plasmon resonance. It should also be noted that preparations of metal nanoparticles have a highly developed surface, high capacitance of the electric double layer, and high catalytic activity [10]. Due to these specific properties of nanosized crystals, the dynamics of their generation can be reliably recorded using many high-precision analytical methods. Along with spectroscopy in the UV and visible range (UV–vis absorption), which is common for biological studies, this can be *X*-ray fluorescence (RFS), as well as electronic (transmission electron microscopy TEM) and scanning electron microscopy (field emission scanning electron microscopy FESEM). To study metal nanoparticles, it is possible to carry out surface enhanced Raman scattering spectroscopy (surface enhanced Raman scattering SERS), registration of the distribution of linear sizes of nanoparticles (particle size distribution PSD), dynamic light scattering (DLS), *X*-ray angular scattering (*X*-ray powder diffraction XRD), thin layer chromatography (TLC) and others [3,11,12]. It should be emphasized that it is the crystal structure of nanoparticles that makes it possible to use most of the above methods for recording the parameters of generated *de novo* biogenic nanoparticles directly against the background of the presence of microorganism cells or other biological objects that ensured the *in situ* reduction (directly in the samples under study) of artificially introduced cations. It has been accurately shown that all optical and other properties of synthesized nanocrystals are completely and strictly determined by their linear dimensions, shape, and atomic composition [13,14]. Since the experimenter has the opportunity to control the physicochemical parameters and conditions when de novobiogenic nanocrystals, it becomes possible to isolate the influence of the biological object present in the reaction mixture, which is the main reducing agent

of cations. Thus, since the use of traditional high-precision analytical methods for studying the parameters of nanocrystals can be effectively used to monitor the generation of biogenic nanoparticles. All of them can be used to solve many important problems in microbiology, biotechnology, and medicine.

The chemical reduction of cations itself implies the participation of various sources/ donors of free electrons in the reaction. Both inorganic substances and molecular groups of organic biogenic compounds with reducing properties (for example, –OH) can serve as electron donors during the generation of metal clusters and nanoparticles [7]. The level of presence of molecular electron donors in the reaction mixture significantly affects the ratio of reduced atoms and unreduced (residual) cations ingenerated *de novo* nanocrystalline structures. With a constantly high presence of reducing agents in the reaction mixture, the proportion of cations and, accordingly, the charge level of the surface of nanocrystals constantly decreases, which contributes to the acceleration of self-assembly of nanoclusters and the rapid enlargement of nanoparticles. It is important to note that it is metabolically active cells that have a natural ability to constantly secrete low molecular weight compounds into the external environment, many of which have reducing properties. It is this property of living metabolically active cells that allows them to act as electron donors for a long time, i.e., serve as stable cation reducers and, accordingly, ensure the generation of metal nanoparticles [15]. Less active biological objects (resting dormant forms of microorganisms, spores, viral particles) can reduce cations only at the expense of various electron donor groups localized on the cell surface or included in surface biopolymers. Virus particles can only act as extremely weak cations reducing agents due to the presence of reducing amino acid groups in the proteins of their capsids [6,16,17].

Another specific natural factor that negatively affects the possibility of enlargement of biogenic metal nanoparticles due to a decrease in the interaction forces of nanoclusters has been well studied. Many organic compounds capable of being adsorbed on the surface of growing nanocrystals have this effect. Based on modern concepts, biogenic molecules react with residual positively charged Me^{n+} atoms of nanoclusters and form a surface layer that prevents further self-assembly and enlargement. Such compounds are called size stabilizers at the early stages of nanoparticles generation [6].

1.2. Main research principles and provisions applied in the development protocol of the DBNG method

At all stages of the biosynthesis of metal nanoparticles *de novo*, the ongoing processes of cation reduction and the formation of a solid crystalline phase in the reaction mixture significantly and quite definitely depend on the reaction conditions and on the combination of the components present. That is why we proposed to use the measured dynamic parameters of nanocrystalline products obtained as a result of the reduction of cations to assess the general physiological state of cells [1,7,15]. In general, the experimentally measured actual parameters of biogenic nanostructures generated *in situ* are an indicator of the properties of those cells that ensure the restoration of introduced cation sources.

First of all, the protocol of the DBNG method involves the introduction of salt

as a source of cations (in the form of low concentrated sterile solution) directly into the aqueous suspension of the biological object under study (i.e., *in situ*). To confirm the fact that the reducing agents are of biogenic origin, the protocol provides for the preparation of a control aliquot of the tested sample, freed from cells using a mechanical method (filtration, centrifugation). The obligatory use of control (sterile, cell-free) variants of the studied samples is necessary, since the cells of biological samples are usually found in growth media, that is, in multicomponent solutions of organic compounds and the necessary growth factors, many of which are electron donors. At the same time, it should be emphasized that the reducing ability of such compounds, even in the composition of full-fledged growth media, cannot ensure the full generation of metal nanoparticles, but only leads to the appearance of their precursors – nanoclusters (**Fig. 2**).

As emphasized above, the physicochemical conditions in the reaction mixture during the in situgeneration of both nanoclusters and larger nanoparticles significantly affect the parameters of the final crystalline self-assembly products [16,17]. An increase in temperature, as well as stirring (vibration) of test tubes with reaction mixtures during the reduction of cations, accelerates the process of self-assembly of nanoclusters, which ultimately leads to an increase in the size of the generated nanoparticles.

It is important to note that the use of different salts as a source of cations can give different results. In particular, it was noted that the use of Tollens' reagent $Ag(NH_3)_2NO_3$ as silver cations source makes it possible to form larger nanoparticles in the presence of microbial cells than when using the $AgNO_3$ salt under identical conditions.

The DBNG protocol involves the introduction of very small amounts of cation sources (~mM) into the test samples, which are sufficient only to form a noticeable amount of nanoparticles with minimal toxic effect on the metabolism of tested cells under study. It is important to note that the use of low concentrations of cation sources retains the possibility of isolating pure cultures of the detected microorganisms from the studied aliquots.

Metabolically active cells are able to generate silver nanoparticles in a few minutes. For standard experiments according to the DBNG protocol, the duration of all reactions for the reduction of introduced cations by microorganism cells was limited to 20 minutes [1]. This time does not exceed the length of normal metabolic responses of cells to the addition of excess concentrations of various salts to the medium [6,18], and also does not

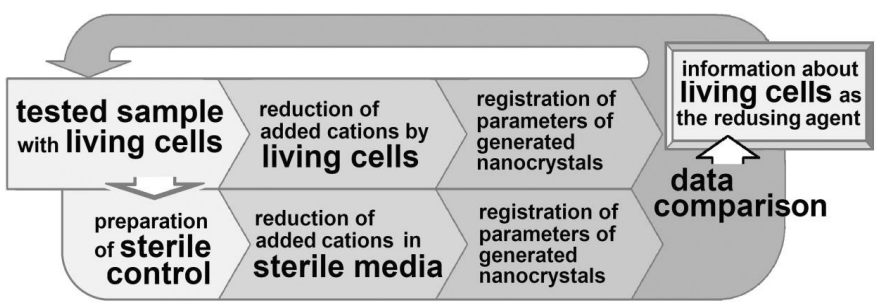

Fig. 2. *The concept of the DBNG methodological approach*.

exceed the generation time of most microorganisms. Thus, a short time of carrying out the reduction reaction makes it possible to fix the physiological state of the studied cultures (samples) precisely at the moment of introducing the source of cations. To detect viral particles (as weak reducing agents), the reaction time with introduced cations was increased to 50 minutes.

Since the generation of metal nanoparticles is carried out *in situ* directly in the studied cell suspensions, it was proposed for the first time to record the spectral characteristics of nanoparticles in the *vis*-range using an Ulbricht integrating sphere [1]. This method of measuring spectral characteristics in a reflected light flux makes it possible to register even nanoparticles that form directly on the surfaces of biological objects, which is impossible with a standard transmitted light flux.

It has been shown that the DBNG protocol (using TEM) makes it possible to register metabolically active cells of microorganisms by their ability to generate biogenic nanoparticles with a sensitivity of ~10 ml^{-1}. The use of other analytical methods for the detection of nanocrystalline structures can increase the sensitivity of the method.

For generation *in situ* of metal nanoparticles by cells or tissue fragments, it was proposed to place the studied biomaterial itself directly into a solution of a cation source. In such cases, standard inactive preparations should be used as controls.

According to the DBNG protocol, the generation of biogenic metal nanoparticles is carried out in microliter volumes of the reaction mixture. This allowed us to develop a concept for applying this innovative method in a microfluidic version (Lab-on-Chip).

2. MATERIALS, METHODS, EQUIPMENT

Pure cultures of microorganisms were stored and prepared for research using standard growth media LB [1] or M9 [20] according to standard microbiological methods. Natural water samples were taken with standard instruments in an aseptic way, transported and stored at a low temperature.

Preparations of tumor tissue cells from neoplasms of the adnexal apparatus of the eye, as well as healthy tissue from the same eye as a control, were surgically removed. Paired tissue samples were placed under aseptic conditions in equal volumes of a sterile solution of a cation source.

The sources of cations were sterile aqueous solutions of ammonia silver $Ag(NH_3)_2NO_3$ obtained according to the protocol of the Tollens reaction [1, 19]. To obtain Na_2PdCl_4, $PdCl_2$ and an excess of NaCl in distilled water were used [20].

The generation of metal nanoparticles was carried out in situ directly in the studied water samples or in bacterial suspensions at the late logarithmic phase of culture growth. The reaction mixture contained aliquots of the studied cell suspensions (about 10^6 mL^{-1}) with a volume of 45 μL and 5 μL of a sterile solution of the cation source in a final salt concentration of 0.1 mM. The cation reduction reaction time was 20 min. Aliquots of the studied suspensions freed from microorganisms after complete sedimentation of cells by centrifugation at 12000 g for 15 min were used as control [1].

Hydrogels were prepared using low EEO agarose (0.4 wt %) and silver nitrate (5 μg/mL) [21].

Microorganisms were visualized using an Amplival microscope (DDR) with a phase contrast device.

Registration of the generation of biogenic nanoparticles *in situ* directly in cell suspensions was performed using an OceanOptics USB-2000 spectrometer (USA) with an Ulbricht integrating sphere.

Measurement of the intensity of small-angle *X*-ray scattering of preparations was carried out on an automatic diffractometer "AMUR-K" with a single-coordinate position-sensitive detector OD3M (in a capillary with a volume of 20 μL) at a fixed radiation wavelength of $\lambda_{0.1542}$ nm with a signal accumulation time of 40 minutes according to a certified method [1]. The scattering measurement results were processed to calculate the volumetric size distribution function of nanoparticles $D_V(R)$ using the MIXTURE program.

Particle size was measured by PCS on a Delsa Nano Submicron Particle Size and Zeta Potential Particle Analyzer (USA).

Images of nanoparticles were obtained using thetransmission electron microscope JEM-1400 (JEOL, Japan) at the UNIQEM Collection Core Facility, Research Center of Biotechnology of the Russian Academy of Science equipped with the microanalyzer (Oxford Instruments, Great Britain) at an accelerating voltage of 80 keV.

The determination of the linear dimensions of metal nanoparticles was carried out using the computer program "Compass 3*D-V*14" and a specially developed calculation algorithm for electronic photographs, at least 300 nanoparticles for each sample.

3. RESULTS

3.1. Basic protocol of the method DBNG

The basic protocol of the method DBNG was tested on a model organism of gram-negative mycobacteria *Mycobacterium smegmatis* cultivated in a rich LB growth medium. It was obvious that a significant amount of various organic growth factors in the composition of the LB medium can serve as electron donors, i.e., they can participate in the reduction reaction of Ag^+ cations introduced into the cell suspension, and thereby initiate the formation of reduced Ag^0 silver nanoparticles. A series of initial experiments to study the dynamics of the formation of biogenic silver nanoparticles was carried out using the method of measuring small-angle *X*-ray scattering (SAXS). The SAXS method is based on the effects of the elastic interaction of *X*-rays with bound electrons in a sample. This method of structural diagnostics provides a resolution in the range from 1 to 10^3 nm, which is most accurately suited for in-depth analysis of the structure and properties of biogenic nanocrystalline materials generated *de novo* in biological solutions. Indeed, according to the results of the determination using SAXS, the introduction of a sterile $Ag(NH_3)_2NO_3$ solution into a sterile LB growth medium resulted in a rapid (in 1–2 minutes) mass formation of silver nanoclusters with sizes up to 2 nm. Over a longer time, larger nanocrystalline structures formed in the reaction mixture (**Fig. 3***A*). Similar measurements in cell suspensions of *M. smegmatis* revealed two types of nanoparticles with contrasting differences in size: small nanoparticles up to 3 nm in diameter and large nanoparticles with a wide size distribution of 20-40 nm (Fig. 3*C*).

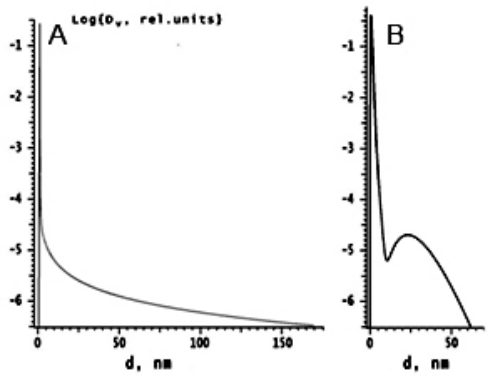

Fig. 3. *Formation of reduced silver nanoclusters in the LB growth medium (A) and biogenic Ag^0NPs nanoparticles in the presence of Mycobacterium smegmatis cells (B).*

Thus, in sterile samples, there is a reduction according to the "chemical" type – with the depletion of reducing agents and slowing down the agglutination of nanoclusters. In a suspension of active cells, a high level of secreted electron donors activates (according to the "green" type) the reduction of cations sorbed on nanoclusters and, accordingly, activates the generation of ever larger nanostructures. In fact, the detection of living cells by the formation of nanocrystals *in situ* is reduced to discrimination of the "chemical" or "green" type of this process.

3.2. Evaluation of the size distribution of biogenic silver and palladium nanoparticles from dynamic light scattering

Light scattering methods are indispensable for determining the hydrodynamic radii of nanocrystals and biopolymer molecules in biological fluids, their molecular weights, as well as the intensity distributions of scattered light over their sizes. We used this method in experiments with an isogenic pair of obligate methylotroph *Methylopilusquaylei* to compare the ability of their cells to generate nanoparticles of two metals differing in the valence of silver Ag^+ and palladium Pd^{2+} cations. It can be noted that comparisons of the properties of the initial wild-type microbial culture and the mutant derived from it are widely used in genetic engineering and biotechnological studies, but have practically not been used to assess the possibilities of synthesizing biogenic metal nanoparticles.

The linear dimensions and distributions of biogenic nanoparticles in these experiments were recorded using a Delsa Nano Analyzer that implements the principles of dynamic light scattering (DLS). The growth characteristics of the original wild type strain *M. quaylei* WT and its streptomycin-resistant derivative *M. quaylei* Sm^R did not differ under standard cultivation conditions on media with methanol as the sole carbon and energy source [20]. It was shown that the cells of the *M. quaylei* Sm^R mutant are resistant to the presence of up to 4 mg/mL of streptomycin, are characterized by reduced secretion of exopolysaccharides, and have a reduced surface hydrophobicity. In the presence of cells of both methylotrophic cultures *M. quaylei* WT and *M. quaylei* Sm^R under standard conditions of the DBNG protocol, large reduced silver nanoparticles of average size 45 nm and 70 nm, respectively, were generated (**Fig. 4**). The survival rate of the streptomycin-resistant mutant *M. quaylei* Sm^R in these reaction mixtures was 8 times lower than that of the initial culture. Under similar conditions, after the introduction of a source of palladium cations, the formation of Pd^0NPs nanoparticles occurred only in the presence of cells of a *M. quaylei* Sm^R culture, which correlated with a much higher degree of resistance of such cells (12 times higher) to palladium salt than in wild-type cells. Since the generation of numerous optically dense nonmetallic particles (not containing palladium nanoparticles) was observed in the reaction mixture in which *M. quaylei* WT cells were present, it can be concluded that

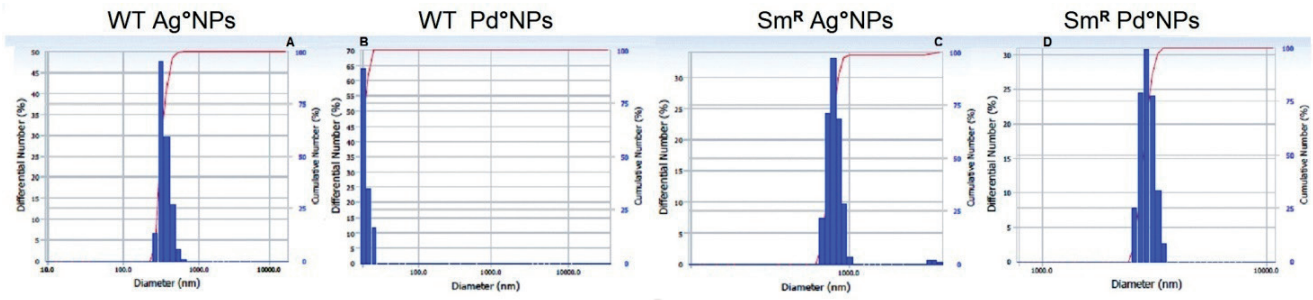

Fig. 4. *Sizes of biogenic silver and palladium nanoparticles formed in the presence of cells of methylotrophic cultures of M. quaylei wild type (WT) and isogenic streptomycin-resistant derivative (Sm^R).*

the reduction of Pd^{2+} cations was inhibited at the stage of nanoclusters present in the form of a high polymer complex with secreted methylotrophic exopolysaccharides. Thus, the preservation of the natural level of exopolysaccharide biosynthesis in the wild-type *M. quaylei* WT culture does not compensate for the high sensitivity of cells to Pd^{2+} cations, which generally does not allow them to generate Pd^0NPs nanoparticles. It is obvious that both cultures are almost equally capable of reducing silver cations and can serve as producers of Ag^0NPs nanoparticles when cultivated on simple synthetic media with methanol.

3.3. Spectrometry of preparations of biogenic silver nanoparticles

Absorption spectrophotometry is one of the most common physical and chemical methods for studying solutions and solids, based on recording absorption spectra in the λ range from 200 to 1000 nm. The recorded dependence of the intensity of absorption of incident light on the wavelength reflects the structure and composition of various compounds, the qualitative and quantitative composition of biological solutions, and shows the presence of trace elements in the objects under study. The atoms of each chemical element have strictly defined resonant frequencies, as a result of which it is at these frequencies that they emit or absorb light. This property is especially important (for us) when analyzing the composition and size of (biogenic) metal nanoparticles. Obtaining absorption spectra is easy to perform, does not require complex preparation of samples for analysis, and is possible in the presence of a small amount of the analyte. Currently, a large number of different models of spectrophotometers are being produced, including very compact ones, which allows them to be used even in the field studies.

3.3.1. Study of microbial cultures of active slut

Many technological processes include, at the final stages, the treatment of water waste with the use of activated sludge for the biosorption of toxic metal ions in the form of nanoparticles. Thus, in the effluents of electroplating, textile, uranium and silver processing industries, Ni^{2+}, Zn^{2+}, Cu^{2+}, and U(VI) cations can be present in significant amounts [22]. The DBNG approach was applied in the selection of microbial cultures capable of efficiently extracting metals from solutions for a long time without loss of vital activity in artificially created activated sludge. Since cations Ag^+ are much more toxic for most microorganisms than cations of other elements, it was silver salts that were used in assessing the levels of resistance of sludge preparations and pure cultures isolated from it to other metals. Several cultures capable

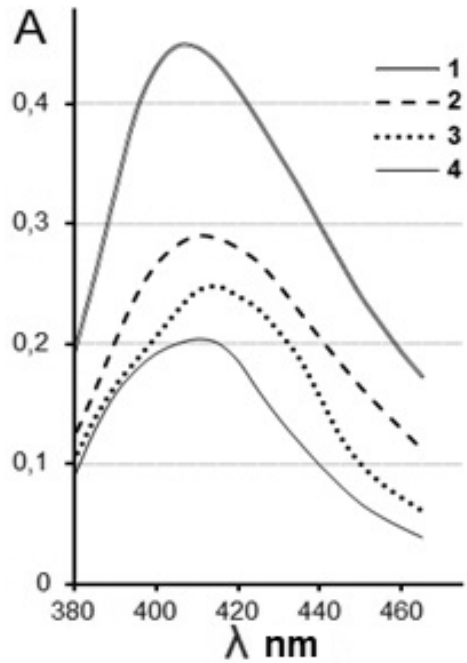

Fig. 5. *Levels of production of biogenic Ag^0NPs by cells of pure cultures of Penicillium glabrum (1), Fusarium nivale (2), Trichosporon cutaneum (3), Agrobacterium tumifaciense (4).*

of rapidly forming Ag^0NPs were selected. The most promising crops for biosorption of toxic cations were identified as *Fusarium nivale* and *Penicilliumglabrum* (**Fig. 5**). Artificial activated sludge, created on their basis, had the form of multilayer granules with a given composition and structure: the cells of cultures less resistant to metals were shielded by a layer of cells, the most resistant to high concentrations of toxic metals. It was shown that at a content of 20 mg/L Ag^+ in the initial sludge, the level of cell survival did not exceed 7%; for the most stable pure cultures of *F.nivale* and *P.glabrum*, the survival rate was about 12-24%. The artificial activated sludge arranged in this way remained viable and developed even in the presence of up to 70 mg/L Ag^+ in the medium. Such sludge was capable of accumulating silver up to 50% of the dry mass of cells, which corresponds to a sorption capacity of up to 380 mg/g and showed the degree of silver extraction up to 95% in just 3-5 minutes (at a concentration of cations Ag^+ ~100 mg/L).

3.3.2. Growth of yeast culture in the top layer of hydrogel

In recent years, 3*D* bioprinting technologies have been increasingly used in practice for the formation of artificial biomaterials for restoration of damaged human organs. Usually, living cell structures are included in a shaping gel, which ensures their optimal physiological state for normal cell growth. In our experiments, the model eukaryotic microorganism *Yarrowia lipolytica* Y-3603 was grown for up to 7–8 days in cuvettes filled with two-layer hydrogels with an agarose concentration of 0.4 wt% in a complete LB medium [21]. The bottom sterile layer of the gel contained 5 μg/mL of silver nitrate as a source of cations Ag^+ (**Fig. 6**). It is important to emphasize that for the implementation of the DBNG approach, we used low electroendoosmotic agarose (EEO type), since it was shown that only this type of agarose is not able to reduce introduced cations without the participation of cells (Fig. 6*B*).

The growth of the *Y. lipolytica* culture in the upper layer of the hydrogel was controlled by increasing the optical density of the samples using a fiber optic spectrometric system. Similarly, the dynamics of the generation of biogenic Ag^0NPs (by reducing the optical

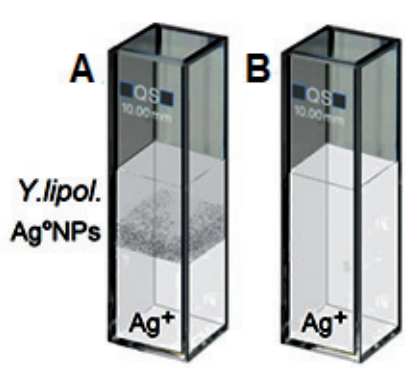

Fig. 6. *Formation of silver nanoparticles in the presence of Y. lipolytica yeast culture growing in the EEO agarose hydrogel.*

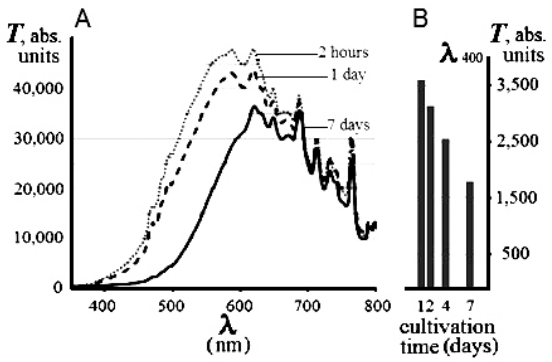

Fig. 7. *Growth dynamics of Y. lipolytica yeast and in situ formation of biogenic Ag^0NPs in EEO agarose hydrogel layer.*

permeability of the hydrogel) was recorded at a specific wavelength of silver nanoparticles λ_{400} nm. As can be seen from the presented data (**Fig. 7**), the transparency of the samples containing yeast steadily decreased over several days as the culture grew in the thickness of the hydrogel (Fig. 7*A*).

Since the decrease in transparency measured at λ_{400} was also observed throughout this time, it can be concluded that the level of reductive activity of the *Y. lipolytica* culture remains at a sufficiently high level for long-term generation of nanoparticles *in situ* (Fig. 7*B*). In general, the application of the DBNG approach in these experiments showed that the methodology for assessing the possibility of generating biogenic nanoparticles *in situ* allows one to control the physiological state of living *Y. lipolytica* yeast cells during submerged cultivation in an agarose hydrogel medium [21].

3.3.3. Comparison of malignant and benign tumors

Malignant neoplasms are among the most common tumors of all types of tissues. The clinical course of malignant tumors is characterized by high polymorphism, due to which their differential diagnosis can present significant difficulties. Preoperative diagnostics in order to determine the volume of surgical intervention makes it possible to determine the structure and localization of the pathological process, the exact size of neoplasms, and the relationship with surrounding tissues. But the issue of urgent intraoperative morphological diagnosis of benign and malignant tumors is still relevant. As is known, the defining feature of the tumor process is abnormal uncontrolled proliferation, to maintain which tumor cells undergo oncogene-oriented metabolic reprogramming [23,24]. A dramatic increase in the metabolic activity of cancer cells leads to a noticeable increase in their ability to generate biogenic nanoparticles during the interaction of cell metabolites with added salts [25,26]. We used the innovative DBNG approach to study adnexal tumors identified clinically in patients. Healthy tissue from the same eye was used as controls for each patient (**Fig. 8**).

Photometric determination at wavelengths close to those specific for silver nanoparticles (λ_{400}) showed that for all studied pairs of

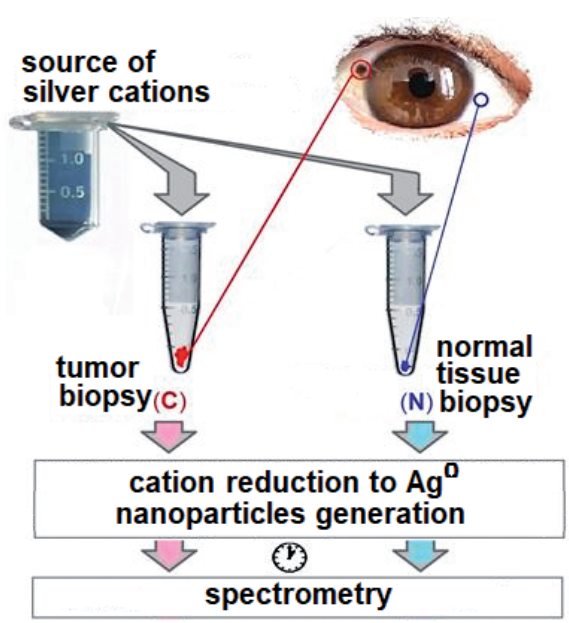

Fig. 8. *Scheme of sample preparation for studying the restorative activity of eye conjunctival cells.*

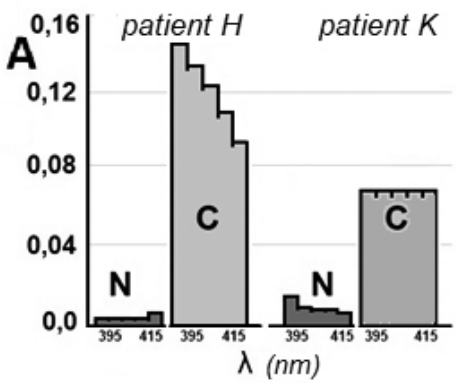

Fig. 9. *Comparison of the vis spectra of silver nanoparticles formed from tumor (C) and healthy (N) conjunctival tissues.*

samples (Cancer *vis* Normal tissue), the optical density of reaction mixtures (that is, the volume of silver nanoparticles formed in 3-5 minutes) in all samples with in malignant and benign types of tumors of the adnexal apparatus of the eye is higher than in control samples of similar healthy tissues (**Fig. 9**).

Thus, the proposed methodological approach of DBNG makes it possible to quickly solve the problem of determining the degree of malignancy of tumors based on the spectrometric rapid assessment of their metabolic activity in order to optimize the tactics of surgical intervention.

3.3.4. Registration of nanoparticles using the Ulbricht integration sphere

The observation of generation *in situ* biogenic silver nanoparticles by their specific absorption spectrum at a wavelength of about λ_{400} nm can be hindered by the high density of the studied cell suspension. Performing spectrometric measurements using an Ulbricht integrating sphere as a detector eliminates this problem (**Fig. 10**). In addition, monitoring the dynamics of the generation of nanoparticles from the very beginning of the cation reduction reaction makes it possible not to carry out measurements in control (freed from cells) sample aliquots. Indeed, a fresh culture of

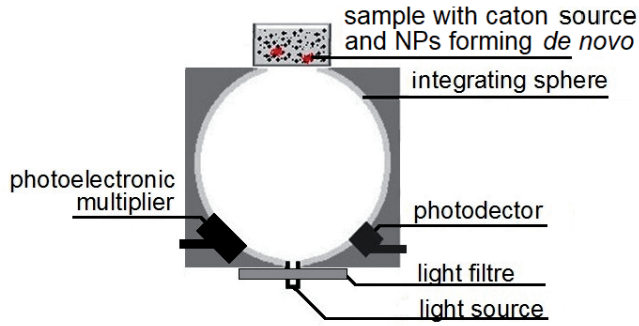

Fig. 10. *Scheme of an integrating sphere for registration of biogenic metal nanoparticles.*

M. smegmatis grown in complete LB growth medium does not show the characteristic Ag^0NPs peak (**Fig. 11**).

After adding of silver cations source (4 μg/mL $Ag(NH_3)_2NO_3$), a series of measurements of the spectra of the suspension of the reaction mixture was carried out. On Fig. 11 shows that as early as 10 minutes after the addition of cations Ag^+, a specific peak for Ag^0NPs at λ_{400} nm can be recorded, followed by a gradual increase in its amplitude. Such a bathochromic shift of the peak maximum indicates a constant increase in the size of silver nanoparticles generated *in situ* in the studied reaction mixture.

When carrying out similar experiments with higher concentrations of Tollen's reagent, as well as when using $AgNO_3$ salt as a source of cations, there was a delay in

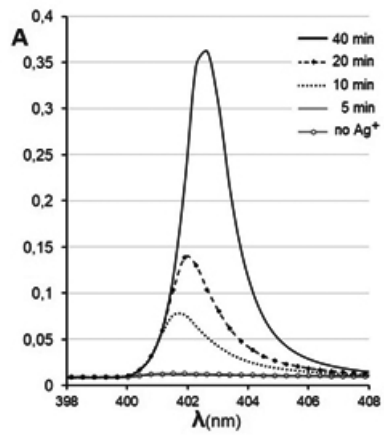

Fig. 11. *Dynamics of formation of Ag^0NPs nanoparticles in the presence of M. smegmatis cells.*

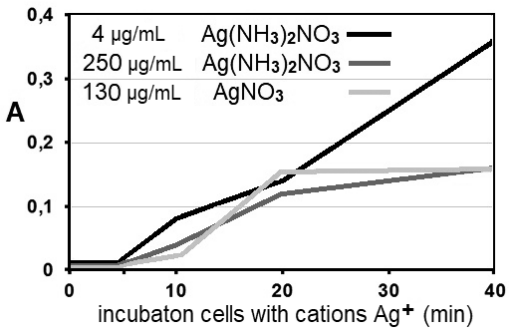

Fig. 12. *Dependence of the dynamics of in situ formation of biogenic nanoparticles in the presence of M. smegmatis cells on the source of silver cations.*

the appearance of the peak at an early stage of nanoparticle formation and a cessation of their enlargement already by the 20th minute of the reaction (**Fig. 12**). Such a change in the dynamics of the generation of biogenic nanoparticles indicates a significant suppression of the reductive activity of mycobacteria cells. Such effects should be taken into account when developing special protocols for applying the method DBNG to various biological objects.

3.3.5. Fluorescence spectrometry of biogenic metal nanoparticles

As noted above, for the detection of metal nanoparticles, their specific optical properties due to the phenomenon of surface plasmon resonance, highly developed surface, high capacitance of the electrical double layer, and the ability of nanoparticles to amplify the signal in Ramanscattering, light and fluorescence spectrometry are widely used. One of the unique features of nanoclusters of many metals ranging in size from 2-5 nm is their pronounced fluorescent properties under certain parameters of exciting illumination. If the sizes of nanoclusters of reduced metal atoms are commensurate with the Fermi wavelength for electrons, the supramolecular properties of nanocrystals manifest themselves due to discrete electronic states caused by strong quantum confinement of free electrons. The fluorescent properties are retained during the self-assembly of nanoclusters during generation *de novo* of nanoparticles. As the size of metal nanocrystalline structures increases (during the self-assembly of nanoclusters), the ratio of surface and deep atoms changes, which leads to a shift in fluorescence radiation and even its complete quenching when nanocrystalline structures reach a certain size [27,28].

We propose to use this natural feature of the fluorescence of metal nanoclusters/nanoparticles, i.e., the dependence on the size of nanocrystalline structures, in the method for determining the metabolic activity of cells (when assessing the reductive cellular activity necessary for *de novo* formation of nanoparticles from cation solutions). In this case, the generation of biogenic nanoparticles occurs precisely *de novo*, that is, it goes through the stages from the "primary" (equimolar) reduction of cations to zero-valent atoms, then clustering with the gradual formation of di- and tetraatomic nanoclusters (Fig. 1), then self-assembly and gradual enlargement of nanocrystalline structures (**Fig. 13**). This means that at the moment when a certain amount of nanoclusters capable of exhibiting their fluorescence is formed in the reaction mixture,

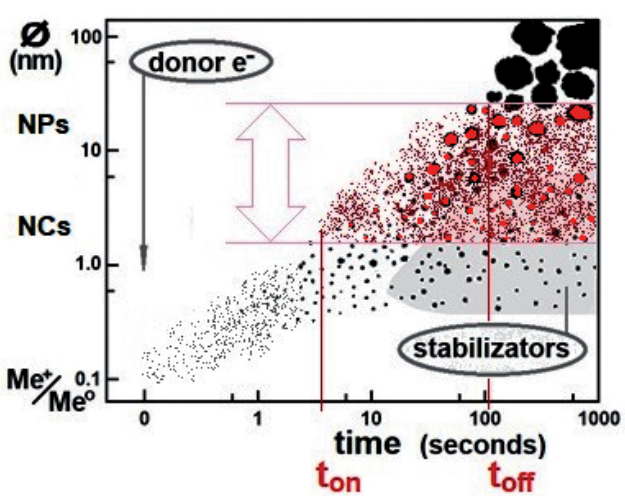

Fig. 13. *Schematic diagram of the dependence of the fluorescence of metal nanoparticles on their size.*

it can be detected by standard methods. The fluorescence of the nanocrystalline structures will continue to persist, all the time in the process of self-assembly of nanoclusters and enlargement of nanoparticles, until all (most) of the formed nanoparticles exceed the fluorescence quenching size.

Thus, by periodically measuring the presence (or intensity) of fluorescence in a sample, it is possible to determine two points that characterize the reducing activity of cells present in the sample under study: *i.* is the time required for the formation (measured) amount of fluorescent nanoclusters of reduced metal atoms (Fig. 13, t_{one}); *ii.* is the time required for all formed nanoparticles to exceed the size corresponding to fluorescence quenching (Fig. 13, t_{off}).

Crystal structures, including atoms of various elements, also differ in their fluorescent properties and in the parameters of exciting illumination. It is known that the fluorescent properties of nanoclusters can be enhanced by including reduced atoms of different metals in them [29]. We propose to use this natural feature of the fluorescence of nanocrystalline structures in the framework of the method DBNG to determine the integral metabolic activity of cells. To enhance the fluorescence of biogenic nanoclusters generated *de novo*, use a sterile solution as a source of cations for introduction into the reaction mixture, for example, containing a silver salt with the addition of, for example, lanthanide salts.

3.4. Use of transmission electron microscopy in the analysis of reaction mixtures in which metal nanoparticles are generated de novo

The use of transmission electron microscopy in the analysis of reaction mixtures in which metal nanoparticles are generated *de novo* makes it possible not only to observe optically dense crystalline structures of various shapes and sizes, but also to record the distribution of such nanocrystals in the samples under study. It is the results obtained using TEM that can be considered exhaustive for the characterization of cells of taxonomically different bacterial species, spores of bacilli, preparations of bacterial components of activated sludge granules, preparations of viral particles. It is TEM photographs that show that the generation of nanocrystals in the presence of cells of different cultures differs significantly, while the degree of association of the generated nanocrystals with biological objects present in the samples reflects the integral properties of the cell surface and their physiological state. It is important to emphasize that TEM studies of preparations prepared according to the protocol of the DBNG method provide high sensitivity to the presence of biological objects in the studied samples. When adding Tollens' reagent solution to a series of samples of *Bacillus* cell suspension, successively diluted with a sterile LB growth medium, it was found that even with a strong dilution of the cell suspension (up to $3\text{-}10^2 \cdot 10$ cells/mL) using TEM, one can easily detect the generated silver nanoparticles (in their complete absence in the control sterile samples of a complete growth medium).

3.4.1. Comparison of biogenic silver nanoparticles generated by metabolically active and dormant bacterial cells

The use of TEM made it possible to compare the features of the generation of metal nanoparticles in the presence of metabolically active and resting microorganism cells. For example, for mycobacteria *M. smegmatis*, the peculiarity

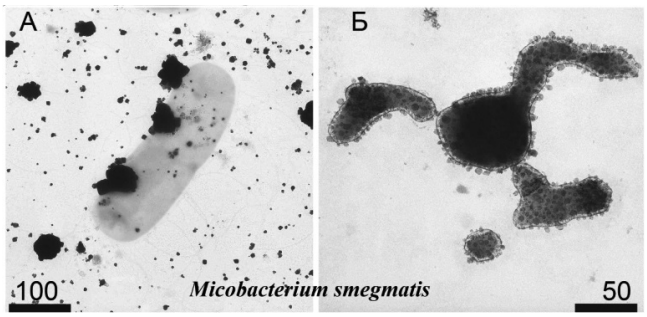

Fig. 14. *Biogenic silver nanoparticles formed by metabolically active (A) and resting (B) M. smegmatis cells.*

of cells, when cultivated in a long stationary phase, goes into an inactive, dormant state [30]. It was shown that growing cultures of *M. smegmatis* generate silver nanoparticles with a clearly uniform distribution in the sample volume (**Fig. 14***A*), while preparations of resting cells of these mycobacteria generated silver nanoparticles associated with cell wall surfaces and no larger than 10 nm in size (Fig. 14*B*). Such localization of the obtained nanoparticles indicates that the main contribution to their formation is made by the reductive chemical groups of surface biopolymers. The almost complete absence of nanoparticles in the intercellular space is in good agreement with the suppression of the secretion of low molecular weight reducing agents, which is typical for the transition of metabolically active *M. smegmatis* cells to a dormant state.

3.4.2. Generation of silver nanoparticles by psychroactive bacteria Cryobacterium arcticum under suppression of cell division

The study of the ability to generate silver nanoparticles when modeling the "turn off" of biosystems responsible for the synthesis of nucleic acids and cell division was carried out using a structural fluorine-containing analogue of uracil 5-fluorouracil (5-FUra). Cell suspensions of a pure culture of psychoactive bacteria *Cryobacterium arcticum* were incubated for 24 hours at their optimal temperature (+8°C) in a liquid medium with 5-FUra. To assess the reducing activity, suspensions fully grown in the presence of 0.32 and 1.0 μg/mL 5-FUra were used (a higher concentration of 3.2 μg/mL significantly suppressed bacterial viability). The use of TEM made it possible to establish that with a clear inhibition of cell division (the number of separate, unpaired cells did not exceed 10%), almost all silver nanoparticles were clearly associated with cells (**Fig. 15***A*), similar to silver nanoparticles generated by resting mycobacteria cells (see Fig. 14). It is important to note that the biogenic Ag^0NPs in these preparations had an anisotropic needle shape (Fig. 15*B*). The generation of such nanoparticles may indicate a special physiological state of *C. arcticum* bacteria, which had a normal metabolism prior to the introduction of the 5-FUra analogue, but are under stress due to intracellular DNA/protein imbalance. In preparations with an even lower content of 5-FUra (0.32 μg/mL), a significant proportion of cells of the standard uninhibited appearance (Fig. 15*C*), similar to cells not treated with the analogue, were retained (Fig. 15*D*).

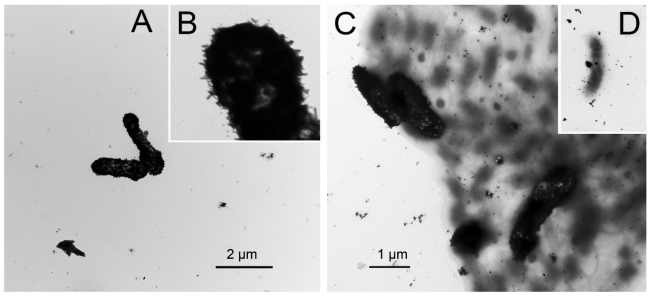

Fig. 15. *Formation of silver nanoparticles by Cryobacterium arcticum bacteria incubated with the addition of 1.0 μg/mL 5-FUra (A), anisotropic (needle) form of Ag^0NPs nanoparticles (B), Cryobacterium arcticum bacteria incubated with the addition of 0.32 μg/mL 5-FUra (C), the formation of silver nanoparticles by metabolically active cells (D).*

Generally, it can be concluded that the ability of the cells of psychoactive bacteria *C. arcticum* to generate certain forms of silver nanoparticles may reflect a change in the composition of biogenic reducing agents (forcations Ag^+) secreted into the growth medium. In addition, the heterogeneity of the cell population becomes apparent, which is detected by pronounced differences in the linear dimensions and zones of localization of generated silver nanoparticles.

3.4.3. Nanocells are able to reduce cations and generate nanoparticles

The use of TE microscopy made it possible for the first time to demonstrate the ability of nanocells of filtering bacteria to act as silver cation reducers. The interest in these living biological objects with dimensions of 0.2–0.5 μm and a volume of about 0.004–0.04 $μm^3$ is associated with their ability to pass through sterilizing filters with a pore size of 0.22 μm [32,33]. Nanocells are perceived as microbial&biochemical water pollutants, as sources of DNA, proteins, components of cell membranes and, therefore, are undesirable, for example, in drinks consumed by humans.

We have shown that the presence of metabolically active nanocells in water samples can be detected by their ability to generate silver nanoparticles with an average size of about 8 nm (**Fig. 16**). When the cell membrane is destroyed, the nanocells quickly lose their reductive ability, the lysis products become stabilizers of silver nanoclusters, which leads to a slowdown in their self-assembly during the formation of Ag^0NPsparticles.

3.4.4. Viral particles enlarged with metal nanocrystals

The ability of viral capsid proteins to ensure the generation of metal nanoparticles makes

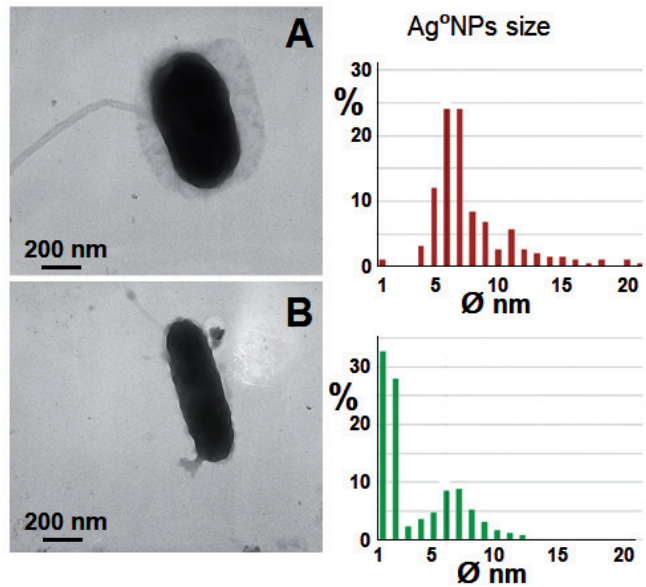

Fig. 16. *Biogenic silver nanoparticles formed by metabolically active and damaged nanocells.*

it possible to use the DBNG approach to detect viruses and bacteriophages when they are in the extracellular space (even in the complete absence of metabolic reactions controlled by them). The generation of biogenic metal nanoparticles in the presence of viral particles occurs due to reducing amino acid groups exposed on the surface of capsids (**Fig. 17**). Due to this localization of electron donors and reduction products (nanocrystals), the word combination "encrusted viral particles" has become fixed in the literature. It should be noted that the differences in amino acid groups of capsids of different virus strains are reflected in the

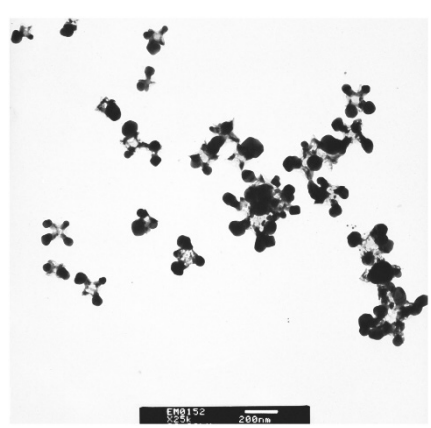

Fig. 17. *Silver nanoparticles encrusted with G7C coliphage particles.*

form of differences in the generated metal nanocrystals [17]. The application of the DBNG protocol showed the acceptability of this innovative method to detect (using TEM) in water samples viral particles of coliphage G7C [33] at a concentration of 10^2 ml^{-1}.

3.5. Analysis of the elemental composition of biogenic nanocrystals

All modern transmission electron microscopes are equipped with microanalyzers that allow elemental analysis of samples. This possibility is very important and useful in the study of biogenic metal nanoparticles. Since growth media for cultivating microorganisms always contain certain salts that can enter into substitution reactions with cation sources added (according to the protocol of the method DBNG), it is necessary to constantly monitor the elemental composition of biogenic nanocrystals. Confirmation of the fact that in our experiments optically dense nanoparticles generated de novo from introduced silver cations observed in the TEM field of view was obtained by *X*-ray microanalysis. The presence in the studied nanoparticles (regardless of their size) of reduced silver atoms, as well as other metals, was judged by the presence of the corresponding specific peaks in the spectra.

3.5.1. Study of natural metal nanoparticles of Lake Onega

Lake Onega is located at the junction of two large geological structures – the Baltic Shield in the northern part of the lake and the Russian Platform in the southern. Many areas of the lake are characterized by thick ferromanganese ore formations with accumulation of Cu, Fe, Zn, Mo, As, Ni, Cd, and Pb due to subaqueous discharge groundwater [34]. According to the available data, in such zones, extremely low rates of silt accumulation, and the microbial communities of the surface layer of bottom sediments are characterized by low taxonomic diversity. We assumed that the formation of ore deposits begins with the reduction of cations supplied with subaqueous discharge, that it should be accompanied by the generation of biogenic metal nanoparticles formed in the presence of cells of a community of autochthonous resistant microorganisms. Accordingly, it was of interest to show the participation of cells of autochthonous microorganisms from the bottom horizon of Lake Onega in the formation of such metal nanoparticles. In all samples of lake water from various parts of Lake Onega and Unitskaya Bay, the presence of natural polymetallic nanoparticles, similar in elemental composition to cations, which are most represented in the corresponding samples of lake water, was recorded. The concentration of autochthonous microbiota cells in different samples varied from 10^2 to 10^8 mL^{-1}.

Enrichment cultures of aboriginal microbiota were prepared from aseptically taken water samples from the bottom layer in a liquid medium depleted in organic matter (5% LB), which were then used to obtain biogenic nanoparticles (**Fig. 18**). Under standard conditions for the DBNG protocol, when using natural water samples as a source of cations, the formation of biogenic iron nanoparticles was recorded

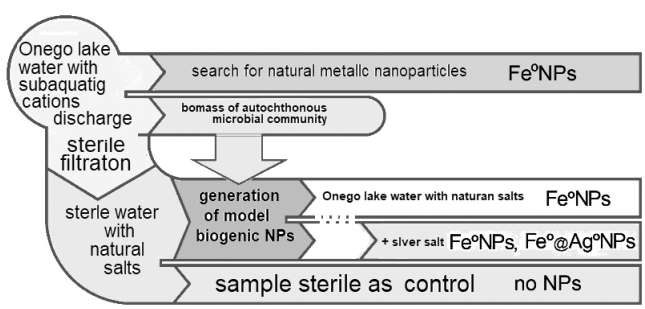

Fig. 18. *Scheme of the experiment showing the participation of the autochthonous microbial community of the bottom layer of Lake Onega in the formation of ore iron-bearing deposits.*

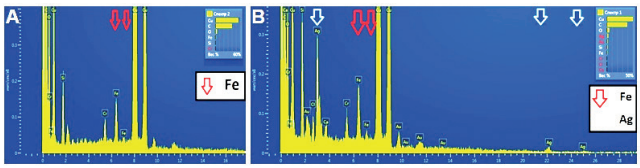

Fig. 19. *Spectra showing the elemental composition of natural (A) and model (B) nanoparticles formed in the presence of autochthonous microorganisms of Lake Onega*

(in the control sterile variants, without the addition of suspensions of microorganisms, nanoparticles were not formed). Elemental analysis of the obtained biogenic nanoparticles showed that they consist of reduced iron atoms.

In those variants of the experiment, where Tollens' reagent was added to the cell suspension of enrichment cultures of native microbiota together with lake water, silver nanoparticles were found, as well as nanoparticles containing both iron and silver atoms (**Fig. 19**). Simultaneous inclusion of zero-valent iron and silver atoms into biogenic nanoparticles unambiguously indicates the ability of cells of autochthonous microorganisms to actively reduce various cations, both those naturally present in the bottom waters of the Onega Basin and artificially added cations Ag^+ as a model element.

3.6. Acoustic methods for registration of nano- and microsized biological objects

Currently, to detect the presence of viral particles and microorganism cells in liquid solutions (and hydrogels), rather complex innovative solutions are increasingly being used, such as molecular ligands, functionalized magnetic structures, microfluidic devices with nanostructured surfaces to retain bacteria, volumetric acoustics, and advection [35]. One of the most common acoustoelectronic methods for studying various materials and structures is the use of acoustic delay lines (ADL). Acoustic sensors are able to detect various chemical and biological types of objects by measuring the corresponding changes in density, viscosity, conductivity, dielectric constant and temperature of liquids, while the sensors do not require large sample volumes. Optimization of acoustic modes for electrical and viscous measurements in liquid and hydrogel media made it possible for the first time to develop an acoustoelectronic technique and prototypes of acoustoelectronic sensors that do not contain sensitive coatings for detecting the presence of viral particles and microorganism cells in various liquids [36]. When the properties of the medium changed, for example, due to the presence of biological objects or their derivatives, the wave changed its speed, phase and amplitude. Changes in the acoustic characteristics were recorded at the output of the device as phase and amplitude "responses" of the acoustoelectronic sensor.

It was shown that the proposed technique and sensors are applicable to the detection in liquid growth media of such biological objects as viral particles, bacterial cells, as well as yeast cells and nanoparticles immobilized in hydrogels. It was found that the response threshold of the sensors used is 0.04% for a sterile diluted 10% LB growth medium, 0.07% for an aqueous suspension of bacterial cells, and 0.6% for a cell suspension in a 10% LB medium.

4. DISCUSSION

Assessment of the physiological state of certain biological objects is a constantly encountered problem in industrial microbial biotechnology, ecology, and medicine. However, the well-studied ability of living metabolically active cells to generate metal nanoparticles (when interacting with salt solutions by reducing cations) is not used to

solve these issues in practice. We propose to use this fundamental natural ability to study various aspects of the functioning of cells as such. In this work, we have shown that the dynamics of generation *de novo* of biogenic nanoparticles makes it possible to compare the integral properties (levels of metabolic activity) of pure cultures of microorganisms, their natural communities, and preparations of human cells.

We postulate a fundamental feature of the interaction of clusters of reduced atoms generated *de novo* in the presence of living cells: only in the presence of metabolically active cells, due to their reducing ability, can the relative fraction of residual cations in nanoclusters of metal atoms be reduced. Only in the presence of such cells, the process of enlargement of nanoclusters by agglutination and successive self-assembly leads to a fairly rapid generation of ever larger nanosized metal particles. Instrumental determination of the presence of biogenic nanoparticles generated *in situ* in reaction mixtures can provide a fairly accurate assessment of the level of metabolic activity and other properties of cells acting as cation reducers. The developed DBNG approach eliminates the need to use ready-made preparations of nanoparticles in research, reduces the duration and overall laboriousness of experiments.

5. CONCLUSION

The paper analyzes the possibilities of measurements that are most suitable for instrumental registration of the parameters of biogenic metallic nanocrystalline structures generated *in situ* according to the protocol of the innovative method DBNG. Examples of the application of the high-precision SAXS method and DLS nanosizer, several options for using spectrometry and transmission electron microscopy to assess the level of metabolic activity of cells by their ability to reduce cations and generate nanoparticles of silver and other metals are given. Generally, it has been shown that the application of traditional analytical methods for studying the parameters of generated biogenic nanoparticles can be effectively used to solve some of the most important problems of microbiology, biotechnology, and medicine.

REFERENCES

1. Sorokin VV, Skladnev DA, Volkov VV, Tereshchenko EY, Mulyukin AL, Gal'chenko VF. The pathways of silver nanoparticles formation by Mycobacterium smegmatis. *Dokl. Biol. Sci.*, 2013, 452:325-328.
2. Gadd G. Metals, minerals and microbes: geomicrobiology and bioremediation. *Microbiology*, 2010, 156:609-643.
3. Hilger A, Guppers N, Tenfelde H, Kreibig U. Surface and interface effects in the optical properties of silver nanoparticles. *Eur.Phys.J.*, 2000, 10:115-128.
4. Hussain S, Bashir O, Khan Z, Al-Thabaiti SA. Steroidal saponin based extracellular biosynthesis of AgNPs. *Journal of Molecular Liquids,* 2014, 199:489-494.
5. Kharissova OV, Dias HVR, Kharisov BI, Pérez BO, Pérez VMJ. The greener synthesis of nanoparticles. *Trends in Biotech.,* 2013, 31(4):240-248.
6. Zhou Y, Wang H, Lin W, Lin L, Gao Y, Yang F, Du M, Fang W, Huang J, Sun D, Li Q. Quantitative nucleation and growth kinetics of gold nanoparticles via model-assisted dynamic spectroscopic approach. *J. of Colloid and Interface Sci.*, 2013, 407:8-16.
7. Tan S, Chee S, Lin G, Mirsaidov U. Direct observation of interactions between nanoparticles and nanoparticle self-assembly in solution. *Acc. Chem. Res.*, 2017, 50(6):1303-1312.

8. Patil MP, Kim GD. Eco-friendly approach for nanoparticles synthesis and mechanism behind antibacterial activity of silver and anticancer activity of gold nanoparticles. *Appl. Microbiol. Biotechnol.*, 2017, 101:79-92, doi: 10.1007/s00253-016-8012-8.
9. Siddiqi K, Husen A, Rao R. A review on biosynthesis of silver nanoparticles and their biocidal properties. *J. Nanobiotechnol.*, 2018, 16:14-30.
10. Xie Y, Dong H, Zeng G, Tang L, Jiang Z, Zhang C, Deng J, Zhang L, & Zhang Y. The interactions between nanoscale zero-valent iron and microbes in the subsurface environment. *J. Hazard. Mater.*, 2017, 321:390-407.
11. Luo B, Smith JW, Ou Z, Chen Q. Quantifying the self-assembly behavior of anisotropic nanoparticles using liquid-phase transmission electron microscopy. *Acc. Chem. Res.*, 2017, 50(5):1125-1133, doi: 10.1021/acs.accounts.7b00048.
12. Wang J, Lin X, Shu T, Su L, Liang F, Zhang X. Self-assembly of metal nanoclusters for aggregation-induced emission. *Int. J. Mol. Sci.*, 2019, 20:1891-1904.
13. Siddiqi KS, Husen A, Rao RAK. A review on biosynthesis of silver nanoparticles and their biocidal properties. *J. Nanobiotechnol,* 2018, 16:14, doi: 10.1186/s12951-018-0334-5.
14. Alkilany AM, Thompson LB, Boulos SP, Sisco PN, Murphy CJ. Gold nanorods: their potential for photothermal therapeutics and drug delivery, tempered by the complexity of their biological interactions. *Adv. Drug Delivery Rev.*, 2012, 64:190-199.
15. Skladnev DA, Vasilyeva LV, Berestovskaya YuYu, Kotsyurbenko OR, Kalenov SV, Sorokin VV. Detection of microorganisms in low-temperature water environments by in situ generation of biogenic nanoparticles. *Front. Astron. Space Sci.,* 2020, 7:59, doi: 10.3389/fspas.2020.00059.
16. Priscyla D. Mechanistic aspects in the biogenic synthesis of extracellular metal nanoparticles by peptides, bacteria, fungi, and plants. *Appl. Microbiol. Biotechnol.*, 2011, 90:1609-1624.
17. Shukla S, Steinmetz NF. Virus-based nanomaterials as positron emission tomography and magnetic resonance contrast agents: from technology development to translational medicine. *Wiley Interdiscip Rev. Nanomed. Nanobiotechnol.*, 2015, 7(5):708-21, doi: 10.1002/wnan.1335.
18. Robinson CK, Webb K, Kaur A, Jaruga P, Dizdaroglu M, Baliga NS, Place A, Di Ruggiero J. A major role for nonenzymatic antioxidant processes in the radioresistance of Halobacterium salinarum. *J. Bacteriol.*, 2011, 193(7):1653-1662.
19. Anh-Tuan L, Huy P, Tam P. Green synthesis of finely-dispersed highly bactericidal silver nanoparticles via modified Tollens technique. *Cur. Appl. Physics,* 2010, 10:910-916.
20. Sorokin V, Pshenichnikova A, Kalenov S, Suyasov N, Skladnev DA. Comparison of the wild-type obligate methylotrophic bacterium Methylophilus quaylei and its isogenic streptomycin-resistant mutant via metal nanoparticle generation. *Trace Element Research,* 2020, 193:564-573, doi: 10.1007/s12011-019-01740-4.
21. Vyazmin A, Pokusaev B, Karlov S, Skladnev D, Shumova N, Volkova E. Features of biogenic nanoparticle formation in agarose gels and their effect on cell growth during bulk cultivation. *Chem. Engin. Transactions*, 2021, 84:73-78, doi: 10.3303/CET2184013.
22. Tyupa DV, Kalenov SV, Baurina MM, Yakubovich LM, Morozov AN, Zakalyukin RM, Sorokin VV, Skladnev DA. Efficient continuous biosynthesis of silver nanoparticles by activated sludge micromycetes with enhanced tolerance to metal ion toxicity. *Enzyme and Microbial Technology,* 2016, doi: 10.1016/j.enzmictec.2016.10.008.
23. Rinaldi G, Rossi M, Fendt S-M. Metabolic interactions in cancer: cellular metabolism at the interface between the microenvironment, the cancer cell phenotype and the epigenetic

landscape. *WIREs Syst. Biol. Med.*, 2017, e1397, doi: 10.1002/wsbm.1397.

24. Heiden MGV, DeBerardinis RJ. Understanding the intersections between metabolism and cancer biology. *Cell,* 2017, 168(4):657-669, doi: 10.1016/j.cell.2016.12.039.
25. Hassoun M, Schie IW, Tolstik T, Stanca SE, Krafft C, Popp J. Surface-enhanced Raman spectroscopy of cell lysates mixed with silver nanoparticles for tumor classification. *Beilstein J. Nanotechnol.,* 2017, 8:1183-1190, doi: 10.3762/bjnano.8.120.
26. Sánchez GJ, Maury P, Stefancikova L, Campion O, Laurent G, Chateau A, Bouraleh FH, Boschetti F, Denat F, Pinel S, Devy J, Porcel E, Lacombe S, Bazzi R, Roux S. Fluorescent radiosensitizing gold nanoparticles. *Int. J. Mol. Sci.*, 2019, 20:4618, doi: 10.3390/ijms20184618.
27. Zijlstra P, Orrit M. Single metal nanoparticles: optical detection, spectroscopy and applications. *Rep. Prog. Phys.*, 2011, 74, 106401 (55 pp), doi: 10.1088/0034-4885/74/10/106401.
28. Deng H, Yu H. Silver nanoparticle surface enabled self-assembly of organic dye molecules. *Materials,* 2019, 12:2592, doi: 10.3390/ma12162592.
29. Liaw J-W, Wu H-Y, Huang C-C, Kuo M-K. Metal-enhanced fluorescence of silver island associated with silver nanoparticle. *Nanoscale Res. Let.*, 2016, 11:26, doi: 10.1186/s11671-016-1247-6.
30. Kuznetsov BA, Davydova ME, Shleeva MO, Shleev SV, Kaprelyants AS, Yaropolov AI. Electrochemical investigation of the dynamics of Mycobacterium smegmatis cells' transformation to dormant, nonculturable form. *Bioelectrochemistry,* 2004, 64(2):125-131.
31. Wang Y, Hammes F, Düggelin M, Egli T. Influence of size, shape, and flexibility on bacterial passage through micropore membrane filters. *Environ. Sci. Technol.*, 2008, 42(17):6749-6754, doi: 10.1021/es800720n.
32. Belova SE, Fedotova AV, Dedysh SN. Prokaryotic ultramicroforms in a Sphagnum peat bog of upper Volga catchment. *Microbiology,* 2012, 81:614-620, doi: 10.1134/S0026261712050050.
33. Kulikov EE, Kropinski AM, Golomidova A, Lingohr E, Govorun VM, Serebryakova M, Prokhorov N, Letarova M, Manykin A, Strotskaya A, Letarov A. Isolation and characterization of a novel indigenous intestinal N4-related coliphage vB_EcoP_G7C. *Virology*, 2012, 426:93-99.
34. Slukovskii Z, Sidorova A, Kalinkina N. Estimation of heavy metal concentrations in organisms of the Baikalian amphipod G melinoides fasciatus Stebbing (Crustacea: Amphipoda) in Petrozavodsk Bay, Lake Onego. *J. of Elementology,* 2019, 24(1):267-279, doi: 10.5601/jelem.2018.23.2.1633.
35. Sande MG, Çaykara T, Silva CJ, Rodrigues LR. New solutions to capture and enrich bacteria from complex samples. *Med. Microbiol. Immunol.*, 2020, 209:335-341, doi: 10.1007/s00430-020-00659-1.
36. Anisimkin VI, Kuznetsova IE, Kolesov VV, Pytaikin II, Sorokin VV, Skladnev DA. Plate acoustic wave sensor for detection of small amounts of bacterial cells in micro-litre liquid samples. *Ultrasonics,* 2015, 62(9):156-159.

DOI: 10.17725/rensit.2022.14.415

Magnetically Structured Composite Materials Based on Elastomeric Matrices with Different Viscoelastic Properties

Aram A. Khachaturov, Eugene E. Potapov
MIREA – Russian Technological University, https://www.mirea.ru/
Moscow 119435, Russian Federation
E-mail: xa4aram@mail.ru, svitar@yandex.ru
Alexander S. Fionov, Vladimir V. Kolesov, Sergey S. Safonov, Rustem Tlegenov
Kotelnikov Institute of Radioengineering and Electronics of RAS, http://www.cplire.ru/
Moscow 125009, Russian Federation
E-mail: fionov@cplire.ru, kvv@cplire.ru, sergej-safonov-81@bk.ru, bartirust@gmail.com
Received 21 November 2022, peer-reviewed 28 November 2022, accepted 05 December 2022

Abstract: **Composite materials based on elastomeric matrices (sulphur-regulated chloroprene rubber - PCP and cold curing polydimethylsiloxane - SKTN-A) and magnetic fillers: hard magnetic (SmCo, NdFeB) and soft magnetic (natural magnetite Fe_3O_4, ZnNiCo-ferrite) in the concentration range of 30…100 mass parts per 100 mass parts of the elastomeric matrix have been obtained. The kinetics of curing of the considered elastomeric compositions was studied, on the basis of which the optimal molding modes were proposed. The samples were molded both in the presence of a magnetic field up to 0.3 T and without it. It has been established that the viscosity of the elastomeric matrix at various stages of curing significantly affects the microstructure and properties of the resulting composites. The electrophysical and magnetic properties of the samples have been studied. It is shown that the degree of structuring, which is directly related to the anisotropy of the characteristics under study, depends on the type of matrix used and decreases in the series SKTN-PCP. The studied materials can be used as "smart" materials controlled by an external influence (magnetic or electric field).**

Keywords: **elastomers, magnetically structured composites, functional material, electrophysical properties, magnetic properties**

UDC 678.046, 678.4, 539.4, 620.22, 620.17, 621.315.61, 621.37.029.6

Acknowledgments: The work was supported by the Russian Science Foundation, grant no. 22-29-20176.

For citation: Aram A. Khachaturov, Alexander S. Fionov, Vladimir V. Kolesov, Eugene E. Potapov, Sergey S. Safonov, Rustem Tlegenov. Magnetically Structured Composite Materials Based on Elastomeric Matrices with Different Viscoelastic Properties. *RENSIT: Radioelectronics. Nanosystems. Information Technologies,* 2022, 14(4):415-426e. DOI: 10.17725/rensit.2022.14.415.

Contents

1. INTRODUCTION

One of the conditions for the development of important science-intensive industries such as robotics, electronic computing systems, radio engineering in the era of active scientific and technological progress is the creation of new materials with special properties that can change nonlinearly under the influence of external factors such as electromagnetic field, magnetic and electric fields, mechanical action, etc. Such systems are called stimulus-sensitive or controlled materials. The names smart materials or metamaterials are also often found.

There are a mass examples of smart materials which distinguish feature consist of a special structure that allows to obtain systems with an "unexpected" property on the basis of known to science components [1-4]. Polymer composites that can change their characteristics under the action of an external magnetic field is paid much attention among smart materials [2,5,6]. Magnetostructured polymer materials, ferrofluids, magnetorheological fluids, magnetic gels, and magnetic elastomers or magnetoelastics are of great interest to high-tech industries and technology [5,6,7,8]. The latter are characterized by a number of interesting effects due to the controlled change in the Poisson's ratio [1], the modulus of elasticity [2,5,9,10], the anisotropy of elastic properties [5,6,10,11], the ability to control swelling [2,6], which provides a number of extraordinary applications of these materials in medicine, industry, and technology as artificial muscles [5, 6], energy storage and transfer systems [12], targeted drug delivery systems [2], selective sorbents [2], and much more [5,6,12]. In addition, research is being carried out in the field of multisensitive magnetic elastomers [2], which can change their characteristics simultaneously under the influence of several external factors (magnetic field, temperature, pH of the medium). It is also important to note that the magnetic field is a convenient influencing factor for application in technology from the hardware point of view, which is an additional argument for the development and application of such systems.

One of the omissions of a number of research works in the field of creating magnetostructured materials is the insufficient attention paid to the technology of manufacturing such materials, the study of the dependence of the degree of structuring, the nature of the distribution of the magnetic filler in the polymer matrix, temperature, exposure time, and viscoelastic properties of the matrix used. A number of works can be single out [13,14,15] in which due attention was paid to these issues, but there are many examples [4,9–11] where the obtained structure is studied after the fact. To a greater extent, the properties of the resulting material are considered, rather than questions of the relationship, method of preparation and final properties. In this work, the selection of the most optimal way for obtaining samples characterized by the optimal degree of structuring was carried out on the basis of data from rotorless rheometry.

Based on the described earlier principles of structuring magnetic powders in an elastomeric matrix the maximum mobility of the magnetic filler at the initial stage of the process is necessary to be ensure.

This one is possible if two conditions are simultaneously observed - the minimum viscosity of the matrix and the magnetic field strength at a level that allows to overcome the resistance movement of the particles. In addition to these factors it can be assumed that the influence of the action of a magnetic field, particle size distribution, the volume content of the powder in matrix, particle morphology, specific surface, the nature of the physicochemical interaction between magnetic powder and matrix during structuring process should be also considered. These aspects of the structuring process were not affected in this work, however, in subsequent studies, it is planned to consider them and establish the relationship between the indicated parameters and the complex of electrophysical and magnetic characteristics of the obtained magnetoelastics.

2. MATERIALS, TECHNOLOGIES, EXPERIMENTAL TECHNIQUE

The following materials were used to prepare elastomeric composites:

- Sulfur-Modified Chloroprene Rubber Denka PS-40AH (Denka Company Limited, Japan), provided by OOO «ETS-M» with a Mooney viscosity of ML 1+4 (100°C) – 45. An oxide curing group consists from ZnO and MgO.
- Cold-curable silicone compound Viksint PK-68 (OOO PO Tekhnologiya-Plast) based on SKTN-A and a curing agent Catalyst No. 68 (tin diethyldicaprylate in a mixture of ethyl silicate-32 and toluene). Viscosity according to VZ1 viscometer (nozzle 5.4 mm) for SKTN-A is 90…150 s.
- Natural magnetite Fe_3O_4 – iron ore concentrate TU 07.10.10-006-00186803-2016 (hereinafter referred to as magnetite), provided by Lebedinsky Mining and Processing Plant JSC, Russia.
- ZnNiCo-ferrite obtained by ceramic technology, as well as SmCo and NdFeB powders purchased from company «Special Purity Substances».

The sample preparation process included two stages: mixing and subsequent curing, combined with the process of structuring the magnetic filler in the matrix under the action of an external magnetic field. The mixing step differed depending on the matrix. For composites based on chloroprene rubber mixing was carried out in two stages. In the first stage, the components of the formulation were mixed using a internal rubber mixer for 10 minutes at a temperature of 60°C at a rotor speed of 60 rpm. To improve the distribution of powdered components in the elastomeric matrix, the mixtures obtained at the first stage were procesed on roll mills for 3-5 minutes.

For composites based on polydimethyl siloxane (SKTN-A), mixing was also carried out in two stages. At the first stage, magnetic filler was introduced into the liquid SKTN-A matrix and dispersed by stirring in a porcelain mortar for 5 minutes. In order to improve the distribution of powdered fillers in the matrix, the mixture obtained at the first stage was subjected to ultrasound in a bath with an ultrasonic generator GRAD 95-35 (OOO Grad-Technology, Russia) at a power of 220 W (ultrasonic frequency 35 kHz) and a temperature of 25-30°C within 10 minutes. Next, a curing agent (catalyst No. 68) was introduced into the resulting mixture in an

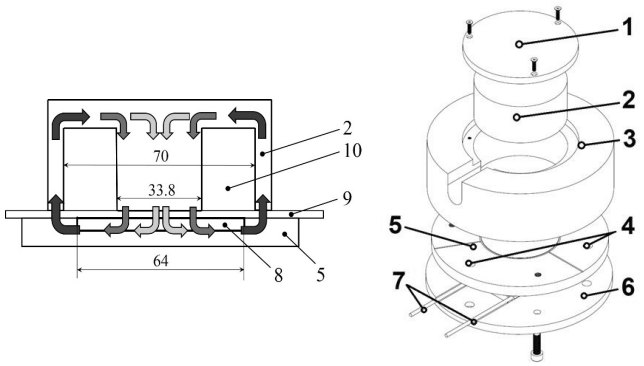

Fig. 1. *Device for curing elastomeric materials in the presence of an external magnetic field.*

amount of 10 phr on 100 phr SKTN-A and stirred for 1-2 minutes in a porcelain mortar.

Compositions based on chloroprene rubber, SKTN-A and magnetic fillers Fe_3O_4, SmCo, NdFeB, ZnNiCo-ferrite were cured in a mold (**Fig. 1**), which allows to combine the processes of magnetic structuring and curing. The upper half-mould (3) is a cylinder made of non-magnetic material (duralumin D16), in the cavity of which an electromagnet (2) with windings (10) is fixed due a cover (1). The field of the electromagnet is 0.30 ± 0.02 T. The lower half-mold (5) is consist from forming part made of magnetically soft steel and has a forming cavity and flash grooves for removing excess material from the forming cavity and of heat-insulating platform (6) made of stainless steel. The heating of the mold is carried out by two heating elements (7), placed in the lower half-mold in such a way that the heating of the material in the mold cavity is carried out evenly. Technological gasket (9) with a thickness of 1.4 mm closes the forming cavity from above. The Atmega 328 on the Arduino Nano board is used as a microcontroller. The control of the electromagnet and the thermoregulation system

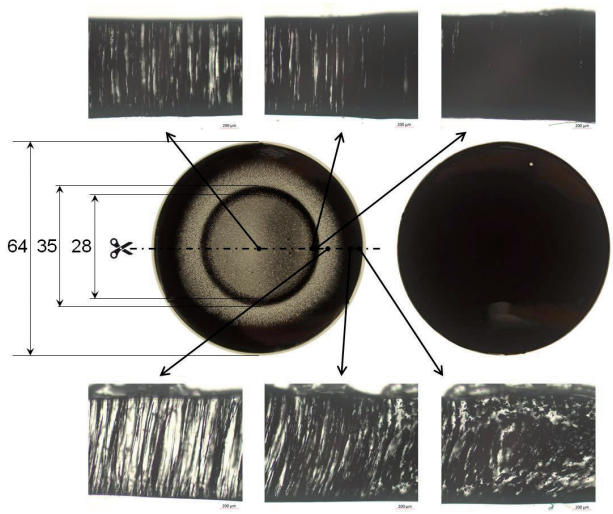

Fig. 2. *Samples of elastomeric composites based on the SKTN-A matrix and Fe_3O_4: structured on the left, unstructured on the right.*

of the mold is carried out by sending commands from the PC through the COM-port.

The samples obtained as a result of curing are plane-parallel round plates with a diameter of 64 mm and a thickness of 1.1-1.4 mm (**Fig. 2**).

On Fig. 1 also shows a scheme of the magnetic flux through sample (8) and the magnetic circuit formed by the core of the electromagnet and the lower half-mould.

On Fig. 2 – micrographs of different regions of the diametrical section of a structured sample based on the SKTN-A matrix and Fe_3O_4 cured in a magnetic field. The unstructured sample cured without applying a magnetic field shown in Fig. 2 on the right.

The manufacturing process of magnetostructured samples included several stages. The first stage is the exposure of the material for 30 minutes at a temperature at which the matrix is characterized by a minimum viscosity, but the vulcanization processes, which limit the mobility of the magnetic filler in the elastomer matrix, are slowed down. These conditions ensure the optimal distribution of the magnetic powder

in the elastomeric matrix in accordance with the map of the distribution of the magnetic field strength in the volume of the mold cavity. The second stage includes heating at a rate of 1.5°C/min to the temperature at which the vulcanization processes for the given matrix proceed most efficiently. The third stage includes holding at the vulcanization temperature until the optimum vulcanization is reached, which is determined from the data of rotorless rheometry as the time to reach 90% of the difference between the maximum and minimum torque. Throughout the process, a constant magnetic field is maintained in the volume of the mold cavity.

Reference unstructured samples were made in the same mold under similar process conditions, excluding the first stage and in the absence of a magnetic field.

The study of the kinetics of the curing process of the elastomeric matrix was carried out using a dynamic moving die rheometer D-RPA 3000 (MonTech Werkstoffprüfmaschinen GmbH, Germany [16]). The measurements were carried out in the half-form oscillation mode. For chloroprene rubber-based elastomeric materials at a frequency of 1.67 Hz and an amplitude of 0.5° at initial stage temperatures ranging from 90 to 120°C and a final stage temperature of 150°C. For elastomeric materials based on the SKTN-A matrix at a frequency of 5.0 Hz, an amplitude of 0.167° at an initial stage temperature of 30°C and a final stage temperature of 50°C. The temperature increase between stages was carried out at a rate of 1.5°C/min.

The volume resistivity of the material plates $\rho_V, \Omega \cdot m$ was measured using an high resistance meter Agilent 4339B in a special measuring cell 16008B, the measuring electrode diameter was 26 mm. The clamping device of the cell provides a tight contact between electrode and sample surface. The sample resistance was determined after holding it at a voltage of 100 V for 200 s. The thickness of the samples was measured with a micrometer type MK 0…25 mm at 6 points of the plate and then the average value was calculated. The calculation of the volume resistivity ρ_V was made according to the formula:

$$\rho_V = \frac{R \cdot S}{L},$$

where R – is measured sample resistivity, Ω; S – is the surface area of the sample covered with the electrode, m^2; L – is the sample thickness, m.

The dielectric parameters were determined using an precision LCR Meter Agilent E4980A with a 16451B measuring cell, measuring electrode diameter 38 mm. The value of gap between the electrodes was determined using a built-in micrometer. The determination technique of relative dielectric permittivity ε is based on the dependence of the capacitance of a flat capacitor on the permittivity of the material between the electrodes [17]. The value of ε is calculated with formula:

$$\varepsilon = \frac{C_\varepsilon \cdot d}{\varepsilon_0 \cdot S} = \frac{(C_x - C_p) \cdot d}{\varepsilon_0 \cdot S},$$

where C_x – is the measured capacitance, F; C_p – is the correction, consisting of the sum of the parasitic capacitance and the side capacitance of the measuring capacitor, F; d – is the value of the gap between the electrodes, sample thickness, m; ε_0 – is the dielectric constant equal to $8.854 \cdot 10^{-12}$ F/m; S – is the area of flat capacitor electrodes, m^2.

The dielectric loss tangent tgδ of the studied composites is calculated with formula:

$$tg\delta_{\varepsilon} = tg\delta_{x} \cdot \frac{C_x}{C_x - C_p},$$

where $tg\delta_x$ – is the measured value of the dielectric loss tangent of the measuring capacitor.

The demagnetization curves were obtained using a VM-2K vibromagnetometer by measuring the magnetic moment of the test sample during its reciprocating motion in a constant magnetic field up to 10 kiloersted. The samples for measurements were discs 4 mm in diameter, cut from the central part of the composite plates (see Fig. 2). The control of the sample position in a constant magnetic field were carried out with turn indicator on the sample holder bar.

3. RESULTS AND DISCUSSION

The curing graphs of rubber compounds based on chloroprene rubber and various magnetic fillers at a concentration of 30 phr are shown on **Fig. 3**. The duration of the period which is characterized by a minimum torque (corresponding to the minimum viscosity of the system) is reduced with

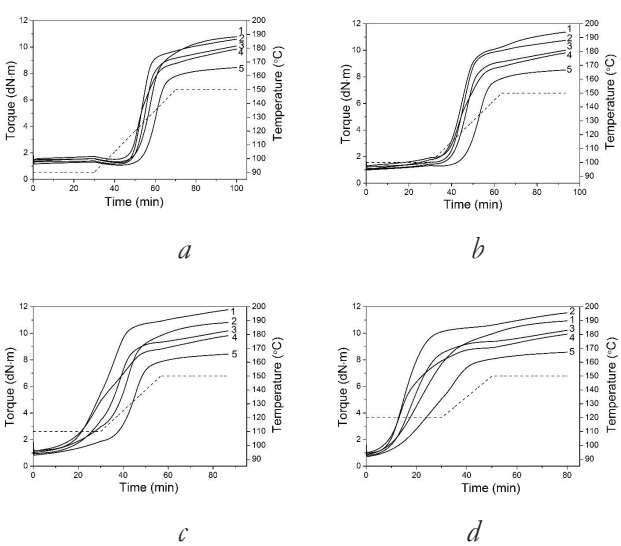

Fig. 3. *Curing kinetics for rubber compounds based on chloroprene rubber.*

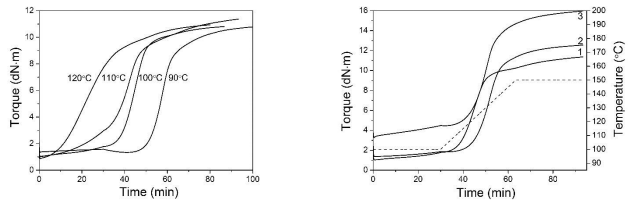

Fig. 4. *Curing kinetics for rubber compounds based on chloroprene rubber and Fe_3O_4.*

an increase in the initial temperature of the process: *a*) 90°C; *b*) 100°C; *c*) 110°C; *d*) 120°C. The optimal mode in terms of the initial viscosity of the system and the duration of the structuring process for all studied compositions corresponds to an initial temperature of 100°C, which is clearly seen in **Fig. 4***a*. The view of the cure graphs depends on the nature of the magnetic filler. Thus, in previous works, the influence of magnetite (curves 1 in Fig. 3) on the process of curing mixtures based on chloroprene rubber as an additional vulcanizing agent was demonstrated [18,19]. ZnNiCo ferrite behaves similarly (curves 2 in Fig. 3), which is probably due to the similarity of this compound in structure and physicochemical characteristics to magnetite. For other studied magnetic fillers (SmCo and NdFeB, curves 3, 4 in Fig. 3), an acceleration of the curing process is also observed compared to an unfilled matrix containing curing agents ZnO and MgO (curves 5 in Fig. 3).

The curing graphs for chloroprene rubber filled with magnetite (30 mass parts) depending on the initial temperature of the process (Fig. 4*a*) and on the concentration of the filler (Fig. 4*b*) are shown on Fig. 4. It has been established that the initial torque is growing up with increasing of the filler concentration (1 – 30 wt; 2 – 60 wt; 3 – 100

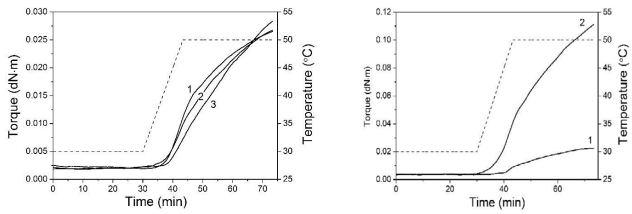

a *b*

Fig. 5. *Curing kinetics for SKTN-A.*

wt), which complicates the process of particle structuring in a magnetic field.

The curing graphs of: a) SKTN-A and b) magnetoelasts based on it are shown on **Fig. 5**. Determination of rheokinetic characteristics for the liquid oligomeric matrix SKTN-A is difficult due to the weak response to sinusoidal deformations (3 – 1.67 Hz, 0.5°). SKTN-A was additionally tested in various modes with an increase in the oscillation frequency and a decrease in amplitude in accordance with the requirement of GOST R 54547-2011 (2 – 2.0 Hz, 0.5°) and a subsequent increase in the oscillation frequency (1 – 5.0 Hz, 0.167°) in order to search the most optimal ratio of measurement parameters for maximum response. The curing process of the liquid matrix SKTN-A occurs at relatively low temperatures – 30…50°C. In this regard, a significant effect of the type of magnetic filler on the kinetics of curing and on the initial viscosity of the system was not revealed. This is confirmed by curing graphs for SKTN-A filled with Fe_3O_4 in the amount: 1 – 30 phr, 2 – 100 phr are shown on Fig. 5*b*.

Determination of the rheokinetic parameters at different temperature conditions makes it possible to choose the optimal mode for manufacturing magnetostructured composites based on various elastomeric matrices and the optimal concentration of the magnetic filler to obtain the most pronounced effect of structuring.

The results of measurements of electrophysical parameters and magnetic moment of the obtained samples of elastomeric composites with magnetic fillers are presented in **Tables 1-8.** We note the following: the increase in ε and tgδ, as well as the decrease in relatively unfilled matrices, are higher for the samples molded in a magnetic field. In this case, the relative changes are higher for composites based on the SKTN-A matrix.

Table 1

Composites based on chloroprene rubber and Fe_3O_4

Matrix	C, w.p.	B, T	h, mm	ε·(tgδ)		$\rho_V, \Omega \cdot m$	M_{max}, mT	
				1 kHz	1MHz		Bottom	Top
PCP	0	0	1.24	6.0 (0.027)	5.2 (0.097)	$(1.5\pm0.001)\cdot10^{10}$	0	0
PCP	30	0	1.16	5.9 (0.014)	5.4 (0.077)	$(5.7\pm0.09)\cdot10^{9}$	0	0
PCP	30	0.3	1.14	8.0 (0.018)	7.0 (0.086)	$(1.3\pm0.04)\cdot10^{10}$	-0.07	0.16
PCP	60	0	1.15	6.4 (0.015)	5.9 (0.070)	$(5.6\pm0.1)\cdot10^{9}$	-	-
PCP	60	0.3	1.15	10.0 (0.024)	8.5 (0.079)	$(7.1\pm0.2)\cdot10^{9}$	-0.16	0.22
PCP	100	0	1.28	9.5 (0.030)	8.3 (0.084)	$(4.0\pm0.07)\cdot10^{9}$	0	0
PCP	100	0.3	1.26	17.3 (0.073)	12.9 (0.092)	$(2.3\pm0.6)\cdot10^{7}$	-0.20	0.19

Table 2

Composites based on SKTN-A and Fe_3O_4.

Matrix	C, w.p.	B, T	h, mm	ε·(tgδ)		$\rho_V, \Omega \cdot m$	M_{max}, mT	
				1 kHz	1MHz		Bottom	Top
CKTH-A	0	0	0.94	2.7 (0.001)	2.7 (0.001)	$(3.9\pm10)\cdot10^{13}$	0	0
CKTH-A	30	0	0.93	3.8 (0.011)	3.7 (0.005)	$(2.4\pm3)\cdot10^{9}$	0	0
CKTH-A	30	0.3	0.90	8.7 (0.079)	6.8 (0.029)	-	-0.15	0.33
CKTH-A	60	0	0.94	5.5 (0.028)	5.0 (0.013)	$(2.4\pm0.3)\cdot10^{12}$	-	-
CKTH-A	60	0.3	1.02	13.6 (0.098)	9.9 (0.040)	-	-0.17	0.20
CKTH-A	100	0	0.96	6.7 (0.027)	6.1 (0.013)	$(1.3\pm0.1)\cdot10^{12}$	-	-
CKTH-A	100	0.3	1.01	15.4 (0.091)	11.5 (0.026)	-	-0.19	0.19

Here: C (w.p.) – filler concentration in weight parts; B(T) – magnetic field strength during vulcanization; h (mm) – the sample thickness; ε (tgδ) – permittivity (dielectric loss tangent) at frequencies of 1 kHz and 1 MHz; ρ_V (Ohm·m) – specific volume resistance; M_{max} (mT) – the maximum magnetic moment on each side of the sample, conditionally marked bottom and top.

Table 3

Composites based on chloroprene rubber and ZnNiCo-ferrite.

Matrix	C, w.p.	B, T	h, mm	ε·(tgδ)		$\rho_V, \Omega \cdot m$	M_{max}, mT	
				1 kHz	1MHz		Bottom	Top
PCP	0	0	1.24	6.0 (0.027)	5.2 (0.097)	$(1.5\pm0.001)\cdot10^{10}$	0	0
PCP	30	0	1.21	5.5 (0.035)	4.6 (0.061)	$(9.0\pm0.006)\cdot10^{9}$	0	0
PCP	30	0.3	1.16	7.3 (0.032)	5.9 (0.114)	$(8.2\pm0.1)\cdot10^{9}$	0	0
PCP	60	0	1.13	7.7 (0.049)	5.9 (0.118)	$(4.9\pm0.07)\cdot10^{9}$	-	-
PCP	60	0.3	1.18	8.4 (0.048)	6.1 (0.129)	$(4.2\pm0.05)\cdot10^{9}$	0	0.08
PCP	100	0	1.12	9.6 (0.050)	6.7 (0.135)	$(1.1\pm0.03)\cdot10^{10}$	-	-
PCP	100	0.3	1.14	10.1 (0.057)	6.8 (0.142)	$(1.1\pm0.03)\cdot10^{10}$	-0.02	0.08

Table 4

Composites based on SKTN-A and ZnNiCo-ferrite.

Matrix	C, w.p.	B, T	h, mm	ε·(tgδ)		$\rho_V, \Omega \cdot m$	M_{max}, mT	
				1 kHz	1MHz		Bottom	Top
SKTN-A	0	0	0.94	2.7 (0.001)	2.7 (0.001)	$(3.9\pm10)\cdot10^{13}$	0	0
SKTN-A	30	0	0.93	3.6 (0.025)	3.5 (0.048)	$(1.4\pm2)\cdot10^{13}$	0	0
SKTN-A	30	0.3	0.75	3.5 (0.048)	2.5 (0.067)	$(8.6\pm0.6)\cdot10^{10}$	0	0.11
SKTN-A	60	0	0.94	4.5 (0.038)	3.4 (0.061)	$(7.3\pm10)\cdot10^{12}$	-	-
SKTN-A	60	0.3	0.97	8.7 (0.095)	4.5 (0.139)	$(1.2\pm0.2)\cdot10^{11}$	-0.06	0.14
SKTN-A	100	0	0.93	5.0 (0.037)	3.8 (0.069)	$(6.4\pm10)\cdot10^{12}$	-	-
SKTN-A	100	0.3	0.95	9.2 (0.087)	4.7 (0.151)	$(9.4\pm0.7)\cdot10^{10}$	-0.05	0.11

Table 5

Composites based on chloroprene rubber and NdFeB.

Matrix	C, w.p.	B, T	h, mm	ε·(tgδ)		$\rho_V, \Omega \cdot m$	M_{max}, mT	
				1 kHz	1MHz		Bottom	Top
PCP	0	0	1.24	6.0 (0.027)	5.2 (0.097)	$(1.5\pm0.001)\cdot10^{10}$	0	0
PCP	30	0	1.14	7.4 (0.023)	6.3 (0.102)	$(1.1\pm0.01)\cdot10^{10}$	0	0
PCP	30	0.3	1.18	8.4 (0.036)	7.0 (0.099)	$(7.2\pm0.08)\cdot10^{9}$	-0.10	0.18
PCP	60	0	1.15	7.8 (0.027)	6.6 (0.099)	$(1.8\pm0.04)\cdot10^{10}$	-	-
PCP	60	0.3	1.16	8.6 (0.034)	7.3 (0.082)	$(9.7\pm0.2)\cdot10^{9}$	-0.19	0.21
PCP	100	0	1.17	7.2 (0.023)	6.4 (0.072)	$(2.1\pm0.2)\cdot10^{10}$	0	0
PCP	100	0.3	1.17	9.2 (0.032)	8.0 (0.064)	$(1.6\pm0.6)\cdot10^{10}$	-0.38	0.36

Table 6

Composites based on SKTN-A and NdFeB.

Matrix	C, w.p.	B, T	h, mm	ε·(tgδ)		$\rho_V, \Omega \cdot m$	M_{max}, mT	
				1 kHz	1MHz		Bottom	Top
SKTN-A	0	0	0.94	2.7 (0.001)	2.7 (0.001)	$(3.9\pm10)\cdot10^{13}$	0	0
SKTN-A	30	0	0.92	3.6 (0.009)	3.5 (0.002)	$(4.5\pm5)\cdot10^{13}$	0	0
SKTN-A	30	0.3	0.93	5.0 (0.037)	4.6 (0.008)	$(1.1\pm0.02)\cdot10^{10}$	-0.07	0.16
SKTN-A	60	0	0.89	3.7 (0.012)	3.6 (0.003)	$(2.0\pm0.8)\cdot10^{13}$	-	-
SKTN-A	60	0.3	0.94	6.6 (0.040)	6.1 (0.009)	$(3.4\pm0.07)\cdot10^{10}$	-0.16	0.22
SKTN-A	100	0	0.95	4.1 (0.016)	4.9 (0.004)	$(1.2\pm0.2)\cdot10^{13}$	0	0
SKTN-A	100	0.3	0.97	7.8 (0.041)	7.1 (0.009)	$(1.5\pm0.04)\cdot10^{10}$	-0.20	0.19

Table 7

Composites based on chloroprene rubber and SmCo.

Matrix	C, w.p.	B, T	h, mm	ε·(tgδ)		$\rho_V, \Omega \cdot m$	M_{max}, mT	
				1 kHz	1MHz		Bottom	Top
PCP	0	0	1.24	6.0 (0.027)	5.2 (0.097)	$(1.5\pm0.001)\cdot10^{10}$	0	0
PCP	30	0	1.28	6.5 (0.023)	5.7 (0.090)	$(8.2\pm2)\cdot10^{10}$	-0.11	0.16
PCP	30	0.3	1.26	17.3 (0.028)	12.9 (0.101)	$(2.7\pm0.03)\cdot10^{9}$	-0.09	0.24
PCP	60	0	1.32	5.8 (0.018)	5.2 (0.080)	$(4.2\pm0.03)\cdot10^{9}$	-	-
PCP	60	0.3	1.33	6.0 (0.018)	5.4 (0.078)	$(3.1\pm0.02)\cdot10^{9}$	-0.19	0.19
PCP	100	0	1.41	6.6 (0.024)	6.0 (0.067)	$(3.9\pm0.05)\cdot10^{9}$	-	-
PCP	100	0.3	1.38	9.5 (0.027)	8.4 (0.073)	$(3.0\pm0.4)\cdot10^{9}$	-0.68	0.58

Table 8

Composites based on SKTN-A and SmCo.

Matrix	C, w.p.	B, T	h, mm	ε·(tgδ)		$\rho_V, \Omega \cdot m$	M_{max}, mT	
				1 kHz	1MHz		Bottom	Top
SKTN-A	0	0	0.94	2.7 (0.001)	2.7 (0.001)	$(3.9\pm10)\cdot10^{13}$	0	0
SKTN-A	30	0	0.94	3.2 (0.003)	3.2 (0.001)	$(2.4\pm7)\cdot10^{13}$	0	0
SKTN-A	30	0.3	0.95	5.4 (0.011)	5.2 (0.004)	-	-1.35	1.59
SKTN-A	60	0	0.94	3.9 (0.004)	3.8 (0.002)	$(6.0\pm7)\cdot10^{12}$	-	-
SKTN-A	60	0.3	0.93	4.4 (0.006)	4.3 (0.003)	$(4.5\pm2)\cdot10^{11}$	-0.43	0.49
SKTN-A	100	0	0.97	9.5 (0.008)	8.3 (0.004)	$(2.4\pm10)\cdot10^{13}$	-	-
SKTN-A	100	0.3	0.97	17.3 (0.013)	12.9 (0.006)	-	-1.62	1.03

The characteristic magnetic profiles of the samples: a) 30 phr Fe_3O_4 in SKTN-A matrix, unstructured; b) 100 phr SmCo in chloroprene rubber matrix, structured; c) and d) 100 phr SmCo in SKTN-A matrix, structured, are shown on **Fig. 6**. Profiles a) and b) depicted double-sided, c) and d) depicted separate for each side of the sample. The value of the vertical axis in the figure is the magnetic moment of the sample part with the X and Y coordinates

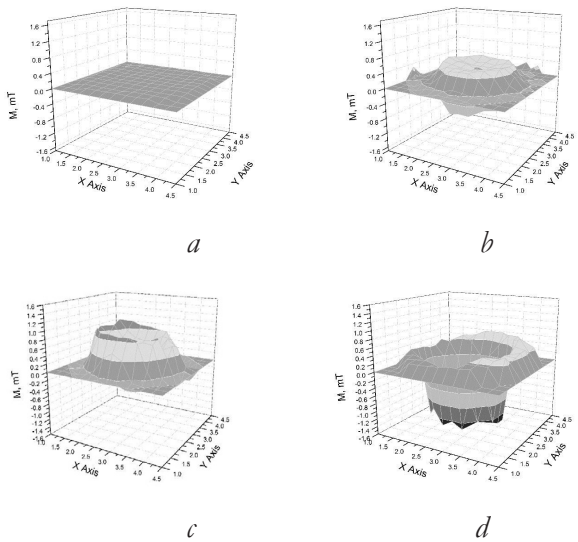

Fig. 6. *Magnetic profiles of the samples.*

(the maximum value along the axis is ±1.6 mT). The magnetic moment was measured with a Mayak-3M Teslameter axial Hall sensor with a step of 5 mm along the *X* and *Y* axes.

The magnetic profiles of the samples demonstrate the degree of magnetic ordering of the filler in the elastomeric composite. More detailed information about the magnetic properties of the magnetostructured and unstructured samples can be obtained by magnetometric methods.

The array of demagnetization curves for composites was obtained according to the scheme shown in **Fig. 7**. The measurements were carried out in two positions of the sample plane: parallel (position 90d on the scale of the turn indicator) and perpendicular (position 0d on the scale of the turn indicator) to the magnetic field. The rotation of the sample relative to the direction of the constant magnetic field in the vibromagnitometer allows estimating the degree of magnetic anisotropy of the composite. Samples with a filler content of 30 phr were chosen for research. Higher concentrations do not allows to obtain high-quality (with saturation) demagnetization curves for all samples. Curve designations on **Fig. 8-11** is following: EM0-0d, EM0-90d - sample cured in the absence of a magnetic field, orientation in the perpendicular and parallel directions, respectively; EM1-0d, EM1-90d – magnetically cured sample, orientation in perpendicular and parallel directions, respectively.

The demagnetization curves of the samples are shown in Fig. 8-11. In all figures *a*) and *b*) is the chloroprene rubber matrix, *c*) and *d*) is the SKTN-A matrix.

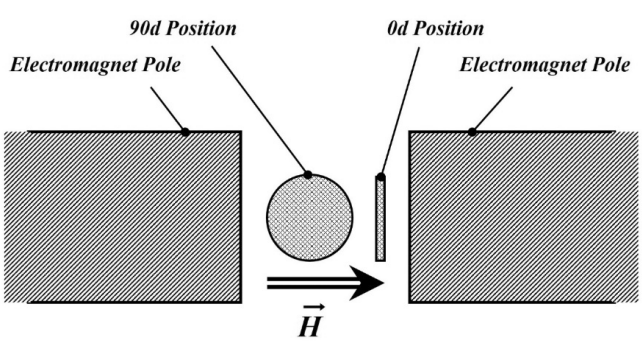

Fig. 7. *Scheme for obtaining families of demagnetization curves.*

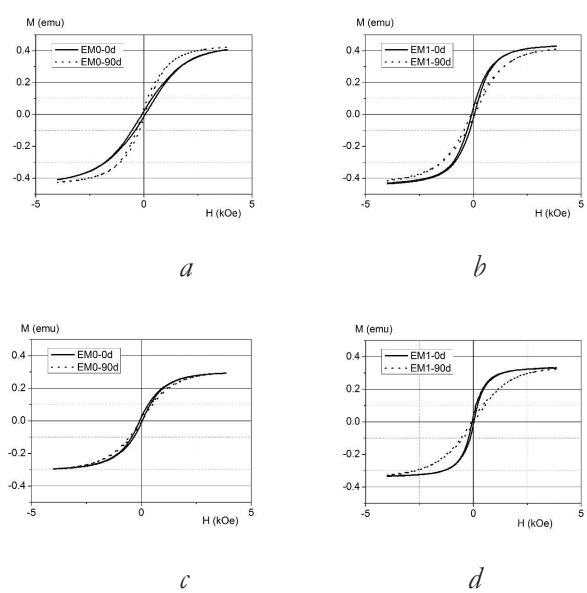

Fig. 8. *Demagnetization curves for composites based on* Fe_3O_4.

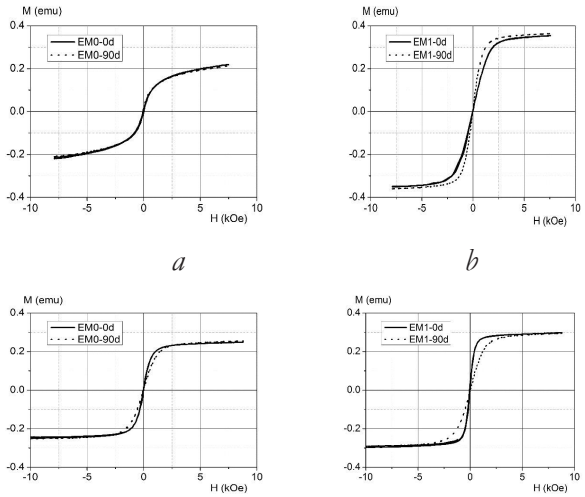

Fig. 9. *Demagnetization curves for composites based on ZnNiCo-ferrite.*

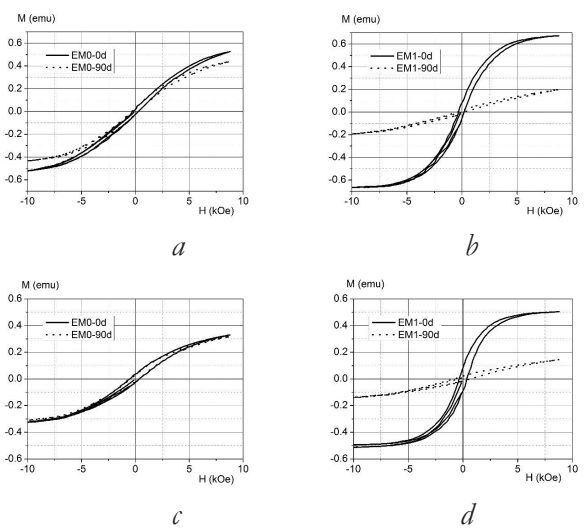

Fig. 10. *Demagnetization curves for composites based on NdFeB.*

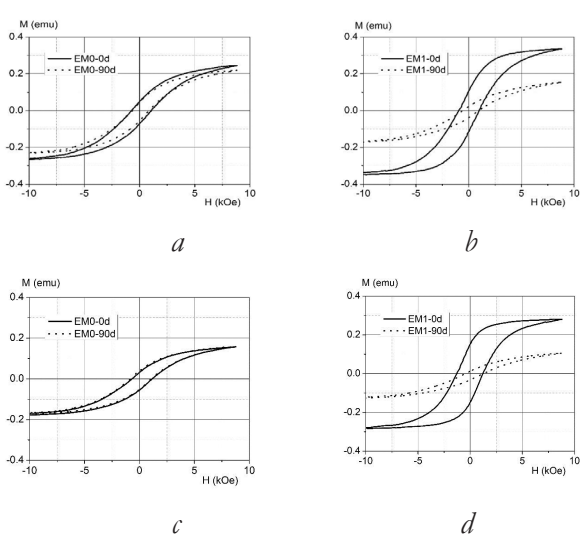

Fig. 11. *Demagnetization curves for composites based on SmCo.*

Summarizing the obtained magnetometric data, we can draw the following conclusions:

- magnetostructured samples (with the exception of chloroprene rubber - Fe_3O_4) have a pronounced anisotropy of magnetic susceptibility relative to the direction of the external magnetic field;
- the degree of anisotropy is higher for the SKTN-A matrix than for chloroprene rubber;
- the magnetic moment in a field of more than 4 kOe is higher for composites, both structured and unstructured, in the case of a chloroprene rubber matrix;
- for composites based on hard-magnetic fillers, the anisotropy fields in both matrices exceed 1 T.

4. CONCLUSION

In this work, the issues of developing technology and creating magnetoelasts with specified electrophysical, magnetic, stress-strain properties, techniques for controlling and detecting the nature of the distribution of a magnetic filler in an elastomer matrix depending on the production mode are considered.

Techniques for evaluating the most optimal mode of structuring magnetoelasts by analyzing the kinetics of the curing process in various temperatures have been developed.

It has been shown that, the content of the magnetic filler less effect on the viscoelastic characteristics of compositions at the initial stage of the process of manufacturing magnetostructured materials for compositions based on a liquid matrix SKTN-A than on chloroprene rubber.

Magnetically structured composites based on two elastomeric matrices, differing

in terms of the principle of curing, stress-strain properties, and a amount of hard and soft-magnetic fillers have been obtained and studied.

It has been shown that magnetoelasts based on chloroprene rubber and SKTN-A matrices have anisotropy of electrical and magnetic properties. The relationship between this anisotropy and the composition of the magnetoelasts and the parameters of its manufacturing process has been established.

REFERENCES

1. Galea R, Dudek K, Farrugia P-S, Mangion LZ, Grima JN, Gatt R. Reconfigurable magneto-mechanical metamaterials guided by magnetic fields. *Composite Structures*, 2022, 280:114921. DOI: 10.1016/j.compstruct.2021.114921.
2. Ganguly S, Margel S. 3D printed magnetic polymer composite hydrogels for hyperthermia and magnetic field driven structural manipulation. *Progress in Polymer Science,* 2022, 131(10):101574. DOI: 10.1016/j.progpolymsci.2022.101574.
3. Roudbarian N, Jebellat E, Famouri S et al. Shape-memory polymer metamaterials based on triply periodic minimal surfaces. *European Journal of Mechanics - A/Solids*, 2022, 96(1):104676. DOI: 10.1016/j.euromechsol.2022.104676.
4. Gan R, Yu M, Li S, Li Y, Fang B, Qi S. A magnetic control reconfigurable coded electromagnetic absorbing metamaterial. *Composites Science and Technology,* 2021, 217(37):109098. DOI: 10.1016/j.compscitech.2021.109098.
5. Bastola A, Hossain M. A review on magneto-mechanical characterizations of magnetorheological elastomers. *Composites Part B: Engineering,* 2020, 200:108348. DOI: 10.1016/j.compositesb.2020.108348.
6. Zrinyi M. Magnetically responsive polymer gels and elastomers: properties, synthesis and applications. In: *Smart Polymers and their Applications.* Woodhead Publishing, 2014, pp. 134-165.
7. Kuznetsova IE, Kolesov VV, Zaitsev BD, Fionov AS, Shihabudinov AM, Stepanov GV, Kramarenko EYu. Electrophysical and acoustic properties of magnetic elastomers structured by an external magnetic field. *Bull. Russ. Acad. Sci. Phys.*, 2017, 81(8):945-949. DOI: 10.3103/S1062873817080184.
8. Iren E. Kuznetsova, Vladimir V. Kolesov, Alexander S. Fionov, Elena Yu. Kramarenko, Gennady V. Stepanov, Michail G. Mikheev, Enrico Verona, Igor Solodov. Magnetoactive elastomers with controllable radio-absorbing properties. *Materials Today Communications,* 2019, 21:100610. DOI:10.1016/J.MTCOMM.2019.100610.
9. Lee CJ, Kwon SH, Choi HJ, Kyung Ho Chung KH, Jae Heum Jung JH. Enhanced magnetorheological performance of carbonyl iron/natural rubber composite elastomer with gammaferrite additive. *Colloid and Polym Sci.,* 2018, 296(9):1609-1613, doi: 10.1007/s00396-018-4373-0.
10. Kwon SH, Lee CJ, Choi HJ, Chung KH, Jung JH. Viscoelastic and mechanical behaviors of magneto-rheological carbonyl iron/natural rubber composites with magnetic iron oxide nanoparticle. *Smart Materials and Structures,* 2019, 28(4). DOI: 10.1088/1361-665X/ab0018.

11. Khayam S, Usman M, Umer M, Rafique A. Development and characterization of a novel hybrid magnetorheological elastomer incorporating micro and nano size iron fillers. *Materials & Design,* 2020, 192:108748, doi: 10.1016/j.matdes.2020.108748.
12. Li Y, Li J, Li W, Du H. A state-of-the-art review on magnetorheological elastomer devices. *Smart Materials and Structures,* 2014, 23:123001–24. DOI: 10.1088/0964-1726/23/12/123001
13. Cabrera D, Lak A, Yoshida T, Materia ME, Ortega D, Ludwig F, Guardia P, Sathya A, Pellegrino T, Teran FJ. Unraveling viscosity effects on the hysteresis losses of magnetic nanocubes. *Nanoscale,* 2017, 9(16):5094-5101. DOI: 10.1039/C7NR00810D.
14. Walter B, Pelteret JP, Kaschta J, Schubert DW, Steinmann P. Preparation of magnetorheological elastomers and their slip-free characterization by means of parallel-plate rotational rheometry. *Smart Materials and Structure,* 2017, 26(8):085004. DOI: 10.1088/1361-665X/aa6b63.
15. Khimi SR, Pickering KL. Comparison of dynamic properties of magnetorheological elastomers with existing antivibration rubbers. *Composites Part B: Engineering,* 2015, 83:175-183. DOI: 10.1016/j.compositesb.2015.08.033.
16. Smesi rezinovye. Opredelenie vulkanizacionnyh harakteristik s ispol'zovaniem bezrotornyh reometrov [Rubber compounds. Measurement of vulcanization characteristics using rotorless cure meters]. *GOST R 54547-2011*, Moscow, 2011, 16 p. (in Russ.).
17. Lushchejkin GA. *Metody issledovaniya elektricheskikh svojstv polimerov* [Techniques of investigation the electrophysical properties of polymers]. Moscow, Khimiya Publ., 1988, 160 p.
18. Khachaturov AA, Milova AO, Potapov EE, Kovaleva AN. Issledovanie vlijanija zhelezorudnogo koncentrata na processy vulkanizacii rezinovyh smesej na osnove polihloroprena. [Study of the Effect of Iron Ore Magnetite Concentrate on the Vulcanization of Polychloroprene-Based Rubber]. *Kauchuk i rezina*, 2020, 79(3):146-149, doi: 10.47664/0022-9466, (in Russ.)
19. Khachaturov AA, Milova AO, Potapov EJe, Kovaleva AN. Modificirovannyj magnetit, kak komponent vulkanizujushhej sistemy dlja PHP sernogo regulirovanija. [Modified Magnetite as a Component of a Curing System for Sulfur-Modified Chloroprene Rubber] *Kauchuk i rezina,* 2022, 81(1):38-43, (in Russ.).

DOI: 10.17725/rensit.2022.14.427

Synthesis of Conductive Silver Ink with a Low Sintering Temperature for Inkjet Printing Applications

Ekaterina G. Rustamova, Maria S. Kagirina
Scientific and Production Association "GRAFENIKA", https://www.grafenika.ru/
Moscow 107143, Russian Federation
E-mail: nebukina@yandex.ru, mariakagirina@rambler.ru
Alexey A. Gridnev, Gulnaz M. Mukhametova, Alexander A. Gulin
N.N. Semenov Institute of Chemical Physics of Russian Academy of Sciences, https://www.chph.ras.ru/
Moscow 119991, Russian Federation
E-mail: 99gridnev@gmail.com, mukhametova@mail.ru, aleksandr.gulin@phystech.edu
Sergey P. Gubin
N.S. Kurnakov Institute of General and Inorganic Chemistry of Russian Academy of Sciences, http://www.igic.ras.ru/
Moscow 119991, Russian Federation
E-mail: gubin@igic.ras.ru
Received September 22, 2022, peer-reviewed September 29, 2022, accepted October 6, 2022

Abstract: **Transparent silver ink based on silver amino complex for inkjet printing has been developed. 1,2-diaminopropane, which acts as a solvent and complexing agent, significantly lowered the decomposition temperature of the silver salt and ensured the chemical stability of the resulting ink at room temperature. The annealed films were characterized by close packing and low electrical resistance values (8.5 μOhm·cm at an annealing temperature of 150°C). The ink provides productive inkjet printing while maintaining stable operation of the print head nozzles.**

Keywords: **silver, conductive inks, organic silver complex, inkjet printing, low-temperature sintering, printed electronics**

UDC 546.05'57'06

For citation: Ekaterina G. Rustamova, Alexey A. Gridnev, Gulnaz M. Mukhametova, Alexander A. Gulin, Maria S. Kagirina, Sergey P. Gubin. Synthesis of Conductive Silver Ink with a Low Sintering Temperature for Inkjet Printing Applications. *RENSIT: Radioelectronics. Nanosystems. Information technologies,* 2022, 14(4):427-436e. DOI: 10.17725/rensit.2022.14.427.

Contents

1. INTRODUCTION

Printed electronics is a relatively new area for the production of various electronic components and printed circuit boards based on them. It is successfully used in such areas as: the manufacture of RFID tags [1], NFC modules [2], in the production of "flexible electronics",

including various sensors [3]. The main advantages of this technology are the simplicity and speed of manufacturing the final products. It is especially useful in prototyping tasks, when one needs to quickly and cheaply make product mock-ups or test the viability of many ideas regarding the design of a device or product. Another advantage of printed electronics is the wide choice of a suitable substrate (glass, ceramics, polymeric materials, etc.).

Currently, inks based on carbon nanoparticles (nanotubes, graphene, etc.) [4] or inks containing metal nanoparticles (silver, gold, copper, platinum, etc.) are most often used as conductive materials for printed electronics [5-7]. The selection of the rheological parameters of the ink is very dependent on the intended printing method. Of the many application technologies, three main types of printing can be distinguished: screen, inkjet and aerosol. In this article, we will talk about inkjet printing using a commercial inkjet printer Dimatix DMP-2831 from Fujifilm Inc., USA.

The most popular type of conductive inkjet ink is silver nanoparticle ink. This is due to the optimal ratio "price-quality". The needs of the market dictate the need to create and produce high-precision small-sized universal and cheap conductive elements on light and flexible substrates. Nanosilver is a readily available source of low electrical resistance at low post-processing temperatures for printed structures. This is due to the lowest electrical resistivity of silver as a metal, the relative ease of obtaining and concentrating silver sols, and resistance to oxidation in air. The conductivity of such ink is provided by the effect of lowering the melting temperature of particles with a decrease in their size [8].

However, often silver ink, which is concentrated silver sols, tends to coagulate and form various kinds of aggregates. This is facilitated both by the properties of the nanoparticles themselves and by the hydrodynamics of the printing process of the flow of ink through narrow capillary channels inside the printer cartridge, as well as the process of drop formation and printing itself, in which a build-up of a silver layer can be observed at the base of the nozzles near the meniscus of the liquid due to evaporation. volatile components of the solvent.

One of the potential solutions to these problems can be the so-called particleless ink - ink containing complex silver salts, which are destroyed by heating, irradiation with UV light or other activation method with the formation of metallic silver. This forms a conductive coating. Such inks do not contain silver particles and are true solutions, so they are largely devoid of the disadvantages of inks containing particles. When creating such inkjet inks, it is important to observe the following criteria:

- the composition of the ink must be selected in such a way as to ensure long-term chemical stability and optimal rheological parameters (viscosity, surface tension);
- print stability (stable formation of ink droplets without clogging the nozzles

of the print head during the printing process);
- the silver concentration should ensure maximum conductivity of the printed and annealed structures;
- low annealing temperature (for creating flexible electronics elements).

In connection with the above, the main goal of this study was to develop a stable conductive silver ink with a low sintering temperature for inkjet printing on equipment similar to a Dimatix DMP printer (Fujifilm Inc., USA).

2. EXPERIMENTAL PART

The following materials were used to perform this work: silver nitrate (chemically pure, Petronit LLC), potassium oxalate (chemically pure, RusChem LLC), 1,2-diaminopropane, (Purity 99%, CAS Number 78-90-0, Sigma-Aldrich), 2-propanol (high purity grade, JSC EKOS-1), deionized water (resistivity 18 MΩ cm), hydrazine hydrate (100%, RusChem LLC), polyethersulfone syringe membrane filter (PES 0.22 μm, Millipore), polyimide film (PI, 40 μm thick).

For inkjet printing on Dimatix DMP equipment, the synthesized ink must have the following characteristics: viscosity – 10-12 mPas, surface tension – 28-33 dynes, low solvent volatility (boiling point above 100°C) and density ≤ 1.

The silver ink used in this study was synthesized by dissolving silver oxalate in organic solvents.

Silver oxalate was obtained under laboratory conditions by an ion-exchange reaction by mixing aqueous solutions of silver nitrate and potassium oxalate, taken in stoichiometric ratios. The resulting white precipitate was centrifuged, washed several times with deionized water, and dried at 40°C.

The preparation of the ink was carried out by dissolving 2 g of silver oxalate with cooling and intensive stirring on a magnetic stirrer in 1.5 ml of deionized water and 2.5 ml of 1,2 diaminopropane until a clear solution was formed. The resulting composition contained 36 wt.% silver and was characterized by a viscosity of more than 120 mPas and a density of 2.96 g/cm^3. These parameters significantly exceeded the optimal physical criteria for inkjet printing. In this regard, to achieve the necessary rheological properties, the original ink was diluted with a mixture of deionized water and isopropyl alcohol.

Thus, in this study, by selecting the ratio of solvents, it was possible to synthesize transparent silver ink with suitable rheological parameters for inkjet printing (viscosity – 10 mPas, surface tension 33-35 mN/m, density 1.01 g/cm^3). The final ink was filtered using a 0.22 μm syringe filter for further testing and research.

The absorption spectra of silver ink were recorded on a Leki SS2107UV spectrophotometer (ZAO LOIP, Russia) in the wavelength range from 200 to 1100 nm. The sample volume was 3 ml, the optical path length was 1 cm.

The thermal behavior of the ink was studied on a thermogravimetric analyzer (TGA) from Perkin Elmer (Germany) using aluminum trays. 20 μl of ink

(m = 20 mg) was placed in the bath, dried at a temperature of 90°C until a film was formed (m = 8.6 mg), and then heated in the analyzer to 300°C in an air atmosphere with a heating rate of 10°C/min.

Ink testing in printing was carried out on a Dimatix DMP-2831 inkjet printer. During the printing process, Model DMC-11610 cartridges with a drop volume of 10 pl, equipped with a piezoelectric print head with 16 nozzles with a diameter of 21 microns, were used. Printing was carried out at room temperature without substrate heating, using standard settings (Wave 2 waveform, nozzle voltage 23 V).

The formation of printed elements (squares 7×7 mm, lines 20 mm) was performed by layer-by-layer printing with ink (5 layers) on PI film. To improve the wettability and adhesion of the ink to the substrate, the PI was preliminarily cleaned of contaminants, degreased, and hydrophilized by keeping the film in hydrazine hydrate for 1 min. The printed structures were annealed at various temperatures for 30 min. The cured square films were used for surface morphology, print quality, and electrical measurements.

The identification of the phase composition of the annealed samples was carried out on a Bruker D8 Advance facility (Germany) operating in reflection mode on Cu-Kα radiation (40 kV, 40 mA, λ = 1.54056 Å) with a scanning step of 4° min^{-1}.

The morphology and thickness of the silver film on the surface of the polymer substrate was studied using a Prisma E scanning electron microscope (Thermo Scientific, Czech Republic) in a high vacuum mode (~$5 \cdot 10^{-4}$ Pa) with an accelerating voltage of 3.5 kV. The sample was frozen in liquid nitrogen for 20 min, then a cut was made with a sharp scalpel from the side opposite to the deposited silver layer. The sample was fixed on an *L*-shaped holder with carbon tape in such a way that the resulting cut was perpendicular to the optical axis of the microscope.

The viscosity of silver ink was measured on an AND SV 10A vibratory viscometer (Japan).

The surface tension of the ink was evaluated by stalagmometry.

The resistance of silver films was measured using a JG WeChat Support Type ST 2258C four-point probe system (Suzhou Jingge Electronic Co, China). The resistivity (ϱ) of the printed silver films was calculated as $\varrho = R_s \times W$, where R_s is the sheet resistance and W is the film thickness.

To measure the adhesion strength of silver films to a polyimide substrate, a standard test method, the adhesive tape method (test method B), was used. To do this, cuts were made on the film in the form of a lattice: four cuts in both directions up to the substrate. A pressure-sensitive adhesive tape was applied to the "lattice" and then torn off. Adhesion strength was determined by comparative analysis of the film before and after tearing off the adhesive tape.

3. RESULTS AND ITS DISCUSSION

An important factor in the creation of conductive ink in this work was the choice of the correct compound as a precursor. Most of the non-metallic phases must leave the system during thermolysis and evaporation. The chemical precursor must be designed in such a way that the chemical transformation into a pure metal phase occurs at a sufficiently low temperature to ensure the elimination of inorganic and organic compounds.

Following the above and relying on the achievements of studies described in scientific publications over the past few years [9-14], in this work, the process of complexation between a silver salt and an organic amino compound was used to form silver ink.

Silver oxalate was chosen as a precursor, the advantage of which is a high content of silver among carboxylates and, according to experimental data [15], a relatively low decomposition temperature (T_{dec} = 210°C).

According to literature sources, amino compounds, entering into donor-acceptor interaction with silver ions, form $Ag(R\text{-}NH_2)^{2+}$ complexes, which contribute to a significant decrease in the thermal decomposition temperature of the silver precursor [16]. This property is especially pronounced in silver complexes with bidentate amines. In this regard, 1,2-diaminopropane was used as a complexing agent. This compound has an optimal boiling point (120°C), has good solubility in water, alcohols and is characterized by chemical stability.

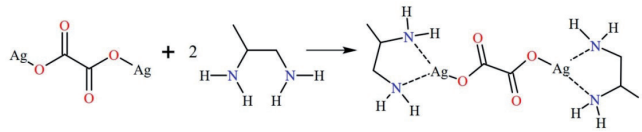

Fig. 1. *Formation reaction of a complex of silver-1,2 oxalate-diaminopropane.*

The advantage of the synthesis of the silver oxalate-1,2-diaminopropane complex is its ease, simplicity and cheapness. A schematic reaction for the formation of a silver organocomplex is shown in **Fig. 1**.

On the basis of the synthesized compound, an ink formula was developed that satisfies the requirements attached to a liquid for inkjet printing on a Dimatix DMP unit. Such organic silver ink was a transparent liquid with a solid metal content of 15 mass%. When keeping the ink for a month at room temperature, no degradation elements (precipitation, color change) were noticed, the transparency of the liquid remained unchanged. These observations are confirmed by spectral studies. In the spectra of the UV-visible absorption region, recorded with freshly prepared ink and kept for a month at room conditions, there are no plasmon resonance bands in the range of 390–600 nm, which are characteristic of nanosized silver (**Fig. 2**).

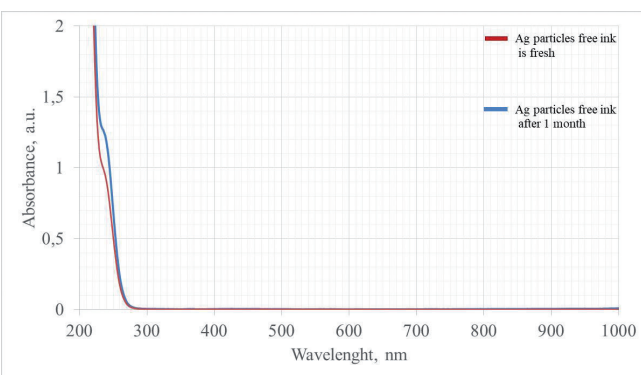

Fig. 2. *UV-visible absorption spectra of ink: 1 – freshly prepared, 2 – aged at room temperature for a month.*

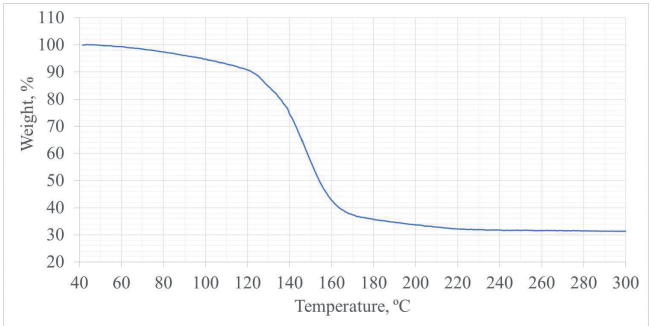

Fig. 3. *TGA curve of organic silver ink.*

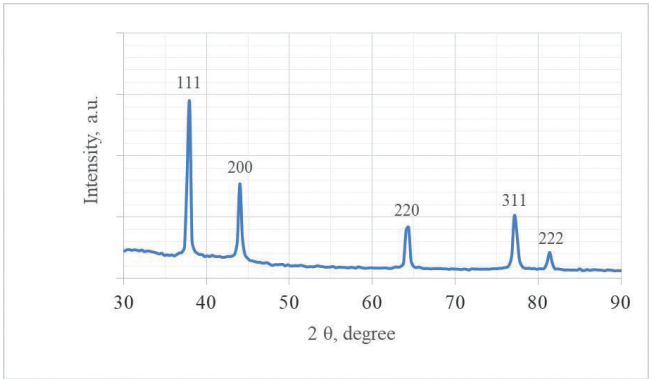

Fig. 4. *X-ray diffraction pattern of a silver film obtained upon annealing at 150°C.*

Chemical resistance is an indisputable advantage of the ink obtained in this study. In addition, the absence of silver particles in the composition of the liquid is an advantage for using this ink in inkjet technology, as this will eliminate the risk of clogging of the print head nozzles.

The thermal behavior of silver organic ink is shown in **Fig. 3**.

The TG curve shows two main stages of weight loss. First stage between 40°C and 120°C, corresponds to the evaporation of residual volatile components in the film: water, acetic acid and traces of alcohol. The second stage (120-165°C) is due to the decomposition of the silver oxalate-1,2-diaminopropane complex with the formation in the ink composition that is capable of destructing with the formation of a metal component at sufficiently low temperatures, in comparison with the decomposition temperature of silver oxalate. The recommended temperature for annealing is 150°C, because many polymer substrates cannot withstand higher temperatures.

The remaining metal phase must be of high purity in order to provide high electrical conductivity. To find this out, samples of annealed films were studied by *X*-ray phase analysis.

The diffraction pattern (**Fig. 4**) of the film formed at 150°C contains strong reflections at angles of 38.1°, 44.7°, 64.3°, 77.5°, and 81.2°, which correspond to the (111) planes, (200), (220), (311) and (222) silver crystals. These characteristic diffraction peaks confirm the single-phase composition of the sample, which is silver with a face-centered cubic structure.

Another important criterion that an ink must have is stability during the printing process.The ink obtained in this work has a suitable rheology for piezo inkjet printing on a Dimatix DMP machine (viscosity ~10 mPas, surface tension 33–35 mN/m, density 1 g/cm^3). The cartridges for your printer are designed for one-time refilling only, without the possibility of cleaning the print head nozzles with flushing liquids at the end of the printing process. Therefore, the ink is forced to remain in a closed system until it is completely used up.

After refilling the cartridge, the silver ink was in it for 24 hours and seven days with active use. Every day, observations were made of the appearance of the ink and the process of formation and departure of drops from the nozzles from the video camera was monitored in real time. It was

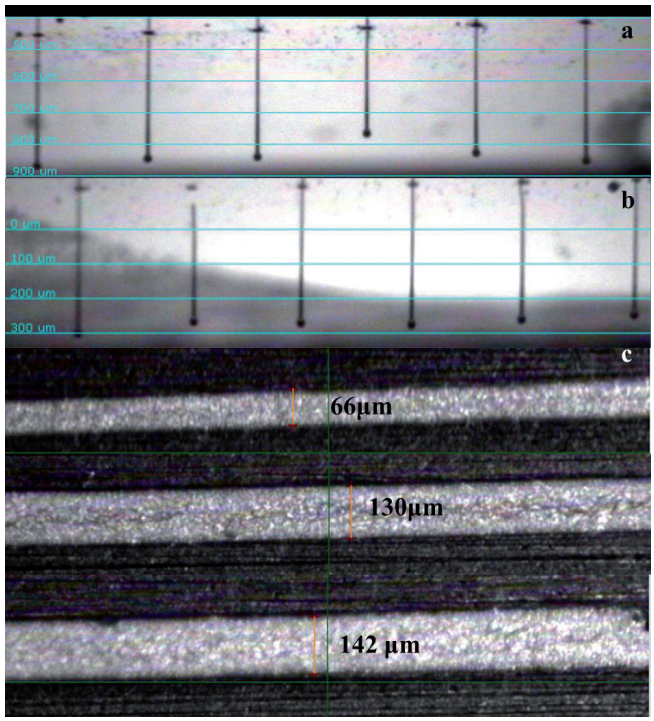

Fig. 5. *Departure of drops from the nozzles of the print head: a – the first day of printing, b – is the seventh day of printing. c – silver lines of various widths.*

noted that during the entire period the cartridge worked properly, the printing liquid remained invariably transparent and provided stable printing. On **Fig. 5***a,b* show photographs of droplet departures on the first and seventh days of printing. The droplets are round without satellites (satellite droplets) and are characterized by a straight projection. The printed lines (Fig. 5*c*) have clear edges, which also confirms the straightness of the droplets, the stable operation of the printing nozzles, and also indicates the satisfactory wettability of the surface of the polyimide material by liquid drops.

When the ink is annealed above 120°C, a rapid evolution of gaseous products is observed, which can contribute to the loosening of the silver film and the violation of its integrity. To ensure the maximum conductivity of the material, the annealed

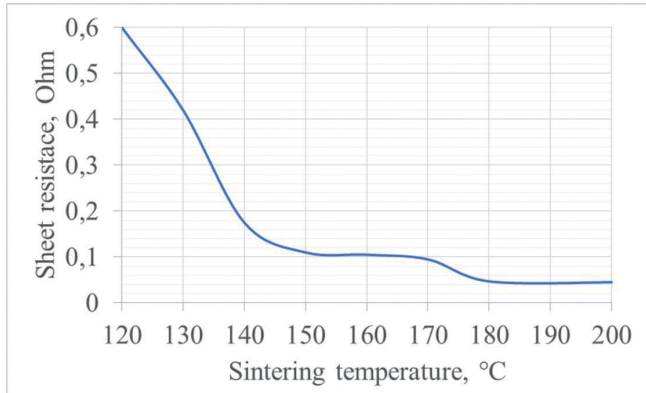

Fig. 6. *Surface resistance of silver films annealed at different temperatures.*

structures must be densely packed. In this regard, the heat treatment of the printed squares was carried out in a stepwise manner. First, the films were heated to 100°C, kept under these conditions for 5 min to remove volatile components, and then the heating temperature was increased to the required one (120-200°C) and annealed for another 30 min.

Fig. 6 describes the effect of sintering temperature on the surface resistance of the silver layer. There is a clear dependence of the resistance on the processing temperature. The higher the annealing temperature, the lower the resistance of the silver element. When films are sintered at 180°C and higher, the resistivity values differ little from each other.

Cured silver films annealed at 130°C, 150°C and 180°C were examined by SEM to study morphology and structure at the micro/nano scale. At the micro level, the surface of the films (**Fig. 7***a,b*), regardless of the annealing temperature, has an integral relief structure (multiple branched folds are found). The width and height of the folded formations lies in the range of 1-2.5 microns. The microphotographs

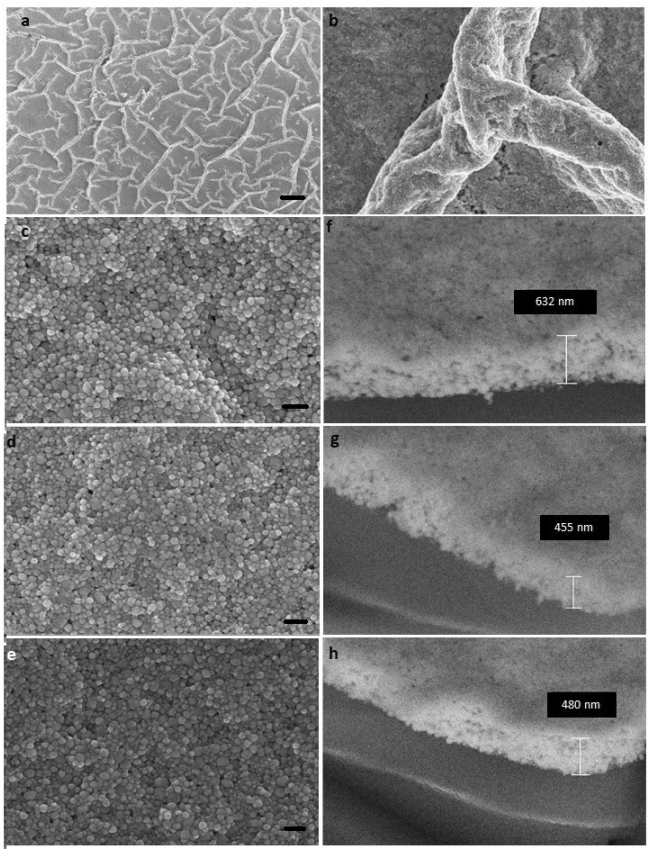

Fig. 7. *SEM images: a – surfaces of the hardened silver film on a microscale (reference 20 μm), b – folds; the surface of films on the nanoscale (reference 200 nm) annealed at different temperatures: c – 130°C, d – 150°C, e – 180°C; thickness of films annealed at f – 130°C, g – 150°C, h – 180°C.*

obtained at a higher resolution show that the structure of the silver films is formed by spherical nanoparticles (Fig. 7*c-e*), which are closely adjacent to each other. Their formation is due to the processes of nucleation and growth. The silver amino complex under the action of temperature (above 100°C) decomposes into ultra-small silver nuclei AgO, which, colliding with each other, form closely bound nanoparticles. These interconnected nanostructures provide many continuous channels for electron transport, which helps to reduce the resistance of the silver layer. Films have compact packing not only on the surface, but also in volume. The average height of

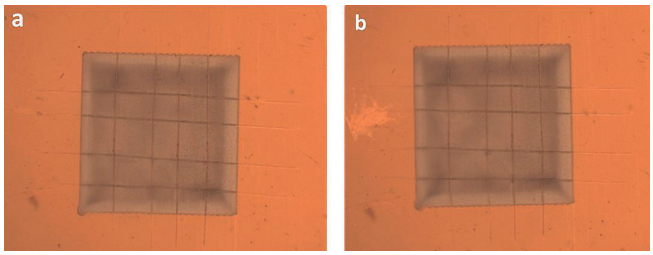

Fig. 8. *Photos of silver films: a – before and b – after tearing off the adhesive tape.*

the smooth sections of films annealed at 130°C is 650 nm, at 150°C and 180°C its value does not exceed 500 nm (Fig. 7*f-h*).

Taking into account the geometric parameters, the electrical resistivity of the silver printed elements was calculated. The obtained values allow us to conclude that the annealed printed structures are characterized by low values of resistivity. For films annealed at 130°C, 150°C and 180°C on PI they are 13 μOhm·cm, 8.5 μOhm·cm and 6.5 μOhm·cm, respectively.

On **Fig. 8** the results are showed of a test of thermoset films to determine the adhesion of silver to a polyimide film. After tearing off the adhesive tape, the edges of the cuts retained their previous appearance, the integrity of the film remained unchanged. This indicates that the silver structures annealed on polyimide have high adhesive properties, which correspond to the 5V scale.

The resulting organic ink retains long-term chemical stability for more than 1 month when stored at +25°C and more than 6 months at +5-10°C.

4. CONCLUSION

As a result of the study, a conductive organic ink based on a complex of silver-1,2-diaminopropane oxalate with a suitable rheology for inkjet printing was developed.

The carefully selected formula ensures the chemical resistance of the ink, which makes it easy to work with them at room temperature.

The successful choice of the complexing agent provided a decrease in the decomposition temperature of the silver precursor and the formation of a high-purity metal component at sufficiently low temperatures.

Silver oxalate-1,2-diaminopropane complex inks have potential as a low cost alternative to nanoparticle inks. They can provide high conductivity at low annealing temperatures (8.5 μOhm·cm at 150°C). The formula is particle free and has been shown to provide consistent inkjet printing.

Thus, the developed silver ink is an inexpensive and promising material for low-temperature fabrication of high-performance printed electronics.

REFERENCES

1. Dang MC, Nguyen DS, Dang TMD, Tedjini S, Fribourg-Blanc E. Design and testing of RFID sensor tag fabricated using inkjet-printing and electrodeposition. *Advances in Natural Sciences: Nanoscience and Nanotechnology,* 2014, 5(2):025012.
2. Ortego I, Sanchez N, Garcia J, Casado F, Valderas D, Sancho JI. Inkjet Printed Planar Coil Antenna Analysis for NFC Technology Applications. *International Journal of Antennas and Propagation*, 2012, 8:1-6. DOI: 10.1155/2012/486565.
3. Vasiliev AA, Kim VP, Tkachev SV, Kornilov DYu, Gubin SP, Vlasov IS, Sizov AS. Platinum Based Material for Additive Technology of Gas Sensors. *Proceedings,* 2018, 2(13):738. DOI: 10.3390/proceedings2130738.
4. Saidina DS, Zubir SA, Fontana S, Herold C, Mariatti J. Synthesis and Characterization of Graphene-Based Inks for Spray-Coating Applications. *Journal of Electronic Materials,* 2019, 48(9):5757–5770. DOI: 10.1007/s11664-019-07376-3.
5. Tkachev SV, Gubin SP, Kim VP, Kushnir AE, Kornilov DYu. The dispersions of nanoparticles in water-organic solvents as the basis for the silver nano-ink for inkjet printing. *RENSIT: Radioelectronics. Nanosystems. Information technologies*, 2016, 8(2):171-184.
6. Tiyyagura H, Majeric P, Bracic M, Anzel I, Rudolf R. Gold Inks for Inkjet Printing on Photo Paper: Complementary Characterisation. *Nanomaterials,* 2021, 11(3):599.
7. Rustamova EG, Kagirina MS, Gubin SP. Obtaining ink based on palladium nanoparticles for possible use in printed electronics. *RENSIT: Radioelectronics. Nanosystems. Information technologies,* 2022, 14(2):127-134. DOI: 10.17725/rensit.2022.14.127.
8. Asoro M, Kovar D, Damiano J, Ferreira P. Scale Effects on the Melting Behavior of Silver Nanoparticles. *Microscopy and Microanalysis,* 2010, 16(S2):1802-1803.
9. Cai Ya, Yao Xu, Piao X, Zhang Z, Nie Er, Sun Z. Inkjet printing of particle-free silver conductive ink with low sintering temperature on flexible substrates. *Chemical Physics Letters,* 2019, 737:136857. DOI:10.1016/j.cplett.2019.136857.
10. Mou Y, Zhang Y, Cheng H, Peng Y, Chen M. Fabrication of highly conductive and flexible printed electronics by low temperature sintering reactive silver ink. *Applied Surface Science*, 2018, 459:249-256. DOI: 10.1016/j.apsusc.2018.07.187.
11. Bhat KS, Ahmad R, Wang YS and Hahn Y-B. Low-temperature sintering of highly conductive silver ink for flexible electronics. *J. Mater. Chem. C,* 2016, 4(36):8522-8527. DOI: 10.1039/c6tc02751b.

12. Zope KR, Cormier D, Williams SA. Reactive Silver Oxalate Ink Composition with Enhanced Curing Conditions for Flexible Substrates. *ACS Appl. Mater. Interfaces,* 2018, 10(4):3830-3837. DOI: 10.1021/acsami.7b19161.
13. Bei Y, Cheng H, Zu M. Research Status and Prospects of Particle-Free Silver Conductive Ink. *Materials Science and Engineering,* 2018, 394(4):042060. DOI: 10.1088/1757-899X/394/4/042060.
14. Yang W, List-Kratochvil EJW, Wang C. Metal particle-free inks for printed flexible electronics. *J. Mater. Chem. C*, 2019, 7(48):15098-15117. DOI: 10.1039/c9tc05463d.
15. Dong Y, Li X, Liu S, Zhu Q, Li J-G, Sun X. Facile synthesis of high silver content MOD ink by using silver oxalate precursor for inkjet printing applications. *Thin Solid Films*, 2015, 589:381-387. DOI: 10.1016/j.tsf.2015.06.001.
16. Chang Y, Wang D-Y, Tai Y-L and Yang Z-G. Preparation, characterization and reaction mechanism of a novel silver-organic conductive ink. *J. Mater. Chem.*, 2012, 22(48):25296-25301. DOI: 10.1039/c2jm34569b.

DOI: 10.17725/rensit.2022.14.437

Information Technologies Based on Noise-like Signals: IV. Algorithmic Pseudo-random Number Generators Based on Dynamic Chaos

Vladimir I. Grachev, Viktor I. Ryabenkov, Anastasiya V. Surgay, Vladimir V. Kolesov

Kotelnikov Institute of Radioengineering and Electronics of RAS, http://www.cplire.ru/
Moscow 125009, Russian Federation

E-mail: grachev@cplire.ru, ryabenkov.vi@list.ru, ya.a1997@yandex.ru, kvv@cplire.ru

Received December 11, 2022, peer-reviewed December 15, 2022, accepted December 21, 2022

Abstract: **Numerical simulation is used to investigate the statistical, fractal and structural properties of sequences of integers generated by the algorithm with delay. It is shown that the statistical properties of the generated discrete sequences, close to a random process, are provided by such generating coding algorithms, in which both the one-dimensional probability distribution and the distributions of the conditional probabilities of the generated numbers are close to uniform. The structure of the phase space of a discrete coding algorithm with delay defined on a closed interval of integers is studied. It is established that the phase space consists of a finite number of cycles of different periods, the behavior of the system on which is pseudorandom. The possibility of creating generators of this type with more complex circuits is discussed. It is shown that with an appropriate choice of parameter values, the algorithm allows the formation of a non-periodic pseudo-random sequence of arbitrary given length for encoding information in telecommunication systems.**

Keywords: **information technology, chaotic dynamics, pseudorandom sequences, redundant codes, noise-like signals**

UDC 621.391

Acknowledgments: The work was carried out within the framework of the state task of the Kotelnikov IRE of RAS from the Ministry of Education and Science of the Russian Federation.

For citation: Vladimir I. Grachev, Viktor I. Ryabenkov, Anastasiya V. Surgay, Vladimir V. Kolesov. Information Technologies Based on Noise-like Signals: IV. Algorithmic Pseudo-random Number Generators Based on Dynamic Chaos. *RENSIT: Radioelectronics. Nanosystems. Information Technologies*, 2022, 14(3):437-462e. DOI: 10.17725/rensit.2022.14.437.

Contents

1. INTRODUCTION

Currently, in a number of science areas and technology, random and pseudo-random numbers are widely used in the process of solving practical problems. These areas include mathematical modeling, cryptography, information security in computers and telecommunications networks, as well as when encoding information in ultra-wideband radio systems. To solve these problems, it is necessary to generate random numbers huge arrays with a wide variety of properties. Of greatest importance for practice are numerical sequences with a uniform distribution law. The random numbers problem is that there is no algorithmic random number generator yet. If the resulting sequence obeys some algorithmic regularity, then by definition it is not random.

Thus, the main task of such an algorithm is to generate a sequence of numbers that, not being random, would be indistinguishable from random, would not have visible patterns. In this sense, algorithms are bad and good. Moreover, the quality of the algorithm, i.e. its ability to generate numerical sequences close in properties to random ones can be verified by methods of mathematical statistics.

One of the main elements in such systems are random and pseudo-random number generators (RNG and PRNG), the quality and speed of which significantly affect the results of solving the tasks. Currently, intensive fundamental work is being carried out in the field of generating random and pseudo-random numbers, and a large number of patents and inventor's certificates are being published, which indicate an ever-increasing interest in these areas. Pseudo-random sequence generators are used in numerous applications where sequences with properties similar in their statistical characteristics to random number series are needed. The sequences of numbers formed by such generators are calculated using deterministic algorithms, which was the reason to call them pseudorandom sequences (PRS) [1].

The characteristics of these sequences are subject to a variety of often specific requirements associated with the characteristics of their specific applications. Because of this, interest in the development of new algorithms that form such pseudo-random sequences, not only does not decrease, but rather grows. This is also due to the urgent need to protect information in systems and networks that are rapidly developing on a global scale for processing, storing and transmitting information [2]. The emergence of new ideas in this area, in particular, is associated with the development of ideas about the possibility of chaotic dynamics of deterministic systems even under the assumption that they do not contain any noise [3].

Despite the fact that quite a few algorithms for generating pseudo-random sequences (PRSs) are known, in practice, as a rule, a recurrent algorithm is used. Binary sequences based on recurrence relations are quite easily implemented on a computer in the form of programs and circuitry based on high-speed multi-bit binary shift registers. The known classes of PRS, both linear and non-linear, have certain disadvantages and do not satisfy all the necessary requirements. An alternative solution to the problem is the use of noise-like signals (NLS) generated by nonlinear systems with dynamic chaos. Such NLSs, having correlation properties no worse than those of M-sequences, have a practically unlimited set of lengths, can form ensembles of both binary and multilevel signals of large volumes and are non-linear, which makes it difficult to recognize them for subsequent playback in case of unauthorized access to the coded information [4].

On the basis of a mathematical model of a ring self-oscillating system with strong amplitude-phase nonlinearity, filtering and delay, a discrete generating algorithm for a

chaotic signal has been developed and studied, which belongs to the class of algorithms of a recurrent-parametric type with delay. The algorithm form of this class in general terms has the form of a discrete functional transformation (mapping):

$$x_n = f(x_{n-1}, x_{n-2}, ..., x_{n-Nz}),$$

where x_n are the members of the generated pseudo-random sequence at the n-th step, Nz is the delay parameter that determines the number of sequence members on the delay interval x_{n-1}, x_{n-2}, ..., x_{n-Nz}, which completely determine the new value of x_n and must be are given as the initial condition at the first step, and the function $f(x)$ reflects the amplitude and phase transformations in the generating ring self-oscillatory system in the chaos mode.

The algorithm is defined on the integers set M of the natural series belonging to the closed numerical interval [M1, M2], (M2 > M1, M = M2 – M1 + 1), and forms a practically uncorrelated pseudo-random sequence of integers with a probability distribution close to uniform, and correlation characteristics that meet the requirements for coding signals. The advantage of integer sequences is that they are identically reproduced on various types of computing devices and, when implemented in hardware, are easily reproduced in circuitry [5].

One of the simplest generators that form pseudo-random sequences are generators based on the Fibonacci algorithm, which are still used in practice [6].

In the Fibonacci algorithm, when calculating each next sequence member, several previously calculated previous members are used. This is the so-called generator with lagging arguments. As a rule, a limited numerical interval is used as the definition domain of the phase space in which the representing point of the system state moves. Due to the limitedness of the phase space determined by the dimension of the algorithm, taking into account the finite accuracy of the numbers representation, sooner or later, as a result of a successive calculations chain according to a given deterministic algorithm, the trajectory of the system in its phase space must close.

This means that the trajectory will enter a cycle, and then the calculation results will be repeated after some certain (although it may be very large) number of calculation steps, which is called the period.

When developing such algorithms, they seek to find conditions for obtaining numbers sequences that have the largest possible (largest) repetition period, and at the same time, on any arbitrary trajectory section, less than the period length, possessing the characteristics random numbers sequence. The advantage of class of the algorithms with delay is that, despite the great simplicity of computational operations, they allow us to study the patterns of sequences formation with large periods depending on the characteristic parameters of the algorithm (of the interval for determining the allowable numbers {1, M}, of the length of the delay Nz). The algorithm is supplemented by the returning rule a newly calculated number to in the specified interval in case of exit from it. This operation provides an important for chaotization mixing mechanism [7].

2. PSEUDO-RANDOM SEQUENCE OF INTEGERS GENERATED BY A ALGORITHM WITH DELAY AS A MARKOV PROCESS

The problem of protecting information in open information and computer networks from unauthorized access, as well as the task of increasing the noise immunity of telecommunication channels, are associated with the use of complex coding algorithms and noise-like signals with a large information capacity. Therefore, the development of complex coding algorithms and criteria for an objective assessment of their statistical properties is a rather urgent task.

As a test algorithm, we consider an algorithm with a delay based on a Fibonacci-type mapping. To restrict the definition domain of the algorithm to a finite closed integer interval [1, M], M > 1, the mapping is supplemented by the operation of converting the interval [1, M] into itself with "reflecting boundaries":

$$\begin{aligned} &\tilde{x}_n = x_{n-1} + (-1)^{x_{n-Kz}} \cdot x_{n-Nz}, \quad Kz \in [2,\ Nz-1], \\ &x_n \in [1,\ M], \\ &x_n = \tilde{x}_n, \quad if \quad \tilde{x}_n \in [1,\ M], \\ &x_n = \tilde{x}_n - M, \quad if \quad \tilde{x}_n > M, \\ &x_n = \tilde{x}_n + M, \quad if \quad \tilde{x}_n < 1. \end{aligned} \tag{2.1}$$

Here Nz is the delay parameter, it determines phase space (PS) dimension and the radius vector $R_n(x_{n-1}, x_{n-2}, \ldots, x_{n-Nz})$ of this discrete dynamic system (DDS) state in this space. The number of possible states in the PS is finite and equal to M^{Nz}. Depending on the initial conditions $R_0(x_{-1}, x_{-2}, \ldots x_{-Nz})$, DDS (2.1) at each step of the algorithm describes one or another "trajectory" in the PS, which are sequential discrete transitions from one state point to another according to pseudorandom law (**Fig. 2.1**). Due to the limited scope of the PS, these trajectories form closed cycles, which, due to the uniqueness of the transformation (2.1), do not intersect and have no common points. All PS points belong to only one cycle or an isolated point with coordinates (M,M,… M). So, for example, with M = 5, Nz = 4, Kz = 3, the PS of the algorithm has one 562-stroke cycle, two cycles with a period T = 27, one 8-stroke cycle, and one singular point. At Nz = 5, Kz = 3 and M = 13 (M^{Nz} = 371293) there are cycles in the PS with periods T = 332373, 21721, 7966, 4959, 3640, and at Nz = 6, Kz = 4 and M = 15 one " long" cycle with period T = 11099897 includes the vast majority (0.974 M^{Nz}) of the PS points.

The cycles of the algorithm (1.1) have an important distinctive feature: the behavior of the dynamic system on the cycle before its closure (and we will be interested in processes just before the cycle is closed) has a random, chaotic character (Fig. 2.1). In this case, the non-periodic sequence {xn} generated by the algorithm is of a pseudo-random type. The set of points of states of a dynamic system in an PS, united in such a cycle, called a pseudo-random cycle. In contrast to the regular cycle, which corresponds to regular motion in the phase space before the cycle closes. An example of a simple regular cycle ($x_n = x_{n-3} + 2$ with the transformation of the interval [1,21] into itself) is shown in Fig. 2.1*b*. Thus, a pseudo-random cycle is a finite set of seemingly chaotic, but successive points of states of a discrete dynamical system in the phase space of the algorithm in a strictly deterministic way.

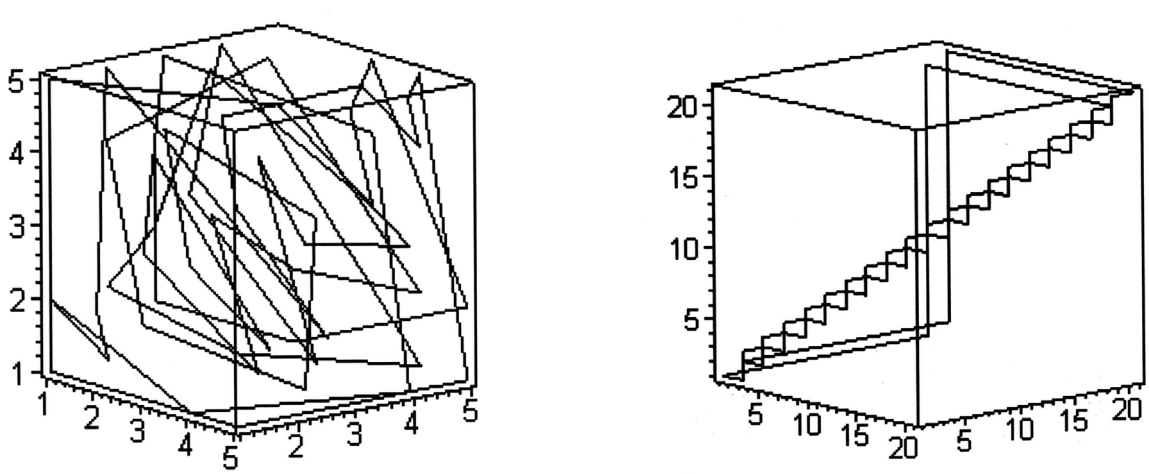

a *b*

Fig. 2.1. *Phase portrait of a signal with closed a) pseudo-random cycle, b) regular cycle.*

For practical applications, non-periodic pseudo-random sequences of great length are of the greatest interest. With an appropriate choice of parameters of the algorithm (2.1) and initial conditions, the segment of the non-periodic PRS, generated by the algorithm on a pseudo-random cycle before the system exits for a period, can be arbitrarily long and, as analysis has shown, in terms of its statistical properties, it is close to a sequence with a uniform probability distribution of the generated numbers $p(x)$. So, at the algorithm definition domain interval [1,63] (M = 63) and the delay Nz = 3, the length of the non-periodic SRP is $N = 7.8317 \cdot 10^4$, at Nz = 5 $N = 3.3174 \cdot 10^8$, at Nz = 7 $N = 1.676 \cdot 10^{12}$, at Nz = 9 the length of the non-periodic PRS is more than $5 \cdot 10^{12}$.

Note that the discrete PRS with discrete numbers $\{x_n\}$ is close in its form to the sequence of tests of the classical probability theory. Each transition in this sequence from the number xn to the next number x_{n+1}, as well as to the number x_{n+s} after s steps of the algorithm, is completely determined due to the determinism and uniqueness of the process (2.1). However, to an outside observer, it is no different from a process of random testing. Abstracting, therefore, from the determinism of process (2.1), we show that the sequence formed by it, with an appropriate choice of algorithm parameters, can be very close to a random sequence of Markov type and, moreover, to a random sequence of independent equally probable events.

As is known, a Markov process is a process without a probabilistic aftereffect, when the conditional probability for all $t > t_0$ is uniquely determined by the value of x_0 taken at the moment t_0 and does not depend on the previous history [8]. For a discrete sequence with discrete values x_n – a simple Markov chain, this means that there is a probability $p(x_j, n \mid x_i, k)$ of transition from any of the process values x_i at the k-th trial to any value x_j at the n-th trial ($n > k$, $i,j = 1, 2, \ldots, M$) [9]. In a particular case of a sequence of independent trials, the probability of transition to the state x_j coincides with the probability of this state in the nth trial $p(x_j, n \mid x_i, k) = p(x_j)$ regardless of the results of other trials. For a homogeneous Markov chain, the transition probabilities depend only on the number of steps $s = n - k$ between trials $p(x_j, n \mid x_i, k) = p(x_j, \mid x_i, s) = p_{ij}(s)$. The values $p_{ij}(s)$ form a matrix π_s of transition probabilities in s steps. For a homogeneous chain, the relation (Markov equation) [10] must be satisfied: $\boldsymbol{\pi}_s = (\boldsymbol{\pi}_1)^s$, i.e. transition probabilities in s steps are expressed in terms of transition probabilities in one step.

Consider algorithm (2.1). At first glance, the sequence generated by this algorithm with delay is not a process without aftereffect. Further more, each new value of the PRS is determined by the prehistory from the Nz values of the delay adopted at the previous stages. On the other hand, the operation of "transforming a numerical interval into itself" sort of breaks this connection (without violating the uniqueness of the process in the forward direction, but making it irreversible) with each ejection of a new number beyond the interval boundaries [1,M]. Let us check whether the relation $\pi_s = (\pi_1)^s$ is valid for the PRS formed by algorithm (2.1). That is, to what extent this sequence corresponds to the Markov equation. The assumption about the homogeneity of the process $\{x_n\}$ is quite natural if there is preliminary information about the closeness of the probability distribution $p(x)$ to the uniform one.

To visualize the results, we will carry out a numerical experiment for algorithm (2.1) with small values of parameters, but with the presence in the phase space (PS) of a pseudo-random cycle with a period sufficient to non-periodic sequence generate with the number of terms N, which providing the array necessary for statistical processing. Let M = 3, Nz = 9, Kz = 5, i.e. the algorithm has a 9-dimensional phase space and a definition domain of three numbers. In this case, there is a long cycle in the PS with a period T = 19677 with a total volume of the PS equal to $M^{Nz} = 19683$. The probability distribution of the

numbers $p(x)$ in the sequence generated by the algorithm is almost uniform with a root-mean-square deviation from this law equal to $4.8\cdot10^{-5}$, and the maximum deviation modulo $6.8\cdot10^{-5}$.

Based on the implementation of the PSP generated by the algorithm with length $N = 19677$, we determine the probabilities $P(A)$ of generating the number x_i (i = 1, 2, ..., M) by counting the occurrences of event A equal to $n(x_i)$: $P(A) = n(x_i)/\mathrm{N}$. Following the definition of conditional probability according to Kolmogorov: $P(B \mid A) = P(AB)/P(A)$, where $P(AB)$ is the probability of the simultaneous occurrence of events A and B. In the implementation of N tests, we will count the number of $n(x_j, x_i, s)$ that occurred simultaneously events A (generation of the number x_i) and B (transition from this number through s steps of the algorithm to the number x_j). Then the probability $P(AB) = n(x_j, x_i, s)/(N - s)$, and the conditional probability $P(B \mid A) = [\mathbf{n}(x_j, x_i, s)/(N - s)]/[n(x_i)/N] = p_{ij}(s)$. The transitions matrix $\boldsymbol{\pi}_s = \|p_{ij}(s)\|$. For a sequence of independent equally probable events, all $p_{ij}(s) = 1/\mathrm{M}$ and the corresponding transitions probability matrix will be denoted by $\boldsymbol{\pi}_0$.

When analyzing the PRS implementation with length $N = 19677$, the following transition matrices were obtained:

$$\pi_1 = \begin{pmatrix} 0.33335 & 0.33335 & 0.33335 \\ 0.33325 & 0.33340 & 0.33340 \\ 0.33320 & 0.33350 & 0.33320 \end{pmatrix},$$

$$\pi_2 = \begin{pmatrix} 0.33321 & 0.33352 & 0.33337 \\ 0.33326 & 0.33342 & 0.33342 \\ 0.33315 & 0.33337 & 0.33321 \end{pmatrix}, \ldots,$$

$$\pi_{20} = \begin{pmatrix} 0.33321 & 0.33382 & 0.33382 \\ 0.33342 & 0.33357 & 0.33372 \\ 0.33330 & 0.33367 & 0.33376 \end{pmatrix}.$$

The establishment of this fact alone, that all probabilities of transitions $p_{ij}(s) = p(x_j, \mid x_i, s) = p(x_j, n \mid x_i, \mathrm{k})$ exist, is already sufficient to consider this process as a Markov one [11]. In addition, we see that all matrix elements are very close to the equiprobable value $p_{ij} = 1/\mathrm{M} = 1/3$. At this, since the sum of the elements of each row of matrices π_s is equal to one, these matrices are stochastic [12]. The largest difference between the Euclidean norms of the matrices π_s from unity was less than 10^{-5}.

We will evaluate the validity of equality (2.2) for the PRS under study based on the calculation of the rms deviation of the elements of the matrices $\boldsymbol{\pi}_s$ and $(\boldsymbol{\pi}_1)^s$:

$$\sigma_S = \sqrt{(1/M^2)\sum_{i,j=1}^{M}(p_{i,j}(s) - p_{i,j}^{(s)}(1))^2} = \\ = (1/M)\cdot\|\Delta\pi_s\|, \qquad (2.2)$$

where $\|\boldsymbol{\Delta\pi}_s\|$ is the Euclidean norm of the matrix $\boldsymbol{\Delta\pi}_s = \boldsymbol{\pi}_s - (\boldsymbol{\pi}_1)^s$, and $p_{ij}(s)$ (1) are the elements of the matrix $(\boldsymbol{\pi}_1)^s$.

The obtained numerical values of σs are plotted on the graph in **Fig. 2.2** (curve 1*a*). We see that the differences of the matrix elements in the left and right parts of (2) for all transition intervals s = 1, 2, …, 20 are less than $4\cdot10^{-4}$ in absolute value or about 10^{-3} in relative value. This result shows that the tested sequence generated by algorithm (2.1) with delay can be considered as very close to a Markov process. More over, as the analysis of the proximity of the transitions matrices $\boldsymbol{\pi}_s$ to the matrix $\boldsymbol{\pi}_0 = \|p_{ij} = 1/\mathrm{M}\|$ shows, this sequence for the given values of the parameters M and Nz practically does not differ from the independent equiprobable

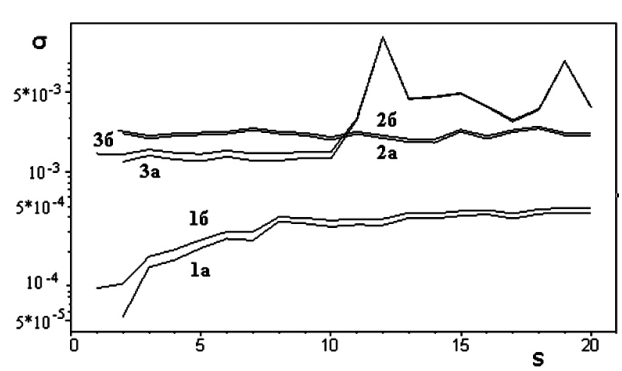

Fig. 2.2. *Root-mean-square deviation of matrix elements* $\boldsymbol{\pi}_s$ *and* $(\boldsymbol{\pi}_1)^s$.

tests sequence. Indeed, characterizing the difference between the matrices $\boldsymbol{\pi}_s$ and $\boldsymbol{\pi}_0$ by the rms deviation of their elements:

$$\sigma_O = \sqrt{(1/M^2)\sum_{i,j=1}^{M}(p_{i,j}(s)-1/M)^2} = (1/M)\cdot\|\Delta\pi_0\|, \quad (2.3)$$

where $\|\boldsymbol{\Delta\pi}_0\|$ is the norm of the matrix $\boldsymbol{\Delta\pi}_0 = \boldsymbol{\pi}_s - \boldsymbol{\pi}_0$, we plot the values of σ_0 obtained in the numerical experiment for s = 1, 2, …, 20 on the graph of Fig. 2.2 (curve 1*b*). We see that the differences transition matrices elements $p_{ij}(s)$ from the values of 1/M upon all analyzed transitions s do not exceed the level of $5\cdot10^{-4}$ or, in relative terms, about 0.1%.

Similar calculations were performed in the analysis of the transition matrices for the PRS of algorithm (2.1) with the parameters M = 9, Nz = 9, Kz = 5, i.e., with a definiton domain of nine numbers and a PS with a volume of 387420489 points of states. The length of the studied implementation of the PRS with the initial vector R_0(1, 1, …, 1) was chosen to be N = 180000. The probability distribution of the generated numbers $p(x)$ is close to uniform with a root-mean-square deviation from this law equal to $6.42\cdot10^{-4}$ and a maximum deviation modulo $1.45\cdot10^{-3}$. Differences in the elements of the transitions matrices $\boldsymbol{\pi}_s$ and $(\boldsymbol{\pi}_1)^s$, as well as the matrices $\boldsymbol{\pi}_s$ and $\boldsymbol{\pi}_0$, are shown by graphs 2*a* and 2*b* in Figs. 2.2. The values of the root-mean-square deviation, as it follows from the constructed dependencies, are at the level $\sigma = 2\cdot10^{-3}$, i.e. less than 1% in relative value. This also testifies in favor of making a conclusion about the closeness of the generated pseudo-random process to the Markov chain and to the sequence of independent equiprobable trials.

Curves 3*a* and 3*b* in Fig. 2.2 refer to the case of the PRS formed by algorithm (2.1) with the following parameters: M = 9, Nz = 5, Kz = 3. This variant differs from the previous case by a smaller magnitude of delay. In PS of algorithm presented cycles with periods T = 55070, 3230, 260, 130, 50. The longest pseudo-random cycle with the initial vector R_0(1, 1, …, 1) was taken for numerical analysis. The length of the studied implementation of the PRS is N = 55070. The probability distribution of the generated numbers $p(x)$ is close to uniform with a standard deviation from this law of $7.3\cdot10^{-4}$, and a maximum deviation modulo $1.05\cdot10^{-3}$, which practically does not differ from the degree of closeness to a uniform distribution of generated numbers in the previous test sequence.

Indeed, as studies have shown, the probability distribution function tends to improve as the delay parameter, and hence the dimension of the algorithm, increases, i.e. to approximation to a uniform law, but for Nz of the order of 6 and more, the density of distribution $p(x)$ practically does not differ from this law. As evidenced by the course of curves 3*a* and 3*b*, the transitions matrices $\boldsymbol{\pi}_s$ and $(\boldsymbol{\pi}_1)^s$, as well as the matrices $\boldsymbol{\pi}_s$ and $\boldsymbol{\pi}_0$ differ little over the transition intervals s = 1, 2, …, 10, but over large intervals s = 12, 13, …, the differences in matrices increase to units of percent. This computer experiment confirms that knowledge about the uniformity of the probability distribution of the occurrence of numbers $p(x)$ is still not enough to estimate the PRS as close to a sequence of independent tests. It is important that and all distributions of conditional probabilities $p(x_j, n \mid x_i, k)$ be uniform. Comparison of the course of graphs 2 and 3 in Fig. 2.2 shows that an increase in the delay from Nz = 5 to Nz = 9 leads to an improvement in the statistical characteristics of the pseudo-random process generated by the algorithm, bringing them closer to the characteristics of a Markov chain and a sequence of independent equiprobable events.

Note that the determination of matrices of probabilities transitions for large values of the parameter M requires processing large numerical arrays, therefore, for express analysis of the statistical quality of the generated PRSs, it is quite acceptable, as is known, to construct simplified transition matrices that inform only whether the probabilities of transition of $p_{ij}(s)$ are different from zero or not. The construction

of such matrices is possible when analyzing implementations that are not necessarily large in length. Herewith, not all matrics cells may turn out to be correctly filled: for large values of M and insufficient length N of the analyzed PRS ($N < s \cdot M^2$), such a matrix, even for processes with all nonzero $p_{ij}(s)$, has the form of a uniformly filled "starry sky". Nevertheless, consideration of the form of transitions matrices $p_{ij}(s)=, \neq 0$ sequentially in number s, gives important information about the quality of discrete process under study.

A process with a delay is a process with an aftereffect. However, the introduction of the operation of converting the interval [1,M] into itself into the algorithm breaks this aftereffect at each step when the number x_n goes beyond the boundaries of this interval. Herewith, the pseudo-random sequence formed by algorithm (2.1), with an appropriate choice of algorithm parameters, can actually be considered as a process without aftereffect, i.e., as a simple homogeneous Markov chain with probabilities of transitions $p_{ij}(s) \approx 1/M$. It is shown that with an appropriate choice of algorithm parameters and initial conditions, under which the difference between the transitions matrices $\boldsymbol{\pi}_s$ and $(\boldsymbol{\pi}_1)^s$ becomes noticeable, the statistical properties of the generated PRS worsen compared to a purely random process, even if herewith the probability distribution $p(x)$ is practically uniform.

3. PRS COMBINED GENERATOR

In [13], the characteristics of pseudo-random sequences defined on a limited interval of integers, formed by the simplest algorithms such as the Fibonacci algorithm, are proposed and studied. Expressions are given, as well as a method for calculating the maximum period TM, Nz of the PRS for a standard Fibonacci-type generator, depending on the interval of integers {1,M} and the delay parameter (dimension of the phase space) Nz. Knowing the exact value of the maximum period TM, Nz makes it possible to combine two generators, to significantly improve the statistical properties in such a way that the PRS period becomes many times greater than the period of each individual partial generator. The work of each such generator is performed in accordance with the algorithm for generating and returning a newly calculated value to the definition domain {1, M}

$$X_n = X_{n-1} + X_{n-Nz}, \quad X_n = X_n - M \text{ for } X_n > M. \tag{3.1}$$

The definition domain {1, M} and the delay Nz are different for each of the partial generators. The combined PRS generator functions as follows: two partial generators operate synchronously and the numbers generated by them at each step are added, generating a new sequence. If the result of addition is outside the interval {1, M_0}, then the return algorithm is switched on, similar to (3.1). The above can be written as:

$$\begin{aligned} &X_{1,n} = X_{1,n-1} + X_{1,n-Nz1} \rightarrow \\ &\rightarrow X_{1,n} = X_{1,n} - M_1 \text{ for } X_{1,n} > M_1; \\ &X_{2,n} = X_{2,n-1} + X_{2,n-Nz2} \rightarrow \\ &\rightarrow X_{2,n} = X_{2,n} - M_2 \text{ for } X_{2,n} > M_2; \\ &X_{0,n} = X_{1,n} + X_{2,n} \rightarrow \\ &\rightarrow X_{0,n} = X_{0,n} - M_0 \text{ for } X_{0,n} > M_0. \end{aligned} \tag{3.2}$$

In accordance with the results of [6], in order to obtain the maximum period, it is necessary to set the initial conditions (IC) as a sequence of Nz units. Then, if $Nz_1 > Nz_2$, then for the 1st generator, in order to achieve the maximum period, IC – a sequence of Nz_1 units. And the 2nd generator as a IC, respectively, has Nz_2 units. The numbers missing to start the operation of the combined generator algorithm ($Nz_1 - Nz_2$) must first be calculated using the algorithm of the 2nd partial generator. Thus, for the combined generator, the ICs are actually Nz_1 of numbers, and the first Nz_2 of them are equal to 2. Therefore, the ICs for the combined generator will be repeated and the sequence generated by it will reach the period (T_0) when exactly (and simultaneously) the ICs are repeated for each

from partial generators. The corresponding condition can be written as:

$$N_1 T_{M1,Nz1} = N_2 T_{M2,Nz2} = T_0, \quad (3.3)$$

where N_1 and N_2 are integers. Thus, T_0 must be divisible by $T_{M1,Nz1}$ and $T_{M2,Nz2}$ without remainder and, therefore, the maximum value for T_0 is determined by the product $(T_{M1,Nz1})(T_{M2,Nz2})$ and to achieve this value it is necessary that $T_{M1,Nz1}$, $T_{M2,Nz2}$ would have no common the comultipliers and, moreover, would be multiples.

Knowing the dependence of the PRS period on the maximum value in the definition domain of M and of the delay Nz, it is possible to choose such M_1, Nz_1 and M_2, Nz_2 that the period of the combined oscillator will significantly exceed the periods of the partial oscillators $T_{M1,Nz1}$ and $T_{M2,Nz2}$. In the case of small periods, this can be checked fairly easily. For example, $T_{3,2} = 8$ and $T_{4,3} = 14$. The smallest number that is divisible by 8 and 14 without a remainder is 56. It is this value that is obtained as a result of direct generation; $T_{15,7} = 97655$, $T_{17,8} = 83520$, the period of the generated numbers sequence for the combined generator is 1631229120, which is much larger of each as periods of the partial generators. As an example in **Fig. 3.1** shows the frequency distribution of the appearance of integers in the PRS for the combined generator in the definition interval {1,257}, while the partial generators parameters are as follows: $M_1 = 257$, $Nz_1 = 11$, $M_2 = 253$ and $Nz_2 = 15$. This distribution was obtained for an array of 10^9 numbers, the maximum value is 3896607, the minimum is 3885514, the difference between them is 11093 and the difference referred to the maximum value is 0.0028; average value ~$3.89 \cdot 10^6$; rms deviation ~$1.89 \cdot 10^3$. The given frequency distribution of integers is close to uniform according to statistical criteria.

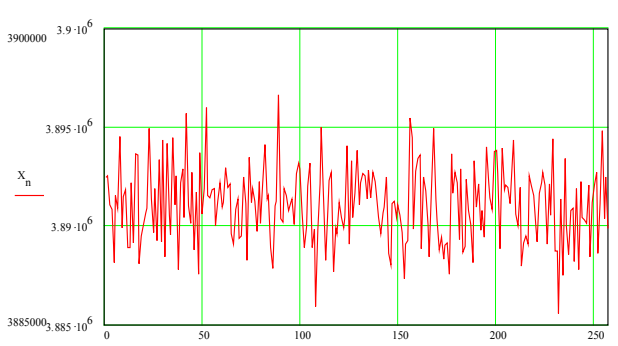

Fig. 3.1. *Distribution of the appearance of integers in the PRS for the combined generator in the definition interval {1,257}.*

The proposed algorithm and its characteristics are of methodological interest, since to obtain a period of arbitrarily long duration, the number of master oscillators can be increased, and X_{0n} can be a linear combination of the numbers X_n with weight coefficients C_n different from unity for each of the partial generators, i.e.

$$X_{0n} = \sum_{i=1}^{N} C_{in} X_{in}. \quad (3.4)$$

4. CHAOTIC ENCODING ALGORITHM BASED ON TWO-DIMENSIONAL MAPPING

A one-dimensional algorithm of the Fibonacci random number generator type $x_n = f(x_{n-1},\ldots, x_{n-Nz}, Nz, M)$ [13] was chosen as the basic discrete algorithm. General view of the two-dimensional algorithm under study:

$$\begin{aligned} x_n &= f_1(x_{n-1},\ldots,x_{n-Nz1}, y_{n-1},\ldots,y_{n-Nz2}, Nz1, Nz2, M), \\ y_n &= f_2(y_{n-1},\ldots,y_{n-Nz2}, x_{n-1},\ldots x_{n-Nz1}, Nz1, Nz2, M). \end{aligned} \quad (4.1)$$

The definition domain of the algorithm is a closed interval of integers [1, M]. In the process of generating the sequence, when the numbers x_n, y_n left the interval [1, M], the transformation of refund $x_n \rightarrow x_n \pm M$ and $y_n \rightarrow y_n \pm M$ was applied.

The phase space (PS) of the algorithm has the dimension (Nz_1+Nz_2). The number of system states in this space for an algorithm certain on a bounded discrete set is finite and equal to $\mathbf{M^{(Nz1+Nz2)}}$. Since each system state is certain on a finite and limited numbers set and the explicit form of the algorithm is a unambiguous mapping, the system will sooner or later fall into the initial state and the process will become periodic. Until leaving for the

period, the generated sequence, as showed by the numerical experiment, is pseudo random. The appearance of a period in the sequence $\{\mathbf{x}_n\}$, as well as in the sequence $\{\mathbf{y}_n\}$, is realized in the case of simultaneous exact repetition of complete initial conditions sets from the delayed members $(\mathbf{x}_{n-1}, \ldots, \mathbf{x}_{n-Nz1})$ and $(\mathbf{y}_{n-1}, \ldots, \mathbf{y}_{n-Nz2})$.

The study of the structure PS of the algorithm was carried out in the accessible for numerical analysis range of parameters M, Nz_1, Nz_2: $\mathbf{M^{(Nz1+Nz2)}} \le 10^6 \div 10^7$. **Tables 1** and **2** show the results of studying the structure PS of the algorithm for odd (M = 3) and even (M = 4) values of the parameter M in comparison with the cycles spectra of the basic one-dimensional algorithm with the corresponding parameter values.

In Tables 1 and 2, the cycles number of same period is indicated in round brackets.

The PS of the algorithm under study consists of a set of cycles of different multiplicity and length and one special isolated point with coordinates (M, M, ..., M). It can be seen from Table 1 that for odd M all cycles have a single multiplicity, just like in the PS of the basic algorithm. At the same time, there is no obvious regularity between the cycles sizes in the PS of the compared algorithms. The size of the largest cycle is ~0.5 of the total number of states in the phase space $\mathbf{M^{(Nz1 + Nz2)}}$.

Table 1

Nz = 3	18, 8, 1	$\mathbf{M^{Nz}} = 27$
Nz = 4	44, 29, 7, 1	$\mathbf{M^{Nz}} = 81$
Nz = 5	118, 70, 22, 16, 13, 3, 1	$\mathbf{M^{Nz}} = 243$
Nz = 6	457, 100, 61, 31, 28, 26, 25, 1	$\mathbf{M^{Nz}} = 729$
$Nz_1 = 4$ $Nz_2 = 3$	1258, 351, 270, 88, 26, 1	$\mathbf{M^{(Nz1+Nz2)}} = 2187$
$Nz_1 = 5$ $Nz_2 = 3$	3614, 862, 798, 645, 496, 70, 16, 1	$\mathbf{M^{(Nz1+Nz2)}} = 6561$
$Nz_1 = 5$ $Nz_2 = 4$	8789, 5677, 2725, 1391, 613, 207, 39, 1	$\mathbf{M^{(Nz1+Nz2)}} = 19683$
$Nz_1 = 6$ $Nz_2 = 4$	24844, 23261, 5908, 2781, 400, 1	$\mathbf{M^{(Nz1+Nz2)}} = 59049$

Table 2

Nz = 3	14(4), 7, 1	$\mathbf{M^{Nz}} = 64$
Nz = 4	30(8), 15, 1	$\mathbf{M^{Nz}} = 256$
Nz = 5	42(22), 21, 14(4), 7, 6(2), 3, 1	$\mathbf{M^{Nz}} = 1024$
Nz = 6	126(32), 63, 1	$\mathbf{M^{Nz}} = 4096$
$Nz_1 = 4$ $Nz_2 = 3$	186(68), 93, 62(8), 31, 1	$\mathbf{M^{(Nz1+Nz2)}} = 16384$
$Nz_1 = 5$ $Nz_2 = 3$	60(544), 30(8), 15, 1	$\mathbf{M^{(Nz1+Nz2)}} = 65536$
$Nz_1 = 5$ $Nz_2 = 4$	465(412), 31(3), 1	$\mathbf{M^{(Nz1+Nz2)}} = 262144$
$Nz_1 = 6$ $Nz_2 = 4$	84(1149), 42(43), 21, 14(4), 1	$\mathbf{M^{(Nz1+Nz2)}} = 1048576$

For even values of M (Table 2), the cycles in the PS are usually short and multiple, as in the case of the basic algorithm. Cycles spectra of the two-dimensional algorithm with parameters Nz_1 and Nz_2 do not contain cycles of partial basic algorithms with $Nz = Nz_1$ and $Nz = Nz_2$, but have basic algorithm cycles with $Nz = (Nz_1 + Nz_2)/2$ with addition doubled period cycles. In this case, the main periods of cycles of the two-dimensional algorithm differ by an integer number of times from the fundamental period in each of the cycles series: for example, with $Nz_1 = 4$, $Nz_2 = 3$, the spectrum of cycles is 31 (fundamental period), 62, 93, 186. Such a character of the cycles spectrum is also characteristic of the one-dimensional algorithm for even values of M.

Table 1 shows that the cycles size of the greatest length of the two-dimensional algorithm is almost two orders of magnitude larger than the cycle size of the corresponding one-dimensional algorithm for $Nz_1 = Nz$. But this gain is due not so much to the specific two-dimensional mapping features compared to the one-dimensional analog, but to a real increase in the PS dimension. The ratio between the cycle length of the maximum size and the full number of states in the PS remains the same ~0.5.

The statistical characteristics evaluation should be carried out not at small, but at real, i.e. relatively large parameters values corresponding to developed chaos and the formation of long pseudo-random sequences with good correlation properties. Therefore, the calculations were performed with parameters M = 255, $Nz_1 = 16$,

$Nz_2 = 11$. It is shown that the two-dimensional algorithm generates a pseudo-random sequence with an almost uniform probability distribution $p(x) = 1/M$. For a sequence segment with $N = 210000$, the difference from this distribution is: relative average difference modulo $\Delta\mathbf{p}_{av} = 0.028$ at maximum $\Delta\mathbf{p}_{max} = 0.10$, rms $\boldsymbol{\sigma} = 0.002$.

The evaluation of the correlation characteristics of the generated sequences was carried out on the basis of the analysis of 100 pairs of unclipped and clipped segments of 128 and 1024 symbols, sequentially generated by the algorithm without any selection, including without selection by code balance. It was found that the emissions level of auto- and cross-correlation functions did not exceed following values: $(1.5\div4.8)/\sqrt{N}$ for segments with $N = 128$ and $(2.5\div4.9)/\sqrt{N}$ for segments with $N = 1024$, which consistent with the appropriate level side emissions of purely random sequences correlation functions with uniform distribution, and sequences generated by basic algorithm.

Counting blocks of identical symbols at the clipped sequence implementation of 270,000 numbers showed that the appearance probability of such blocks completely obeys the law $\mathbf{p(k) = 1/2^k}$ up to a block of size $\mathbf{k} = 12$ with insignificant differences from this law for blocks of $\mathbf{k} = 13\div18$ characters. The latter differences are due more to the data insufficiency for results statistical processing than the properties of the algorithms themselves.

The evaluation of the signals system volume generated by the two-dimensional and basic algorithms was estimated by selecting balanced codes with specified correlation properties from the generated clipped sequence. It is shown that for the same sequence implementation lengths, the selected codes number and rate of their selection are close for both compared algorithms.

The phase space structure of two-dimensional algorithm is analyzed. The periods spectrum of cyclic trajectories in phase space is found, which differ in initial conditions. It has been established that the pseudo-random sequences statistical properties generated by basic discrete algorithm and algorithm with a two-dimensional mapping are close with comparable parameters. However, the two-dimensional algorithm has an increased complexity, which greatly complicates its reconstruction based on the implementation of generated by the algorithm sequence.

5. METHODS OF CHAOTIC ALGORITHMS FRACTAL ANALYSIS

For the chaotic signals effective implementation in radio engineering complexes, telecommunication systems, as well as for their use as an information carrier in new generation information technologies, along with conventional methods for studying statistical and correlation characteristics, it is necessary to develop alternative estimate methods of algorithm structural complexity and PRS fractal dimension. [14].

The fractal analysis methods of random number generators currently include the determination of dynamic systems fractal dimensions, computer processing of both the these systems trajectory in phase space (PS), and formed by system of processes in projections on plane in the PS and on coordinate axes. In the latter case, we are talking about the study of the properties of the sequence directly generated by the algorithm.

For the fractal processing algorithms effective application, it is necessary to represent an algebraic object – a numbers sequence or signs in form of a graphic image. As geometric images that characterize the chaotic algorithms properties, you can choose a step-by-step mapping on plane of the recurrent sequence members (**Fig. 5.1**a), the two-dimensional section of chaotic algorithm multidimensional phase space (Fig. 5.1b), as well as the projection of the chaotic algorithm multidimensional phase space onto one of coordinate planes with or

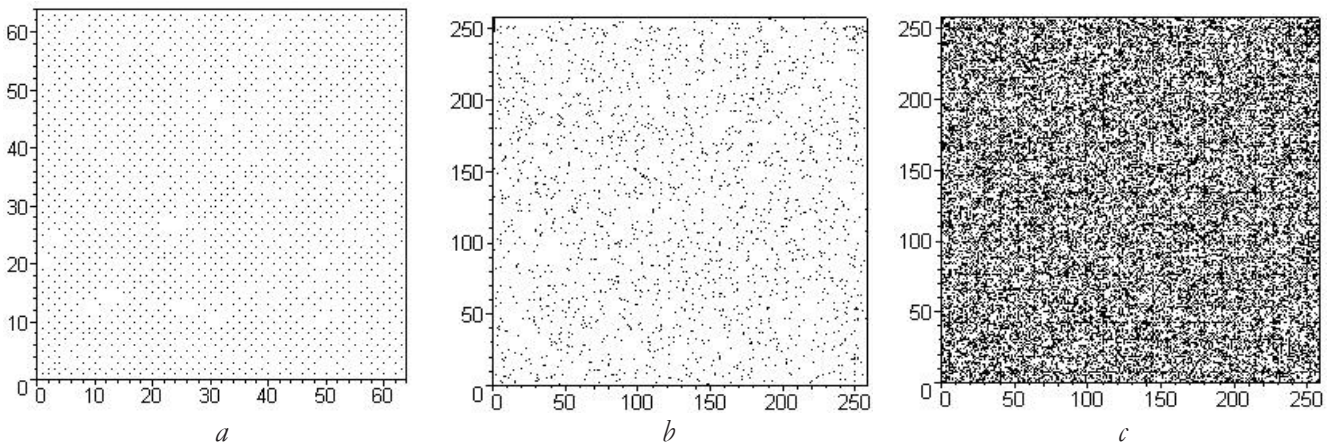

Fig. 5.1. *a) Mapping on the plane of members pairs of a recurrent chaotic sequence, b) Two-dimensional section of the multidimensional phase space of a chaotic algorithm, c) The FP projection of a chaotic algorithm with delay.*

without the multiplicity factoring each point of system state (Fig. 5.1c). An example of such a FP algorithm projection with parameters N = 30000 is shown (presented) in Fig. 5.1*c*.

The fractal characteristics were measured using the brightness field of the images. When measurements by two-dimensional field, two methods can be used. The first – the "sliding window" method – allows you to get the dependence $S = f(\delta)$, where S is measured parameter that determines the fractal signature, δ is smoothing window size. The second is a method for measuring of local dispersion dimension, which consists in measuring the brightness variance of a image small area on two scales. This method makes it possible to obtain a fractal dimensions spectrum by an image.[14].

For this purpose, we analyzed the simplest algorithms for generating of integers $\{x_n\}$ pseudo-random sequences with delay, using the Fibonacci mapping and its modifications:

$$Algorithm\ F-1 \quad \tilde{x}_n = x_{n-1} + (-1)^{x_{n-Kz}} x_{n-Nz} \quad 5(1)$$

$$Algorithm\ F-2 \quad \tilde{x}_n = x_{n-1} + (-1)^{x_{n-Nz}} x_{n-Nz} \quad 5(2)$$

$$Algorithm\ F-3 \quad \tilde{x}_n = x_{n-1} + x_{n-Nz} \quad 5(3)$$

where Nz and Kz are algorithms parameters, $2 \le Kz \le (Nz - 1)$. In contrast to [13], the sign in front of the retarded term in F-1 and F-2 does not change randomly independently, but is determined by the system internal dynamics. The feedback parameter Nz determines the phase space dimension of algorithm and, accordingly, the radius vector dimension $R_n(x_{n-1}, x_{n-2}, ..., x_{n-Nz})$ of the discrete dynamical system state at each step.

The phase space (PS) volume of the Fibonacci mapping of dimension Nz is practically unlimited. For the real application of PRS algorithms in radio engineering systems and the formation of modulating digital signals of a finite capacity, it is necessary to set the algorithm definition domain on a numbers finite set of a natural series closed interval [1, M], where $M > 1$. For this, mappings (5.1-5.3) must be supplemented by the operation of converting numerical interval [1, M] into itself, for example, of following form:

$$\begin{aligned} x_n &= \tilde{x}_n, && if \quad \tilde{x}_n \in [1, M], \\ x_n &= \tilde{x}_n - M, && if \quad \tilde{x}_n > M, \\ x_n &= \tilde{x}_n + M, && if \quad \tilde{x}_n < 1. \end{aligned} \qquad (5.4)$$

This transformation, corresponding to segment contraction [1, M] into a ring, plays an important role in the chaotic behavior mechanism of these dynamical systems. This operation limits the phase space volume, making it finite, equal of $V_{PS} = M^{Nz}$ state points and provides additional trajectories mixing in the phase space. The operations of mapping the interval [1, M] into itself make the transformations of the algorithm ambiguous, which does not allow restoring the

formula and parameters of the algorithm by the clipped process well-known implementation.

It should be noted that one transformation of numer interval into itself is not enough for effective trajectories mixing in phase space. A randomization certain mechanism should already be contained in the mapping function. In this case, this is provided by the Fibonacci mapping properties. These two conditions – the phase space limited volume and the presence of a powerful mixing mechanism – are necessary conditions for any dynamic system chaotic behavior.

Algorithm F-4 based on the Fibonacci mapping (5.3) was also considered as an alternative, but with a different operation of converting the numerical interval [1, *M*] into itself, the type of reflecting boundary:

$$\begin{aligned} x_n &= \tilde{x}_n, && if \quad \tilde{x}_n \in [1, M], \\ x_n &= M, && if \quad \tilde{x}_n > 2 \cdot M, \\ x_n &= 2 \cdot M - \tilde{x}_n, && if \quad M < \tilde{x}_n < 2 \cdot M. \end{aligned} \tag{5.5}$$

Depending on the initial conditions choice, the radius vector Rn describes a trajectory in the algorithm phase space, which is successive discrete transitions from one point of the dynamic system (DS) state to another according to a random law. These motion "trajectories" of a discrete DS in the PS, due to the limited PS volume, form closed cycles, which, due to the transformations uniqueness, do not intersect and have no common points. In addition, cycle pools and isolated points can exist in the PS. The cycles of the studied algorithms F-1, F-2, F-3, F-4 have an important distinctive feature: the behavior of dynamic system before the cycle is closed (and also on the movement trajectory of the pool, if it exists) is chaotic, and generated by algorithm non-periodic sequence at the same time – pseudo-random type.

The such points set in the PS, united in a cycle, we called a pseudo-random cycle (PRC) if the non-periodic process formed by the algorithm before the cycle is closed is chaotic, in contrast to the regular cycle, which corresponds a regularic process before the DDS exits to a period. A pseudo-random cycle (until it closes) corresponds to an irregular motion in the phase space, and a regular cycle corresponds to a regular one. In both cases, the behavior of the dynamic system on the cycle is completely determined. The trajectory of a pseudo-random cycle is a deterministic set of points of discrete dynamical system states chaotically following one another in the entire volume of the algorithm phase space. An analogue of the pseudo-random cycle of a discrete system is the continuous dynamical system strange attractor [15].

The differences between pseudo-random and regular cycles are quite intuitive. Periodic motion is always regular, but regular motion is not necessarily periodic. Thus, PRC is such a discrete dynamical system (DDS) movement, which, at consideration intervals less than a period, is random chaotic, and at intervals greater than a period (more precisely, $N > 2T = 2Np$), the system behavior should be considered already as regular and periodic.

Depending on the values of the parameters Nz ≥ 3, Kz and M, there are a cycles whole row of different periods in the phase space of the F-1, F-2, F-3 algorithms. Each long ($N \sim V_{PS}$) cycle before its closure corresponds to a non-periodic PRS with an almost uniform distribution $p(x) \approx 1/M$ of generated numbers in a given interval of the domain $p(x) \approx 1/M$ and with uniform distributions of conditional probabilities. To characterize the chaotic set of points fractal properties on the PRC, we confine ourselves to an analysis of the geometric and correlation dimensions [16].

The fractal analysis methods can be applied, in principle, to any numerical set. In particular, in the discrete DS study, these methods can be directly applied to the points set of system states in an *n*-dimensional PS, and can also be applied to the points set of these states projections onto selected surfaces in the phase space. The

fractal analysis methods can also be successfully extended to phase space projections onto coordinate axes; in the latter case, we are dealing with the fractal properties study of sequences directly formed by discrete algorithms.

To characterize the fractal properties of a chaotic set of points on a pseudorandom cycle in an Nz-dimensional PS, we restrict ourselves to analyzing the Euclidean D and correlation dimensions D_2. Computer analysis was carried out for parameters small values of the chaotic algorithm with delay, which is of fundamental importance for estimating the PRC majority properties. With an increase in the algorithm dimension, the DDS behavior becomes much more complicated and the generated PRSs statistical characteristics improve.

An correlation dimension D_2 estimate of studied pseudo-random motion of a discrete dynamical system along a trajectory in a multidimensional PS can be given based on correlation integral $C(l)$ calculation given on the set of distances l between all pairs of DS state vectors on a cycle in PS, plotting the dependence $\lg C(l) = f(\lg(l))$ shown in **Fig. 5.2**, and determining angular coefficient of straight part at it.

Curve 1 in this figure corresponds to the algorithm with parameters Nz = 3, Kz = 2, M = 15, PRC with initial vector $R_0(1, 1, 1)$ and process

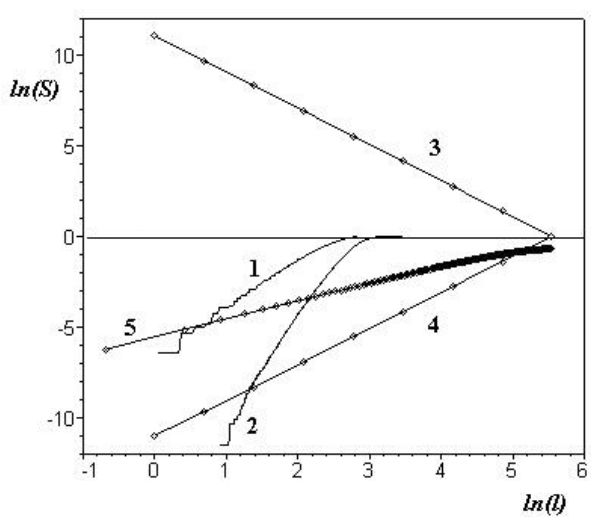

Fig. 5.2. *Fractal signatures for determining the Hausdorff and correlation dimensions.*

implementation length N = 630. By calculating the local angular coefficient, we can give the following correlation dimension estimate of the cycle under study: $D_2 \sim 2.4$. The obtained value is consistent with the Euclidean dimension D = 3, $D_2/D \sim 0.8$. The value of the latter ratio can serve as the degree characteristic of filling uniformity of the full PS volume with cycle points.

Curve 2 in Fig. 5.2 corresponds to the logarithm of correlation integral for the PRC with $R_0(1, 1, ..., 1)$ algorithm with parameters Nz = 7, Kz = 4, M = 15, N = 630. Graphs 1 and 2 of the function $\lg C(l) = f(\lg(l))$ in Fig. 5.2 are identical to each other, but have a extended straight sections different angular coefficient due to PS dimensions differences. For curve 2, the angular coefficient corresponds to the correlation dimension of the analyzed cycle $D_2 \sim 5.85$, $D = 7$, $D_2/D = 0.83$. Note that algorithm long cycles correspond to PRSs with good statistical and correlation properties, especially when the delay Nz increases more than 5.

An fractal characteristics analysis of the projection points of the DS states onto the two-dimensional coordinate plane (X_{-1}, X_{-2}), taking into account their multiplicity, was carried out by covering the numerical set with elementary cells with side l, calculating the required number of them $S(l)$ and then calculating the Hausdorff and correlation dimensions. Curve 3 in Fig. 5.2 corresponds to the dependency $\ln S(l) = f(\ln(l))$ of the PRC projection with the initial vector $R_0(2, 2, \ldots, 2)$ of the algorithm with parameters Nz = 16, Kz = 9, M = 255, the length of the process implementation N = 650000. D_0 = 2.0, D = 2, D_2/D = 1. Curve 4 in the figure was obtained by calculating the sums of squares logarithm of the observed occurrence frequencies of the DS state projections in unit cells covering the numerical set, which gives the following estimate of the PRC correlation dimension projection D_2 = 1.989, D = 2, D_2/D = 0.994.

The correlation dimension definition by the standard method, applied to a one-dimensional ($D = 1$) chaotic array of $N = 6500$ PRS numbers, formed by an algorithm with parameters Nz = 16, Kz = 9, $M = 255$ (curve 5 in Fig. 5.2) gave the correlation dimension value $D_2 = D_2/D = 0.988$, which indicates a fairly good filling uniformity interval [1, M] with generated numbers. This is confirmed by the analysis of the one-dimensional probability distribution of the numbers in the sequence.

On **Fig. 5.3** the computer calculation results of fractal signatures $\ln S = f(\ln a)$ are given, where S is the brightness characteristic of the graphic PS image of the chaotic algorithm, a is the window side (the measuring window is square, the relative window size varied from 3 to 30 pixels).

It can be seen from figure that all signatures have sections with different dominant slopes, which characterizes degree of statistical connection between corresponding members of recurrent chaotic sequence. Numerical analysis showed that the fractal signatures of mappings of algorithms with good mixing (weak statistical connection between members pairs of a recurrent chaotic sequence) are characterized by a smaller spread and almost the same slope.

Methods of computer analysis were used to study chaotic algorithms F-1, F-2, F-3, F-4 with delay with different characteristics (delay parameter, various mixing mechanisms). For the F-1 algorithm, the correlation dimension of the points set on cycle with initial vector $R_0(8,6,7,1)$ (curve 1) is equal to $D_2 = 3.3$. The obtained value agrees with the Euclidean dimension $D = 4$, $D_2/D = 0.83$. The latter ratio value can serve as a characteristic of the uniformity degree of the full volume filling of the PS with cycle points. As the analysis showed, the studied cycle with the initial vector $R_0(8,6,7,1)$ corresponds to a non-periodic PRS of length $N = 14030$ with a generated numbers distribution close to uniform.

The linear section of graph (curve 2), obtained for the points set of the trajectory basin and cycle in the F-2 algorithm phase space, has a somewhat smaller slope, which corresponds to the correlation dimension value about $D_2 = 3.0$. Curve 3 in Fig. 5.2 corresponds to logarithm of correlation integral for a pseudo-random cycle with initial conditions $R_0(1,6,6,7)$ of the tested algorithm F-3. Graphs 1 and 3 of the function $\log C(l) = f(\log(l))$ in **Fig. 5.4** almost exactly repeat each other and have an extended rectilinear section with a slope $D_2 = 3.3$, which and makes it possible to obtain a quantitative estimate of the filling uniformity of the space with DS states points on pseudo-random cycles. Note that PRSs with good statistical and correlation properties, especially when the delay increases more than 5 correspond to algorithms F-1 and F-3.

For the F-4 algorithm cycle with initial radius vector $R_0(7,14,6,15)$, the period $T = 613$, the

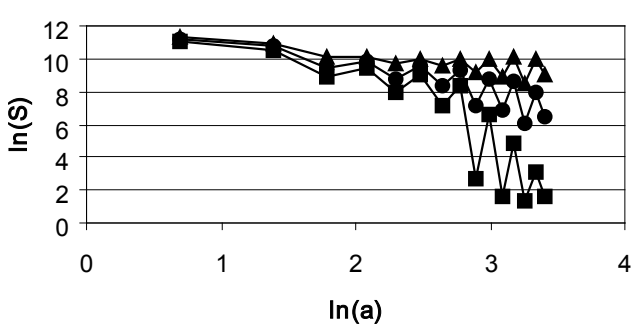

Fig. 5.3. *Fractal signatures of pairwise mappings: square – mapping* $(x_n; x_{n+1})$, *circle –* $(x_n; x_{n+2})$, *triangle –* $(x_n; x_{n+9})$.

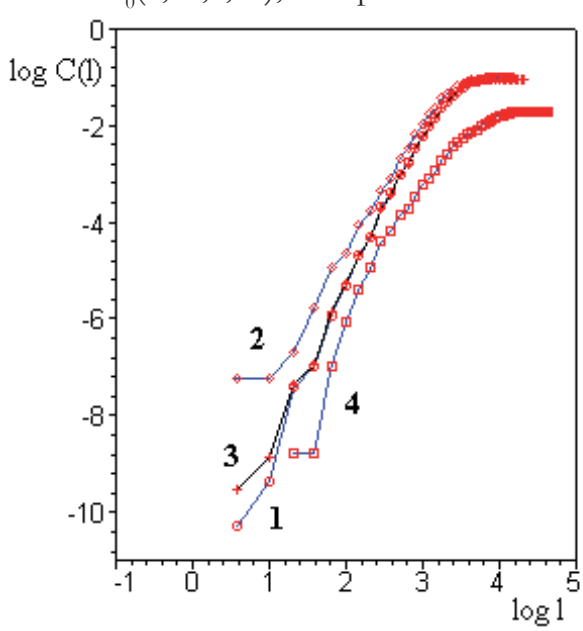

Fig. 5.4. *Dependence of* $\log_2 C(l)$ *on* $\log_2 l$ *for chaotic algorithms with delay and various delay parameters.*

dependence $\log C(l) = f(\log(l))$ (curve 4 in Fig. 5.2) does not have a clearly defined straight section. This means that correlation integral has significant deviations from law $C(l) \sim 1 - D$ and, therefore, this pseudo-random cycle points are located unevenly in PS.

Fractal analysis can be applied not only to a chaotic points set in a multidimensional PS, but also to a one-dimensional set of PRS implementation numbers. The correlation dimension definition by the standard method, applied to a one-dimensional (Euclidean dimension $D = 1$) chaotic array of $N = 1000$ PRS numbers, formed by the algorithms F-1, F-2, F-3, F-4 with different delay parameters, gave the following results. For all tested algorithms, the correlation dimension value is within $D_2 = D_2/D = 0.91 \div 0.96$, including for the random number generator RND of the Maple mathematical software package. The obtained ratio D_2/D values indicate a fairly good filling uniformity definition domain with the generated numbers. This is also confirmed by analysis of one-dimensional probability distribution of the numbers in the sequence.

It can be seen from given data that studied chaotic algorithms, as well as certified random number generator RND, demonstrate a sufficiently high structural quality of the generated sequences. When the distribution function of the generated numbers $p(x)$ and the correlation coefficient change, the proposed method for estimating degree of structural complexity effectively captures the corresponding change in the PRS statistical properties.

Thus, it is shown that calculation of fractal characteristics of recurrent chaotic sequences and their graphical images makes it possible to quantify effectiveness of mixing mechanism and degree of statistical connection between the chaotic sequence members, which ultimately determines complexity of the chaotic generating algorithm

6. STATISTICAL CHARACTERISTICS OF PSEUDO-RANDOM SIGNALS GENERATED BY DISCRETE ALGORITHMS WITH DELAY

The most complete information about statistical properties of discrete sequences is provided by the distributions analysis of pairwise conditional probabilities of the sequence members $p(i + j, x_n | i, x_k)$, $j = 1, 2, 3, \ldots; k, i = 1, 2, 3, \ldots, M$. The pairwise conditional probability is the generating probability number x_n at the $(i+j)$-th algorithm step, if the number x_k was obtained at the i-th step. In this case, the definition domain of the discrete algorithm is an arbitrary closed integer interval [M1, M2], M = M2 – M1 + 1, $x_n \in$ [M1, M2].

If conditional probabilities distribution for any j practically coincides with uniform distribution, $p(i+j, x_n | i, x_k) \approx 1/M$, $j = 1, 2, 3, \ldots$ with an arbitrary choice i. At the same time, if the probability distribution of generated numbers $p(x_n)$ is close to uniform, then value probability x_n is practically also equal to $1/M$. Thus, the transition probabilities to state x_n at the j-th step coincide with this value probability at this step, regardless of the sequence values at the previous algorithm steps, which is typical for random sequences in independent trials. More over, the pseudo-random sequence generated by such an algorithm will be close in its probabilistic characteristics to sequence of independent equiprobable numbers from the interval $[M_1, M_2]$ [17]. In the latter case, the given sequence can be expected to have best statistical properties. The establishment of such a fact emphasizes studying importance the conditional probabilities distributions for a priori judgments about generated pseudo-random sequences quality

To characterize the conditional distributions $p(x_{i+j} | x_i)$, the location form of points (x_{i+j}, x_i) on the plane for mapping $x_{i+j} = f(x_i)$ given by the discrete algorithm is of great importance for corresponding values $j = 1, 2, 3, \ldots$ and $i = 1, 2, 3, \ldots, N$ [18]. Obtaining the points scatter

(x_{i+j}, x_i) and visualizing them on screen does not require large computational resources compared to direct conditional probabilities calculation, although the this scatter nature does not directly give the shape of the conditional probability distribution. The scatter visualization indicates the regularity degree of these distributions, the functional relationships presence, the forbidden transitions existence, and even entire forbidden zones, which inevitably affects the correlation and other statistical properties of the sequence.

Consider the simplest formula of algorithm with delay: $x_n = x_{n-1} + x_{n-Nz}$, where Nz is delay parameter, supplemented by operation of returning to interval $[M_1, M_2]$ in case the newly obtained value x_n is thrown out of its limits. In this algorithm, mixing, chaotization of formed process is carried out by adding a random value of the sequence retarded member and by clipping resulting numbers sum on the boundary of definition domain M_2.

For numerical simulation, the following algorithm values parameters were taken: $M_1 = 1$, $M_2 = 255$, Nz = 16. The analyzed algorithm, with the selected parameter values and given initial conditions, which are a 16 random numbers set (delay vector), form a pseudo-random sequence with a probability distribution close to uniform distribution $p(x) = 1/M$. The difference from uniform distribution is characterized by total discrepancy between occurrence frequencies observed in numerical experiment in the generated sequence of numbers x_m and the value $1/M$:

$$\Delta p_\Sigma = \sum_{m=1}^{M} \left| n(x_m)/N - 1/M \right|,$$

where $n(x_m)$ is the numbers number xm in sequence of N members. This total discrepancy numerically coincides with relative average difference from uniform law $\Delta p_{av.rel.}$. The largest relative difference between the occurrence frequency of observed numbers and the value of $1/M$: $\Delta p_{max.rel.} = [1/(1/M)]\,|n(x_m)/N - 1/M|_{max}$.

Table 3

Algo-rithm	$p(x)$		$p(x_{i+j}\|x_i)$		
	N = 210 000		N = 52 000 000, k = 6		
	$\Delta p_{av.rel.}$	$\Delta p_{max.rel.}$	j	$\Delta p_{av.rel.}$	$\Delta p_{max.rel.}$
1	0.03	0.10	1	0.03	0.12
			16	0.031	0.12
2	0.03	0.10	1	0.997	1.12
			2	0.5	1.04
			16	0.03	0.10
RND	0.03	0.15	-	-	-

The obtained estimates of probability and conditional probability distributions for sequences generated by algorithms analyzed in this paper in comparison with standard RND generator are grouped in **Table 3**:

Two-dimensional distribution of points pairs (x_{i+j}, x_i), where $i = 1, 2, \ldots, N$ is a uniformly filled area of randomly scattered points, for any $j = 1, 2, 3, \ldots, 16, \ldots, 32$. Such nature of uniform, complete and random filling of numerical interval $[M_1, M_2]$ with points (x_{i+j}, x_i) indicates the process chaotization under study.

More accurate information about transition probabilities to each of the x_n values is given by the construction distributions conditional probabilities. For a visual representation in **Fig. 6.1** histograms of transition frequencies are constructed only for 6 generated numbers values $x_k = (k - 1)\cdot 50 + 1$, $k = 1, 2, ..., 6$ with a step $j = 1$. Frequencies histograms are calculated by implementing sequence from $5.2\cdot 10^7$ members. Values $\Delta p_{av.rel.}$ and $\Delta p_{max.rel.}$, characterizing

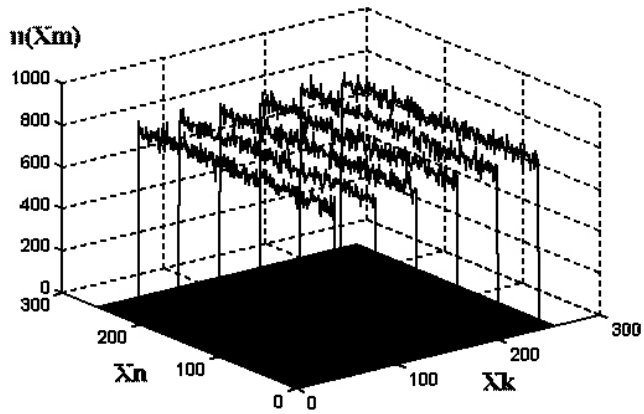

Fig. 6.1. *Transition frequency histograms for 6 values of generated numbers $x_k = (k - 1)\cdot 50 + 1$, $k = 1, 2, \ldots, 6$ with step $j = 1$.*

differences from uniform distribution of one of the histograms (x_k = 251) for j = 1 and 16, are given in Table 3. From the data obtained, it follows that for algorithm No. 1 of the distribution of conditional probabilities for any j practically coincide with the uniform distribution.

After a corresponding change in algorithm, in which one-dimensional distribution remains uniform, and distributions functions of conditional probability $p(x_{i+1}|x_i) = 0$ (j = 1) through one value depending on the parity of number x_i on previous step. The distribution pattern of points on the plane in this case is regular (**Fig. 6.2**). This is confirmed by quantitative differences in $\Delta p_{av.rel.}$ and $\Delta p_{max\ rel.}$ from a uniform distribution (see Table 3).

The sequences correlation characteristics generated by algorithms 1 and 2 were evaluated based on analysis of clipped and non-clipped 100 segments of size N = 128 and 1024 symbols, sequentially generated by algorithms without any selection. Despite significant differences in distributions form $p(x_{i+1}|x_i)$, lateral outliers value of auto- and cross-correlation functions relative to level $1/\sqrt{N}$ for both algorithms is approximately the same and is: (1.3÷3.8) for ACF N = 128, (1.5÷4.3) for CCF N = 128, (2.2÷4.8) for ACF and CCF N = 1024. These data indicate that the algorithms considered above features had little effect on correlation properties of both the sequences themselves and the results of their clipping. At the same time, a numerical

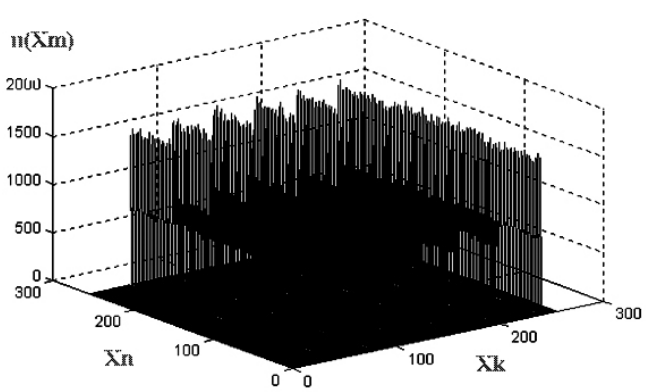

Fig. 6.2. *Distribution of conditional probabilities.*

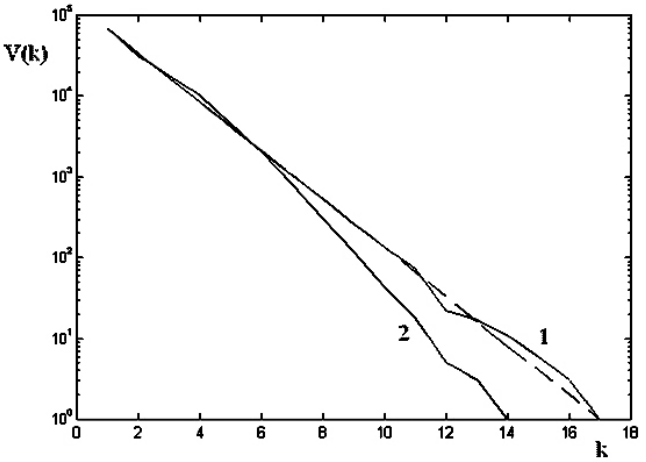

Fig. 6.3. *Block structure of sequences generated by algorithm No. 2.*

experiment on block structure over the length of a clipped sequence of $2.7 \cdot 10^5$ members showed that if algorithm No. 1 generates sequences with a block structure close to the law $p(k) = 1/2^k$ before blocks of size k = 17-18, then sequences block structure generated by algorithm No. 2 deviates significantly from this law (**Fig. 6.3**), which is directly related to uneven distribution of transition probabilities even at one step j = 1.

The volume of the signals system generated by algorithms was estimated by selecting from generated clipped sequence of balanced codes with a length of 128, 256 and 512 symbols with following correlation properties: lateral outliers of the aperiodic autocorrelation function do not exceed $R_{max} = 2.26/\sqrt{N}_{code}$, and the outliers of aperiodic crosscorrelation functions over entire array of selected codes are less than or equal to $R_{max} = 3.39/\sqrt{N}_{code}$. Correlation functions were calculated using the formula for balanced sequences [4].

As numerical experiment showed, the uneven conditional distributions and the forbidden transitions existence affected the select codes speed into signal system as sequence duration N increased (**Fig. 6.4**). In this figure, all curves corresponding to algorithm No. 2 are significantly lower than those of algorithm No. 1.

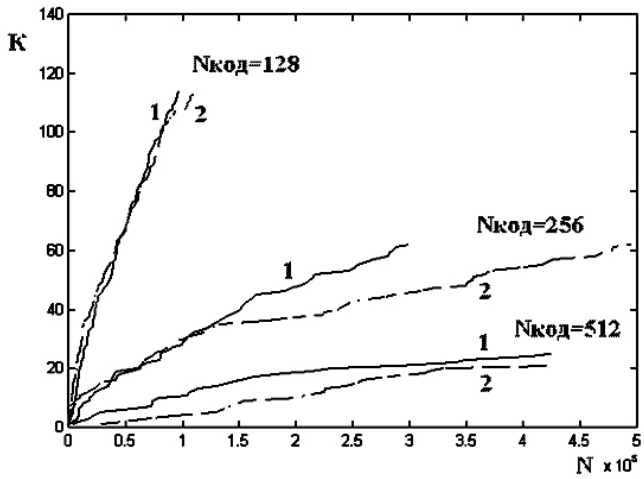

Fig. 6.4. *The number of balanced codes with lengths of 128, 256 and 512 characters.*

7. ANALYSIS METHOD FOR CODING PSEUDO-RANDOM ALGORITHMS BASED ON CODE GROUPS DISTRIBUTION

A promising direction in the modern radio communication systems development of is the broadband noise-like signals use [4,11]. Broadband communication systems have a advantages number over traditional narrowband systems. These advantages are associated with an increase in the users number, dense filling of the frequency range, and the need to ensure reliable confidential information transmission.

The spectrum expansion of transmitted signal, necessary for broadband systems operation, is achieved by using pseudo-random sequences generated by various special algorithms. These and other such sequences applications (redundant coding of information in digital communication channels, cryptography, Monte Carlo modeling) encourage search for new algorithms, including those with different characteristics and probabilities distribution functions. At the same time, search for new methods for statistical properties analyzing, the sequences they form, and estimating their proximity to an ideal random process continues [19].

A method for estimating statistical properties of digital multilevel pseudo-random sequences by statistics analyzing of code groups distribution in them from full code for selected pseudo-random signal base is considered. The this approach development is to find out intervals statistics between successive occurrences of identical code groups from the complete code. It is expected that this approach will allow, in particular, to analyze unknown algorithm structure that generates studied pseudo-random sequence. The specified intervals characteristics for sequences generated by various algorithms, including those used in standard software packages, are compared.

Statistical characteristics estimation of pseudo-random sequences generated by some algorithm and proximity to an ideal random sequence can be viewed as a forming process a steps series, the result of which at each step is completely independent of results at previous steps. Moreover, if the under study algorithm is defined on the integers set, for example, on the interval [1, M], where M-max is integer, then we can assume that ideal random sequence corresponding to these parameters will be formed as a result of throwing an M-dimensional die, on each face of which one of integers included in specified interval is plotted.

The approach allowing to analyze statistical structural features of pseudo-random integer sequences is considered. The investigated sequence is compared with a code group of a certain length and structure. The group length is sequence members number equal to chosen base of the pseudo-random signal (B), and group structure is a specific set of B integers from interval [1, M]. The total number of all different codes in this case is equal to elements number of the complete M^B code [20].

The described procedure makes it possible to construct the distribution functions of probabilities code groups coincidence coinciding with current implementation when repeatedly passing through the selected sequence section for code groups of different lengths and structures. Based on ideal random sequence model, one can obtain an closeness estimate of analyzed sequence to it for all relevant distribution functions. Such procedures have been performed for sequences generated by some algorithms. These sequences had indicated distributions, close to uniform, and differed little in variance from average variance for an ideal random sequence.

It has been established that for pseudo-random sequences generated by a number of algorithms (even close to an ideal random sequence), when analyzing intervals (K is interval length) between matches, when code group is shifted along pseudo-random sequence, some features are found. For the class of Fibonacci-type algorithms [5], close to uniform probability density distributions over all code groups for a given base were obtained.

However, when statistics analyzing of the certain code group occurrence (for $B = 1$), there was a gap in distribution $N_K = 0$, where N_K is the matches number. This interval (K) is equal to delay parameter, which is a analyzed algorithm characteristic for base $B = 1$. The distributions characteristic form of intervals (K) for 2 different code groups (11 and 19) (parameters of algorithm $M = 19$, delay Nz = 8) for $B = 1$ are shown in **Fig. 7.1***a,b*. For all other code groups, for a given B, this dependence has the same form as in Fig. 7.1*a*.

If the occurrence probability of a code group of length B for an ideal random sequence is $p = 1/M^B$, and T is members number of analyzed sequence, then occurrences average number of codes is T/M^B. Then expected matches number with a length B code group over an interval K in a length sequence T is:

$$N_K = (T / M^B) \cdot (1-p)^{K-1} p. \quad (7.1)$$

On Fig. 7.1*a,b* this dependence $N_K = F(K)$ is presented for an ideal random process (curve 2). It has a character close to exponential.

For large signal bases ($B > 1$), the analyzed distribution of intervals has a more complex form: for interval K, which is equal to algorithm delay parameter Nz, there are code groups for which $N_K = 0$ and several codes for which N_K significantly exceeds expected average level corresponding to ideal random process model. Thus, the proposed method for statistics analyzing of intervals of appearance distribution of the of code groups makes it possible to decipher the structure of an unknown forming algorithm.

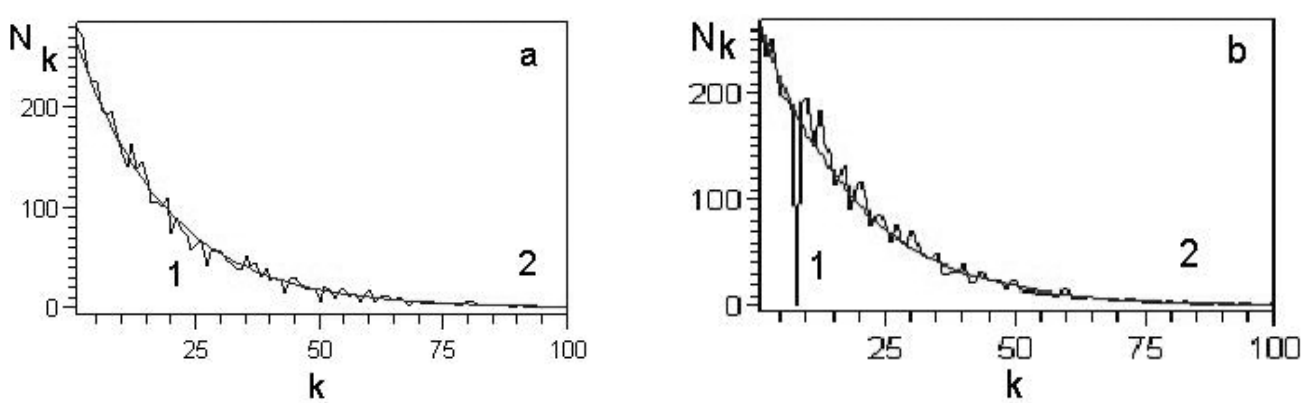

Fig. 7.1a,b. *Distribution over intervals between occurrences of identical code groups at B = 1 for a sequence generated by a Fibonacci-type algorithm (with parameters: M = 19, delay Nz = 8; a – curve 1 for code 11; b – curve 1 for code 19; curves 2 for a perfect random sequence.*

8. FILLING EFFICIENCY PHASE SPACE OF ENCODING DISCRETE ALGORITHM WITH DELAY

One of the promising ways to form a pseudo-random sequence of integers $\{x_n\}$ is algorithm with delay created on basis of processes modeling in ring self-oscillatory systems with dynamic chaos [13]. The algorithm discrete version is defined on integers set M of natural series from integer interval $[M_1, M_2]$ ($M_2 > M_1, M = M_2 - M_1 + 1$).

Along with M, the algorithm main parameter is delay parameter Nz, which determines number of delayed sequence members (x_{n-1}, x_{n-2}, x_{n-3}, ..., x_{n-Nz}) that must be known at each step to determine a new member x_n. The algorithm formula is supplemented with returning operation the number x_n to interval $[M_1, M_2]$ in case new value received is outside it.

The numbers x_{n-1}, x_{n-2}, x_{n-3}, …, x_{n-Nz} are generalized coordinates in Nz-dimensional phase space given dynamical system, and each specific set of them determines radius vector $R_n(x_{n-1}, x_{n-2}, \ldots, x_{n-Nz})$ and the corresponding system state point in this space. The total number of different delay vectors and system state points in phase space is equal to M^{Nz}. And each of these states can be accepted by system at least as initial conditions.

With algorithm parameters appropriate choice and initial conditions for changing state vector, i.e. transitions from one point of the phase space with coordinates R_i to another point with coordinates R_{i+1} are pseudorandom. But only as long as vector R_n takes on more and more new values. If the radius vector hits same point in the phase space again, due to the complete determinism of the algorithm, the system motion in phase space will repeat itself exactly, i.e. system enters a closed trajectory (cycle). This corresponds to occurrence of periodicity in sequence generated by algorithm.

Since, for given values of M and Nz, there are a finite number of different vectors in the phase space, sooner or later system will necessarily find itself on a cycle. The problem is to find longest realization N of pseudo-random sequence generated by algorithm that fills entire phase volume M^{Nz}.

The properties of algorithms study that generate pseudo-random sequences with a large period is an urgent task. One of most important parameters of such algorithms that characterize their quality is filling degree and structure of phase space.

Consider a discrete Fibonacci-type delay algorithm that generates a pseudo-random sequence with good statistical properties:

$$X_n = X_{n-1} + X_{n-Nz}, \quad X_n = X_n - M \text{ for } X_n > M. \tag{8.1}$$

The algorithm main parameter is delay parameter Nz, which determines number of memorized sequence members and phase space (PS) dimension. The algorithm is defined on a integers finite set of natural series from closed interval [1, M]. If newly calculated number of sequence is outside this interval, then a linear transformation of shift $\mathbf{x_n} \rightarrow \mathbf{x_n} \pm \mathbf{M}$ is performed, returning this number to the boundaries of definition domain. This transformation, in addition to functional action of Fibonacci-type algorithm itself, plays a significant role in chaotization mechanism of dynamic system under study behavior [7].

The number of system states points in phase space of algorithm is finite and equal to $\mathbf{M^{Nz}}$. The system movement in PS is carried out by jumping from one state to another. The system's motion trajectories occupy entire volume of PS, i.e. all possible states. Each such trajectory of system's motion follows its own closed cycle containing a system states limited number. The PS structure consists of a cycles finite set of different periods, the system behavior on which is pseudo-random. All cycles are located in a complex way in PS

entire volume. Thus, the PS of algorithm for Nz = 4 and $M = 17$ consists of five cycles with a periods of 73684, 3619, 2549, 2471, 529 and one singular point with coordinates (17, 17, 17, 17). The cycle choice is determined by setting a initial conditions set.

The system behavior pseudo-random nature on a cycle on an interval less than period is confirmed by the change dependence in distances in PS $\Delta R(n)$ between neighboring points on the cycle, shown in **Fig. 8.1** for algorithm with Nz = 3, $M = 13$. This distance at algorithm each step changes randomly, reaching values close to largest geometric PS dimensions.

The phase space under study of algorithm for Nz > 2 consists of one singular point with coordinates $(M, M, \ldots, M)$ and cycles family of different or same period. Each PS point belongs to only one specific cycle, while different cycles do not have a single common point.

The algorithm enters one or another cycle depending on the choice of the initial state vector. Until the cycle is closed, the state vector describes a pseudo-random process, by which corresponds to a non-periodic segment of a pseudo-random sequence generated by the algorithm of the appropriate size.

In the phase spaces ensemble of algorithms with different parameters M and

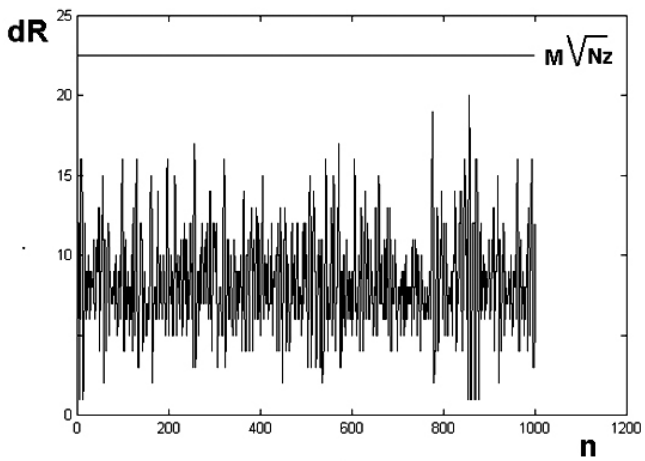

Fig. 8.1. *Distances in PS between neighboring points on cycle, Nz = 3, M = 13.*

Nz, both "short" cycles are observed, which periods T are much less than total number of points in phase space $\mathbf{M^{Nz}}$ ($T << \mathbf{M^{Nz}}$), and "long" cycles, whose periods are comparable to last value: $T \sim \mathbf{M^{Nz}}$. For even M, short cycles prevail in PS algorithm, and for odd M, short cycles do not exist at all, or they are presented in a small amount, occupying a small PS volume, which ensures existence of a long cycle. Thus, at odd M, longest cycles are observed. The such cycles period for certain values algorithm parameters can approach maximum possible value $\mathbf{T_{max}} = \mathbf{M^{Nz}}$.

A numerical experiment fixed case when PS contains only one long cycle and one isolated point: M = 2, Nz = 15, $\mathbf{T/M^{Nz}} = 1.0$. A close result was obtained at $M = 3$, Nz = 9, when period long cycle is $\mathbf{T/M^{Nz}} = 0.999$, and in addition to it and one isolated point, there is only one short fivecycle cycle in FS of system. All this confirms that value $\mathbf{T_{max}} = \mathbf{M^{Nz}}$ can serve as estimate of maximum non-periodic segment of sequence generated by algorithm. It should be borne in mind that this maximum period $\mathbf{T_{max}}$ can only be realized with certain ratios of the parameters M and Nz.

It is shown that by long cycles correspond to generated numbers distributions that are close to uniform. The change nature in the distribution functions of generated numbers with an increase in parameter Nz (for $M = 255$) is shown in **Fig. 8.2**. Here: $\Delta\mathbf{p_{av}}$, $\Delta\mathbf{p_{max}}$, $\boldsymbol{\sigma}$ – mean (1), maximum (2) relative modulo and root-mean-square (3) deviations of distributions from uniform ($n = 210000$). It can be seen that algorithm generates a sequence with an almost uniform distribution for Nz > 5. In this case, all conditional probabilities $\mathbf{p(x_i|x_j)}$ are also close to a uniform distribution. This means that pseudo-random sequence generated by this algorithm differs little in its probabilistic properties from sequence of independent equiprobable numbers from interval [1, M].

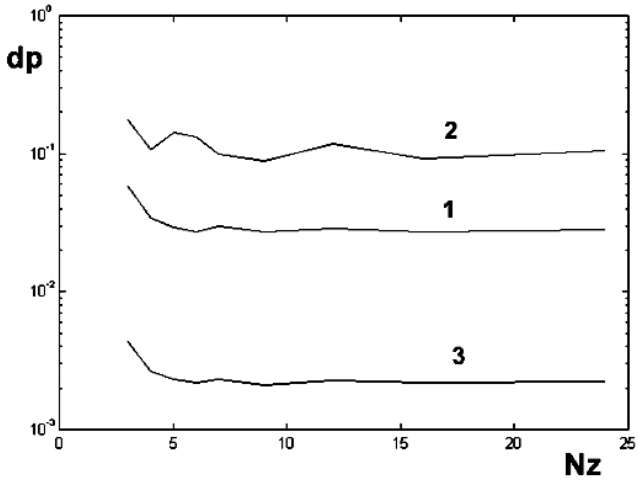

Fig. 8.2. *Difference of distribution from uniform depending on Nz (M = 255). 1 – Δp_{at}, 2 – Δp_{max}, 3 – σ.*

For large values of M and Nz, the structure study of system phase space by direct enumeration of its elements is very difficult. Therefore, study of system phase portrait was carried out at small values of phase space "volume", no more than $10^6 \div 10^7$. In this case, without limiting results obtained generality, in numerical analysis we will assume, as a rule, that $M_1 = 1$, $M_2 = M$.

The numerical study results of phase space structure for different values of *M* and Nz (*M* = 2÷21, Nz = 2÷18, $M^{Nz} \le 10^7$) showed that algorithm phase space is a finite cycles set, except for cases Nz = 2 for odd *M*, when in addition to cycles in phase space of system there are points that do not belong to any cycle, but belong to "pools" of these cycles. Thus, if system is at one of these points, then after a certain steps number a system will reach corresponding cycle. In this case, system trajectories in phase space are separate closed cycles, number of which and value of their periods depend on system parameters. As an example, we can give spectra of periods (i.e., cycles periods existing in phase space, and their number) for case of Nz = 4 (**Tables 4, 5**).

Table 4

M	Spectrum of periods
2	1, 15
4	1, 15, 30 (8)
8	1, 15, 30 (8), 60 (64)
16	1, 15, 30(8), 60(64), 120(512)
6	1, 15(3), 30(3), 80, 90(12)
12	1, 15, 30(72), 80, 90(192), 240(5)
18	1, 15(6), 30(21), 80, 90(105), 240(27), 270(324)
10	1, 15(5), 30(10), 150(6), 312(2)
20	1, 15, 30(93), 150(918), 312(2), 1560(6)
14	1, 3(2), 15(7), 30(21), 210(168), 342(7)

It can be seen from data presented that as $M = 2^k$ (k = 1, 2, 3, 4), $M = 6^k$ (k = 1, 2, 3), and $M = 10^k$ (k = 1, 2) increase, the cycles spectrum is supplemented by one a new value with a large period, and the spectrum always contains cycles of multiplicity 1, 15, and 30 (*M* > 2). At even *M* > 2 and Nz = 3, cycle spectra always exhibit periods 1, 7, and 14. At odd values of *M*, such simple regularities are not observed in structure of cycle spectrum.

The results obtained allow us to draw following conclusions.

1. The system's motion trajectory occupies entire phase space volume, i.e. all possible states, which total number is equal to MNz.

2. The algorithm phase space for Nz > 2 consists of one singular point with coordinates R(M, M, …, M) and a cycles family of different or same period. Each phase space point belongs to only one specific cycle, while different cycles do not have a single common point.

Table 5

M	Spectrum of periods
3	1, 7, 29, 44
5	1, 8, 27 (2), 562
7	1, 9, 22, 427, 653, 1289
9	1, 7, 10, 20, 22, 24, 29, 44, 75, 134, 296, 767, 5132
11	1, 21, 24, 41, 101, 173, 250, 14030
13	1, 626, 2992, 3712, 5056, 7977, 8197
15	1, 27, 44, 176, 562, 828, 1637, 4702, 7764, 11405, 11484, 11881
17	1, 529, 2471, 2549, 3619, 73684
19	1, 4182, 4219, 5067, 5408, 5916, 28778, 75061
21	1, 1289, 2833, 5228, 5401, 25900, 58208, 88633

3. The system enters one or another cycle, depending on which phase space point the initial state vector falls into. Until loop closes, the state vector describes a pseudo-random process, i.e. to cycles correspond to pseudo-random sequence segments of corresponding size.

4. In the phase spaces ensemble of algorithms with different parameters M and Nz, both "short" cycles are observed, which period T is much less than points total number in phase space M^{Nz} ($T << M^{Nz}$), and "long" cycles, which periods comparable with last value: $T \sim M^{Nz}$. For even M values, short cycles predominate in algorithm phase space, and for odd M, short cycles do not exist at all, or they are presented in a small amount, occupying a small phase space region, which and ensures existence of a long cycle. Thus, at odd M, the longest cycles are observed. The such cycles period for certain (previously unknown) values of algorithm parameters can approach maximum possible value $T_{max} = M^{Nz}$. On **Fig. 8.3** shows numerical experiment results to determine three largest cycle periods (curves 1, 2, 3) for different M values for the same delay parameter Nz = 3 in comparison with points total number in phase space – M^{Nz} (curve 4) and with estimate of maximum period $T(M) = M^{0.645Nz}$ at Nz = 3 (curve 5).

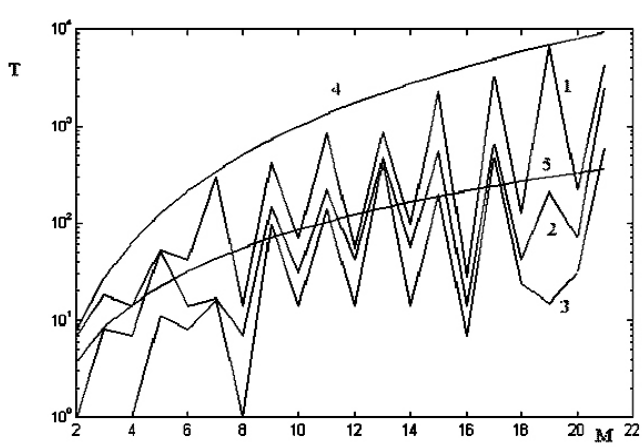

Fig. 8.3. *Cycle periods (curves 1, 2, 3) for different values of M with same delay parameter Nz = 3 in comparison with total number of phase space points – M^{Nz} (curve 4) and estimate of maximum period $T(M) = M^{0.645Nz}$ at Nz = 3 (curve 5).*

5. For an odd M value, all cycles, as a rule, have a different period, i.e. presented in singular. When M is even, same period cycles occur many times, although they are all different in terms of state vector accepted values.

6. For certain values of the algorithm parameters M and Nz, the period of a long cycle can be very close to the maximum possible value M^{Nz}: $T/M^{Nz} = 0.9 \div 1.0$. Moreover, experiment fixed case when phase space contains only one long cycle and one isolated point: M = 2, Nz = 15, $T/M^{Nz} = 1.0$. Almost the same result can be obtained at M = 3, Nz = 9: period of long cycle is $T/M^{Nz} = 0.999$, and in addition to it and one isolated point in system phase space there is only one 5-stroke short cycle.

All this testifies in favor of fact that value of $T_{max} = M^{Nz}$ can serve as an maximum period estimate of sequence generated by algorithm. It should be borne in mind that this maximum period T_{max} can only be realized with parameters certain ratios M and Nz. On Fig. 8.3 the boundary line $T(M) = M^{0.645Nz}$ (Nz = 3) is often exceeded not only by the longest period, but also by the periods of two more smaller cycles, therefore characteristic $T = M^{0.645Nz}$ should be considered as an average value for long cycles.

7. By long cycles correspond to distributions of generated numbers that are close to uniform. Thus, for a cycle with $T/M^{Nz} = 0.895$ (M = 13, Nz = 5), relative average difference on modulus from uniform distribution is 0.2% with a relative maximum of 0.45%, and root-mean-square deviation is 0.07%. It is these long cycles that can be used to generate pseudo-random sequences of long duration with a uniform probabilities distribution of

generated numbers. Based on monotonicity of the dependences considered, the results obtained can be considered valid for significantly large volumes and phase space dimensions

9. CONCLUSION

With an appropriate choice of parameters, the developed discrete algorithms form long non-periodic segments of pseudo-random sequences with a uniform probability distribution, which can be effectively used in cryptography, as well as when encoding information in telecommunication systems and computer networks [21].

REFERENCES

1. Knuth DE. *The art of computer programming. Volume 2: Seminumerical Algorithms.* Third edition, Addison–Wesley, 2007, 832 p.
2. Petrov AA. *Komp'yuternaya bezopasnost'. Kriptograficheskie metody zashchity* [Computer security. Cryptographic methods of protection]. Moscow, DMK Publ., 2000, 445 p.
3. Kuznetsov SP. *Dinamichesky khaos. Kurs lektsiy* [Dynamic chaos. Lecture course]. Moscow, Fizmatlit Publ., 2001, 295 p.
4. Varakin LE. *Sistemy svyazi s shumopodobnymi signalami* [Communication systems with noise-like signals]. Moscow, Radio i svyaz' Publ., 1985.
5. Bykov VV. *Tsifrovoe modelirovanie v statisticheskoy radiotekhnike* [Digital modeling in statistical radio engineering]. Moscow, Sovetskoe radio Publ., 1971, 328 p.
6. Hayes Brian. The Vibonacci Numbers. American Scientist: Computing Science. July-August 1999.
7. Shuster G. *Deterministic chaos. Introduction.* Moscow, Mir Publ.,1988, 240 p.
8. Bulinsky AV, Shiryaev AN. *Teoriya sluchaynykh prozessov* [Theory of random processes]. Moscow, Fizmatlit Publ., 2005.
9. Kemeny JG, Snell JL. *Finite Markov chains. The University Series in Undergraduate Mathematics.* Princeton, Van Nostrand, 1960.
10. Bharucha-Reid AT. *Elements of the Theory of Markov Processes and Their Applications.* New York, McGraw-Hill, 1960.
11. Rytov SM. *Vvedenie v statisticheskuyu radiofiziku* [Introduction to statistical radiophysics]. Moscow, Nauka Publ., 1966.
12. Gantmakher FR. *Teoriya matrits* [Matrix theory]. Moscow, Nauka Publ., 1966.
13. Belyaev RV, Vorontsov GM, Kolesov VV. Sluchaynye posledovatelnosti, formiruemye nelineynym algoritmom s zapazdyvaniem [Random sequences generated by a non-linear algorithm with delay]. *Radiotekhnika i electronika*, 2000, 45(12):954-960.
14. Potapov AA. *Fraktaly v radiofizike i radiolokatsii* [Fractals in radiophysics and radoilocation]. Moscow Logos Publ., 2002.
15. Malinetsky GG. *Khaos. Struktury. Komp'yuterny eksperiment. Vvedebie d nelineynuyu dinamiku* [Chaos. Structures. Computer experiment. Introduction to nonlinear dynamics]. Moscow, Editorial URSS Publ., 2002.
16. Ruell D, Takens D. *Comm. Math. Phys.*, 1971, 20(3):167.
17. Venttsel' ES. *Teoriya sluchaynykh protsessov i yeye inzhenernyye prilozheniya* [Theory of random processes and its engineering applications]. Moscow, Vysshaya shkola Publ., 2007, 479 p.
18. Kahaner D, Moler C, Nesh S. *Numerical Methods and Software.* Prentice-Hall, Inc. A Divisioon of Simon & Shuster Englewood Cliffs. NJ, 1989.
19. Bykov VV. Tsifrovoye modelirovaniye v statisticheskoy radiotekhnike [Digital modeling in statistical radio engineering]. Moscow, Sovetskoye radio Publ., 1971, 328 p.
20. Golenko DI. Modelirovaniye i statisticheskiy analiz psevdosluchaynykh chisel na elektronnykh vychislitel'nykh mashinakh [Modeling and statistical analysis of

pseudo-random numbers on electronic computers]. Moscow, Nauka Publ., 1965, 227 p.
21. Petrov AA. Komp'yuternaya bezopasnost'. Kriptograficheskiye metody zashchity [Computer security. Cryptographic methods of protection]. Moscow, DMK Publ., 2000, 445 p.

DOI: 10.17725/rensit.2022.14.463

Performance Comparison of Decoders of Non-orthogonal Multiple Access Signals Considering Modulation and Coding Schemes from LTE Networks

Yakov V. Kryukov, Dmitry A. Pokamestov, Andrey A. Brovkin, Eugeniy V. Rogozhnikov
Tomsk State University of Control Systems and Radioelectronics, https://tusur.ru/
Tomsk 634050, Russian Federation
E-mail: kryukov.tusur@gmail.com, dmaltomsk@mail.ru, soldierbrovkin@gmail.com, udzhon@mail.ru

Received August 12, 2022, peer-reviewed August 19, 2022, accepted August 26, 2022

Abstract: **A comparative analysis of the performance of SL-SIC (Symbol-Level Serial Interference Cancellation) and CWL-SIC (Code Word-Level SIC) decoders of PD-NOMA (Power Domain Non-Orthogonal Multiple Access) baseband signals in a system with two users is presented. Real modulation and coding schemes (MCS) from the 3GPP LTE (Long Term Evolution of 3rd Generation Partnership Project) communication standard are used. The performance of CWL-SIC achievable in practice in real systems for all possible designs of a group PD-NOMA signal consisting of different pair combinations of noise-immune MCS has been obtained. With the help of mathematical modeling, weighting power factors that provide the maximum average performance of the group signal for two user channels are obtained. The high efficiency of CWL-SIC and the expediency of its use in real systems, especially in conditions of a low signal-to-noise ratio, are shown.**

Keywords: **access power domain, interference cancellation at the level of modulation symbols and at the level of code word, signal-to-noise ratio, bit error rate, quadrature amplitude modula-tion, modulation and coding schemes**

UDC 621.396.4

Acknowledgments: The work was supported by the Russian Science Foundation within the framework of 2022 competition "Conducting Research by Research Groups Led by Young Scientists" of the Presidential Program of Research Projects Implemented by Leading Scientists, including Young Scientists. Project No. 22-79-10148.

For citation: Yakov V. Kryukov, Dmitry A. Pokamestov, Andrey A. Brovkin, Eugeniy V. Rogozhnikov. Performance Comparison of Decoders of Non-orthogonal Multiple Access Signals Considering Modulation and Coding Schemes from LTE Networks. *RENSIT: Radioelectronics. Nanosystems. Information Technologies,* 2022, 14(4)463-472e. DOI: 10.17725/rensit.2022.14.463.

Contents

1. INTRODUCTION

The method of organizing multi-channel data transmission performed by many users is one of the key ways to increase the efficiency of multi-user communication systems. In modern multi-channel systems, Orthogonal Multiple Access (OMA) methods based on the maximum possible elimination of inter-channel interference are used. While developing physical layer protocols for the fifth generation (5G) networks, a new approach to providing multi-channel communication was proposed, which allows for controlled inter-channel interference to increase spectral efficiency. Such multiple access methods were called Non-Orthogonal Multiple Access (NOMA).

The NOMA group combines several approaches proposed by different teams. One of the most efficient approaches is non-orthogonal multiplexing of channels in the power domain (PD-NOMA) [1]. The advantage of PD-NOMA is that it can be jointly used with OMA, for example, with Orthogonal Frequency Division Multiple Access (OFDMA) and (or) with Space Division Multiple Access (SDMA) channels. The combination of these technologies makes it possible to perform multiplexing of users simultaneously in four domains: frequency, time, power, and space.

The formation of a PD-NOMA group signal is based on the principle of superposition coding [2]. The signals of different subscribers are summed up together, using different power weighting factors. The joint calculation of the weighting factors is based on a priori information about the state of the transmission channels. The highest weighting power factor is assigned to the subscriber with the lowest signal-to-noise ratio (SNR) so that it is possible for the subscriber to demodulate their own signal the most accurately. In contrast, the lowest power factor is assigned to the subscriber with the highest SNR, so that it is sufficient to perform accurate demodulation. Thus, users can be divided into "weak" (with low SNR) and "strong" (with high SNR). At the same time, the signal of the "weak" user has the highest power and vice versa.

PD-NOMA processing is carried out by the Serial Interference Cancellation (SIC) method [3], which consists in sequential decoding of user signals one after another. First, the most powerful signal of the "weak" user is decoded. Then it is regenerated (restored to its original state) and subtracted from the received group signal. After that, it is possible to decode the second most powerful signal, and so on, until the least powerful signal of the "strong" user is decoded.

2. PROBLEM STATEMENT

The main issue with the SIC decoder is that there is the possibility of making an error when eliminating interference signals, which leads to additional errors during decoding. There are two approaches to the SIC decoder implementation: the regeneration of interference noise at the level of modulation symbols, SL-SIC (Symbol-Level SIC), and at the level of a code word, CWL-SIC (Code Word-Level SIC). The advantage of CWL-SIC is that it makes it possible to use the error-correcting capability of a noise-immune decoder to reduce the likelihood of errors when eliminating an interference signal.

The disadvantage lies in an increase in the computational complexity of signal processing due to the need to perform additional decoding/encoding operations. Alternatively, SL-SIC has less precision in eliminating interference noise and less computational complexity. Therefore, the search for a compromise between CWL-SIC and SL-SIC is a pressing issue. The block diagram of SL-SIC and CWL-SIC receivers is shown in **Fig. 1**.

The performance gain of CWL-SIC relative to SL-SIC can be obtained graphically using the dependency of Bit Error Rate (BER) probability on SNR. As an example, **Fig. 2** shows these dependencies for the channel of a "strong" user. The PD-NOMA group signal is formed using 4-QAM and 64-QAM superpositions with weighting power factors equal to 0.85 and 0.15, respectively. Fig. 2 shows the range in which CWL-SIC provides the same BER value as SL-SIC, but at a lower SNR value. Let us call the difference in SNR at the same BER level the performance gain of CWL-SIC relative to SL-SIC.

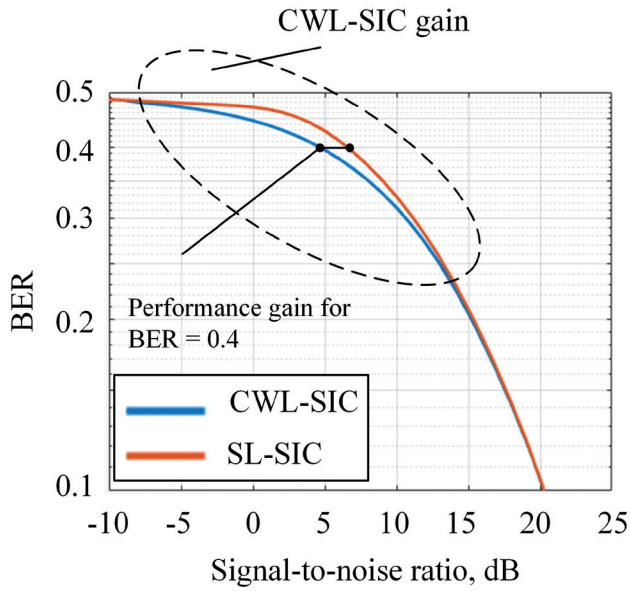

Fig. 2. *Gain in noise immunity of CWL-SIC relative to SL-SIC.*

Thus, CWL-SIC reduces the probability of erroneous signal decoding in a limited SNR range, increasing the system performance. The range limits and the amount of gain directly depend on the PD-NOMA signal structure. Currently, there is no limited set of structures that could be applicable in real PD-NOMA systems proposed. Therefore, a vital task is to develop and study various sets of PD-NOMA signal structures, and the

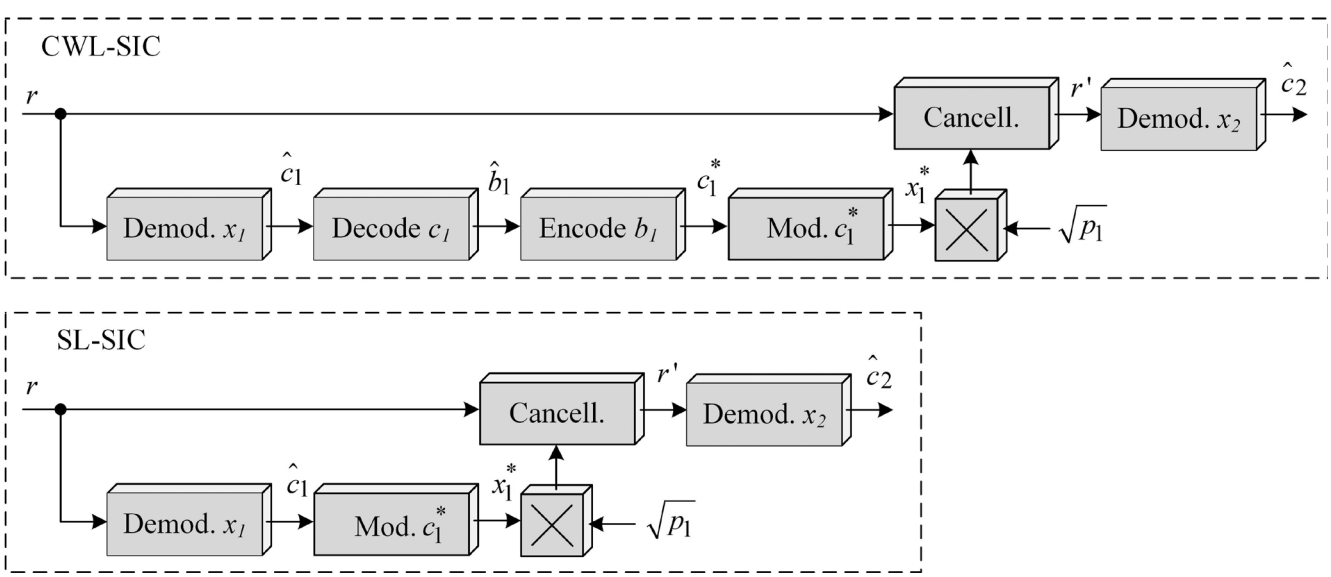

Fig. 1. *Block diagram of CWL-SIC and SL-SIC decoders.*

comparison of CWL-SIC and SL-SIC performance for these sets is an important direction to investigate.

In open access, there are works devoted to the study of CWL-SIC and its comparison with SL-SIC. Work [4] shows that the CWL-SIC performance is close to the SIC performance with an ideal compensation; however, the authors do not take into consideration the comparison of CWL-SIC with SL-SIC. In addition, the emphasis in this work is shifted to evaluating the impact of weight power factors to achieve the required level of data transmission quality.

In [5], the authors compare CWL-SIC and SL-SIC in the form of BER-SNR dependencies for a typical PD-NOMA signal configuration. The paper does not consider real modulation and coding schemes (MCS); therefore, the resulting performance cannot be obtained in practice in existing telecommunication systems.

A common disadvantage of the known works is that they use typical PD-NOMA scenarios, where 1–2 structures of a group signal are considered. They demonstrate the overall efficiency and prospects of CWL-SIC, but do not consider real structures consisting of real MCS (for example, from the 4G LTE or 5G NR standard). As a result, the matter of CWL-SIC efficiency assessment in a system with real MCS remains open.

The aim of this work is to determine the maximum achievable CWL-SIC performance gain in practice relative to SL-SIC for all possible PD-NOMA signal structures formed by the MCS superposition from the LTE standard.

3. SYSTEM MODEL

We consider a downlink PD-NOMA group channel, where the data of "weak" (UE_1) and "strong" (UE_2) users are transmitted. The formation of group signal s is described using the expression

$$s = \sqrt{p_1}x_1 + \sqrt{p_2}x_2 \ , \qquad (1)$$

where $\mathbf{p} = \{p_1, p_2\}$ are weighting power factors, and $\mathbf{x} = \{x_1, x_2\}$ is information QAM (Quadrature Amplitude Modulation) symbols of users UE_1, UE_2 with modulation orders $\mathbf{Q} = \{Q_1, Q_2\}$. The basic PD-NOMA scenario is used, according to which UE_1 receives the highest power factor, keeping to $p_1 > p_2$. The sum of power coefficients $p_1 + p_2 = 1$.

The model uses a transmission channel with complex additive white Gaussian noise (AWGN). The signal at the input of the SIC decoder UE_2 is described, using the expression

$$r = s + n, \qquad (2)$$

where $n \sim CN(0,N)$ is the implementation of complex AWGN with zero expectation and power N. Let us denote the signal-to-noise ratio in the channel by variable W. UE_1 signal decoding in CWL-SIC and SL-SIC is implemented in the same manner; therefore, the signal decoding on the UE_2 side implemented in two consecutive stages is further considered. First, symbols $\hat{x}_1$ of the "weak" user are evaluated in background and interference noise from the "strong" user $\sqrt{p_2}x_2 + n$, using the criterion of the minimum Euclidean distance:

$$\hat{x}_1 = arg \min_{x_1 \in A_1} \left| r - \sqrt{p_1}x_1 \right|^2 , \qquad (3)$$

where $\mathbf{A}_1$ is the alphabet of all possible states in Q_1-QAM constellation.

The interference noise is eliminated by generating compensation signal x_1^* from $\hat{x}_1$ and subtracting its weighted component $\sqrt{p_1}x_1^*$ from r. Consider the formation of x_1^* in SL-SIC and CWL-SIC.

In SL-SIC, symbol x_1^* is formed directly from $\hat{x}_1$, so $x_1^* = \hat{x}_1$. The errors made during the execution of (3) are not eliminated.

In CWL-SIC, the formation of x_1^* is carried out in several successive stages (Fig. 1):

- QAM demodulation of $\hat{x}_1$ according to constellation map Q_1-QAM; code word $\hat{\mathbf{c}}_1$ is formed at the demodulator output.
- Noise-immune decoding of $\hat{\mathbf{c}}_1$; message $\hat{\mathbf{b}}_1$, in which bit errors are eliminated if possible, is formed at the output.
- Noise-immune coding of $\hat{\mathbf{b}}_1$; regenerated code word c_1^* is formed at the output.
- QAM modulation of c_1^* according to constellation map Q_1-QAM; compensation signal x_1^* is formed at the output of modulator.

The interference noise elimination is described using the expression

$$r' = r - \sqrt{p_1}x_1^*, \quad (4)$$

where r' is the signal after compensation containing only the UE_2 signal. Next, r' is demodulated and its own useful symbols $\hat{x}_2$ are evaluated, perceiving only noise n as interference:

$$\hat{x}_2 = arg\min_{x_2 \in \mathbf{A}_2} \left| r' - \sqrt{p_2}x_2 \right|^2, \quad (5)$$

where $\mathbf{A}_2$ is the alphabet of all possible states in constellation Q_2-QAM.

To compare SL-SIC and CWL-SIC, it is required to obtain performance for various structures of the group PD-NOMA signal. Further, we describe the approach of calculating BER and provide group signal structures used.

3.1. Calculation of BER for SL-SIC and CWL-SIC

Let us denote $\boldsymbol{\rho} = \{\rho_1, \rho_2\}$ the probability of bit errors at Q_1, Q_2-QAM demodulation of $\hat{x}_1$, $\hat{x}_2$ in the UE_2 receiver. In communication systems, data transmission is carried out with the required level of quality that is determined by the acceptable error probability during reception.

Let us denote by variables ρ_1^z, ρ_2^z the maximum allowable (threshold) probability of bit errors in $\hat{\mathbf{c}}_1$, $\hat{\mathbf{c}}_2$ at the output of the demodulator (input of the decoder). In real systems, values ρ^z are calculated in such a way that the decoder can correct bit errors with a high probability. Therefore, to simplify the work, we hold to the assumption, according to which all errors in the compensation signal are corrected in CWL-SIC if the error probability at the decoder input does not exceed the threshold error, i.e. $\rho_1 \le \rho_1^z$. There is the need for simplification as it is not possible to derive such a general analytical expression to calculate ρ_2 that would consider the omission of bit errors at the decoding/encoding stage in the UE_1 compensation signal.

In SL-SIC, ρ_2 is calculated using (20) from [6]: it takes into account that the accuracy of the "weak" user channel demodulation influences the accuracy of the "strong" user channel demodulation. Let us describe the calculation of ρ_2 in CWL-SIC and look into two situations that occur when demodulating the UE_1 signal in the UE_2 receiver.

1) When demodulating $\hat{x}_1$, the bit error probability is $\rho_1 \le \rho_1^z$. According to

the assumption made, all bit errors in the UE_1 signal are corrected, allowing for the formation of an accurate compensation signal x_1^* and its ideal elimination from r (4). Then, the signal after compensation r' is a normal Q_2-QAM signal with power p_2. In this case, ρ_2 is calculated by formula (10) from [7], taking into account that $E_s = p_2$.

2) When demodulating $\hat{x}_1$, the bit error probability is $\rho_1 > \rho_1^z$. The decoder does not correct bit errors in the UE_1 signal, which leads to incorrect formation of x_1^* and its inaccurate elimination from r, and the signal after elimination r' is demodulated with errors. In this case, it is impractical to use CWL-SIC, because the correcting ability of the decoder does not allow increasing the accuracy of x_1^* formation. The decoding of the group signal is carried out by SL-SIC, and formula (20) from [6] is used for ρ_2 calculation.

3.2. Characteristics of MCS used for transmission

PD-NOMA group signals consist of MCS used in the 3GPP Long Term Evolution (LTE) standard and based on QAM and Turbo codes. There have been 15 MCS identified. There characteristics are shown in **Table 1**, where Q is a modulation order; $R_c/1024$ is an encoding rate; Z is a threshold level of SNR, at which 10% BLER is provided; ρ^z is a bit error probability at the decoder input, at which 10% BLER is obtained at the decoder output, that is, the specified level of information transmission quality is provided.

The value of Z is determined by the decoding algorithm, and it is possible to reduce it using more efficient and complex algorithms. Our paper uses the Z values for MCS LTE obtained in [8].

Table

SCC from 3GPP LTE

i	Q	Rc	Z	ρ^z
1	4	78	-9.478	0.3685517
2	4	120	-6.658	0.3208912
3	4	193	-4.098	0.2663857
4	4	308	-1.798	0.2081311
5	4	449	0.399	0.1476374
6	4	602	2.424	0.0931680
7	16	378	4.489	0.1779069
8	16	490	6.367	0.1354970
9	16	616	8.456	0.0903190
10	64	466	10.266	0.1479521
11	64	567	12.218	0.1113804
12	64	666	14.122	0.0787522
13	64	772	15.849	0.0516968
14	64	873	17.786	0.0265724
15	64	948	19.809	0.0096117

3.3. Formation of PD-NOMA group signal structures

The group PD-NOMA signal structure means a pair of MCS with indices i_1, i_2 (taken from Table 1) and a pair of weighting power factors p_1, p_2 used for UE_1 and UE_2 data transmission. The structures are compiled from paired combinations of MCS (Table 1) according to the "each with each" principle. The combination number is indicated by symbol j, and the total number of combinations $J = 120$. **Fig. 3** shows the number of the compiled structures and paired MCS combinations from Table 1 assigned to them. For example, the tenth ($j = 10$) structure is composed of two MCS with indices $i_1 = 1$ (for transmitting UE_1) and $i_1 = 10$ (for transmitting UE_2).

3.4. Calculation of weighting power factors

The use of QAM imposes a restriction on the ratio between p_1 and p_2, violation of which inevitably leads to incorrect

MCS index of the «strong» user

MCS index of the «weak» user	1	2	3	4	5	6	7	8	9	10	11	12	13	14	15
1	1	2	3	4	5	6	7	8	9	10	11	12	13	14	15
2		16	17	18	19	20	21	22	23	24	25	26	27	28	29
3			30	31	32	33	34	35	36	37	38	39	40	41	42
4				43	44	45	46	47	48	49	50	51	52	53	54
5					55	56	57	58	59	60	61	62	63	64	65
6						66	67	68	69	70	71	72	73	74	75
7							76	77	78	79	80	81	82	83	84
8								85	86	87	88	89	90	91	92
9									93	94	95	96	97	98	99
10										100	101	102	103	104	105
11											106	107	108	109	110
12												111	112	113	114
13													115	116	117
14														118	119
15															120

PD-NOMA configuration index

Fig. 3. *PD-NOMA group signal configurations.*

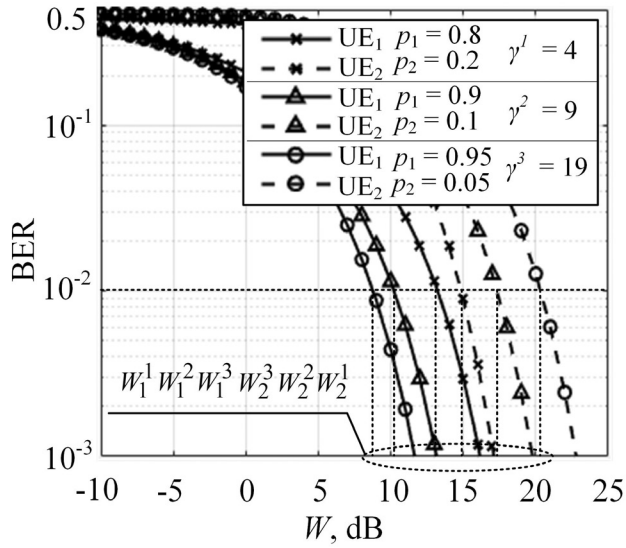

Fig. 5. *Noise immunity of channels with different distribution p_1, p_2.*

superposition of signals and an increase in the number of errors at the reception. Let us denote this relation by $\gamma = p_1/p_2$. Power factors should be selected in such a way that the symbols of the UE$_2$ constellation are located inside the symbol detection area in the UE$_1$ constellation. The boundaries of the detection areas are marked in **Fig. 4** with dotted lines by the example of a group signal constellation composed of two 16-QAM.

The restriction on **p** is written as follows

$$\begin{cases} \dfrac{\left(\sqrt{Q_2}-1\right)(Q_1-1)}{Q_1\left(\sqrt{Q_2}-1\right)+2} < p_1 \le 1 \\ 0 \le p_2 < 1 - \dfrac{\left(\sqrt{Q_2}-1\right)(Q_1-1)}{Q_1\left(\sqrt{Q_2}-1\right)+2} \end{cases}. \quad (6)$$

p_1 increase leads to p_2 decrease, which is the reason for an increase in the UE$_1$ signal performance and a decrease in the UE$_2$ signal performance, and vice versa. This is shown in **Fig. 5**, which demonstrates

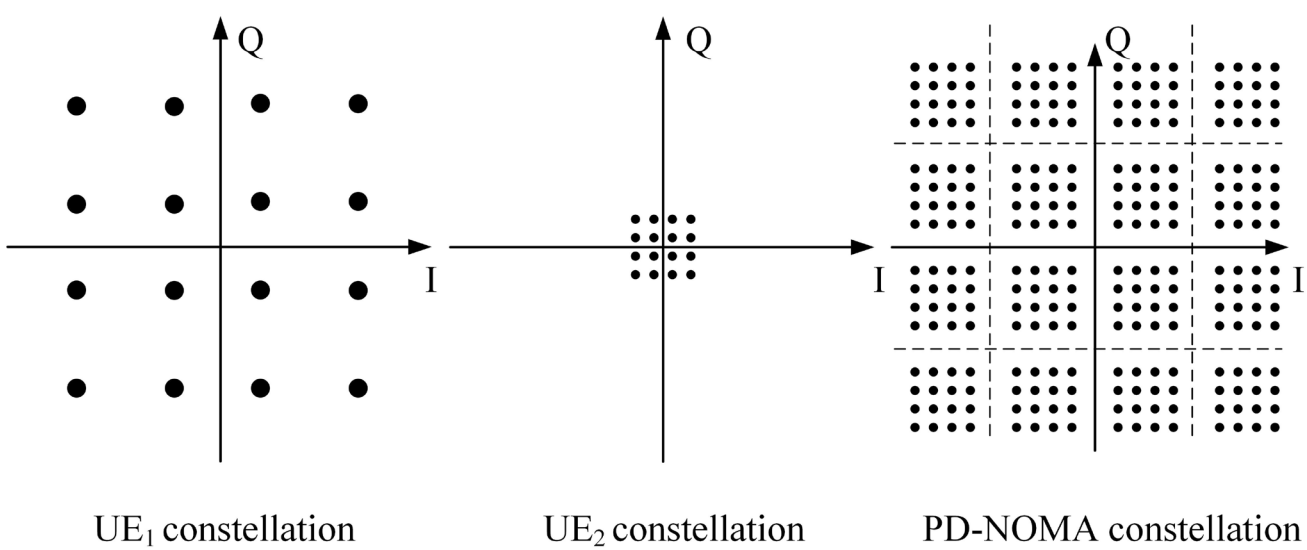

Fig. 4. *Constellation of group PD-NOMA signal.*

examples of $\boldsymbol{\rho}$ dependencies on W for three different $\mathbf{p}$ distributions in the group PD-NOMA signal.

In general, there are an unlimited number of γ values that satisfy constraint (6). One of the problems stated is to determine a single γ for each structure that provides maximum performance. This problem is solved by brute-force search.

Taking into account (6), the compilation of sample $\boldsymbol{\nu}_j = \{\gamma_j^1, \gamma_j^2, ..., \gamma_j^K\}$ of all possible ratios with given discrete increment Δ of change in γ value participating in brute-forcing is performed for structure j. The sample size is denoted by K, and the k index denotes a specific element of the sample.

To evaluate performance, metric of sustained performance W_{m} is introduced, which shows the average SNR value in user channels, at which the threshold probability of a bit error ρ^z during their demodulation is reached. For the k-th ratio of power coefficients, value W_m^k is calculated using formula

$$W_m^k = 10\log_{10}\left(\frac{10^{\frac{W_1^k}{10}} + 10^{\frac{W_2^k}{10}}}{2}\right), \quad (7)$$

where W_1^k and W_2^k are SNR values (on a linear scale) in channels UE_1 and UE_2, at which ρ_1^z, ρ_2^z is reached. Values W_1^k and W_2^k can be determined graphically using dependency $\rho(\text{W})$.

Let us consider an example of calculating W_m^k to get ρ_1^z, ρ_2^z = 10^{-2} and select γ for a specific PD-NOMA signal structure. Fig. 4 shows the dependencies of BER on SNR for three ratios: γ^1 = 4, γ^2 = 9, γ^3 = 19. Ratio γ^1 requires that SNR values W_1^1 = 8.75dB for UE_1 and W_2^1 = 20.3 dB for UE_2. Similarly, for ratios γ^2, γ^3, it is required that W_1^2 = 10.2 dB, W_2^2 = 17.3 dB and W_1^3 = 13.25 dB, W_2^3 = 14.8 dB. W_{m} calculated by formula (7) for γ^1, γ^2, γ^3 are the following: W_m^1 = 17.58 dB, W_m^2 = 15.06 dB, and W_m^3 = 14.09 dB. Comparing these values, one can conclude that γ^3 has the maximum energy efficiency, because given ρ_1^z, ρ_2^z = 10^{-2} is reached at a minimum averaged SNR equal to W_m^3 = 14.09 dB. Accordingly, the distribution of power factors is p_1 = 0.95, p_2 = 0.05.

Using the approach described above, the power factors for all PD-NOMA group signal structures (Fig. 3) are determined using mathematical modeling by the brute-force search, providing maximum sustained performance W_{m} for each of them. **Fig. 6** shows p_1 values for each structure, and p_2 can be calculated using $p_2 = 1 - p_1$.

3.5 Calculation of performance gain

For all PD-NOMA group signal structures with the corresponding factors obtained (Fig. 6), dependency $\rho_2(\text{W})$ at the SL-SIC and CWL-SIC output is calculated in the range $W \in [-10, 45]$ with step ΔW = 0.1 dB. After that, the graphical method is used to search for SNR W^{SL} and W^{CWL} values, at which the level of the bit error probability $\rho_2\left(W^{SL}\right) = \rho_2^z$ and $\rho_2\left(W^{CWL}\right) = \rho_2^z$. set for each MCS is provided. The performance gain of CWL-SIC relative to SL-SIC is calculated by formula

$$G = W^{SL} - W^{CWL}. \quad (8).$$

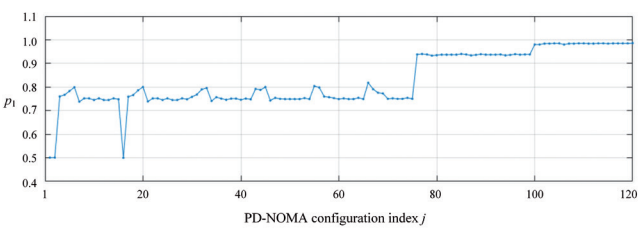

Fig. 6. *Factors p_1 obtained for all structures.*

4. ANALYSIS OF SIMULATION RESULTS

The values of G for all group PD-NOMA signal structures are obtained using the mathematical model and are shown in **Fig. 7**. The simulation result demonstrated that the maximum gain in CWL-SIC performance is achieved in PD-NOMA signals consisting of noise-immune MCS. This is due to the fact that the operational range of the signal-to-noise ratio of noise-immune MCS coincides with the effective range of CWL-SIC, so the greatest performance gain of noise-immune MCS is provided by PD-NOMA signal configurations.

Analyzing the obtained result, it can be concluded that CWL-SIC provides a significant performance gain of the "strong" user channel that lies in the range of 1.5-6.4 dB for noise-immune MCS (indices 1–6). When using less noise-immune, but higher-rate MCS (indices 7–15), the performance gain lies in the range of 0-1.5 dB. This proves the high efficiency of CWL-SIC and the feasibility of its use in real systems, especially under conditions of a low signal-to-noise ratio.

The following is an illustrative example demonstrating the gain in performance G for the second ($j = 2$) structure, which is the result of MCS superposition with indices $i_1 = 1$, $i_2 = 2$ (Table 1) at $p_1 = 0.510$,

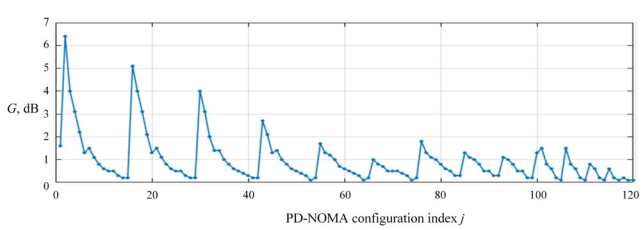

Fig. 7. *CWL-SIC performance gain relative to SL-SIC for all configurations.*

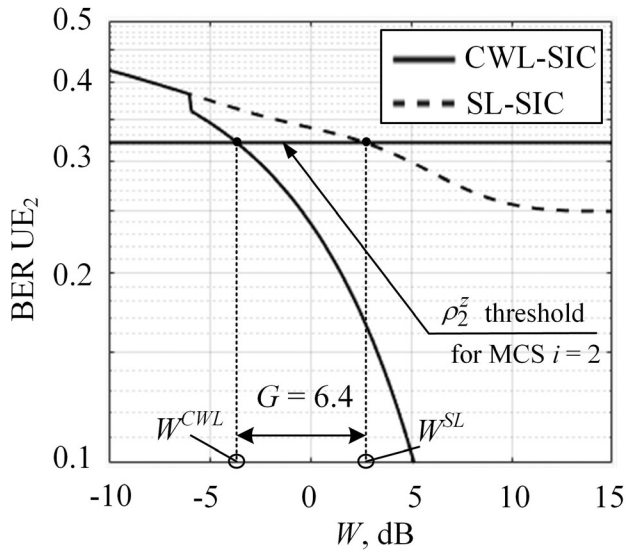

Fig. 8. *Evaluation of performance gain for the second group PD-NOMA signal structure.*

$p_2 = 0.490$ (Fig. 6). **Fig. 8** shows dependency $\rho_2(W)$ and threshold level $\rho_2^z = 0.3208912$ (Table 1). The SNR values, at which $\rho_2 = \rho_2^z$ is reached: $W^{SL} = 2.8$, $W^{CWL} = -3.6$ are found graphically. Accordingly, the performance gain for the second structure can be calculated by (8) and $G = 6.4$ dB.

5. CONCLUSION

The paper presents a comparative performance analysis of two SIC approaches to decoding PD-NOMA group signals in a system with two users. The key feature of the work is that the PD-NOMA system under consideration with two users exploits real MCS from the 3GPP LTE communication standard.

A set of 120 group PD-NOMA signal structures that can be used for data transmission in PD-NOMA systems is formed from paired MCS combinations following the "each with each" principle. For each structure, we have found the weighting power factors providing maximum sustained performance for two user channels by means of the brute-force method.

It is shown that the maximum CWL-SIC performance gain relative to SL-SIC is reached in the PD-NOMA group signals composed of noise-immune MCS. CWL-SIC provides a significant performance gain of the "strong" user channel that lies in the range of 1.5–6.4 dB for noise-immune MCS (indices 1–6). When using less noise-immune, but higher-rate MCS (indices 7–15), the performance gain lies in the range of 0–1.5 dB. This proves the high efficiency of CWL-SIC and the feasibility of its use in real systems, especially under conditions of a low signal-to-noise ratio.

REFERENCES

1. Benjebbour A, Saito K, Li A, Kishiyama Y, Nakamura T. Non-orthogonal multiple access (NOMA): Concept, performance evaluation and experimental trials. *Proc. International conference on wireless networks and mobile communications* (WINCOM), 2015:1-6. DOI: 10.1109/WINCOM.2015.7381343.
2. Vanka S, Srinivasa S, Gong Z, Viki P, Stamatiou K, Haenggi M. Superposition coding strategies: Design and experimental evaluation. *IEEE Transactions on Wireless Communications*, 2012, 11(7):2628-2639.
3. Higuchi K, Benjebbour A. Non-orthogonal multiple access (NOMA) with successive interference cancellation for future radio access. *IEICE Transactions on Communications*, 2015, 98(3):403-414.
4. Saito K, Benjebbour A, Harada A, Kishiyama Y, Nakamura T. Link-level performance of downlink NOMA with SIC receiver considering error vector magnitude. *IEEE 81st Vehicular Technology Conference* (*VTC Spring*), 2015:1-5. DOI: 10.1109/VTCSpring.2015.7145913.
5. Yan C, Harada A, Benjebbour A, Lan Y, Li A, Jiang H. Receiver design for downlink non-orthogonal multiple access (NOMA). *IEEE 81st Vehicular Technology Conference* (*VTC Spring*), 2015:1-6. DOI: 10.1109/VTCSpring.2015.7146043.
6. Assaf T, Al-Dweik A, El Moursi M, Zeineldin H, Al-Jarraj M. Exact bit error-rate analysis of two-user NOMA using QAM with arbitrary modulation orders. *IEEE Communications Letters,* 2020, 24(12):2705-2709.
7. Kryukov Y, Pokamestov D, Novichkov S. Symbol Error-Rate Analytical Expressions for a Two-User PD-NOMA System with Square QAM. *Symmetry,* 2021, 13(11):2153.
8. Fan J, Yin Q, Li G, Peng B, Zhu X. MCS selection for throughput improvement in downlink LTE systems. *Proceedings of 20th international conference on computer communications and networks* (ICCCN), 2011:1-5.

DOI: 10.17725/rensit.2022.14.473

Natural Nucleosynthesis

Gennady V. Mishinsky
Joint Institute for Nuclear Research, http://www.jinr.ru/
Dubna 141980, Moscow Region, Russian Federation
E-mail: mysh@jinr.ru

Vladimir D. Kuznetsov
Center for Applied Physical Researches, http://cpfi.wallst.ru/
Dubna 141980, Moscow Region, Russian Federation
E-mail: kuznetsov@mail.ru

Victor I. Starostin
Lomonosov Moscow State University, http://msu.ru/
119234 Moscow, Russian Federation
E-mail: vistar.geol@gmail.com

Received September 12, 2022, peer-reviewed September 19, 2022, accepted September 26, 2022

Abstract: **The possibility of generating strong and ultrastrong magnetic fields in condensed ionized media in the presence of unidirectional motion of an ensemble of free electrons with a density > 10^{21} e/cm^3 is demonstrated. It is shown that atomic and nuclear matter in strong and ultrastrong magnetic fields is transformed into a new state of matter - into transatom, in which atomic electrons and nuclear protons and neutrons are bound in pairs into orthobosons with a spin equal to unity S = 1ħ. Examples of radiationless, low-energy nuclear reactions of transatoms, including those without the Coulomb barrier between identical atomic nuclei, are presented. The mechanism of natural nucleosynthesis, based on the results of the low-energy nuclear reactions registered in various experiments in many laboratories of the world and on the creation of the theory of those reactions, at different stages of the development of the Universe, stars and planets is presented.**

Keywords: **low energy nuclear reactions, multinuclear reactions, nuclear reactions without a Coulomb barrier, resonant interference exchange interaction, electron pairing, strong magnetic fields, quantum physics, nucleosynthesis**

PACS: 03.75.Mn; 03.75.Nt; 25.60.Pj; 25.70.Hi; 26.00.00; 31.10.+z; 32.10.-f; 52.25.Xz

For citation: Gennady V. Mishinsky, Vladimir D. Kuznetsov, Victor I. Starostin. Natural Nucleosynthesis. *RENSIT: Radioelectronics. Nanosystems. Information technologies,* 2022, 14(4):473-496e. DOI: 10.17725/rensit.2022.14.473.

1. INTRODUCTION

In 1989-1992 of the last century, low-energy nuclear reactions: cold nuclear fusion reactions and low-energy transmutation reactions of chemical elements were discovered [1-3]. It turned out that nuclear reactions with the transformation of some chemical elements into other chemical elements can occur in ionized, weakly excited condensed media with low, only ~ 1 eV/atom in the reaction region excitation energy. This phenomenon was called: low-energy transmutation of chemical elements (hereinafter referred to as Transmutation).

The methods of the experiments on transmutation are extremely diverse and they are radically different from the methods of nuclear physics. Transmutation reactions were detected and subsequently reproduced in a glow gas discharge [4-6]; at industrial, electronic, zone melting of zirconium ingots in a vacuum furnace [7]; at explosions of metal targets irradiated by a powerful electron pulse [8,9]; at explosions in liquid dielectric media of metal foils through which a powerful electric current pulse was passed [10,11]; when a lead-copper melt was exposed to a pulsed current [12]; at the passage of electric current in water-mineral media [3]; at ultrasonic treatment of aqueous salt solutions [13]; at irradiation of condensed gases with braking gamma quanta [14-16]; in growing biological structures [17-19] and in many other cases [1-3]. The results of transmutation experiments, despite their diversity, are qualitatively similar to each other.

Transmutation reactions are carried out for all chemical elements, starting with hydrogen, and they occur, as a rule, with the participation of a large number of atomic nuclei, both in the input and output channels of reactions. Experiments show that all chemical elements can be synthesized in transmutation reactions. At that, the reaction products − isotopes of chemical elements − are stable, i.e. non-radioactive.

The appearance of "extraneous" chemical elements under "soft" physical conditions in relatively simple experiments led, almost immediately, their authors to the idea of a low-energy natural synthesis of chemical elements in the Universe.

2. LOW-ENERGY TRANSMUTATION OF ATOMIC NUCLEI OF CHEMICAL ELEMENTS

− A necessary condition for starting the transmutation reactions of atomic nuclei of chemical elements is the presence of atoms in a strong magnetic field $B > 30$ *T*.

− A sufficient condition for transmutation reactions is the presence of unidirectional motion of an ensemble of free electrons with a density of $\rho > 10^{21}$ el/cm^3 in ionized condensed media. The ensemble of such electrons exactly generates strong magnetic fields $B > 30$ *T*.

Both of these processes are characterized by the pairing of both atomic and free electrons into orthobosons with a spin equal to the unit $S = 1\hbar$. The pairing of electrons is associated with the fundamental manifestation, in strong magnetic fields, of an additional, exchange Coulomb interaction between them, and the appearance of new oscillation quantum numbers of electrons.

Analysis of experiments on the transmutation of chemical elements and their results showed that they occur in strong, over 30 *T*, magnetic fields. It turned out that atomic and nuclear matter is transformed into a new state of matter in strong and ultrastrong magnetic fields: spin electron nuclide condensate. A characteristic feature of such a condensate is that it contains paired electrons and paired protons and neutrons (fermions with a spin equal to $s = 1\hbar/2$) in a bound state, in the state of orthobosons, when the total spin of each pair is equal to unit $S = 1\hbar$.

2.1. Magnetic fields in condensed matter

Magnetic fields begin to originate in ionized, gaseous and liquid media as a result of unidirectional flows of free electrons with a density of more than 10^{21} cm^{-3} passing through them [20]. These magnetic fields originate to the magnetic moments of μ_e electrons, which are

parallel to each other in a unidirectional flow. Due to the helicity property of electrons $\mathbf{p}_e \uparrow\uparrow \boldsymbol{\mu}_e$ ($\mathbf{s}_e \downarrow\uparrow \mathbf{p}_e$), the magnetic moments of electrons that move in one direction are mainly directed parallel to their pulses $\mathbf{p}_e$. Thus, an ensemble of electrons moving in one direction generates, in accordance with the Landau formula (1) [21], a seed magnetic field $\mathbf{B}_{\mu 0}$. The direction of the field $\mathbf{B}_{\mu 0}$ coincides, on the average, with the direction of motion of the electrons.

$$\mathbf{B}_{\mu(S)} = \mu_0 \sum_i \frac{3\mathbf{n}_i (\boldsymbol{\mu}_e \cdot \mathbf{n}_i) - \boldsymbol{\mu}_e}{r_i^3}, \quad (1)$$

where $\mu_0 = 1.26 \cdot 10^{-6}$ Gn/m is the magnetic constant; $\mu_e = 9.29 \cdot 10^{-24}$ J/T $= 5.79 \cdot 10^{-5}$ eV/T, r_i is the distance from the electron to the point at which the field $\mathbf{B}_\mu$ is calculated; $\mathbf{n}_i$ is a unit vector in the direction r_i, i – is the number of electrons with parallel spins. The formula (1) shows that the magnetic moment of the electron $\boldsymbol{\mu}_e$ creates a magnetic field equal to 30 T at a distance of 0.092 nanometers along its direction axis (the diameter of hydrogen atom is 0.106 nm).

Due to its nature, the field $\mathbf{B}_{\mu 0}$ generated by the sum of magnetic moments of the electrons is spatially inhomogeneous and anisotropic field. Therefore, free electrons that move in a changing field $\partial \mathbf{B}_{\mu 0}/\partial t$ and have an antiparallel orientation of magnetic moments will change the direction of the latter, $\mathbf{B}_{\mu 0} \uparrow\downarrow \boldsymbol{\mu}_e \rightarrow \mathbf{B}_{\mu 0} \uparrow\uparrow \boldsymbol{\mu}_e$. Thus, the number of free electrons in a state with magnetic moments parallel to the field increases, until the moment when most of the electrons enter this state. Consequently, the seed magnetic field will increase until saturation of $\mathbf{B}_\mu$.

The magnetic moments of the electrons are parallel to each other and antiparallel to their spins $\mathbf{s}_e \downarrow\uparrow \boldsymbol{\mu}_e$. Consequently, the spins of the electrons also become parallel. A magnetic, spin plasma is formed.

Since the electron spins in the spin plasma are parallel, then, in addition to the magnetic field, the electrons generate an exchange, self-consistent field with a negative potential in the plasma volume [22,23]. Electrons with parallel spins are attracted to each other due to the exchange interaction. The Coulomb repulsion of electrons at densities of ~ 10^{21} см$^{-3}$ is compensated by their attraction to positively charged ions, since the Debye radius, i.e. the distance over which the action of the electric field of a single charge in a quasi-neutral medium extends, has an atom size of ~ 10^{-8} см.

The electrons with parallel spins are forced, in the negative potential of the exchange field, to pair into orthobosons with spin S = 1ħ in order to comply with the Pauli principle. Such pairing is carried out due to the appearance of new – oscillation quantum numbers in the electrons in the magnetic field n_b [24]. An orthoboson pair of electrons is a toroidal, annular current of radius R_Z which rotates around an oncoming flow of positive ions that moves at a speed V_i (**Fig. 1***a*). The orthoboson has external and internal strong magnetic fields B_μ of more than 30 T and a strong electric field. External magnetic fields connect orthobosons into electronic orthoboson "solenoids" – "capsules" (Fig. 1*b*). "Capsules" can have a different number of orthobosons. They can fly out the condensed matter. Then the "capsules" are registered as unknown, as "strange" particles [7,10,20].

Consequently, the electrons, which move in the local regions of ionized, gas or liquid plasma unidirectionally and have a density of ≥10^{21} см$^{-3}$, the pairing of electrons into orthobosons S = 1ħ will be carried out automatically. Electronic orthobosons generate strong magnetic fields $B > 30$ *T* in condensed matter.

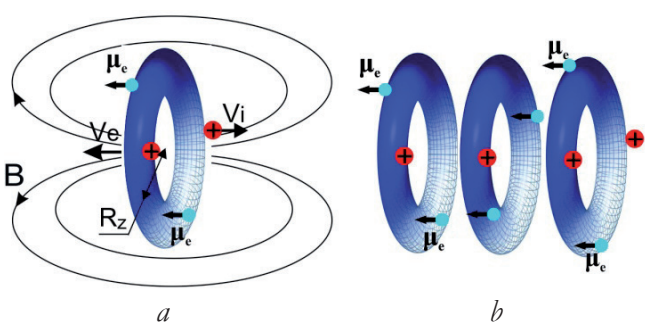

a *b*

Fig. 1. *a – orthoboson;, b – "capsule" – orthoboson "solenoid".*

2.2. Transatoms. Spin nuclide electron condensate

The atoms turn into transatoms in the internal, strong magnetic fields of the "capsules" $B_\mu >$ 30 T [24]. The electrons are also paired into orthobosons in the transatom.

In the absence of a strong magnetic field **B,** firstly, the Coulomb repulsion forces between atomic electrons do not have a dedicated direction. Their average values for the spatial *x, y* and *z* components are zero: $\overline{Fx}=0, \overline{Fy}=0, \overline{Fz}=0$. The electron moves around the nucleus not in a plane, but along a trajectory that resembles a "thread in a clue" [25].

Therefore, secondly, despite the fact that the orbital moments for *p, d, f* - electronic states are different from zero ($\ell \neq 0$), the average values of the orbital and orbital magnetic moments for the *x, y* and *z* components are zero: $\overline{\ell x}=0, \overline{\ell y}=0, \overline{\ell z}=0$ and $\overline{\mu_{\ell x}}=0, \overline{\mu_{\ell y}}=0, \overline{\mu_{\ell z}}=0$. As a result, the magnetic field created by the orbital motion of the electron is reset to zero, $B_i = 0$ (2).

In a strong magnetic field, each electron breaks its **ℓ + s** and **j + j** bonds throughout the atom, not only on the outer, but also on the inner orbitals. The spin *s* and orbital **ℓ** moments of each individual electron independently interact with the external magnetic field **B**. The magnetic field **B**, which has a constant orientation, rigidly aligns the electronic orbitals **ℓ** with respect to its direction in accordance with their magnetic quantum numbers m_ℓ.

The average values of the orbital moments for the *x, y* and *z* components cease to be zero: $\overline{\ell x}\neq 0, \overline{\ell y}\neq 0, \overline{\ell z}\neq 0$. The orbital moments of electrons "freeze" into the magnetic field. An atom from an "amorphous" state is transformed into an ordered, magnetic "crystal" (**Fig. 2***a*). Fig. 2*a* for the sodium atom shows the directions of the orbital moments **ℓ** and the spins **s** of the electrons. The values of magnetic $m_\ell = -1, 0, +1$ and spin $m_s = \pm 1/2$ quantum numbers are given. Yellow circles are S-states $\ell = 0$. Fig. 2*b* shows the fine splitting of the internal, electronic levels in the sodium atom. Electronic states with equal

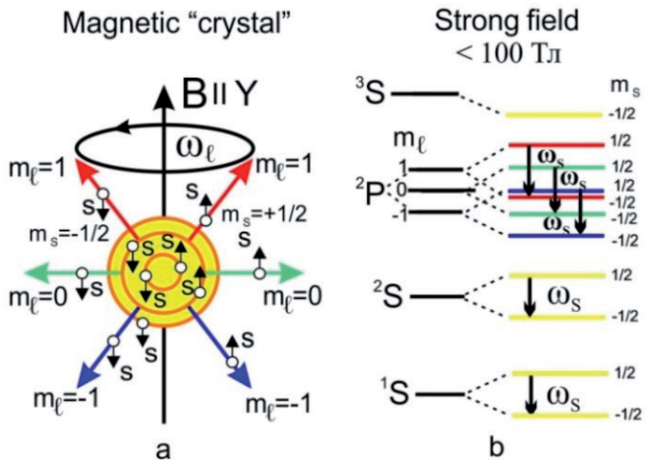

Fig. 2. *a – "frozen" orbitals of the sodium atom, b – the splitting of internal levels in the sodium atom.*

orbital ℓ and magnetic m_ℓ quantum numbers are split into two spin levels with $m_S = \pm 1/2$. The frequency w_S of transitions between them is equal to:

$\omega_S = 2 \cdot \mu_e B/\hbar$.

The frequency ω_S does not depend on the orbital moment of the electron ℓ and on the charge of the nucleus *Z*! All atoms in a strong magnetic field become an "active medium".

In accordance with the orientation, orbital angular momentum **ℓ** of each electron and the resulting orbital magnetic moment $\boldsymbol{\mu}_\ell = -\mu_e \boldsymbol{\ell}/\hbar$ (**Fig. 3***a*) independently precess around the direction of the vector of the external magnetic field with the same Larmor frequency:

$\omega_\ell = \mu_e B/\hbar$.

The orbital magnetic moment $\boldsymbol{\mu}_\ell$ generates its own magnetic field $\mathbf{B}_\ell$ (2) that rotates with the same frequency ω_ℓ (Fig. 3*a*). The magnetic field is a directional, inhomogeneous, anisotropic field.

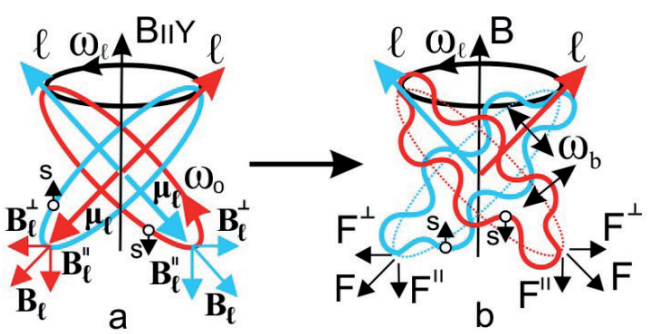

Fig. 3. *a –the formation of magnetic fields; b–the occurrence of oscillations.*

The field $\mathbf{B}_\ell$ is decomposed into components $\mathbf{B}_\ell^{\parallel}$ and $\mathbf{B}_\ell^{\perp}$ (Fig. 3*a*).

$$\mathbf{B}_\ell = \mu_0 \frac{3\mathbf{n}(\boldsymbol{\mu}_\ell \cdot \mathbf{n}) - \boldsymbol{\mu}_\ell}{r^3}. \quad (2)$$

Fig. 3*a* schematically shows two orbitals with equal orbital moments ℓ and their projections mℓ on the *Y* axis parallel to **B**, but with different directions of electron spins $s = \pm 1\hbar/2$. In accordance with the principle of least action, the orbitals of the electrons line up relative to each other with a shift of 180° so that the Coulomb repulsion forces between the electrons become minimal. The spins and magnetic moments of the electrons $\boldsymbol{\mu}_\mathbf{e}$ do not precess around **B**, since they are oriented only in two ways: $m_S = -1/2$ along the field and $m_S = +1/2$ against the field. Electronic orbitals with equal quantum numbers ℓ and m_ℓ precess around *B* synchronously with the frequency ω_ℓ (Fig. 3*a*). The orbital magnetic moments of the two orbitals $\boldsymbol{\mu}_\ell$ form a double magnetic field $2\mathbf{B}_\ell$, which maximum values create the effect of rotation of the field $2\mathbf{B}_\ell^{\perp}$ with a double frequency of $2\omega_\ell$. Thus, the magnetic field $2\mathbf{B}_\ell^{\perp}$ perpendicular to field **B**, and created by two orbitals, stimulates atomic transitions between levels $m_s = 1/2 \rightarrow m_s = -1/2$ (Fig. 2*b*).

This is intraatomic electronic magnetic resonance (IEMR).

In the absence of a strong magnetic field, the transitions $m_s = 1/2 \rightarrow m_s = -1/2$ are forbidden by virtue of the Pauli principle, since the states $m_S = -1/2$ are already occupied by electrons. But this is not the case in a strong magnetic field **B**, because the electrons in the field **B** have additional, oscillation quantum numbers $n_b = 1, 2, 3...$ In a strong magnetic field, the average values of the Coulomb repulsive forces **F** between atomic electrons for *x, y* and *z* components cease to be zero: $\overline{Fx} \neq 0, \overline{Fy} \neq 0, \overline{Fz} \neq 0$. The electrons move in their orbitals, which directions are rigidly connected to each other. These orbitals precess around the field **B**, but they are rigidly bound to its direction. Therefore, the powerful Coulomb repulsive forces between neighboring electrons, which in the absence of the **B** field would force the electron orbitals to rotate freely around the nucleus like "threads in a clue", now they cause the electrons to oscillate around the "frozen" orbitals (Fig. 3*b*) [24,26]. The frequency of these oscillations ω_b is connected to the rotation frequency of the electron in the orbital ω_0 and the precession frequency of its orbital moment ω_ℓ by the following relation [27,28]:

$$\omega_b = n_b \cdot \sqrt{\omega_0^2 + \omega_\ell^2}.$$

Oscillations are a new degree of freedom of the spatial motion of electrons. This new degree of freedom of motion generates a new spatial quantum number n_b for electrons. Thus, the exchange interaction, which attracts a pair of electrons to each other [29], and their antisymmetric coordinate wave function caused by oscillations $n_b^1 = -n_b^2$ ($\mathbf{p}_{e1} = -\mathbf{p}_{e2}$), allow electrons to create an orthoboson with S = 1ħ, by making the transition $m_s = 1/2 \rightarrow m_s = -1/2$. Electrons paired in the state $m_s = -1/2$ have equal orbital ℓ and magnetic m_ℓ quantum numbers, but they have different oscillatory quantum numbers n_b and $-n_b$.

In the whole atom, in all atoms that create an "active medium", $m_s = 1/2 \rightarrow m_s = -1/2$ forced transitions similar to transitions in quantum laser generators are carried out under the action of identical ω_{Sh} photons.

Electron oscillations are carried out both in the longitudinal and transverse directions of the magnetic field **B** ($F^{\parallel}$ and $F^{\perp}$, Fig. 3*b*). Since the electrons in the pair oscillate in the opposite phase n_b and $-n_b$, this movement allows two electrons in the same energy states to be in nonintersecting spatial regions. Electron trajectories can be represented as nested closed spirals located on the surface of a toroid.

Atoms whose electrons, not necessarily all, are in a paired state are called Transatoms (**Fig. 4**).

Atoms inevitably turn into transatomsin a strong magnetic field > 30 *T*!

Orthobosons are created in the whole atom. They form a spin Bose-Einstein electron

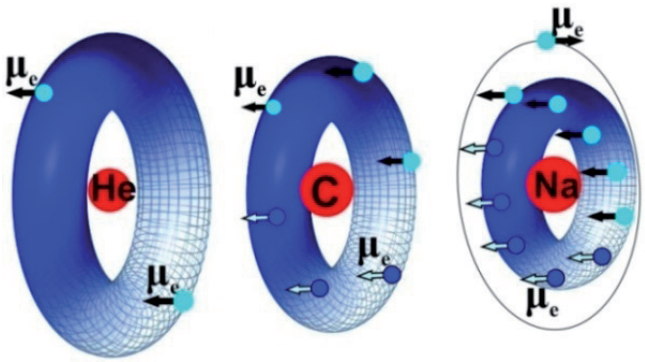

Fig. 4. *Examples of transatoms: helium, carbon, sodium.*

condensate. The magnetic moments of the electrons μ_e in the Bose condensate are directed in one direction, and they generate an ultrastrong directional, inhomogeneous and anisotropic magnetic field B_S ~10^5–10^{10} T (1) inside and around the transatom [30].

The internal ultrastrong magnetic field B_S^0 that interacts with the magnetic spin and magnetic orbital moments of the nucleons in the nucleus, changes the structure of the nucleus, and turns it into a Transnucleus. In the transnucleus, protons and neutrons in pairs are in the state of nuclear orthobosons when the total spin of each pair is equal to unit S = 1ħ. An intranuclear nucleon magnetic resonance occurs in the nucleus. It is important to note that due to the pairing of protons and neutrons into orthobosons, even-even nuclei with spin equal to zero I = 0, starting with helium ^{4}He [31], in an ultrastrong magnetic field acquire mechanical moments, which, apparently, must be either integer I = 1ħ, 2ħ…

The transnucleus with the Bose-Einstein electron condensate surrounding it form a new state of matter: a spin nuclide electron condensate [31,32].

The external ultrastrong magnetic fields B_S^R of transatoms attract them to each other. Electronic Bose condensates of two transatoms are combined into a common Bose condensate. A double transmolecule is formed from the transnuclei. Other transnuclei can join it. A Multinucleus Transmolecule {X} is formed, in which multinucleus reactions occur, including those that involve electron orthobosons. Thus, nuclear-electronic (strong-weak) reactions occur, which products are non-radioactive. Such reactions are called low-energy transmutation reactions. Low-energy nuclear reactions can occur with the formation of several nuclei in the output channel of the reaction. Atomic nuclei fly apart after such reactions are carried out. And, if they are not in a strong magnetic field, then the reaction products form ordinary nuclei and ordinary atoms.

2.3. Resonant interference exchange interaction

Transmutation reactions are carried out due to resonant interference exchange interaction (RIEX) [33].

A well-known exchange interaction occurs between identical objects: elementary particles, atoms, molecules. The nature of the exchange interaction is related to the indistinguishability of identical objects. The exchange interaction is manifested between identical particles 1 and 2, which are in states a and b, when their wave functions $\psi_a(1)$ and $\psi_b(2)$ overlap (**Fig. 5**). The more the wave functions of identical particles overlap, the greater is the exchange interaction. The exchange interaction is characterized by the exchange energy, which is an additional contribution to the total energy of the system. This is expressed in the fact that the energy of interacting identical particles contains an additional interference term, which is not zero due to the identity of the particles. The contribution of the exchange energy to the total energy of the system can be both negative and positive.

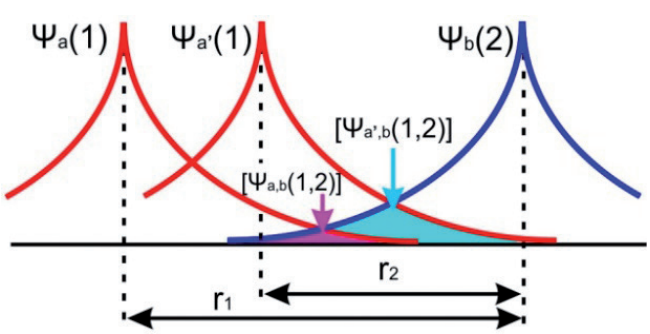

Fig. 5. *Overlap of wave functions of identical particles.*

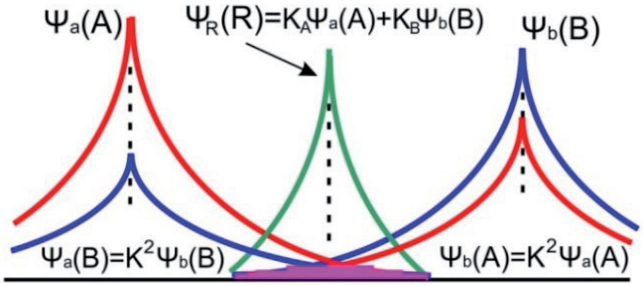

Fig. 6. *Overlap of wave functions of "identical" objects A and B during the formation of the R-state.*

It turned out that exchange interaction can occur between non-identical objects if these objects form a composite system that has resonant *R*-states $\psi_R(R)$ [33,34]. The nature of the RIEX-interaction is related to the overlapping and interference of the wave functions of objects in *R*-states. The wave functions of objects, including transnuclei A, B, C, interfere with each other, both in the R-state and "in each other" (**Fig. 6**). The wave functions of resonant *R*-states contain all wave functions of transnuclei A, B, C... Exactly, thanks to the wave functions of *R*-states, the transnuclei are simultaneously "in each other" through exchange interactions with each other. Fig. 6 demonstrates K_A и K_B as coefficients of the presence of wave functions $\psi_a(A)$ and $\psi_b(B)$ in the *R*-state, $K_2 \equiv K_A K_B$ is the generalized coefficient of similarity of the transnuclei A and B to each other.

The *R*-states are excited at the length of wave functions of the transuclei A, B, C... Thus, short-range strong and local weak interactions between transnuclei become "long-range" interactions. In the *R*-states, both the wave functions $\psi_a(A)$, $\psi_b(B)$, $\psi_c(C)$... of all transnuclei that make up the transmolecule, and all known interactions interfere: strong-weak, electromagnetic, inertial-gravitational [35], and also, obviously, still unknown interactions.

The transnuclei A, B, C... form a multinucleus transmolecule $\{X\}$ with its own energy level. Provided the number of nucleons is preserved, there are obviously many other transmolecules $\{Y\}$, $\{Z\}$,.., which consist of other transnuclei, but with their own energy levels. Due to the RIEX-interaction, exothermic, nuclear

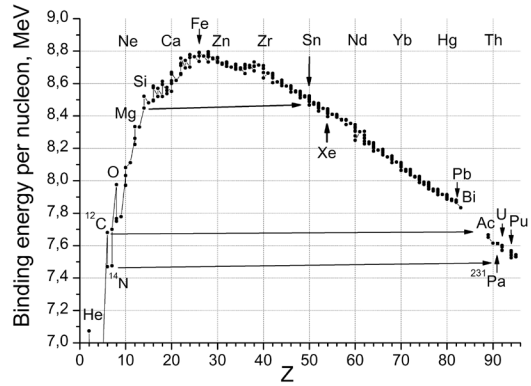

Fig. 7. *Coupling energy per nucleon in stable atomic nuclei.*

strong-weak transitions between the energy levels of transmolecules are carried out: $\{X\} \rightarrow \{Y\}$; $\{X\} \rightarrow \{Z\}$... The more these levels overlap, the greater is the probability of transitions between the levels of transmolecules.

In transmutation reactions, the transition to states in which atomic nuclei are nonradioactive is provided by a weak interaction involving electronic orthobosons, since the wave function of an electronic, orthoboson condensate significantly overlaps with the wave functions of transmolecules: $\{X\}$, $\{Y\}$, $\{Z\}$... The transmutation energy is released due to the difference in the nuclear binding energy of the isotopes involved in the reactions, just as in the case of fission of the uranium nucleus or in nuclear reactions of the synthesis of heavy nuclei up to iron from the nuclei of lighter elements (**Fig. 7**). Transmutation reactions can be represented as reactions of nucleon and multi-nucleon transfers between transnuclei [36] with the transformation of protons into neutrons and vice versa, as well as reactions of radiationless fusion and fission of transnuclei.

Thus, due to the RIEX-interaction, multinuclear, radiation-free and low-energy nuclear transmutation reactions occur.

3. IDENTICAL PARTICLES

The principle of identity states that it is experimentally impossible to distinguish identical particles. So, if two identical particles 1 and 2 are swapped or change their states *a* and *b*: $\psi_a(1)\psi_b(2) \rightarrow \psi_a(2)\psi_b(1)$, then the

result of the interaction between them will not change. Here $\psi_a(1)=[\psi_a(x_1,y_1,z_1)]S(1)$ and $\psi_b(2)=[\psi_b(x_2,y_2,z_2)]S(2)$ are wave functions of particles, which are the products of their coordinate parts $[\psi_{a,b}(x,y,z)]$ by their spin parts S(1) and S(2), and $\psi_a(1)\psi_b(2)$ and $\psi_a(2)\psi_b(1)$ are wave functions of two particles.

The result of the interaction will not change if the wave function of the particles is represented by a superposition of the wave functions of two states − the eigenstate $\psi_a(1)\psi_b(2)$ and the identical state $\psi_a(2)\psi_b(1)$:

$$\psi^{\pm}(1,2)=1/2\{\psi_a(1)\psi_b(2)\pm\psi_a(2)\psi_b(1)\}. \quad (3)$$

The plus sign in expression (3) describes bosons, i.e. particles with zero or integer spin, s = 0, 1ħ, 2ħ… The bosons obey Bose-Einstein $\psi^{+}(1,2)$ statistics, in which the sign of the wave function does not change when the particles are rearranged. The minus sign describes fermions, i.e. particles with a half-integer spin, s = ħ/2, 3ħ/2... The fermions obey Fermi-Dirac statistics, in which, when the particles are rearranged, the sign of the wave function $\psi^{-}(1,2)$ changes to the opposite sign. Our Visible Universe mainly consists of fermions with a spin s = ħ/2: electrons, protons, neutrons, neutrinos, and quanta of electromagnetic radiation with spin s_γ = 1ħ.

The square of the wave function of particles is equal, by definition, to the probability density of their location at a given point in space and at a given time. If expression (3) is squared, then:

$$|\psi^{\pm}(1,2)|^2=1/4\{|\psi_a(1)\psi_b(2)|^2+|\psi_a(2)\psi_b(1)|^2\pm \pm[\psi_a^*(1)\psi_b^*(2)\psi_a(2)\psi_b(1)+\psi_a(1)\psi_b(2)\psi_a^*(2)\psi_b^*(1)]\}. \quad (4)$$

The first two terms in expression (4) are the probability of particles being in the ground state: eigenstate and identical state. The value in the square bracket is the probability of particles being in an exchange state when each particle is simultaneously in two states *a* and *b*.

"**Boson body**". The de Broglie length of the wave function of the particle $\lambda = h/mV$, where h is Planck's constant, mV is the momentum of the particle: the product of its mass m by the velocity V. A hydrogen atom with a mass of 1 atomic mass unit at room temperature 300K has a wave function length λ_H = 0.145 nm (the diameter of the hydrogen atom is 0.106 nm). The lower the velocity V of a particle, the longer is the length of its wave function λ, the greater is the distance at which it interacts with other identical particles in an exchange manner.

If we equate the states *a* and *b*, then for the bosons $|\psi^{+}(1,2)|^2=|\psi_a(1)\psi_a(2)|^2$. Bosons can be in the same state, and thus they can form a Bose-Einstein condensate. Consequently, boson particles, boson atoms, boson molecules will be able to concentrate in one place and form a "boson body". With an increase in the mass of the "boson body" and its crystallization, when the bosons bind, the thermal velocity of the "boson body" decreases. Then, we obtain from thermodynamics $V=\sqrt{\frac{3kT}{N\cdot m}}\cdot\left(\frac{3}{2}kT=\frac{N\cdot m\cdot V^2}{2}\right)$, where k is the Boltzmann constant, T is the temperature, N is the number of identical bosons of mass m in the "boson body". Consequently, the "boson body" reduces the velocity of bosons by $1/\sqrt{N}$ times, and increases the lengths of their wave functions $\lambda=\frac{h}{mV}=h\sqrt{\frac{N}{3kT\cdot m}}$ by $\sqrt{N}$ times. The force that attracts other identical bosons is proportional to the number of bosons N that make up the "boson body". It will be recalled that one mole contains $6\cdot10^{23}$ particles. For this reason, the "boson body" will constantly increase its size by means of adding identical bosons to itself.

For fermions at *a* = *b*, $|\psi^{-}(1,2)|^2=0$ (4). Due to the Pauli principle, the fermions cannot be in the same state. But fermions can create boson molecules by combining with both identical and foreign fermions. These boson molecules, in turn, form a "boson body".

When particle 1 in state *a* tends to occupy state *b* of particle 2, $a \rightarrow b$, then the exchange part of the wave function (4) will compensate for its own and identical parts of the state of the two particles until the total wave function

becomes zero $|\psi^{-}(1,2)|^2 = 0$. The particles have disappeared! The particles have mutually annihilated each other without radiation and compensation of electric, baryon and lepton charges. If the reverse process is possible, then the Big Bang can be represented simply as the energy-free birth of pairs of electrons and pairs of protons, without the birth of antiparticles. The generation of exclusively electrons whose spins are antiparallel to magnetic moments and pulses may be related to the property of asymmetry of the Physical Vacuum. The Physical Vacuum generates only particles: electrons and protons, and does not generate antiparticles.

4. TRANSMUTATION REACTIONS WITHOUT THE COULOMB BARRIER

Since particles have masses, electric, baryonic, lepton charges, spins, spin magnetic moments, they participate in all fundamental interactions. In particular, identical particles participate in fundamental exchange interactions: exchange strong interaction [F] $-\psi_a^*(1)\psi_b^*(2)[F]\psi_a(2)\psi_b(1)$; exchange electromagnetic interaction [EM] $-\psi_a^*(1)\psi_b^*(2)[EM]\psi_a(2)\psi_b(1)$; exchange weak interaction [W] $-\psi_a^*(1)\psi_b^*(2)[W]\psi_a(2)\psi_b(1)$ and exchange inertial-gravitational interaction [IG] $-\psi_a^*(1)\psi_b^*(2)[IG]\psi_a(2)\psi_b(1)$.

The energy of interaction between particles 1 and 2 in perturbation theory is equal to:

$$E^{\pm}(1,2) = \frac{1}{N_{orm}}\int\{(|\psi_a(1)|^2(F,W,EM,IG)|\psi_b(2)|^2 + |\psi_b(1)|^2(F,W,EM,IG)|\psi_a(2)|^2)\}dV_1dV_2 \pm \pm\frac{2}{N_{orm}}\int[\psi_a^*(1)\psi_b^*(2)\{F,W,EM,IG\}\psi_a^*(2)\psi_b^*(1)]dV_1dV_2; \quad (5)$$

$$E^{\pm}(1,2) = C \pm E_C, \quad (6)$$

where N_{orm} is the normalization integral, and $dV_1 = dx_1dy_1dz_1$, $dV_2 = dx_2dy_2dz_2$. The energy of interaction between particles that are in their own and identical states is the main energy – C. In addition, identical particles have an additional exchange energy – Ec, i.e. the third term in expression (5). If the distance between the particles is greater than the radius of the strong F and weak W interactions (> 1 fm), then the main energy C has no strong and weak interactions in the first and second terms in (5)! If the states of two particles are equal $a = b$, then for the Coulomb and gravitational interactions, the main energy is equal to their exchange energy $C = Ec$. At the same time, if the formula (6) has a minus sign before the exchange energy Ec, then the exchange interaction completely compensates the main interaction C!

Thus, two identical particles in strong and ultrastrong magnetic fields, in which the coordinate part of their wave function is antisymmetric $n_b^1 = -n_b^2$ and $a = b$, Coulomb repulsion and gravitational attraction disappear. The paradox is realized: "The Waves extinguish the Wind." In this case, two fermions, for example: protons p, have parallel spins, and bosons, for example: deuterons d (S = 1ħ), have antiparallel spins. – The wave function of two bosons must be a symmetric function. Since the coordinate part of two bosons is an antisymmetric function, then the spin part must also be an antisymmetric function.

Two protons begin to oscillate near their nuclear orbitals in a hydrogen transmolecule in the ultrastrong magnetic field of electron orthobosons $B_S^0 \sim 3.5\cdot10^4$ T. And, thanks to the exchange interaction, they form a nuclear orthoboson (**Fig. 8**). The exchange Coulomb energy of protons completely compensates for the energy of their Coulomb repulsion.

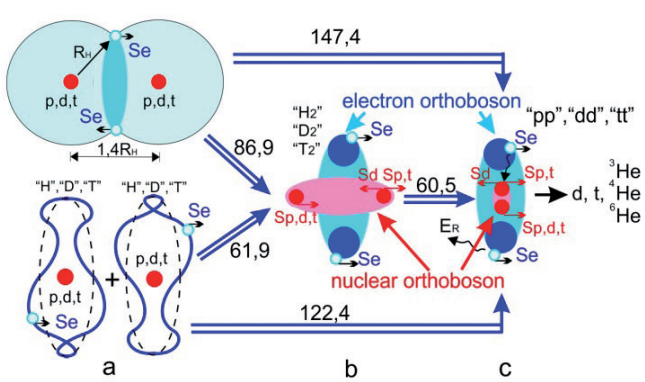

Fig. 8. *a –two hydrogen transatoms "H" in a strong magnetic field and a hydrogen molecule; b – the formation of hydrogen transmolecule "H_2"; c – thetransmolecule formation "pp" ("dd", "tt").*

This will lead to the convergence of protons up to nuclear distances, the formation of a transmolecule "*pp*", and to the beginning of a nuclear reaction without a Coulomb barrier involving an electron orthoboson $2e^-$ that has a binding energy 326.4 eV (Fig. 8):

$p + p + 2e^- \rightarrow d + \nu_e + e^- + 1.44\ MeV - 326.4\ eV.$

In this reaction, the neutrino spectrum is continuous, unlike the reaction:

$p + p + e^- \rightarrow d + \nu_e + 1.44\ MeV,$

for which the neutrino spectrum is monoenergetic [37].

In a strong magnetic field, hydrogen atoms and molecules are transformed into a transmolecule "*pp*" with a ground state of one electron of 163.2 eV. During the conversion process, vacuum ultraviolet light will be emitted (the numbers in **Fig. 8, 9** are given in eV; the double line is the radiation of two photons) [32]. Such emission lines were observed in the experiment of *R.* Mills [38] on ultraviolet spectroscopy of helium-hydrogen plasma. These lines were recorded during microwave discharge in a mixture of helium with 2% of hydrogen at room temperature and at pressures from 1 to 20 torr. They appear only in a mixture of helium and hydrogen, but are absent in pure helium or hydrogen and in mixtures of hydrogen with other noble gases. This is due to the fact that orthohelium is always generated in an ionized medium in which helium is present. Orthohelium itself has a strong magnetic field due to the parallelism of magnetic moments of the electrons. Calculation (1) shows that the magnetic field in the center of the orthohelium atom is ~ 410 *T,* and at its radius $R_2 = 8.76 \cdot 10^{-11}$ m the magnetic field is equal to ~ 70 *T*. As experiments show, the magnitude of such a field is sufficient to trigger transmutation reactions [14].

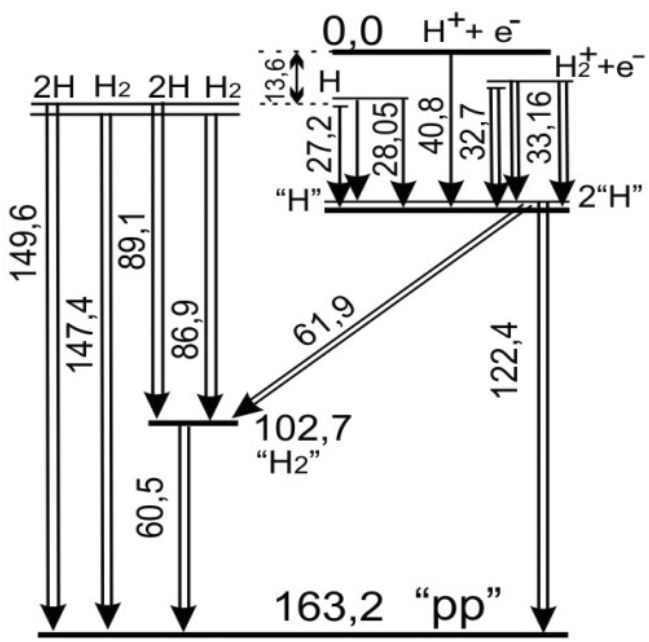

Fig. 9. *Scheme of electron transitions in the "pp" transmolecule in He + H_2 plasma.*

With the production of deuterium (*D-d*) and tritium (*T-t*), transmolecules "*dd*" and "*tt*" will be formed. They enter into nuclear reactions without the Coulomb barrier, including those with the participation of electron orthobosons. These reactions produce protons, neutrons, tritons, the nuclei ^{3}He, ^{4}He, ^{6}He → ^{6}Li (Fig. 8) [39]:

$$\begin{aligned}
&d + d \rightarrow t + p + 4.03MeV,\\
&d + d \rightarrow {}^3He + n + 3.26MeV,\\
&t + t \rightarrow {}^4He + 2n + 11.3MeV,\\
&d + d + 2e^- \rightarrow {}^4He + 2e^- + 23.85MeV,\\
&t + t + 2e^- \rightarrow 2e^- + 12.3MeV +\\
&+ {}^6He(\beta^-, T_{1/2} = 0.8\,c) \rightarrow\\
&\rightarrow {}^6Li + e^- + \tilde{\nu}_e + 3.5MeV.
\end{aligned} \qquad (7)$$

Helium formed as a result of the Big Bang (7 at.%), and helium produced in reactions (7), in strong magnetic fields, forms transmolecules of beryllium "Be".

Two isotopes of orthohelium ^{3}He with the spin of the nucleus $I = \hbar/2$ form a transmolecule "^{6}Be" and a Coulomb-free nuclear reaction begins:

^{3}He + ^{3}He → ^{4}He + 2p + 12.86 MeV.

A paired Coulomb-free nuclear reaction for two isotopes of helium ^{4}He is impossible, since the reaction energy balance is Q < 0. However, two orthohelium ^{4}He form a stable

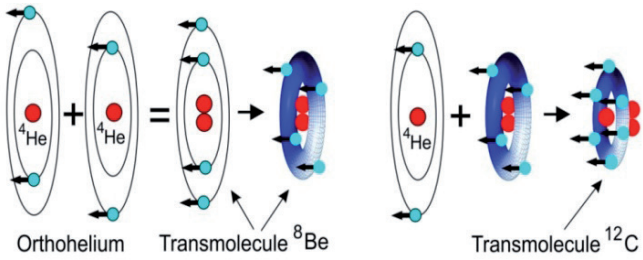

Fig. 10. *The formation of transmolecules "^{8}Be" (a) u "^{12}C".*

transmolecule of beryllium "^{8}Be" (**Fig. 10**). The radius of the transmolecule "^{8}Be" is equal to $R_{Be} = 4.4 \cdot 10^{-12}$ m, and magnetic fields: in the center B_S^0 (Be) = $5.4 \cdot 10^5$ *T* and at a distance of $1.2 \cdot R_{Be}$ from the center B_S^R (Be) = $1.1 \cdot 10^5$ T [30]. The transmolecule "^{8}Be" attaches to itself another atom of orthohelium ^{4}He, and forms a transmolecule of carbon "^{12}C". The transmolecule "^{12}C" is also stable because it consists of three ^{4}He nuclei: two paired helium nuclei and one unpaired ^{4}He. These nuclei cannot unite due to Coulomb repulsion between them. The radius of the transmolecule "^{12}C" $R_C = 3.0 \cdot 10^{-12}$ m, and the magnetic fields: in the center $B_S^0(C) = 2.6 \cdot 10^6$ T and at a distance of $1.2 \cdot R_C$ from the center $B_S^R(C) = 5.2 \cdot 10^5$ T.

Subsequently, orthohelium and transmolecules "^{8}Be", "^{12}C", due to their own ultrastrong magnetic fields, will be attracted to each other, and enter into exchange interaction with their electronic Bose condensates. As a result, multinuclear transmolecules $n \otimes {}^4_2He$ with helium Bose-Einstein condensate will be formed. The creation of such transmolecules leads to multinuclear transmutation reactions without a Coulomb barrier, with the emission of protons, neutrons, alpha particles and with the formation of heavy chemical elements with a nucleus charge $Z \geq 6$ (**Fig. 11**).

$$n \otimes {}^4_2He \rightarrow {}^{4n-1}_{2n-1}A + p + Q,$$

$$n \otimes {}^4_2He \rightarrow {}^{4n-1}_{2n}B + n + Q,$$

$$n \otimes {}^4_2He \rightarrow {}^{4(n-1)}_{2(n-1)}C + {}^4_2He + Q,$$

$$n \otimes {}^4_2He \rightarrow A + B + C + ... + Q,$$

where Q is the energy released as a result of the reaction.

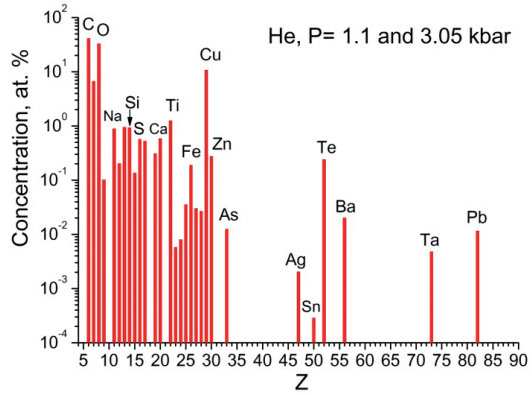

Fig. 11. *The element concentrations in two experiments with He.*

Fig. 11 shows the concentrations of chemical elements averaged over 28 measurements of different synthesized structures and microparticles and obtained in two experiments on irradiation with braking gamma rays with E_{max} = 10 MeV of pure helium at pressures of 1.1 and 3.05 kbar. Both irradiations were carried out for 28 hours at an electron current that produces braking radiation, $(1.0\text{-}1.5) \cdot 10^{14}$ c^{-1} [14-16,39,40]. Fig. 11 shows that chemical elements from carbon to lead are produced as a result of irradiation of helium.

Strikingly, similar spectra are obtained in experiments with pure hydrogen and pure deuterium. **Fig. 12** shows the concentrations of chemical elements averaged over 35 measurements and obtained in two experiments with pure hydrogen H_2 at pressures of 1 and

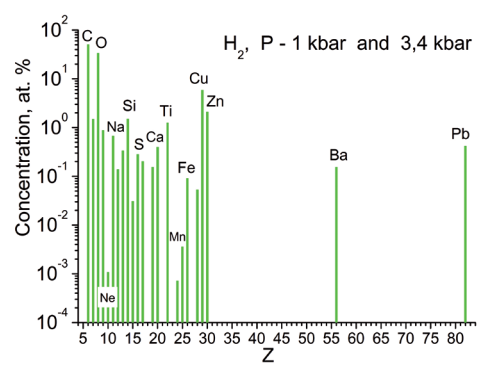

Fig. 12. *The element concentrations in two experiments with H_2.*

3.4 kbar [15, 40]. Irradiations were carried out for 14 and 62 hours, respectively, at electron current of $(1.2\text{-}1.5)\cdot10^{14}$ s^{-1}. **Fig. 13** shows the averaged concentrations of chemical elements obtained in an experiment on irradiating a chamber with deuterium at a pressure of 2.2 kbar [41]. Averaging was carried out over 42 measurements. Irradiation was carried out for 49 hours. The electron current was $(1.2\text{-}1.3)\cdot10^{14}$ s^{-1}. We can conclude from the presented results of the experiments that multinuclear reactions, such as in helium, also occur in hydrogen and in deuterium.

In all numerous transmutation experiments, a characteristic feature of the chemical element distributions is the constant presence of a group of light elements with $Z \leq 30$; the presence of a group of medium-mass elements with $30 < Z \leq 70$ and of a group of heavier elements with $Z > 70$. Let us note that the group of elements with $30< Z \leq 70$ is located in the tin region, and the group with $Z >70$ is centered around lead. Both of these chemical elements have "magic", closed shells for protons $Z = 50$ and $Z = 82$, and for lead and for neutrons $N = 126$.

Based on the assumption that the probability of production of new elements decreases with an increase in the number of nuclei in the input channel, it was concluded [39] that a group of elements up to chlorine $Z < 19$ is generated in multinuclear reactions between primary elements − elements of the initial medium. The production of chemical elements from chlorine to zinc ($Z = 30$) is apparently determined by secondary processes. In these processes, both atoms of primary elements and atoms of daughter chemical elements obtained in previous reactions participate in the multinuclear interactions. Elements that belong to other groups with $30 < Z \leq 70$ and with $Z > 70$ are synthesized in multinuclear reactions by daughter chemical elements, starting with carbon (Fig. 7). It is important to note that carbon is in the distribution maximum in the presented experiments.

Carbon is found in the maximum distributions in many other transmutation experiments, including three experiments on the irradiation with braking gamma-quanta of gaseous, pure xenon with E_{max} = 10 MeV at pressures P = 250, 270, 550 bar with an irradiation time of 43, 60 and 72 hours, respectively. **Fig. 14** shows the concentrations of chemical elements averaged over the results of 289 measurements of different structures and microparticles. The detection of radioactive elements in the samples was of particular interest: technetium $_{43}$Tc, francium $_{87}$Fr and actinium $_{89}$Ac [40]. The absence of possible generators in the same samples of such elements as molybdenum, radium, thorium suggests that $_{43}$Tc and $_{89}$Ac are synthesized in condensed xenon in transmutation reactions independently, like

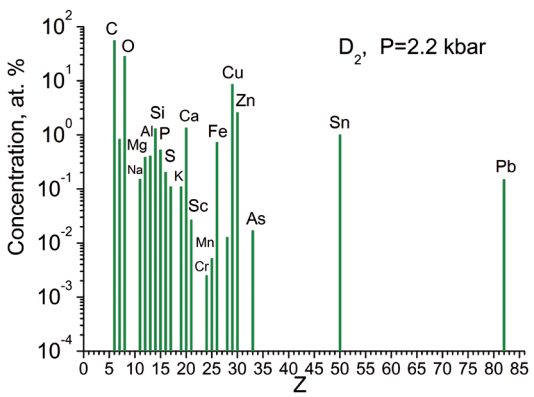

Fig. 13. *The element concentrations in experiment with D_2.*

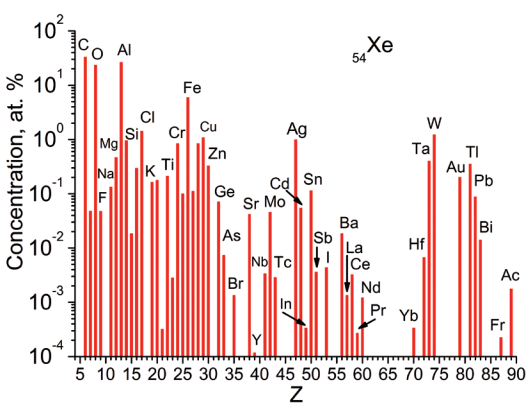

Fig. 14. *The element concentrations in experiments with $_{54}$Xe.*

other stable chemical elements. Francium $_{87}$Fr is the alpha decay product of actinium $_{89}$Ac.

It will be noted that transmutation reactions for identical nuclei occur with a larger cross-section compared to non-identical nuclei, since the former lack a Coulomb barrier. It follows from this that the atomic nuclei of identical chemical elements that make up the "boson body" enter more easily into transmutation reactions that lead to a change in the chemical composition of the media. This is important to know in the production of ultra-pure materials.

It clearly follows from the presented experimental results that not only subsequent light chemical elements, but also medium and heavy chemical elements can be synthesized in transmutation reactions in condensed matter that consist of the lightest elements, such as hydrogen, deuterium, helium.

It can be argued according to the results of all numerous experiments on transmutation that all chemical elements of the periodic table are produced in low-energy transmutation reactions (Fig. 14).

5. MULTINUCLEAR REACTIONS. UNIVERSAL DISTRIBUTION

Many atoms interact simultaneously during transmutation [11,42,43]

$$\sum_i c_i \, {}^{N_i}_{Z_i}A_i + e^- \sum_i c_i Z_i \rightarrow \sum_j c_j \, {}^{N_j}_{Z_j}B_j + e^- \sum_J c_J Z_J + \\ + l\nu(\tilde{\nu}) + Q,$$

where ${}^{N}_{Z}A$, ${}^{N}_{Z}B$ are nuclides with a charge Z and a number of nucleons N; c_i, c_j is a number of nuclides ${}^{N_i}_{Z_i}A$, ${}^{N_j}_{Z_j}B_j$ in the input and output reactions, respectively; e^- are atomic electrons; $l\nu(\tilde{\nu}) - l$ – l-number of neutrinos and antineutrinos, number of weak transitions that change the charge of nuclides Z. Neutrinos and antineutrinos appear in the reaction equations to preserve the lepton charge. At the same time, the conditions for preserving the number of nucleons $\sum_i c_i N_i = \sum_j c_j N_j$, preserving the full charge $\sum_i c_i Z_i \pm l = \sum_j c_j Z_j$ and positive energy balance $Q \geq 0$ must be met. The conclusion about the possibilities of such reactions follows from the consideration of the picture of the binding energy per nucleon in the nuclei of the initial substance (Fig. 7).

It is obvious that if there is a set of chemical elements that transform into each other in the medium, then the quantitative relations between them should be displayed by a certain distribution.

Let's assume that conditions for transmutation processes are always available in the medium, and thus multiple transmutation processes are constantly carried out in it. At the initial stage of the development of transmutation processes, when the number of atoms of the initial, primary chemical elements prevails over the number of atoms of the daughter elements, the nuclide distribution of transmutation products will contain elements from carbon to zinc. The nuclide distribution here should be understood as the distribution of stable nuclides. The distribution of nuclides will begin to change significantly only when the number of daughter atoms increases so much that they begin to enter into transmutation reactions with each other with a greater probability than with the atoms of the original substance. Atomic nuclei of all chemical elements will appear in the products of transmutation. Eventually, multiple, multinuclear transmutation processes will lead to a situation where the number of primary atoms will be comparable or less than the number of atoms of the daughter elements. By this time, the mutual conversion of chemical elements into each other will lead to a certain, quasi-equilibrium distribution.

The distribution would be in equilibrium if the transmutation reactions proceeded without loss of energy. And it is known from statistical physics and thermodynamics that, in a closed system, irreversible processes inevitably end with its transition to an equilibrium state [44]. We have allowed ourselves to apply the laws

of statistical physics and thermodynamics to the transmutation processes on the grounds that transmutation can be represented not as an exchange of energy between particles, but as an exchange between nuclides of portions of nucleons ($E = mc^2$), albeit in a multiparticle interaction. All possible sets of a limited number of stable nuclides can be used as a statistical ensemble.

The energy distribution E for colliding atoms of a gas at temperature T is described by the Maxwell distribution in statistical physics: $f_E = \frac{2\pi}{\sqrt{(\pi kT)^3}}\sqrt{E}\exp\left(-\frac{E}{kT}\right)$. We replace, for transmutation processes, the energy in the Maxwell distribution by the masses of isotopes M_A or by the mass numbers of isotopes A: $E \rightarrow A$, and kT by the number G that characterize the transmutation process: $kT \rightarrow 2G$:

$$f_A = \frac{C}{\sqrt{(2G)^3}}\sqrt{A}\exp\left(-\frac{A}{2G}\right), \quad (8)$$

where C is the normalization coefficient. As the temperature of the system T is a collective parameter of its constituent particles, so the number G determines the collective *energy content* of the system [45]. The greater the energy content of the system, the greater is the G coefficient. The energy content coefficient of a system depends on the total binding energy of its constituent nuclei $G(\varepsilon)$ and it has a maximum value for a system that consists of hydrogen atoms whose binding energy is zero $\varepsilon = 0$. The energy content coefficient is zero $G = 0$ for a system that consists of iron and nickel isotope atoms with a maximum binding energy per nucleon: ^{56}Fe -8.790MeV, ^{58}Fe -8.792MeV and ^{62}Ni -8.794MeV (Fig. 7). The value of the energy content coefficient G of the hydrogen system, apparently, should be determined experimentally. The mass number A varies from 1 to 250, from hydrogen to the isotope californium-250 in the "thermodynamic" distributions that corresponds to formula (8), in **Fig. 15**. The energy content coefficient G in Fig. 15 has three randomly selected values $G = 8$, 12 and 24. These values correspond in the distributions to the maximum values of the mass number Amax, which determines the physical meaning of the coefficient G.

In addition, the energy content coefficient of the system $G(\varepsilon,\xi)$ depends on another, independent parameter – on the energy density of a weakly excited medium ξ, on its ionization. The energy density of the medium determines how many atoms can simultaneously participate in the transmutation reaction. Thus, the energy content coefficient of the system $G(\varepsilon,\xi) = G(\varepsilon)\cdot G(\xi)$ depends on the internal value – the intranuclear energy and on the external value – the energy density of the medium.

In our case, the transmutation processes are indeed irreversible, but they are carried out in an open system, with the loss of internal energy of the atomic nuclei of the medium during transmutation (it will be recalled: the energy during transmutation is released due to a defect in the masses of isotopes). The loss of energy during transmutation reduces the coefficient of its energy content in the system G. It should be

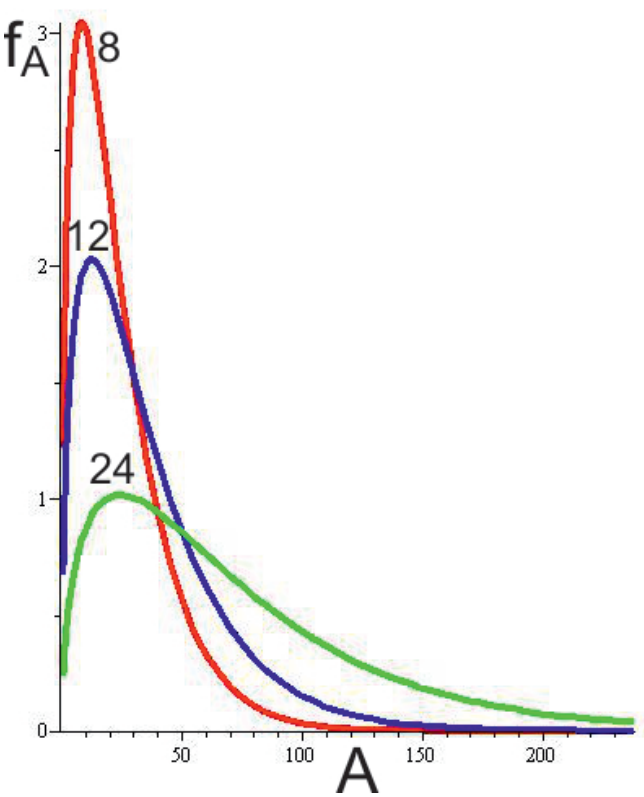

Fig. 15. *"Thermodynamic" mass number distributions A for transmutation processes.*

noted that the lost internal energy is converted into kinetic energy of nuclides, thereby increasing the external energy density of the medium ξ. Part of the internal energy is carried away by neutrinos. In part, the internal energy losses will be compensated by the participation of atoms of the initial substance in the reactions, until the moment when the number of the latter decreases to the level of daughter nuclides. In addition, the calculated energy losses of 0.1-10 MeV per one reaction [43] are significantly less than the mass of the reacting nuclides (>> 1 GeV). Thus, multiple transmutation processes are carried out in a quasi-constant medium that slowly decreases in energy and mass. For this reason, the resulting distribution will be quasi-equilibrium. The distribution, conditionally, will change from the distribution described by the line with A_{max} = 24 in Fig. 15 to the distribution described by the line with A_{max} = 12, and further to the distribution described by the line with A_{max} = 8. It should be emphasized that the distributions shown in Fig. 15, do not take into account differences in binding energies per nucleon in stable atomic nuclei, which are shown in Fig. 7.

If the transmutation process takes place without loss of energy, then the final nuclide distribution would be in equilibrium. In addition, if the binding energy per nucleon were the same for all elements, then the equilibrium distribution would be the same, i.e. it would not depend on the initial elemental composition of the substance in which the transmutation processes began. Such a distribution would characterize the process of transmutation as if in a "pure" form. Such a "universal" distribution will be obtained when the transmutation process begins in a hydrogen medium and ends when the chemical elements iron-nickel are in "equilibrium" with other chemical elements.

Obviously, with the implementation of universal distribution, the process of transmutation will not stop. It will lead, due to the constant release of energy, to the beginning of the predominance of iron and nickel in the distribution as nuclides with maximum binding energy (Fig. 7). Thus, the isotopes ^{56}Fe, ^{58}Fe, ^{62}Ni fall out of "equilibrium" with other chemical elements (**Fig. 16**). If, at the same time, the energy content coefficient of the system $G(\varepsilon,\xi)$ remains unchanged $G(\varepsilon,\xi)$ = const without taking into account Fe-Ni falling out of "equilibrium", then the nuclide distribution will remain universal with A_{max} = const. With a decrease in the energy content coefficient $G(\varepsilon,\xi)$, the "universal" distribution will change, as a quasi-equilibrium, from the line with A_{max} = 24 to the distribution described by the line with A_{max} = 8 (Fig. 16). The transmutation process ends when the isotopes ^{56,58}Fe, ^{62}Ni with the maximum binding energy per nucleon become significantly greater than other elements. That is why the frozen core of the Earth has an iron-nickel composition, and it constantly increases its size due to transmutation reactions outside the core.

We drew, during processing and analyzing experimental data, attention to the increased yield of some groups of elements in transmutation products. These groups include: Na-Si, K-Ca, Mn-Ni, Cu-Zn, Zr-Mo, Ag-Sb, Ta-W, Pb. We obtained a similar

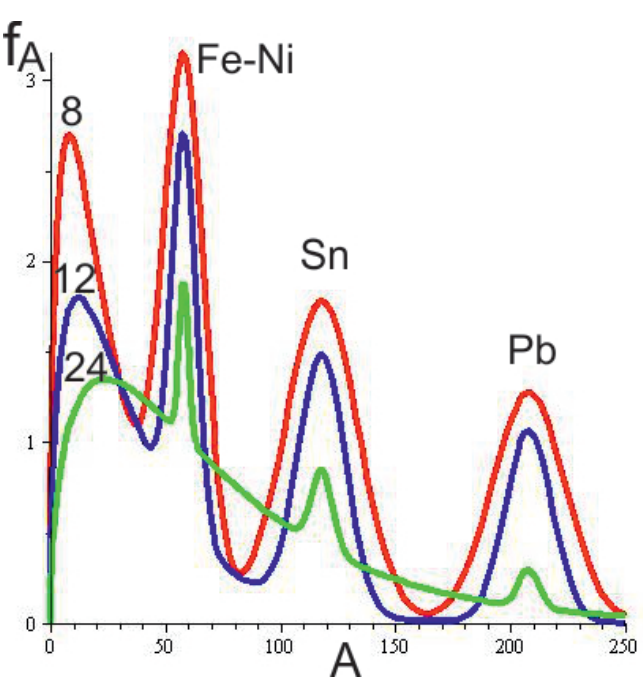

Fig. 16. *Quasi-equilibrium, universal distributions with Fe-Ni, Sn and Pb maxima.*

picture when calculating the appearance of elements, with the participation of *N*-molecules of water (**Fig. 17**) and other elements in the transmutation process [43,44]. Fig. 17 shows, for clarity, in order to avoid sharp even-odd fluctuations, the appearance of even-charged elements is presented. It is quite obvious that the increased probability of the appearance of these elements in the products of transmutation is associated with their proximity to the maxima depending on the binding energy of nucleons in nuclei on the atomic number and the number of isotopes of these elements. These maxima are known to be caused by "magic" nuclear shells with the number of protons and neutrons equal to: 2, 8, 20, 28, 50, 82, 126. Indeed, under equal initial conditions in the input channel, the presence of "magic" nuclides in the final spectrum increases the number of combinations of other nuclides in the output channel. A large number of isotopes in a particular element increases the probability of its occurrence purely statistically. Thus, the universal distribution, in addition to the Fe-Ni maximum, will contain peaks caused by "magic" nuclear shells, for example: tin $_{50}$Sn, lead $_{82}$Pb^{126} (Fig. 16).

Note that distributions in Fig. 15 and 16 extend to elements such as thorium, uranium and further to transuranic and superheavy

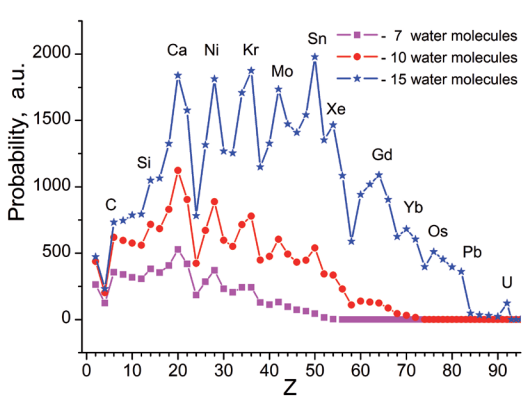

Fig. 17. *Calculation of yield of even-charge elements, at participation in transmutation process of 7, 10 and 15 – molecules of water.*

elements. Thus, protactinium $^{231}_{91}Pa$ ($T_{1/2} = 3 \cdot 10^4$ years) was detected in experiments on irradiation with gamma quanta of hydrogen in the presence of palladium in the *X*-ray spectra of reaction products, along with elements such as barium $_{54}$Ba and lead $_{82}$Pb [15].

Consequently, in any matter, regardless of its chemical composition, in which long, multiple transmutation processes occur, a quasi-equilibrium, universal distribution will be realized in its products, defined by expression (8). In addition, maxima associated with the peculiarities of energy dependence will be superimposed on the universal distribution, to varying degrees of intensity connections of nuclides from the mass number. At the same time, the intensity of the Fe-Ni maximum depends both on the duration of the transmutation process and on the chemical composition of the medium in which this process began.

6. NATURAL NUCLEOSYNTHESIS

To convert atoms of some chemical elements into atoms of other chemical elements in ionized condensed matter, their presence in strong magnetic fields $B > 30$ *T* is necessary. Magnetic fields are known to be extremely widespread in cosmic plasma: in stars and in the interstellar medium. They manifest themselves in the active regions of stellar and galactic clusters. Magnetic fields cause the pumping of energy into cosmic rays, radio emission, anomalous optical and *X*-ray radiation observed in the active zones of the Universe. Magnetic fields are always accompanied by fast, charged particles, including electrons. As mentioned above, free electrons with a density of $\rho > 10^{21}$ el/cm^3, with their unidirectional motion, create strong, and subsequently, due to atomic electron orthobosons, ultrastrong magnetic fields. Thus, the symbiosis of electrons and magnetic fields moving in the cosmic plasma creates conditions for the implementation of low-energy transmutation reactions in all corners of the Universe.

The Universe passes several stages in its development.

When the age of the Universe was $10^{-6} \div 1$ sec, and the temperature was $10^{10} \div 10^{12}$ K, the quark-gluon plasma was in the process of cooling, and electrons, protons and other hadrons were formed. In the era of nuclear fusion, the first lightest nuclei, deuterium and helium, began to be synthesized at the temperatures of the Universe $10^{7} \div 10^{9}$ K and the age of $10 \div 1000$ sec.

After 380000 years, the era of Recombination came in the Universe, when its temperature decreased to ~ 4000 K, and electrons, protons and alpha particles began to form the first neutral hydrogen and helium atoms. At the same time, the Universe entered the stage of Natural nucleosynthesis, which continues to this day.

With the appearance of the first hydrogen, helium atoms and the available free electrons flying away from the center of the Universe, conditions arose for the generation of strong magnetic fields, of the transformation of atoms into transatoms and for the launch of transmutation reactions. In the multinuclear hydrogen and helium transmutation reactions, first of all, chemical elements from carbon to chlorine were synthesized with the maximum operating time of carbon, oxygen, nitrogen (*C, O, N*) (Fig. 11-13). Simultaneously produced chemical elements began to form "boson bodies", namely: organic clusters, in which the chemical synthesis of organic molecules, and, subsequently, biochemical molecules, started with the participation of hydrogen. So, recently a group of scientists identified chemical reactions that could lead to the appearance of life [46]. These chemical reactions occur with the participation of only four chemical elements, which form: ketoacids (derivatives of hydrocarbons that contain *C=O* and *COOH* groups), *HCN* cyanide, ammonia NH_3 and carbon dioxide CO_2, and the products are aminoacids and nucleic acids − building blocks for proteins and DNA.

In parallel, chemical elements from argon to zinc were being produced in transmutation reactions, and later all other, heavier chemical elements.

Thus, organic and biological planets could already be formed from "boson bodies" in the Universe aged more than 10 million years. Primitive organic life must have appeared obligatory on these organic planets first, and intelligent life must have developed later [47]. It is difficult to imagine the possibilities of a Supreme Intelligence aged more than 12 billion years.

The first stars and galaxies began to be formed after $0.15 \div 1$ billion years of the Universe's development. Low-energy transmutation reactions similar to those carried out in the epoch of Recombination were started againat this stage, when the density of matter and the directional movement of free electrons reaches values sufficient for the generation of magnetic fields and the pairing of electrons in them. The epoch of Stars differs from the epoch of Recombination by the fact that its isotopic composition already contains all chemical elements. The involvement of the transmutation mechanism in nucleosynthesis makes it easy to understand the metallicity of stars and the presence of heavy elements even in the oldest stars, which elemental composition is not associated with supernova explosions, since the synthesis of all elements and their isotopes up to uranium becomes obvious. Thus, the "old" and "new" chemical elements produced in the atmospheres of stars and carried away by the stellar wind participate in the formation of planets.

7. PLANETARY NUCLEOSYNTHESIS

Taking into account that the processes of low-energy transmutation take place under fairly "soft" physical conditions and tend to reproduce a quasi-equilibrium universal distribution, the following conclusion can be drawn from the presented material: the process of nucleosynthesis

can be carried out on planets and form their elemental composition [42,43,48-50].

The process of transmutation on the emerging Earth began, apparently, when it was a dense, gas, plasma formation. Now, transmutation processes continue in the magma of the Earth, and the colossal energy released at the same time is observed by us like a volcanic eruption. Experts know that intraplate tectonic activity and volcanism cannot be explained within the framework of plate tectonics. The most common hypothesis that satisfactorily explains volcanism and tectonic activity inside both the oceanic and continental lithosphere is associated with the idea of hot spots and mantle plumes [51]. It is possible that transmutation processes are taking place in these hot spots and mantle plumes.

The fact that nucleosynthesis is determined by transmutation reactions is confirmed by experimental results. So, if we compare the isotope ratios in transmutation products after industrial, electronic melting of zirconium ingots in a vacuum furnace [7] with natural isotope ratios (**Table**) then, on the one hand, their significant difference is striking, for example: for potassium, chromium, copper, zinc, germanium and barium. These elements are highlighted with asterisks (*) in the Table. This circumstance speaks in favor of the existence of the phenomenon of transmutation. On the other hand, there is a fairly good agreement of isotopic ratios of remaining elements with natural, terrestrial elements [42,43]. The difference noted above in isotopic ratios for these elements (K, Cr, Cu, Zn, Ge, Ba) can be explained by the incompleteness of transmutation processes and, as a consequence, the dependence of distributions, including isotopic distributions, on the source element, in this case, on zirconium. The fact that the elements that are products of zirconium transmutation have, in part, a natural, terrestrial isotopic ratio led to the idea of comparing the distribution by mass numbers resulting from the melting of zirconium with the

Table 1

Comparison of natural isotope ratio (Nat.,%) with isotope ratio observed in zirconium transmutation products (Zr, %) [7,42].

Z	A	ТЦ	Ест.	Z	A	ТЦ	Ест.
$_{3}$Li	6	6	7.5	$_{31}$Ga	69	66	60
	7	94	92.5		71	34	40
$_{5}$B	10	78	74	**$_{32}$Ge***	**70**	**73**	**20**
	11	22	26		**72**	**12**	**27**
$_{12}$Mg	24	76	79		**73**	**15**	**8**
	25	11	10		**74**	**2**	**36**
	26	13	11	$_{34}$Se	77	15	7.6
$_{14}$Si	28	89	92.2		78	16	23.5
	29	7	4.7		80	54	44.6
	30	4	3.1		82	6	9.4
$_{19}$K*	**39**	**76**	**93**	$_{38}$Sr	86	24	10
	41	**24**	**7**		87	7	7
$_{22}$Ti	46	8	8.2		88	69	83
	47	8	7.4	**$_{54}$Ba***	**132**	**11**	**0.1**
	48	74	73.8		**134**	**29**	**2.4**
	49	5	5.4		**135**	**11**	**6.6**
	50	5	5.2		**136**	**9**	**7.8**
$_{24}$Cr*	**52**	**70**	**83.8**		**137**	**9**	**11.2**
	53	**16**	**9.5**		**138**	**29**	**71.7**
	54	**14**	**2.4**	$_{63}$Eu	151	56	48
$_{29}$Cu*	**63**	**48**	**69.2**		153	44	52
	65	**52**	**30.8**				
$_{30}$Zn*	**64**	**49**	**48.6**				
	66	**17**	**27.9**				
	67	**14**	**4.1**				
	68	**20**	**18.8**				

prevalence of elements by mass in the Earth's crust. **Fig. 18** shows that the distributions are generally similar to each other. Moreover, there is a correlation between groups of elements in

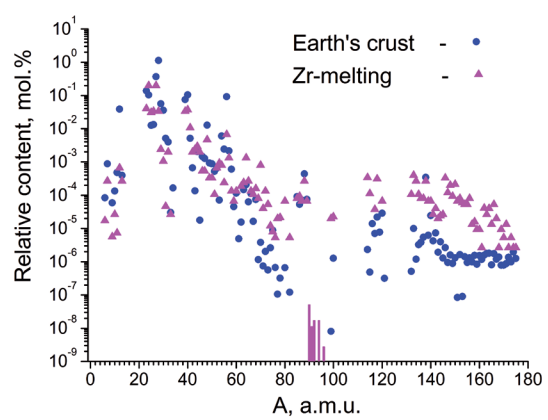

Fig. 18. *Comparison of element distribution in case of zirconium transmutation at its melting with element occurrence in the Earth's crust. For orientation, zirconium isotopes with their relative content are emphasized with bold lines* [7,42].

the distributions. The same elements (Ti, Fe) and groups of elements (Na-Si, K-Ca, Ti, Fe, Cu-Zn, Cd-Sb) have maxima in both distributions. Some difference in the distributions compared is due to the incompleteness of the transmutation processes for the case of zirconium melting and the dependence of the distribution on this element. Indeed, the realization of the universal distribution in the case of zirconium transmutation was carried out on the part of heavy masses (M_{Zr} 90 ÷ 96) relative to the estimated maximum distribution in the Mg-Si region (M – 24 ÷ 30).Therefore, heavy masses prevail in the distribution of nuclides during the melting of zirconium, in comparison with the Terrestrial distribution, approximately, from M = 60 to M = 175. These masses are obtained directly from the initial element zirconium. At the same time, the content of light masses has been reduced; approximately, from M = 6 to M = 30. It is known that the synthesis of elements in the Universe begins with hydrogen and helium. And the synthesis of elements on planets starts, including hydrogen and helium, with heavier elements, starting with carbon, nitrogen, oxygen and others.

It is of interest to compare the distribution of elements in the Earth's crust, as a function of the lower concentration level, with the appearance of elements in time during ultrasonic cavitation [13,49] (**Fig. 19, 20**). It should be emphasized once again that a group of light elements from carbon to zinc always appears in all transmutation experiments, regardless of the environment in which this process takes place. Subsequently, first of all, chemical elements of medium masses are synthesized, located around tin-antimony (Sn-Sb), and chemical elements with a heavy mass of lead-bismuth (Pb-Bi). Then all other chemical elements are produced.

An unexpected event in physics is the discovery of two radioactive isotopes in samples

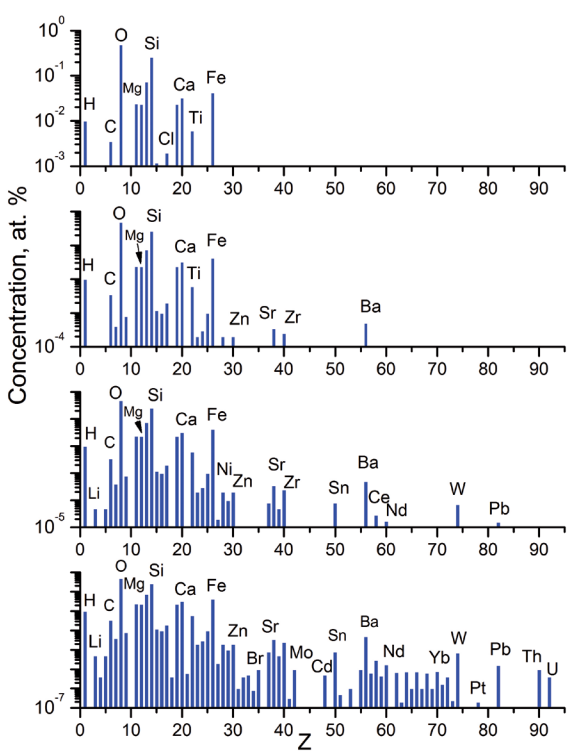

Fig. 19. *The occurrence of elements in the Earth's crust as a function of the lower concentration level.*

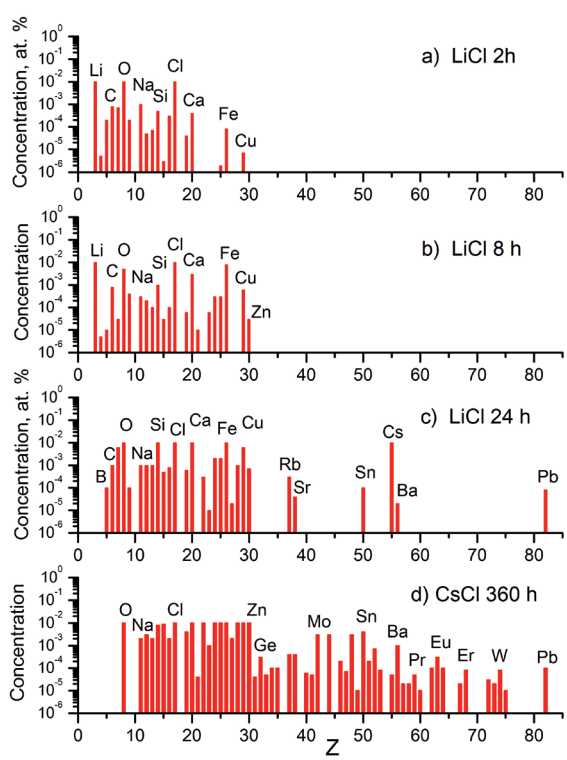

Fig. 20. *Ultrasonic solution cavitation LiCl and CsCl* [13,42].

of deep-sea crust that rose from a height of 1500 meters below the Pacific Ocean [52]. These isotopes $_{26}$Fe-60 ($T_{1/2} = 1.5 \cdot 10^5$ years) and $_{94}$Pu-244 ($T_{1/2} = 8 \cdot 10^7$ years) should have decayed long ago, since the age of the Earth is 4.54 billion years ($4.54 \cdot 10^9$ years). Based on the idea of planetary nucleosynthesis, it can be assumed that these isotopes appeared on Earth as a result of low-energy nuclear reactions.

As already mentioned, transmutation reactions occur in ionized condensed matter, mainly in solutions and in melts, when a stream of electrons flows through them. The flow of high-density electrons creates a strong magnetic field sufficient to transform atoms into transatoms and, consequently, they trigger transmutation reactions, i.e. nucleosynthesis. Transmutation reactions that occur in the Earth's mantle stimulate its geological activity.

Therefore, changing Galactic electric, magnetic and even gravitational fields can stimulate transmutation processes on the Earth, both directly interacting with it and indirectly, thanks to the Sun. Because the changes that take place on the Sun, through the Sun-Earth interaction, lead to changes on the Earth. Based on this assumption, we formulated a new doctrine of the geological development of the Earth [49].

1. The geological development of the Earth is a monotonous, evolutionary process, which is superimposed with revolutionary, discontinuous periods.

2. The evolutionary process is determined by internal energy sources: low-energy nuclear reactions, radioactive decays, gravitational compression, etc. Since the energy coming from internal sources is monotonously decreasing, geological processes are monotonously slowing down.

3. Abrupt, including cyclical periods in the development of the Earth are generated by external energy sources that stimulate internal energy sources, geological processes accelerate, sometimes in a revolutionary way, during these periods.

4. External energy sources are the Sun, jet streams of energy and matter from the Galaxy. Perhaps there are other, external energy sources available. Galactic energy sources can influence the Earth directly or indirectly, through the Sun.

The present concept is based on the concept of open systems both in relation to the Earth and the solar system, and in relation to the Galaxy. Therefore, this concept is not centrist. All energy sources operate in it simultaneously, with varying degrees of intensity.

According to a new study published in the journal Geoscience Frontiers [53], geological activity on Earth has a well-traced cycle of approximately 27.5 million years. Previously, it was believed that geological events are random. But the analysis of geological events over the past 260 million years has shown that, in fact, there is a strict cyclicity in geological activity. **Fig. 21** presents the results of the analysis of 89 geological events using a 10 million-year sliding window centered every 0.5 million years. The number of events that fell into the sliding window was calculated with an interval of 1 million years. Ten peaks, or clusters of events, are surely visible. That analysis was carried out due to significant improvements in radioisotope dating methods and in methods of measuring time according to geological scale.

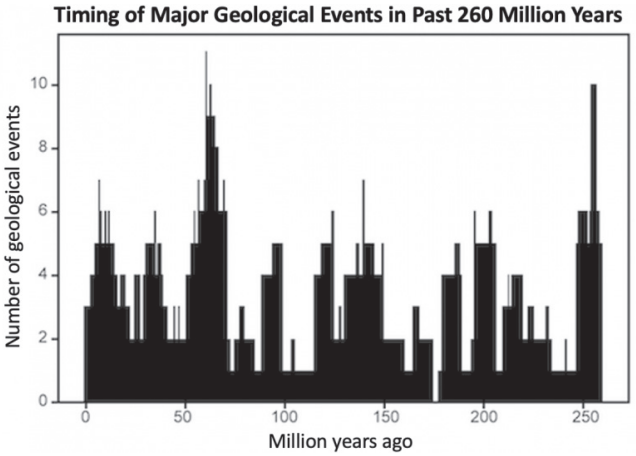

Fig. 21. *The cyclicity of the geological activity of the Earth* [53].

The last cluster of geological events occurred approximately 7 million years ago. This suggests and hopes that the next major, catastrophic geological activity will begin in more than 20 million years.

The availability of cyclical fluctuations ingeological activity of the Earth is a serious deviation from generally accepted views. However, the observed cyclicity fits perfectly into the above-mentioned new doctrine of the geological development of the Earth. The duration of the galactic year is, according to various estimates, from 180 to 250 million years. The Sun and its planets periodically, four times in a galactic year, approximately every 60 million years, are believed to intersect visible jet streams of matter and energy ejected from the center of the Galactic disk [12,54]. If the cycle of geological activity on Earth equal to 27.5 million is connected with galactic energy flows, then four additional, invisible energy flows located between the visible flows are assumed to exist. Based on these considerations and on a cycle of 27.5 million years, the Galactic Year will be equal to 220 million years.

Scientists have called the cycle of 27.5 million years as "pulse" of the Earth. It is obvious that the "pulse" of the Earth is set by the rhythm of the energetic "heartbeat" of our Galaxy. An interesting task for planetary science and astronomy is the registration the invisible energy flows of the Galaxy and detection of their effects on stars and other planets.

8. CONCLUSION

The paper demonstrated that in a quasi-neutral plasma, the directed, collective motion of electrons creates a magnetic field. At electron density $>10^{21}$ cm^{-3}, the magnetic field generates a Coulomb exchange field, which causes the pairing of free electrons into orthobosons $S = 1$h. Such orthobosons create strong magnetic fields >30 *T*, in which atoms turn into transatoms. Transatoms have ultrastrong magnetic fields in the range of 10^5-10^{10} *T*. Due to this mechanism, the existence of strong and ultrastrong magnetic fields in cosmic plasma is explained.

The ultrastrong magnetic fields of transatoms combine them into nuclear transmolecules, in which, due to resonant interference exchange interaction, multinuclear reactions occur. Multinuclear transmutation reactions can be considered as a multinucleon exchange between arbitrary transnuclei. Transmutation reactions that continuously occur in a condensed matter lead to quasi-equilibrium mass-number distributions of isotopes – the reaction products. These quasi-equilibrium distributions reflect the abundance of chemical elements and their isotopes in different objects and regions of the Universe.

In transmutation reactions, nuclear physics has moved from describing resonant transitions in individual nuclei (in individual atoms, molecules) and from describing the interaction between two nuclei to collective nuclide interactions. Moreover, these collective transnuclide interactions through resonant interference exchange interactions simultaneously include all currently known interactions: strong-weak, electromagnetic and inertial-gravitational interactions.

The RIEX-interaction is a universal interaction, because it not only unites all fundamental interactions, but also because its influence extends to the whole of Nature, from elementary particles to complex biological and social systems.

Proceeding from the idea of planetary nucleosynthesis based on the mechanism of multinuclear quantum transitions of some atomic nuclei into others, we formulated a new doctrine of geological development of Earth that caused a creation of a new scientific discipline – Quantum Planetology (Geology) [48-50]. Within the framework of quantum geology, the strict temporal cyclicity observed in the geological activity of the Earth has found its explanation. This cyclicity made it possible to more accurately determine the value of the Galactic year equal to 220 million years.

The synthesis of chemical elements in transmutation reactions and resonant interference exchange interaction already in the era of Recombination triggered first organic chemical reactions, and after the formation of "boson bodies" − biochemical reactions. Already at this stage, the Universe has generated biological and intelligent life on the formed organic and biological planets.

It clearly follows from the above that low-energy transmutation reactions are a natural mechanism for obtaining energy in stars and on planets, in the production of all chemical elements heavier than helium and in the origin of life at different stages of the development of the Universe, stars and planets.

REFERENCES

1. Proceedings of the 1-27th Russian Conferences on Cold Transmutation of Nuclei of Chemical Elements, 1993-2018. (RCCTNCE).
2. Proceedings of the 1-24th International Conferences on Condensed Matter Nuclear Science (Cold Fusion, ICCF).
3. Balakirev VF, Krymsky VV, Bolotov BV, Vasilieva NV, Vachaev AV, Ivanov NI, Kazbanov VI, Pavlova GA, Solin MI, Trofimov VI, Urutskoev LI. *Vzaimoprevrashcheniya khimicheskikh elementov* [Mutual transformation of chemical elements]. Ekaterinburg, Urals Branch of RAS Publ., 2003, 96 p.
4. Karabut AB., Kucherov YaR., Savvatimova IB. Nuclear product ratio for glow discharge in deuterium. *Phys. Letters A*, 1992, 170:265-272.
5. Savvatimova IB, Karabut AB. The products of nuclear reactions recorded at the cathode after experiments in a glow discharge in deuterium. *Poverhnoct' [Surface Investigation: X-Ray, Synchrotron and Neutron Techniques]*, 1996, 1:63-75, 76-81.
6. Savvatimova IB. Transmutation Effects in the Cathode Exposed Glow Discharge. Nuclear Phenomena Or Ion Irradiation Results? Proc. 7th Int. Conf. on Cold Fusion (ICCF), Canada, 1998: 342-350; Reproducibility of Experiments in Glow Discharge and Processes Accompanying Deuterium ions Bombardment. *Proc. 8th ICCF,* Italy, 2000:277-283.
7. Solin MI. Experimental facts of spontaneous appearance of condensate of soliton charges with the formation of nuclear fusion products in liquid zirconium. *Physical Idea in Russia*, 2001, 1:43-58. (in Russ.).
8. Adamenko SV, Selleri F, A. van der Merwe (eds.). *Controlled Nucleosynthesis Breakthroughs in Experiment and Theory,* Series: Fundamental theories in Physics, Springer, 2007, 156:780, http://www.springer.com/physics/elementary/book/978-1-4020-5873-8.
9. Adamenko SV. The concept of artificially initiated collapse of matter and the main results of the first stage of its experimental implementation. *Preprint, 2004,* Kiev, (in Russ), http://proton-21.com.ua/publ/Preprint_ru.pdf.
10. Urutskoev LI., Liksonov VI., Tsinoev VG. Observation of Transformation of Chemical Elements during Electric Discharge. *Annales de la Fondation Louis de Broglie* (*AFLB*), 2002, 27(4):701-726.
11. Kuznetsov VD., Mishinsky GV., Penkov FM., Arbuzov VI., Zhemenik VI. Low energy transmutation of atomic nuclei of chemical elements. *AFLB,* 2003, 28(2):173-214.
12. Krivitsky VA. *Paradoksy transmutatsii i razvitie Zemli* [Paradoxes of transmutation and the development of the Earth]. Moscow, NITs "Academica" Publ., 2016, 238 p.
13. Kladov AF. Cavitation destruction of matter (in Russ.); http://roslo.narod.ru/rao/rao1.htm.
14. Didyk AYu., Wiśniewski R. and Wilczynska-Kitowska T. The carbon-based structures synthesized through nuclear reactions in helium at 1.1 kbar pressure under irradiation with braking γ-rays of 10 MeV threshold energy. *Euro. Phys. Lett.*, 2015, 109:P.22001-P.1-22001-P.6.
15. Didyk AYu, Wiśniewski R, Wilczyńska-Kitowska T, Mishinsky GV, Semin VA. Synthesis of chemical elements under irradiation by bremsstrahlung gamma-rays of palladium in condensed gases. *RENSIT: Radioelectronics. Nanosystems. Information Technologies,* 2019, 11(2):143-160. DOI: 10.17725/rensit.2019.11.143.
16. Wisniewski R, Mishinsky GV, Wilczynska-Kitowska T, Zukowska Z, Rostocki A. Graphite-like structures, synthesized from gaseous He under high pressure, by braking irradiation of maximum energy of 10 MeV − modeling of

the process. *Acta Physica Polonica B, Proceedings Supplement,* 2020, 13(4).
17. Vysotskii VI., Kornilova AA. *Nuclear fusion and transmutation of isotopes in biological systems*. Moscow, Mir Publ., 2003, 304 p.
18. Vysotskii VI., Kornilova AA. Transmutation of stable isotopes and deactivation of radioactive waste in growing biological systems. *Annals of Nuclear Energy*, 2013, 62:626-633.
19. Kornilova AA, Vysotskii VI. Synthesis and transmutation of stable and radioactive isotopes in biological systems. RENSIT, 2017, 9(1):52-64. DOI: 10.17725/rensit.2017.09.052.
20. Mishinsky GV. Magnetic fields and high-temperature superconductivity in excited liquids. Unknown particles. *RENSIT: Radioelectronics. Nanosystems. Information Technologies*, 2021, 13(3):303-318. DOI: 10.17725/rensit.2021.13.303.
21. Landau LD, Lifshitz EM. *Field theory*. Moscow, Nauka Publ., 1973, 504 c.
22. Heisenberg W. Über die Spektra von Atomsystemen mit zwei Elektronen. *Z. Phys.*, 1926, 39(7):499-518.
23. Kulakov AV., Orlenko EV., Rumyantsev AA. *Quantum exchange forces in condensed matter*. Moscow, Science Publ., 1990, 120 p.
24. Mishinsky GV. Atom in a strong magnetic field. Transformation of atoms to transatoms. *RENSIT: Radioelectronics. Nanosystems. Information Technologies*, 2017, 9(2):147-160. DOI: 10.17725/rensit.2017.09.147.
25. Slichter ChP. *Principles of magnetic resonance*. New York, Harper & Row Publishers, 1963, 246 p.
26. Kadomtsev BB. Tyazhely atom v sverkhsil'nom magnitnom pole [Heavy atom in an ultrastrong magnetic field]. *ZhETF*, 1970, 58(5):1765-1769 (in Russ).
27. Fock VA. Bemerkung zur Quantelung des harmonischen Oszillators im Magnetfeld. *Z. Phys.,* 1928, 47:446-448.
28. Heiss WD., Nazmitdinov RG. Orbital magnetism in small quantum dots with closed shells. *Pis'ma v ZhETF,* 1998, 68(12):870-875.
29. Cooper LN. Bound electron pairs in a degenerate Fermi gas. *Phys.Rev*, 1956, 104:1189.
30. Mishinsky GV. Magnitnye polya transatomov. Spinovy-nuklidny-elektronny kondensat [Magnetic fields of transatoms. Spin-nuclide-electronic condensate]. *International Journal of Unconventional Science* (*IJUS*), 2017, № 15-16(5):6-25 (in Russ), http://www.unconv-science.org/.
31. Mishinsky GV. Non-Coulomb nuclear reactions of transatoms. Stellar energy and nucleosynthesis. *RENSIT: Radioelectronics. Nanosystems. Information Technologies*, 2018, 10(1):35-52. DOI: 10.17725/rensit.2018.10.035.
32. Mishinsky GV. Spin electron condensate. Spin nuclide electron condensate. *RENSIT: Radioelectronics. Nanosystems. Information Technologies*, 2018, 10(3):411-424. DOI: 10.17725/rensit.2018.10.411.
33. Mishinsky GV. Resonant interference exchange interaction. *RENSIT: Radioelectronics. Nanosystems. Information Technologies*, 2019, 11(3):261-278. DOI: 10.17725/rensit.2019.11.261.
34. Mishinsky GV. Towards a New Paradigm. *RENSIT: Radioelectronics. Nanosystems. Information Technologies*, 2020, 12(4):529-544. DOI: 10.17725/rensit.2020.12.529.
35. Shipov GI. *Theory of physical vacuum, theory, experiments, technologies*. Moscow, Nauka Publ., 1997, 450 p.
36. Volkov VV. *Nuclear reactions of deep inelastic transfers*. Moscow, Energoizdat Publ., 1982, 182 p.
37. Borexino Collaboration: Bellini G, Benziger J, Bick D et al. Neutrinos from the primary proton–proton fusion process in the Sun. *Nature*, 2014, 512:383-386.
38. Mills R, Ray P. Extreme ultraviolet spectroscopy of helium-hydrogen plasma. *J. Phys. D:Appl. Phys.*, 2003, 36:1535-1542.
39. Mishinsky GV. Multinuclear reactions in condensed helium. *RENSIT: Radioelectronics. Nanosystems. Information Technologies*, 2017, 9(1):94-105. DOI: 10.17725/rensit.2017.09.094.
40. Wiśniewski R, Mishinsky GV, Gulbekian GG, Wilczyńska-Kitowska T, Semin VA. Sintez khimicheskikh elementov i tverdotelnukh struktur pri obluchenii γ-kvantami kondensirovannykh gazov [Synthesis of chemical elements and solid-state structures under irradiation by γ-quanta in condensed gases]. *IJUS*, 2017, 17-18(5):6-15 (in Russ).
41. Didyk AYu, Wiśniewski R, Wilczyńska-Kitowska T, Mishinsky GV, Semin VA. Synthesis of solid-state structures and chemical elements under irradiation by bremsstrahlung γ rays with a maximum energy of 10 MeV in condensed

deuterium at a pressure of 2.2 kbar. *Preprint JINR, P15-2018-3*. Dubna, 2018, 27pp.
42. Mishinsky GV., Kuznetsov VD. Element distribution in the products of low energy transmutation. Nucleosynthesis. *AFLB*, 2008, 33(3-4):331-356.
43. Mishinsky GV, Kuznetsov VD, Penkov FM. Nizkoenergeticheskaya transmutatsiya atomnykh yader khimicheskikh elementov. Raspredelenie po elementam v produktakh transmutatsii. nukleosintez [Low energy transmutation of atomic nuclei of chemical elements. Element distribution in the products of low energy transmutation. Nucleosynthesis]. *IJUS*, 2017, 17-18(5):61-81 (in Russ).
44. Kuni FM. *Statistical physics and thermodynamics*. Moscow, Nauka Publ., 1981, 352 p.
45. Pavlov AN. *Quantum principles of the development of the Earth – a new paradigm of geology. Principles of development and historicism in geology and paleobiology*. Novosibirsk, Nauka Publ., 1990:115-122.
46. Pulletikurti S, Yadav M, Springsteen G. Prebiotic synthesis of α-amino acids and orotate from α-ketoacids potentiates transition to extant metabolic pathways. *Nature Chemistry*, July 2022. DOI: 10.1038/s41557-022-00999-w.
47. Turchin VF. *The phenomenon of science. Cybernetic approach to human evolution*. New York, Columbia University Press, 1977.
48. Krivitsky VA., Mishinsky GV., Starostin VI. Planetary nucleosynthesis and ore formation. Bose-Einstein spin condensate of atomic electrons and atomic nuclei. Moscow, *LLC "MAKS Press" Publ., Smirnov Proceedings* – 2019:246-265.
49. Mishinsky GV., Krivitsky VA., Starostin VI. Quantum geology. The feasibility of nucleosynthesis not only in stars, but also on planets in the process of their evolution. Moscow, *LLC "MAKS Press" Publ., 2021, Smirnov collection* – 2020:96-136.
50. Mishinsky GV., Starostin VI. Quantum geology is a scientific discipline born of a new scientific revolution. Planetary nucleosynthesis and ore formation. Moscow, *LLC "MAKS Press" Publ., 2021, Smirnov collection*–2021:155-192.
51. Grachev AF. Main problems of modern tectonics and geodynamics of Northern Eurasia. *Physics of Earth,* 1996, 12:3-32.
52. Wallner A, Froehlich MB, Hotchkis MAC, Kinoshita N, Paul M, Martschini M, Pavetich S, Tims SG, Kivel N, Yamagata T. ^{60}Fe and ^{244}Pu deposited on Earth constrain the r-process yields of recent nearby supernovae. *Science,* 2021, 372(6543):742-745. DOI: 10.1126/science.aax3972.
53. Rampino MR, Caldeira K, Zhu Yu. A pulse of the Earth: A 27.5-Myr underlying cycle in coordinated geological events over the last 260 Myr. *Geoscience Frontiers* 2021, 12:101245.
54. Barenbaum AA. *Galaxy. Solar system. Earth*. Moscow, GEOS Publ., 2002, 392 p.

MARGARITA N. RODNIKOVA

(to 90th anniversary of birth)

UDC 929.53

DOI: 10.17725/rensit.2022.14.481

October 01, 2022 marks the 90th birthday of Margarita Nikolaevna Rodnikova, Doctor of Chemical Sciences, Professor, Honored Scientist of the Russian Federation, Chief Researcher of the Institute of General and Inorganic Chemistry. N.S. Kurnakov of the Russian Academy of Sciences, a well-known specialist in the field of fundamental and applied physical chemistry of liquids and solutions.

M.N. Rodnikova was born on October 01, 1932 in Moscow into the family of Nikolai Nikolaevich Rodnikov, an employee of the Ministry of Forestry, and Elizaveta Dmitrievna (Ostapova) Rodnikova, a chemistry teacher at a Moscow secondary school. After graduating from secondary school No. 328 in Moscow in 1950, she entered the Chemistry Faculty of Lomonosov Moscow State University.

In 1955 M.N. Rodnikova graduated from the Chemistry Faculty of Moscow State University and went to work at the Kurnakov Institute of General and Inorganic Chemistry of the Academy of Sciences, to the laboratory of solutions.

Under the leadership of O.Ya. Samoilov in 1964 defended his Ph.D. thesis "Temperature dependence of the coordination numbers of alkali metal cations and halide anions in dilute aqueous solutions." In 1998 M.N. Rodnikova defends her doctoral thesis "Features of solvents with a spatial network of hydrogen bonds." In 2007, by the decision of the State Committee of the Russian Federation for Higher Education M.N. Rodnikova was awarded the academic title of professor.

In a marriage with Yuri Alexandrovich Buslaev, Margarita Nikolaevna raised two beautiful daughters – Elena and Olga.

From 1955 to the present, M.N. Rodnikova went through all the positions at her Institute from senior laboratory assistant to the head of the "Solvents with a spatial network of hydrogen bonds" group.

Margarita Nikolaevna pays great attention to the education of scientific personnel. Under her leadership, five candidates of chemical sciences and one candidate of physical and mathematical sciences were defended. She works a lot and with pleasure with students and graduate students.

From 1999 to 2003, Margarita Nikolaevna taught the course "Physical and chemical foundations of bioinorganic chemistry" at the DI. Mendeleev Russian Chemical Technical University. She developed special courses "Solutions, water, hydration" and "Features of water and hydration", which were read at Moscow State University, at the Lomonosov Institute of Fine Chemical Technology RTU-MIREA, at the Mendeleev Chemical-Technological Institute, at the University of Dortmund (Germany) and at the University of Regensburg (Germany).

Margarita Nikolaevna lectured at the conferences of young scientists on inorganic chemistry "The structure of water and hydration of ions" in Vysu (Estonia), on the theory and practice of solutions "The specifics of water

and the molecular-kinetic theory of hydration" in Ivanovo.

For 20 years M.N. Rodnikova was a member of the board of the All-Union Society "Knowledge" of the department "Chemistry". She organized the series of lectures "New in Inorganic Chemistry" at the Polytechnic Museum, "New in the Science of Solutions" at the Kurnakov Institute of General and Inorganic Chemistry of RAS.

Rodnikova Margarita Nikolaevna is a well-known and talented scientist in the field of the structure of liquids and liquid solutions. M.N. Rodnikova discovered a new class of solvents – solvents with a spatial network of hydrogen bonds. These include such vital and widely used substances in technology as water, amino alcohols, diamines, diols, glycerin, sulfuric, phosphoric acids, etc. Rodnikova M.N. the features of the physicochemical properties of these solvents and the phenomena occurring in these solutions were investigated and explained for the first time.

In recent years, Margarita Nikolaevna has proposed topological methods for describing the structure of a liquid – a condensed but mobile phase, investigated the properties of a spatial network of hydrogen bonds in liquids and solutions, studied mixed networks of hydrogen bonds in aqueous systems of diols, amino alcohols and diamines, and revealed their role in biosystems and cryobiology.

Total M.N. Rodnikova published more than 300 publications. Among her publications are about 200 articles in reputable scientific journals (the number of citations of articles in journals according to Web of Science and Scopus is more than 2000) and 5 scientific reviews.

Of particular note is the long-term leadership since 1980, and since 1986 as the Chairman, approved by the Presidium of the USSR Academy of Sciences of the All-Union, and then the All-Russian Seminar of the Academy of Sciences on the study of liquids and solutions structure, working at the Kurnakov IGIC of RAS to the present. This seminar, one of the unique phenomena in the life of Russian science, was founded in 1962 by Margarita Nikolaevna's teacher Oleg Yakovlevich Samoilov, the author of the molecular-kinetic theory of solvation and the discovery of the phenomenon of negative hydration of ions in electrolyte solutions, who managed to make the seminar a center of attraction and consolidation of research on the theory and experiment of liquids and solutions not only in the Soviet Union, but also in many countries of the world.

During the 60 years of its existence, the seminar has seen dozens of outstanding specialists not only from Russia, but also world-class specialists in the field of physical chemistry of liquids and solutions.

With her scientific activity, Margarita Nikolaevna made a significant contribution to the development of fundamental and applied physical chemistry of liquids and solutions. One of the assessments of this contribution is the honorary title "Honored Scientist of the Russian Federation", awarded to her in 2004.

High scientific erudition, efficiency, adherence to principles and responsibility brought M.N. Rodnikova deserved authority and wide popularity among the scientific community.

Friends, colleagues and students sincerely congratulate Margarita Nikolaevna Rodnikova on her glorious jubilee and wish her good health, good luck and success in her scientific and organizational activities.

The editors of the journal RENSIT of the Branch of the Russian Academy of Natural Sciences heartily join these wishes.

Editorial board RENSIT journal